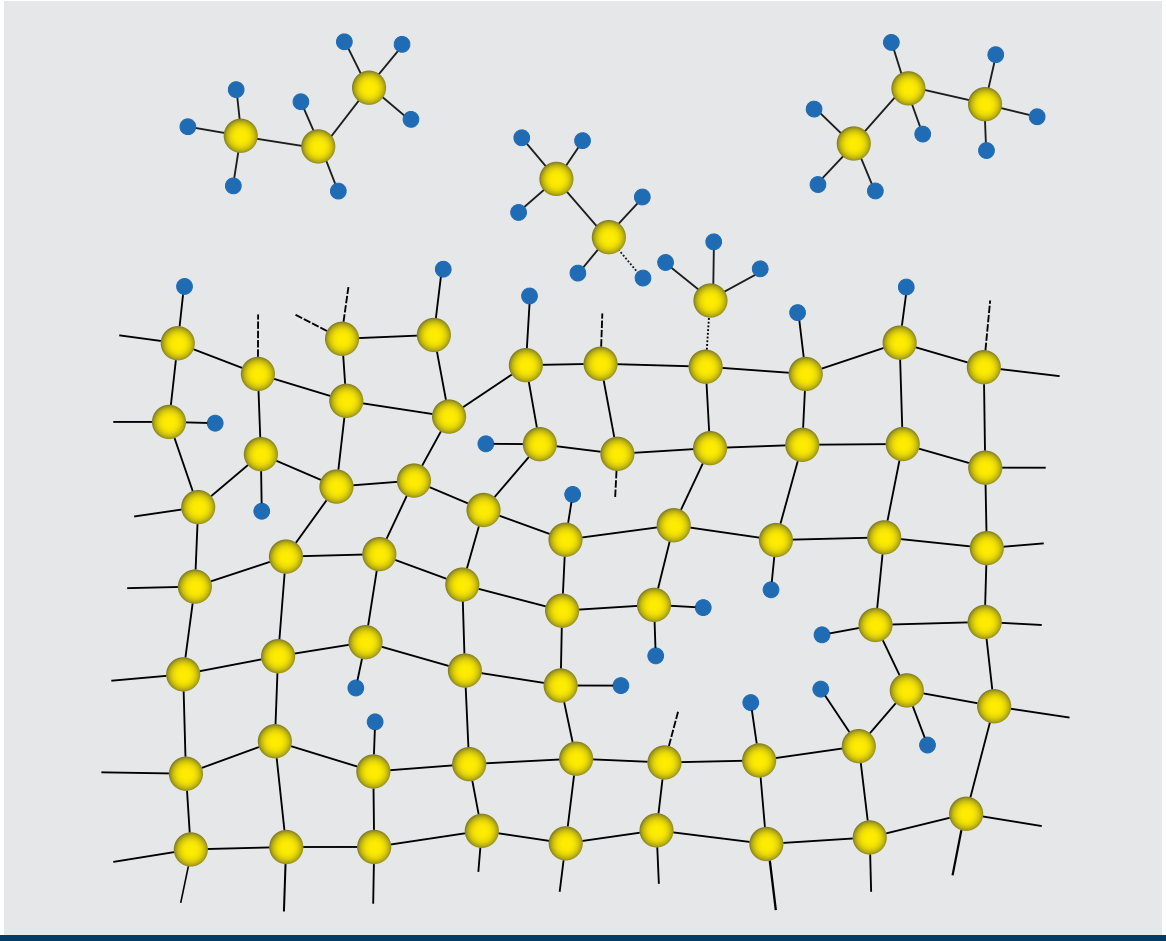


Liquid-Phase Synthesis of Silicon and Silicon Carbide Thin-Films via Atmospheric Pressure Chemical Vapor Deposition

Benedikt Fischer

Energie & Umwelt / Energy & Environment
Band / Volume 733
ISBN 978-3-95806-991-6

Mitglied der Helmholtz-Gemeinschaft

JÜLICH
Forschungszentrum

Liquid-Phase Synthesis of Silicon and Silicon Carbide Thin-Films via Atmospheric Pressure Chemical Vapor Deposition

---

Von der Fakultät für Elektrotechnik und Informationstechnik der Rheinisch Westfälischen Technischen Hochschule Aachen zur Erlangung des akademischen Grades eines Doktors der Naturwissenschaften genehmigte Dissertation

vorgelegt von
Benedikt Fischer, M. Sc. RWTH
aus Simmerath, Deutschland

Berichter: Universitätsprofessor Dr. rer. nat. Uwe Rau
Universitätsprofessor Dr.-Ing. Andrei Vescan

Tag der mündlichen Prüfung: 17.06.2026

Diese Dissertation ist auf den Internetseiten der Universitäts bibliothek online verfügbar.

Forschungszentrum Jülich GmbH
Institute of Energy Materials and Devices (IMD)
Photovoltaik (IMD-3)

Liquid-Phase Synthesis of Silicon and Silicon Carbide Thin-Films via Atmospheric Pressure Chemical Vapor Deposition

Benedikt Fischer

Schriften des Forschungszentrums Jülich
Reihe Energie & Umwelt / Energy & Environment Band / Volume 733

ISSN 1866-1793 ISBN 978-3-95806-991-6

Bibliografische Information der Deutschen Nationalbibliothek.
Die Deutsche Nationalbibliothek verzeichnet diese Publikation in der
Deutschen Nationalbibliografie; detaillierte Bibliografische Daten
sind im Internet über http://dnb.d-nb.de abrufbar.

Herausgeber und Vertrieb:	Forschungszentrum Jülich GmbH Zentralbibliothek, Verlag 52425 Jülich Tel.: +49 2461 61-5368 Fax: +49 2461 61-6103 zb-publikation@fz-juelich.de www.fz-juelich.de/zb
Umschlaggestaltung:	Grafische Medien, Forschungszentrum Jülich GmbH
Druck:	Grafische Medien, Forschungszentrum Jülich GmbH
Copyright:	Forschungszentrum Jülich 2026

Schriften des Forschungszentrums Jülich
Reihe Energie & Umwelt / Energy & Environment, Band / Volume 733

D 82 (Diss. RWTH Aachen University, 2026)

ISSN 1866-1793
ISBN 978-3-95806-990-9 (Print)
ISBN 978-3-95806-991-6 (E-Book)

Vollständig frei verfügbar über das Publikationsportal des Forschungszentrums Jülich (JuSER)
unter www.fz-juelich.de/zb/openaccess.



This is an Open Access publication distributed under the terms of the Creative Commons Attribution License 4.0, which permits unrestricted use, distribution, and reproduction in any medium, provided the original work is properly cited.

Abstract

Hydrogenated amorphous silicon (a-Si:H) and silicon carbide (a-SiC:H) thin films are essential materials for optoelectronic and photovoltaic devices. High-quality layers of these materials are typically produced using vacuum-based deposition techniques, such as plasma enhanced chemical vapor deposition (PECVD). However, these methods require expensive equipment and complex infrastructure, which limits their economic viability. Atmospheric pressure chemical vapor deposition (APCVD) offers a promising alternative, as it avoids the need for ultra-high vacuum infrastructure. Successfully addressing challenges in precursor handling, film quality, and process reproducibility could make this approach a cost-effective method for producing a-Si:H and a-SiC:H thin films.

This thesis seeks to overcome the limitations of existing APCVD systems by developing a custom-built system that can reproducibly deposit high-quality a-Si:H and a-SiC:H films using liquid precursors. The research systematically investigates how key process parameters – such as deposition temperature, deposition time, precursor volume, injection frequency, and precursor dilution with cyclooctane – affect film growth and composition, as well as hydrogen incorporation, purity, defect density, and the resulting electrical and structural properties. The goal is to use the insights gained from these investigations, together with targeted post-deposition treatments, to optimize film properties for a range of applications and thereby demonstrate that liquid precursors, particularly trisilane and 1,4-disilabutane, can enable low-temperature, scalable deposition of high-quality functional semiconductor materials when precisely controlled.

Extensive material characterization was carried out using Fourier transform infrared spectroscopy, Raman spectroscopy, spectroscopic ellipsometry, electron spin resonance spectroscopy, secondary ion mass spectrometry, X-ray photoelectron spectroscopy, and electrical conductivity measurements. For a-Si:H, films with hydrogen contents up to 10 at%, defect densities as low as $3 \times 10^{18}\,\mathrm{cm}^{-3}$ and photosensitivities up to 10^5 were achieved. While the defect density is higher than for standard PECVD

films, such hydrogen content and photosensitivity are typical for functional a-Si:H layers for semiconductor applications. The effective passivation of crystalline silicon (c-Si) substrates resulted in lifetimes of up to 1.9 ms, comparable to those achieved with standard c-Si substrates passivated using PECVD a-Si:H layers. Post-deposition hydrogenation and catalytic doping significantly enhanced electronic properties, and films crystallized without blistering into polycrystalline silicon via rapid thermal annealing, enabling high-throughput annealing processes.

APCVD using 1,4-disilabutane enabled the formation of amorphous SiC films at intermediate temperatures below 600 °C, with carbon concentrations and conductivities comparable to or exceeding PECVD analogs. Post-deposition annealing and laser crystallization facilitated the formation of a nanocrystalline SiC and Si mixture. In-situ nitrogen doping by 1,1,3,3-tetramethyldisilazane – a nitrogen, silicon, carbon and hydrogen containing molecule – during a-SiC:H deposition enabled conductivities up to $0.03\,\mathrm{S\,cm^{-1}}$, typical for n-type nanocrystalline SiC.

The findings demonstrate that APCVD, when combined with well-designed precursor chemistry and deposition control, is a cost-effective alternative for producing a-Si:H, a-SiC:H, and their crystalline derivatives. This enables new application routes in photovoltaic technologies, such as passivated contact solar cells, and in other advanced electronic devices like micro-electro-mechanical systems.

Kurzfassung

Wasserstoffhaltige amorphe Silizium- (a-Si:H) und Siliziumkarbid-Dünnschichten (a-SiC:H) sind zentrale Materialien in optoelektronischen und photovoltaischen Bauelementen. Hochwertige Schichten dieser Materialien werden typischerweise durch vakuumbasierte Abscheidungstechniken wie die plasmaunterstützte chemische Gasphasenabscheidung (PECVD) hergestellt. Diese Verfahren erfordern jedoch kostenintensive Anlagen und komplexe Infrastruktur, weswegen ihre Skalierbarkeit und Wirtschaftlichkeit limitiert sind. Die chemische Gasphasenabscheidung bei Atmosphärendruck (APCVD) stellt eine vielversprechende Alternative dar, da sie keine Ultrahochvakuum-Infrastruktur erfordert. Durch die erfolgreiche Bewältigung der Herausforderungen in Bezug auf die Handhabung der Präkursoren, die Filmqualität und die Reproduzierbarkeit des Prozesses könnte dieser Ansatz zu einer kostengünstigen Methode für die Herstellung von a-Si:H- und a-SiC:H-Dünnschichten werden.

Diese Arbeit zielt darauf ab, die Einschränkungen bestehender APCVD-Systeme zu überwinden, indem ein maßgeschneidertes System entwickelt wird, welches die reproduzierbare Abscheidung qualitativ hochwertiger a-Si:H- und a-SiC:H-Schichten aus flüssigen Präkursoren ermöglicht. Systematisch wird untersucht, wie Prozessparameter – darunter Abscheidungstemperatur, Abscheidungsdauer, Präkursorvolumen, Injektionsfrequenz sowie die Verdünnung mit Cyclooctan – das Schichtwachstum und die Zusammensetzung sowie die Wasserstoffeinlagerung, die Defektdichte und die daraus resultierenden elektrischen und strukturellen Eigenschaften beeinflussen. Das Ziel besteht darin, die aus diesen Untersuchungen gewonnenen Erkenntnisse zusammen mit gezielten Nachbehandlungen nach der Abscheidung zu nutzen, um die Filmeigenschaften für eine Reihe von Anwendungen zu optimieren. Damit wird gezeigt, dass flüssige Präkursoren, insbesondere Trisilan und 1,4-Disilabutan, bei präziser Dosierung eine skalierbare Abscheidung hochwertiger funktioneller Halbleitermaterialien bei niedrigen Temperaturen ermöglichen.

Eine umfassende Materialcharakterisierung wurde mittels Fourier-Transform-Infrarotspektroskopie, Ramanspektroskopie, spektroskopischer Ellipsometrie, Elektronen-

spinresonanzspektroskopie, Sekundärionenmassenspektrometrie, Röntgenphotoelektronenspektroskopie und Messungen der elektrischen Leitfähigkeit durchgeführt. Für a-Si:H-Filme konnten Wasserstoffgehalte von bis zu 10 at%, Defektdichten bis zu $3 \times 10^{18}\,\mathrm{cm}^{-3}$ sowie Photosensitivitäten bis zu 10^5 erzielt werden. Während die Defektdichte höher ist als bei Standard-PECVD-Filmen, sind ein solcher Wasserstoffgehalt und eine solche Lichtempfindlichkeit typisch für funktionelle a-Si:H-Schichten. Eine effektive Passivierung kristalliner Siliziumsubstrate (c-Si) ermöglichte eine Minoritätsladungsträger-Lebensdauer von bis zu 1,9 ms. Diese ist vergleichbar mit Lebensdauern in Siliziumsubstraten, welche mittels PECVD a-Si:H-Schichten passiviert wurden. Durch nachträgliche Wasserstoffanreicherung und katalytische Dotierung ließen sich die elektronischen Eigenschaften weiter verbessern. Zudem konnten die amorphen Schichten ohne Blasenbildung und Delamination zu polykristallinem Silizium umgewandelt werden, wodurch potenziell ein schneller industrieller Kristallisationsprozess ermöglicht werden kann.

Die Verwendung von 1,4-Disilabutan als Präkursor ermöglichte die Abscheidung von amorphen SiC-Schichten bei moderaten Temperaturen unterhalb von 600 °C. Die resultierenden Kohlenstoffkonzentrationen und elektrischen Leitfähigkeiten waren mit denen von PECVD-Schichten vergleichbar oder übertrafen diese. Durch thermische oder laserinduzierte Kristallisation nach der Abscheidung konnten nanokristalline Mischungen aus SiC und Si erzeugt werden. Zudem ermöglichte die Dotierung mit Stickstoff durch Zugabe von 1,1,3,3-Tetramethyldisilazan während der a-SiC:H-Abscheidung elektrische Leitfähigkeiten bis zu $0{,}03\,\mathrm{S\,cm}^{-1}$, wie sie für n-Typ-nanokristallines SiC typisch sind.

Die Ergebnisse belegen, dass APCVD in Kombination mit geeigneten flüssigen Präkursoren und präziser Prozesskontrolle eine kostengünstige Alternative zur Herstellung von a-Si:H, a-SiC:H und deren kristallinen Derivaten darstellt. Dies eröffnet neue Anwendungsmöglichkeiten in der Photovoltaik, beispielsweise für Solarzellen mit passiviertem Kontakt, sowie in modernen elektronischen Anwendungen wie mikroelektromechanischen Systemen.

Contents

Abstract i

Kurzfassung iii

Contents v

List of Figures ix

List of Tables xiii

Abbreviations xv

Symbols xix

1. Introduction 1

2. Fundamentals 6

2.1. Silicon thin films 6

2.1.1. Types and characteristics of silicon used in solar cells 6

2.1.2. Hydrogenated amorphous silicon 10

2.1.3. Surface passivation via a-Si:H 17

2.2. Silicon carbide thin films 19

2.2.1. Amorphous silicon carbide 20

2.2.2. Crystallized silicon carbide 22

2.3. Deposition of Si and SiC thin films 23

2.3.1. APCVD as an alternative to traditional methods 24

2.3.2. Recent developments in liquid silane deposition 25

2.3.3. Pyrolysis of Trisilane 29

3. Methods 32

3.1. Precursors 32

3.2. APCVD system . . . 34
3.2.1. Setup . . . 34
3.2.2. Process . . . 35
3.2.3. Temperature characteristics . . . 40
3.3. PECVD reference films . . . 41
3.4. Thin film analysis methods . . . 42
3.4.1. Fourier transform infrared (FTIR) spectroscopy . . . 42
3.4.2. Raman spectroscopy . . . 48
3.4.3. Spectroscopic ellipsometry . . . 50
3.4.4. Electron spin resonance spectroscopy . . . 50
3.4.5. Secondary ion mass spectroscopy . . . 51
3.4.6. X-ray photoelectron spectroscopy . . . 52
3.4.7. Electrical conductivity . . . 52
3.4.8. Charge carrier lifetime measurement . . . 53
3.5. Post-treatment processes . . . 54
3.5.1. Annealing . . . 54
3.5.2. Hot wire chemical vapor deposition . . . 55

4. Amorphous and crystalline silicon films 58
4.1. a-Si:H from pure trisilane . . . 58
4.1.1. FTIR spectra of APCVD and PECVD a-Si:H . . . 59
4.1.2. Microstructure and electrical properties . . . 62
4.1.3. ESR analysis of APCVD a-Si:H films . . . 67
4.1.4. Depth-resolved analysis of a-Si:H films using SIMS and KOH etching . . . 69
4.1.5. Discussion . . . 73
4.2. a-Si:H from trisilane diluted with cyclooctane . . . 76
4.2.1. FTIR spectrum of a-SiC:H films . . . 76
4.2.2. Impact of the trisilane-to-cyclooctane ratio . . . 79
4.2.3. Films deposited using highly diluted trisilane . . . 81
4.2.4. Film growth mechanism, spatial uniformity, and reproducibility 84
4.2.5. Effect of precursor injection variation . . . 90
4.2.6. Discussion . . . 94

4.3. Applications and post-treatments of APCVD a-Si:H films 97
4.3.1. Passivation of c-Si wafer 97
4.3.1.1. Deposition temperature dependency 99
4.3.1.2. Deposition time and precursor volume dependency . . 102
4.3.1.3. Light soaking 106
4.3.1.4. Passivation with carbon-containing a-Si:H 106
4.3.1.5. Discussion 108
4.3.2. Doping and hydrogenation of a-Si:H films 113
4.3.2.1. Hydrogenation 113
4.3.2.2. Catalytic doping 114
4.3.2.3. Combined catalytic doping and hydrogenation 118
4.3.2.4. Discussion 121
4.3.3. Crystallization of a-Si:H films 125
4.3.3.1. Furnace annealing 126
4.3.3.2. Rapid thermal annealing 127
4.3.3.3. Discussion 131

5. Amorphous and crystalline silicon carbide films 133
5.1. a-SiC:H deposition using disilabutane 134
5.1.1. Microstructure and electrical properties 134
5.1.2. Surface analysis 139
5.1.3. Conductivity and nitrogen doping 141
5.1.4. Discussion 144
5.2. Crystallization of a-SiC:H films 147
5.2.1. Undoped poly-SiC films 147
5.2.2. Doped poly-SiC 150
5.2.3. Laser annealing 153
5.2.4. Discussion 156
5.3. Silicon carbide films from disilabutane diluted with cyclooctane 160
5.3.1. a-SiC:H films from disilabutane and cyclooctane 160
5.3.2. Poly-SiC films from disilabutane and cyclooctane 161
5.3.3. Discussion 163

6. Conclusions and Outlook 165
6.1. Silicon Films 165
6.2. SiC Films 170

6.3. APCVD Process Optimization and Future Perspectives 172

Bibliography **175**

Acknowledgements **206**

List of Publications **208**

Curriculum Vitae **211**

A. Supplementary Figures **A 1**

List of Figures

2.1. Schematic density of state distribution in amorphous silicon 11
2.2. Schematic illustration of an hydrogenated amorphous silicon network 14
2.3. Typical FTIR spectrum of the vibrational modes of Si—H bonds in a-Si:H 15
2.4. Schematic illustration of an a-Si:H/c-Si passivated interface and an schematic band diagram of an passivated c-Si wafer 18

3.1. Structural formulas of trisilane, 1,4-disilabutane, 1,1,3,3-tetramethyldisilazane, and cyclooctane 33
3.2. Technical drawing and schematic of the APCVD system 35
3.3. Flowchart of the APCVD process 38
3.4. Flowchart of the deposition process 39
3.5. Temperature profiles of the APCVD system during heating up . . . 40
3.6. Schematic of the FTIR spectroscopy measurement principle 43
3.7. Schematic of the Raman spectroscopy measurement principle 48
3.8. Photograph and schematic of a sample for conductivity measurements 53
3.9. Schematic of an HWCVD system 56

4.1. FTIR spectra of APCVD and PECVD a-Si:H films 61
4.2. Material properties of a-Si:H films deposited using pure trisilane . . 63
4.3. Light microscope images of a-Si:H films deposited at various temperatures 66
4.4. Raman spectra showing the 480 cm^{-1} peak of amorphous silicon . . 66
4.5. ESR results of a-Si:H films deposited at T_d = 400–500 °C 68
4.6. SIMS depth profiles of PECVD and APCVD a-Si:H films 71
4.7. R measured by Raman along a thickness gradient on an a-Si:H film 72
4.8. FTIR spectra of a-Si:H films made with pure and diluted trisilane . 78
4.9. Material properties of a-Si:H films deposited using various trisilane-cyclooctane mixtures 80

4.10. SIMS depth profiles of APCVD films deposited at 440 °C with a TS concentration of 100 vol% and 2 vol% 81
4.11. Material properties of a-Si:H films deposited using 2 vol% trisilane diluted in cyclooctane 82
4.12. Spatial uniformity of the film growth 86
4.13. Fit of the thickness d calculated by the growth model to the measured thickness of samples from the Time2 series 89
4.14. Arrhenius plot obtained by plotting the logarithm of r_d versus the inverse deposition temperature 89
4.15. Material properties of a-Si:H films deposited with varying precursor injection numbers 91
4.16. SIMS depth profiles of a-Si:H films deposited with varying precursor injection numbers 93
4.17. FTIR spectra of a-Si:H passivation films on n-type wafers 100
4.18. Charge carrier lifetime, passivation layer thickness, and hydrogen concentrations of a-Si:H-covered n-type and p-type c-Si wafers versus deposition temperature 101
4.19. Charge carrier lifetime and hydrogen concentrations of a-Si:H covered n-type c-Si wafers versus passivation layer thickness 103
4.20. Raman spectra of Si-H modes within a-Si:H layers used for passivation 105
4.21. a-Si:H film properties before and after H-treatment 114
4.22. Schematic of various catalytic doping layer stacks 116
4.23. Influence of catalytic doping and post-deposition treatments on the conductivity of a-Si:H films 117
4.24. Influence of catalytic doping in combination with hydrogenation on the conductivity of a-Si:H films 120
4.25. Raman and FTIR spectra of via furnace-annealing crystallized samples 128
4.26. Raman spectra and conductivity measurements of via RTA crystallized samples 130

5.1. FTIR spectra of a-SiC:H films deposited at temperatures between 500 and 600 °C 135
5.2. SIMS depth profiles of a-SiC:H thin films 137
5.3. Raman spectra of a-SiC:H films deposited at temperatures between 500 and 600 °C 138
5.4. XPS atomic composition at the surface of a-SiC:H films 140

5.5. Conductivity of a-SiC:H films deposited with and without N doping 141
5.6. FTIR spectra of nitrogen-containing a-SiC:H films 142
5.7. SIMS depth profiles of a-SiC:H films deposited with DB and a DB-TMD mixture 143
5.8. FTIR spectra and related parameters of a-SiC:H films annealed at various temperatures 148
5.9. SIMS depth profiles of a-SiC:H films before and after annealing at 1100 °C 149
5.10. Raman spectra of SiC films as-deposited and after annealing 150
5.11. Conductivity and FTIR spectra of crystallized SiC films with varying TMD content and annealing temperature 152
5.12. SIMS depth profiles of doped and undoped poly-SiC films 153
5.13. Microscope image of a laser-crystallized SiC film 155
5.14. FTIR spectra of a SiC film before and after laser crystallization . . 155
5.15. FTIR spectra of a-SiC:H films deposited using DB-CO mixtures . . 161
5.16. FTIR spectra of poly-SiC films deposited using DB-CO mixtures . 162

A.1. Photograph of the APCVD deposition system assembled inside a glove box . . . . . A 1
A.2. ESR spectra of a-Si:H films deposited with pure trisilane . . . . . A 2
A.3. SIMS depth profiles of an a-Si:H film deposited by two precursor injections . . . . . A 2
A.4. FTIR spectra of a-Si:H films deposited using trisilane concentrations of 1–100 vol% diluted in cyclooctane . . . . . A 3
A.5. FTIR spectra of a-Si:H films deposited with 2 vol% trisilane diluted in cyclooctane . . . . . A 4
A.6. Raman spectra of a-Si:H films deposited using 2 vol% trisilane diluted in cyclooctane . . . . . A 5
A.7. ESR spectra of a-Si:H films deposited with 2 vol% trisilane diluted in cyclooctane . . . . . A 6
A.8. SIMS depth profiles of three APCVD films deposited under identical conditions . . . . . A 7
A.9. PL picture of n-type c-Si wafers covered with a-Si:H passivation layers A 8
A.10. Charge carrier lifetime after light soaking of a-Si:H-covered n-type c-Si wafers versus passivation layer thickness . . . . . A 8

A.11. Passivation comparison of a-Si:H films deposited via pure TS and 2 vol% TS diluted in CO . . . . . A 9
A.12. Conductivity of via furnace-annealing crystallized silicon films . . . A 10
A.13. Raman and FTIR spectra of via RTA crystallized samples . . . . . A 10
A.14. SIMS depth profiles of crystallized Si films after furnace annealing and rapid thermal annealing . . . . . A 11
A.15. SIMS depth profiles of a Si film before and after furnace annealing . A 11
A.16. Correlation between Si-O/Si-C-H_x and C-H modes . . . . . A 12
A.17. FTIR spectra of crystallized SiC films before and after HF-etching . A 12
A.18. Raman spectra of crystallized SiC films, deposited using various concentrations of TMD . . . . . A 13
A.19. XPS atomic composition at the surface of undoped and doped c-SiC films . . . . . A 13
A.20. Raman intensity of Si-H bonds on several positions of laser crystallized SiC . . . . . A 14
A.21. Bond densities n in c-SiC films deposited using TS-DB mixtures . . A 14
A.22. Conductivity of c-SiC films deposited using DB-CO mixtures . . . . A 15

List of Tables

3.1. Specifications of the liquid precursors used in this study based on the data sheets from the suppliers. 33
3.2. PECVD deposition parameters for intrinsic a-Si:H layers used for SHJ solar cells at the research center in Jülich 42
3.3. Infrared active modes, categorized into C-related, H-related, and O-related modes, along with their absorption strength 47
3.4. Raman active mode positions with their associated vibrations and literature references 49

4.1. Properties of an i2-layer film as used in SHJ solar cells, produced by PECVD 59
4.2. Deposition parameters of various sample series prepared using pure trisilane 62
4.3. Deposition parameters of various sample series prepared using trisilane-cyclooctane mixtures 76
4.4. Deposition parameters of the different passivation sample series 99

5.1. Minimum, average, and maximum atomic carbon density n_C according to SIMS depth profiles on a-SiC:H films 137

Abbreviations

a-Si:H	Hydrogenated Amorphous Silicon
a-SiC:H	Hydrogenated Amorphous Silicon Carbide
APCVD	Atmospheric Pressure Chemical Vapor Deposition
C	Carbon
c-Si	Crystalline Silicon
CC BY	Creative Commons Attribution
CO	Cyclooctane
CPS	Cyclopentasilane
CVD	Chemical Vapor Deposition
CW	Continuous Wave
CZ	Czochralski
DB	1,4-Disilabutane
DOS	Density of States
EPR	Electron Paramagnetic Resonance
ESR	Electron Spin Resonance
FTIR	Fourier Transform Infrared Spectroscopy
FWHM	Full Width at Half Maximum
FZ	Float-Zone
FZJ	Forschungszentrum Jülich
H	Hydrogen
HF	Hydrofluoric Acid
HW	Hot-Wire

HWCVD	Hot Wire Chemical Vapor Deposition
IBC	Interdigitated Back Contact
IMD-3	Institute of Energy Materials and Devices - Photovoltaics
IR	Infrared
ITO	Indium Tin Oxide
KOH	Potassium Hydroxide
LO	Longitudinal Optical
LS	Light Soaking
LVD	Liquid Vapor Deposition
MEMS	Microelectromechanical Systems
MOSFET	Metal-Oxide-Semiconductor Field-Effect Transistor
N	Nitrogen
nc-Si / µc-Si	Nano- / Microcrystalline Silicon
nc-SiC / µc-SiC	Nano- / Microcrystalline Silicon Carbide
O	Oxygen
P	Phosphorus
PECVD	Plasma Enhanced Chemical Vapor Deposition
PL	Photoluminescence
poly-Si	Polycrystalline Silicon
poly-SiC	Polycrystalline Silicon Carbide
QSSPC	Quasi-Steady-State Photoconductance
RF	Radio Frequency
RTA	Rapid Thermal Annealing
SE	Spectroscopic Ellipsometry

SHJ	Silicon Heterojunction
Si	Silicon
SiC	Silicon Carbide
SIMS	Secondary Ion Mass Spectrometry
TA	Transversal Acoustic
TMD	1,1,3,3-Tetramethyldisilazane
TO	Transversal Optical
TOPCon	Transparent Conductive Oxide Passivating Contact
TPCD	Transient Photoconductance Decay
TS	Trisilane
UV	Ultraviolet
XPS	X-ray Photoelectron Spectroscopy

Symbols

α	Absorption coefficient [cm^{-1}]
χ_{DB}	Disilabutane concentration in precursor [vol%]
χ_{TMD}	Tetramethyldisilazane concentration in precursor [vol%]
χ_{TS}	Trisilane concentration in precursor [vol%]
Δn	Excess carrier concentration [cm^{-3}]
μ_B	Bohr magneton [J/T]
ν	Frequency [Hz]
ρ	Density [$g\,cm^{-3}$]
σ	Electrical conductivity [$S\,cm^{-1}$]
σ_d	Dark conductivity [$S\,cm^{-1}$]
σ_{ph}	Photoconductivity [$S\,cm^{-1}$]
σ_{se}	Photosensitivity
τ	Charge carrier lifetime [µs]
τ_{bulk}	Bulk charge carrier lifetime [µs]
$\tilde{\nu}$	Wavenumber [cm^{-1}]
$\tilde{\nu}_R$	Raman shift [cm^{-1}]
A	Absorbance
A_{plate}	Deposition area [cm^2]
A_S	Absorption strength [cm^{-2}]

B	Magnetic field strength [T]
c_{A}	Hydrogen area concentration [cm]
c_{C}	Carbon concentration [at%]
c_{H}	Hydrogen concentration [at%]
d	Film thickness [nm]
D_0	Diffusion coefficient prefactor [$\mathrm{m^2\,s^-1}$]
D_{H}	Hydrogen diffusion coefficient [$\mathrm{m^2\,s^-1}$]
d_{max}	Maximum achievable film thickness for a given precursor volume
E_{A}	Activation energy [eV]
E_{b}	Bonding energy
E_{d}	Diffusion energy [eV]
E_{F}	Fermi energy
g	g-value
h	Planck constant [Js]
I	Integrated absorption peak intensity [$\mathrm{cm^{-1}}$]
I_0	FTIR reference light intensity [a. u.]
I_{S}	FTIR sample light intensity [a. u.]
I_σ	Current [A]
k_{b}	Boltzmann constant, [$\mathrm{m^2\,kg\,s^{-2}\,K^{-1}}$]
l	Gap between electrodes [mm]
M	Molar mass [g/mol]
n	Bond density [$\mathrm{cm^{-3}}$]
N_0	Molecular number of trisilane at the beginning of the deposition

N_A	Avogadro constant
n_C	Atomic carbon density [cm^{-3}]
N_DOS	Density of States
N_d	Molecular number of trisilane deposited on the heated area
n_H	Hydrogen bond density [cm^{-3}]
n_Si	Atomic density of silicon in amorphous silicon [cm^{-3}]
n_S	Spin density [cm^{-3}]
N_TS	Molecular number of trisilane within a given trisilane volume
p	Pressure [mbar]
$P\mathrm{d}$	Plasma power [W]
Q_H2	Hydrogen flow rate [sccm]
Q_SiH4	Silane flow rate [sccm]
R	Microstructure parameter
r_d	Precursor deposition rate [$\%\,\mathrm{min}^{-1}$]
r_l	Precursor leak rate [$\%\,\mathrm{min}^{-1}$]
S_eff	Effective surface recombination velocity [cm/s]
S_front	Front surface recombination velocity [cm/s]
S_rear	Rear surface recombination velocity [cm/s]
T	Temperature [K or °C]
t	Time [s]
T_a	Annealing temperature [°C]
T_d	Deposition temperature [°C]
t_d	Deposition time [min]

T_{IR}	Transmittance
U	Voltage [V]
u_{TS}	Trisilane ulilization
V_{P}	Precursor volume [µL]
W	Wafer thickness [mm]
w	Electrode distance [mm]

1. Introduction

Hydrogenated amorphous silicon (a-Si:H) and silicon carbide (a-SiC:H) thin films are essential materials in various optoelectronic applications, including solar cells, thin-film transistors, anti-reflection coatings, microelectromechanical systems (MEMS), and biomedical applications.[1–6] Traditionally, these materials are deposited using processes like plasma-enhanced chemical vapor deposition (PECVD) or hot wire chemical vapor deposition (HWCVD), which offers excellent control over film properties but requires vacuum infrastructure and sophisticated gas handling systems. As the demand for cost-effective and scalable manufacturing processes increases, alternative deposition techniques are gaining attention.[7]

Thermal activated atmospheric pressure chemical vapor deposition (APCVD) is a promising alternative that eliminates the need for vacuum equipment and allows for continuous processing, potentially lowering production costs and increasing throughput. However, the application of APCVD to a-Si:H and a-SiC:H film deposition has remained limited, primarily due to challenges in precursor selection, process control, and achieving film qualities comparable to vacuum-based methods.[7, 8]

While the decomposition products resulting from pyrolysis of liquid precursors were already analyzed in the 1960s [9], it was in 2006 when Shimoda et al. [10] used liquid precursors to form a-Si:H films via pyrolysis. From this point on, several investigations on this kind of thin film deposition have been done by multiple groups.[8, 11–13] Unlike conventional gas-phase precursors, liquid precursors offer ease of handling and wide applicability not only in solution but also in vapor processes at atmospheric pressure. In addition, liquid precursor can be used for local deposition processes or other specialized processes such as Si deposition in nanopores.[14] In addition, liquid precursor promises a lower temperature for thermal decomposition compared to gaseous precursors like monosilane (600 °C) or methylsilane (750 °C).[15, 16]

While most investigations were conducted on the deposition of thin films via cyclopentasilane [11, 17, 18], Paolo Bedini [19] used better available trisilane (TS, Si_3H_8) to produce inks for the a-Si:H thin film deposition. In addition, a first test

of the deposition using pure trisilane was made, resulting in a-Si:H films deposited at temperatures down to 425 °C. However, the high volatility of the precursor led to reproducibility and process control issues, which made a reliable evaluation of the film properties complicated. To bridge this knowledge gap, this work presents a new version of the APCVD apparatus designed to improve the reproducibility of the deposition and the capability to use untreated trisilane as precursor. With this new tool, a large process parameter space is explored, seeking to improve the quality of the deposited a-Si:H thin films.

Many of the liquid processes found in literature are made using silicon containing inks solved in cyclooctane for improved handling and the possibility of thin film production by spin coating.[20–22] Cyclooctane (CO, C_8H_{16}) was used as a suitable, widely available solvent with a stable carbon ring, which is important to avoid carbon contamination of the amorphous Si films. However, no investigation has been performed on the influence of the solvent on the a-Si:H film properties yet. Therefore, another key topic will be the investigation of the possible incorporation of cyclooctane-related carbon into the film and its influence on the film properties. The deposition of a-Si:H films using pure and diluted trisilane was systematically investigated to understand growth mechanisms, film properties, and the effects of dilution and deposition parameters. The entire deposition parameter space comprises five dimensions: cyclooctane dilution, deposition temperature, deposition time, precursor volume, and number of precursor injections.

While carbon is undesirable in pure a-Si:H films, also research on liquid-processed a-SiC:H films has been done in the literature, mainly by using a two-component liquid precursor containing polyhydrosilanes and hydrocarbons.[23] However, this approach requires pre-processing of the precursor – such as annealing – to form Si-C bonds prior to deposition. In addition, the Si-C bond density in the resulting a-SiC:H films was rather low. Therefore, in this work 1,4-disilabutane (DB, $C_2H_{10}Si_2$) is employed as a precursor already containing a stoichiometric amount of silicon and carbon bonds for the thin film deposition of a-SiC:H.

Beyond characterizing the as-deposited intrinsic a-Si:H and a-SiC:H films, this work evaluates their functional potential by investigating their passivation behavior, hydrogenation and doping capabilities, and their suitability for crystallization into polycrystalline silicon (poly-Si) and polycrystalline silicon carbide (poly-SiC). The surface passivation of crystalline silicon in silicon heterojunction solar cells remains a central challenge for achieving high-efficiency devices and is therefore a subject of

significant research interest.[24–28] Typically, passivation mechanisms are studied using PECVD-deposited films. Interestingly, optimal passivation is observed in underdense a-Si:H films that exhibit a high hydrogen content and a substantial density of voids [24, 25]. By investigating passivation using thermally deposited a-Si:H films, deposited at varying substrate temperatures to control the defect density, this study will provide further insight into the passivation mechanism at the c-Si interface and the influence of a-Si:H film properties.

As the hydrogen content in a-Si:H films strongly influences their electrical performance, hydrogenation via radical treatment is explored as a method to optimize their electrical properties. Doping of amorphous silicon films without hydrogenation was a huge challenge in the beginning of its investigation due to a high defect density.[29, pp. 1–3] Only well-hydrogenated films with low defect concentrations can be effectively doped, making the realization of doped silicon and silicon carbide films a crucial step toward industrially applicable material.[29, pp. 1–3] Therefore, for a-Si:H, the recently emerging method of catalytic doping [30–32] is tested as a post-deposition approach for dopant incorporation. For a-SiC:H and poly-SiC films, in situ nitrogen (N) doping is explored by introducing 1,1,3,3-tetramethyldisilazane (TMD, $\left[(CH_3)_2SiH\right]_2NH$) into the deposition chamber during film growth.

Poly-Si and poly-SiC films are widely used in electronic and photovoltaic applications, such as in transparent conductive oxide passivating contact (TOPCon) solar cells, and are typically fabricated by crystallizing a-Si:H and a-SiC:H films. [33, 34] A major challenge during this process is film delamination (blistering).[35, 36] Therefore, the crystallization behavior of a-Si:H and a-SiC:H films is of particular interest, as pyrolytically deposited films with a lower hydrogen content may exhibit greater resistance to delamination.

By combining fundamental material insights with application-oriented processing strategies, this study situates itself at the intersection of precursor chemistry, thin-film engineering, and semiconductor device development. The introduction of new deposition strategies and the exploration of application pathways for APCVD-derived films contribute to the ongoing transition toward low-cost, scalable, and high-performance fabrication methods for next-generation optoelectronic and photovoltaic technologies. This thesis is structured as follows:

Chapter 2 lays the theoretical foundation by presenting the key physical, structural, and chemical properties of hydrogenated amorphous silicon (a-Si:H) and silicon carbide (a-SiC:H) thin films. The chapter also reviews conventional deposition techniques and

gives an overview of recent developments with regard to APCVD and the use of liquid precursors.

Chapter 3 describes in detail the precursors, experimental setups, and characterization techniques used throughout this work. This includes the development of a tailored APCVD system and the description of the deposition process. In addition, the applied thin film analysis methods are explained: Fourier transform infrared (FTIR) spectroscopy to analyze the H concentration c_{H}, the Si-H bonding configuration, and the incorporation of carbon, Raman spectroscopy used for structural analysis, spectroscopic ellipsometry for thickness measurements, electron spin resonance (ESR) spectroscopy for investigating paramagnetic states, secondary ion mass spectrometry (SIMS) for the determination of the atomic composition, X-ray photoelectron spectroscopy to investigate the bonding structure and atomic decomposition near the film surface and a custom-built setup for electrical conductivity measurements. Subsequently, setups for post-treatment procedures, such as annealing, hydrogenation, and doping, are presented.

Chapter 4 focuses on the deposition of a-Si:H films using pure and diluted trisilane, examining the influence of process parameters on film growth, reproducibility, and material properties. This chapter also evaluates the functional potential of the films through passivation of crystalline silicon (c-Si) wafers, hydrogenation, catalytic doping, and crystallization into polycrystalline silicon (poly-Si). These investigations aim to demonstrate the applicability of a-Si:H films deposited with APCVD in device-relevant processes.

Chapter 5 extends the approach to the deposition of a-SiC:H films using disilabutane as a novel single-source precursor. The structure, electrical behavior, and doping potential via 1,1,3,3 tetramethyldisilazane of these films are studied systematically. This chapter also includes results on the crystallization of amorphous SiC films into polycrystalline SiC (poly-SiC), using either furnace or laser annealing. Finally, it addresses the effect of cyclooctane dilution on both the a-SiC:H and poly-SiC film properties.

Finally, in Chapter 6, the key findings of the investigation are summarized, providing an overview of the contributions made throughout the thesis. The results are discussed in relation to the original objectives, highlighting the successful development and characterization of APCVD-deposited a-Si:H and a-SiC:H films, as well as their potential applications in semiconductor technology. This chapter also outlines the implications of the findings and suggests directions for future research.

Together, the results presented in this thesis contribute to the understanding and advancement of scalable, low-temperature, atmospheric-pressure deposition techniques for group IV semiconductor films. By combining a fundamental investigation of precursor chemistry with the development of process technology and evaluation of material functionality, this work aims to bridge the gap between laboratory-scale experiments and application-oriented thin-film semiconductor processing.

2. Fundamentals

In this chapter, the fundamental concepts and materials investigated in this thesis are introduced. The chapter begins with an overview of silicon thin films, focusing on hydrogenated amorphous silicon (a-Si:H). The properties of a-Si:H, including its structure, electronic and optical characteristics, hydrogenation, and diffusion behavior, are discussed in detail. Next, the fundamentals of silicon carbide thin films are explored, differentiating between amorphous and crystallized forms. Finally, deposition methods for silicon and silicon carbide thin films are covered, with a focus on atmospheric pressure chemical vapor deposition (APCVD) and recent developments in liquid silane deposition.

2.1. Silicon thin films

This section provides a brief overview of the various types of silicon thin films, with a particular focus on hydrogenated amorphous silicon (a-Si:H), which is the primary material explored in this work. The specific properties of a-Si:H will be examined, like its structural characteristics, electronic and optical behavior, and other key factors that make it a material of choice in fields such as photovoltaics and microelectronics.

2.1.1. Types and characteristics of silicon used in solar cells

The growth of thin films is one of the most essential parts of the semiconductor industry. Among the diverse range of materials available, Silicon (Si) is one of the oldest and best known materials for the use in thin film devices, first found in its pure form in 1823 by Berzelius.[37, p. 150] It is the most widely employed semiconducting material and is applied in almost all semiconductor devices such as diodes, transistors, batteries, solar cells, and more.[12, 38–40]

Pure silicon can occur in different forms.[41] In the following, crystalline silicon in wafer form, as used as an absorber in solar cells, is introduced first. Subsequently, the three types of silicon thin films are described, and their applications are outlined.

- **c-Si wafer – crystalline silicon wafer:**

  Due to its four valence electrons, silicon (Si) can form a monoatomic cubic crystal structure. Crystalline silicon (c-Si) represents the purest form of silicon, characterized by a low defect density, which makes it the standard substrate for the fabrication of advanced semiconductor structures.[42, pp. 16–17] Its highly ordered lattice provides the highest electronic mobility among the various forms of silicon. Crystalline silicon exhibits an indirect band gap of 1.1 eV at 300 K.[43] In contrast to direct band gap semiconductors, indirect semiconductors like c-Si have lower photon absorption probabilities near the band edge. Nevertheless, c-Si is particularly well-suited for photovoltaic applications due to its near-optimal band gap for solar energy conversion, its natural abundance in the Earth's crust, the resulting low production costs, and the extensive manufacturing experience that enables the production of highly pure, defect-free material.[42, pp. 16–17] These advantages have made c-Si the most widely used absorber material for large-scale solar cell production. Its comparatively weak absorption near the band edge is compensated by using relatively thick wafers, typically between 100 µm and 200 µm in combination with improved light management using textured surfaces.

  Crystalline silicon wafers are thin slices cut from monocrystalline or multicrystalline silicon ingots. These ingots are made from liquid silicon at high temperatures above the melting point of 1414 °C.[44, p. 156] Multicrystalline silicon is produced by directional solidification (DS), resulting in wafers composed of multiple c-Si grains with typical grain sizes above one millimeter. While multicrystalline Si wafers dominated the solar cell market in the early 2010s,[45] they are no longer employed as absorber material in industrial solar cells today due to the high losses associated with defects at the grain boundaries. Instead, high-quality monocrystalline silicon is used.[46–48] Two main methods are commonly employed to produce monocrystalline Si: (i) the float zone (FZ) process, which yields ultra-low defect densities, and (ii) the more cost-effective Czochralski (CZ) process, which has improved significantly and is now capable of producing solar-grade wafers with sufficiently low defect density.

  At the surface of monocrystalline Si, the periodic crystal order is interrupted, resulting in a high density of defects due to unsaturated (dangling) bonds. These surface states can act as recombination centers for charge carriers by introducing

energy levels within the band gap. To suppress such recombination losses, the unsatisfied (dangling) bonds at the surface must be saturated. This process is known as *surface passivation*.[49] Effective surface passivation is crucial for achieving high efficiencies in monocrystalline Si-based solar cells.

In this work, monocrystalline Si wafers are used as substrate material for the deposition of silicon and silicon carbide layers, which are then characterized in terms of their physical and electrical properties. Furthermore, the deposited films are evaluated for their potential as surface passivation layers for monocrystalline silicon.

- **poly-Si – polycrystalline silicon:**

  Similar to multicrystalline silicon, polycrystalline silicon (poly-Si) consists of multiple silicon crystals with varying orientations. While the term "multicrystalline Si" typically refers to wafer materials with large grain sizes above 1 mm, the term "polycrystalline Si" is commonly used for crystalline silicon thin films not grown by directional solidification but by a thin film deposition method like chemical vapor deposition (CVD) often combined with an subsequent annealing step. This results in a fully crystallized material with grain sizes below 1 mm.[41] The low grain size results in a high proportion of grain boundaries within the material that exhibit high defect densities due to structural disorder, internal stress, and unsatisfied (dangling) bonds.

  Historically, poly-Si thin films were employed as an absorber material in thin film solar cells as a cost-effective alternative to mono- or multicrystalline Si wafer-based solar cells.[50] However, with the decreasing production costs of monocrystalline silicon and its superior electrical properties, the use of poly-Si as an absorber material has declined significantly. Today, in modern photovoltaic technologies, poly-Si is primarily used as a functional layer rather than the main absorber. For instance, in transparent oxide passivating contact (TOPCon) solar cells, poly-Si is implemented as a highly conductive, doped contact layer to collect charge carriers generated in the mono c-Si substrate.[51]

  Although numerous methods exist to fabricate poly-Si thin films, this work focuses on the formation of polycrystalline silicon thin films by thermal recrystallization of amorphous silicon (a-Si) layers. This process typically involves annealing at temperatures above 600 °C.[33]

- **a-Si:H – hydrogenated amorphous silicon:**

  In addition to crystalline forms of silicon, hydrogenated amorphous silicon (a-Si:H) is widely used in semiconductor devices. Amorphous silicon (a-Si) exhibits short-range order similar to that of crystalline silicon, characterized by fourfold coordination and an average bond angle of approximately 109°.[29, p. 36] However, unlike crystalline silicon (c-Si), where the bond angles are fixed and periodicity extends over long distances, the bond angles in a-Si vary slightly, resulting in a disordered, nonrepetitive structure and the absence of long-range order. This disordered bonding network leads to a high density of unsatisfied (dangling) bonds, which act as electronic defects in a-Si films. Consequently, a-Si was initially considered unsuitable for semiconductor applications.[29, pp. 1–3]

  In the late 1960s and 1970s, it was discovered that the incorporation of hydrogen into a-Si significantly improves its electrical properties.[29, pp. 1–3] Hydrogen atoms, with a single valence electron, can passivate dangling silicon bonds, thus reducing the defect density. As a result, amorphous silicon is typically used in its hydrogenated form, known as hydrogenated amorphous silicon (a-Si:H), for device applications.

  In photovoltaic technology, a-Si:H has long been used to fabricate thin-film solar cells, serving both as an absorber and in doped functional layers. These solar cells are cost-effective and can be deposited on large-area substrates. However, due to their relatively low power conversion efficiency of approximately 10 % [52–54], similar to poly-Si solar cells, they have been unable to compete with high-efficiency c-Si-based technologies in large-scale production. Nevertheless, a-Si:H films continue to play an important role in modern electronics, including displays, thin-film transistors, diodes, and solar cells. In particular, in silicon heterojunction (SHJ) solar cells, a-Si:H is used as a critical surface passivation layer.

  A central focus of this study is the deposition of a-Si:H using APCVD with the liquid precursor trisilane (TS, Si_3H_8) and the investigation of its potential applications. Therefore, the structural and electrical properties of a-Si:H films will be discussed in more detail in Section 2.1.2.

- **nc-Si/µc-Si – nano-/microcrystalline silicon:**

  An intermediate form between a-Si:H and poly-Si is called nanocrystalline silicon (nc-Si) or microcrystalline silicon (µc-Si). For this material, small silicon crystals

are embedded within an a-Si:H matrix, while the prefix “nano” or “micro” refers to the grain sizes of the crystal.[41] To avoid confusion, we will use the term “nc-Si” throughout.

Similar to a-Si, nc-Si films are used as passivation and charge carrier transport layers in SHJ solar cells. While the conductivity of nc-Si films is improved compared to a-Si:H films, the passivation quality is usually reduced since H diffusion within dense nc-Si is limited.[55]

In this work, no fabrication of nc-Si films is intended. However, when a-Si:H films are annealed to produce polysilicon films, the a-Si:H films intermediately switch to nc-Si during crystallization. However, the usual way to produce nc-Si is the deposition by using, e.g., plasma enhanced chemical vapor deposition, since, similar to a-Si:H films, nc-Si needs incorporated H that passivates open bonds at the grain boundaries and within the amorphous phase.[56] The formation of the nanocrystalline structure is strongly influenced by the specific deposition conditions, which must be carefully adjusted to promote crystallite growth within the amorphous matrix.

2.1.2. Hydrogenated amorphous silicon

In contrast to c-Si, the absorption behavior of a-Si:H resembles that of a direct band gap semiconductor due to the absence of a well-defined crystal momentum k, which relaxes the momentum conservation rule for optical transitions. The structural disorder leads to localized electronic states and a broader band gap compared to that of crystalline silicon. Consequently, a-Si:H exhibits a larger band gap of approximately 1.5–2 eV [57], as opposed to 1.1 eV in c-Si. The exact value of the band gap depends on the amount of H within the a-Si:H film.

Due to the lack of long-range order, an energy-momentum dispersion relation cannot be defined for a-Si:H. However, the energy-dependent density of states (DOS) remains a valuable concept for understanding its electronic properties. A schematic DOS distribution for amorphous silicon is shown in Figure 2.1. The density of states in a-Si:H consists of three primary contributions:[29, pp. 16–17]

- **The Bands**: The bands in a-Si:H resemble a “smoothed” version of the c-Si DOS, with bonding states forming the valence band and antibonding states forming the conduction band.

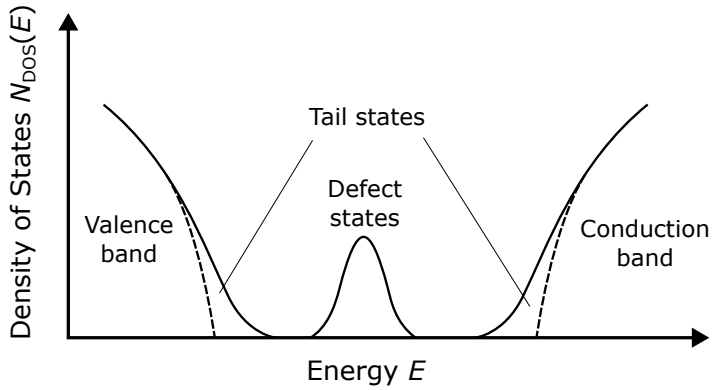


Figure 2.1.: Schematic representation of the density of states in amorphous silicon as a function of energy. The diagram indicates the valence and conduction band states, the band tails, and the deep defect states. Dashed lines represent the corresponding density of states in crystalline silicon. Redrawn from R. A. Street [29, p. 10].

- **The Band Tails**: The band tails arise from atomic lattice disorder, extending into the band gap and creating localized states. These localized states significantly influence both electronic transport and optical behavior. The slope of the band tails is described by the Urbach energy, which quantifies the exponential decay of the density of states and reflects the structural and thermal disorder within the material.[29, pp. 88–91]

- **The Deep Defect States**: The defect states, particularly the dangling bonds, are energetically located deep within the band gap and result from structural defects. Dangling bonds exhibit amphoteric behavior, meaning that they can exist in multiple charge states, with energy levels typically around 0.8–0.9 eV below the conduction band. These defect states contribute to the overall electronic properties of a-Si:H and play a critical role in its optical and transport behaviors.

As a consequence of the larger, but direct band gap, compared to c-Si, a-Si:H has a higher absorption coefficient α for photons with high energy ($E_\mathrm{p} > 1.7\,\mathrm{eV}$), a lower α for photons with an energy between the c-Si and a-Si:H band gaps, and a higher α for photons with $E_\mathrm{p} < 1.1\,\mathrm{eV}$ due to the high density of defect states in a-Si:H.[29, pp. 83–89, 58]

Electronic and optical properties

The electrical properties of intrinsic a-Si:H strongly depend on the defect density of the film. A key measure of film quality is the photosensitivity σ_{se}, which is defined as the ratio of the photoconductivity σ_{ph} to the dark conductivity σ_d:

$$\sigma_{se} = \frac{\sigma_{ph}}{\sigma_d} . \tag{2.1}$$

Within this work, the photoconductivity is defined as the sum of the dark conductivity and the increase in conductivity caused by additional charge carriers generated under illumination (equivalent to 1 sun). High-quality films with low impurity levels and low defect densities exhibit photosensitivities at room temperature exceeding 10^5, with a photoconductivity σ_{ph} of approximately $10^{-5}\,\mathrm{S\,cm^{-1}}$ and a dark conductivity σ_d of around $10^{-10}\,\mathrm{S\,cm^{-1}}$.[59]

For intrinsic a-Si:H films, a low σ_d indicates a low defect density and minimal unintentional doping. A high defect density increases the density of states within the band gap, enhancing electron-hopping probability and, consequently, dark conductivity. Conversely, a high σ_{ph} usually suggests a greater charge carrier mobility and/or a lower charge carrier recombination rate, since the charge carrier concentration is only determined by the illumination intensity and recombination rate for $\sigma_{ph} \gg \sigma_d$. Defects in the a-Si:H network hinder charge carrier mobility in the conduction band for excited electrons but increase the probability of hopping electrons under dark conditions. Therefore, a high defect density in a-Si:H reduces σ_{ph} and increases σ_d, resulting in a photosensitivity close to 1.[29, pp. 16–17]

To enhance the dark conductivity of silicon, doping atoms are intentionally introduced into the material to achieve either n-type or p-type doping. N-type doping involves the incorporation of impurity atoms with five valence electrons, such as phosphorus (P), arsenic (As), or nitrogen (N), into a four-fold coordinated semiconductor lattice like crystalline silicon. These dopant atoms contribute an additional electron to the system, which is only weakly bound and can be thermally excited into the conduction band. This process increases the concentration of free electrons and enhances the electrical conductivity of the material.[60, 61]

P-type doping, on the other hand, is achieved by introducing trivalent impurity atoms, such as boron (B) or aluminum (Al), into the semiconductor lattice. These dopants create electron-deficient sites, known as holes, by forming incomplete covalent bonds with surrounding semiconductor atoms. The presence of holes facilitates charge

transport via electron hopping, effectively increasing the hole concentration and electrical conductivity of the material.

While doping is highly effective in crystalline silicon, the less ordered structure of a-Si:H limits the ability of doping atoms to achieve fourfold coordination. Instead, most dopant atoms are incorporated in coordination environments corresponding to their preferred valence states, rendering them electrically inactive. The fraction of dopants incorporated with four-fold coordination, leading to active doping, is very low. Consequently, the doping efficiency in a-Si:H is also low.[62]

Next to the insertion during the deposition process, dopants can be introduced after film deposition. A recently developed promising way is the catalytic doping process, in which a HWCVD system is used to introduce doping atoms into the substrate.[30–32] This doping process is tested in Section 4.3.2.2, and the experimental procedures are explained in detail in Section 3.5.2.

Hydrogenation

Although theoretically all elements with a single valence electron, such as chlorine (Cl), could be used to passivate dangling bonds in a-Si, hydrogen (H) has emerged as the preferred choice for incorporation into a-Si films. Beyond its natural presence in most silicon-containing precursors, hydrogen also exhibits significantly higher diffusivity within a-Si compared to other elements, making it particularly effective for passivation.[63] In addition to passivating defects in the a-Si matrix, hydrogen significantly influences the structural, electrical, and optical properties of a-Si:H. Consequently, the microscopic integration of hydrogen – specifically the microstructural configuration of Si-H bonds – is of great interest. [64] A schematic representation of the microscopic structure of amorphous silicon with incorporated hydrogen is shown in Figure 2.2. The illustration highlights the random network of Si atoms, various Si–H bonding configurations (Si–H, Si–H_2, Si-H bonded in voids), and dangling Si bonds that contribute to the structural and electronic properties of a-Si:H. It should be noted that this schematic serves only as a simplified representation of the actual amorphous network and is intended to illustrate the general bonding configurations rather than depict an exact atomic arrangement.

Although a hydrogen content of only 0.2 at% would be sufficient to passivate all dangling bonds, a-Si:H films typically contain hydrogen concentrations of 10–30 at% since the defect formation and saturation process in a-Si:H follows a near equilibrium reaction.[65–69] The hydrogen content significantly influences the properties of a-Si:H,

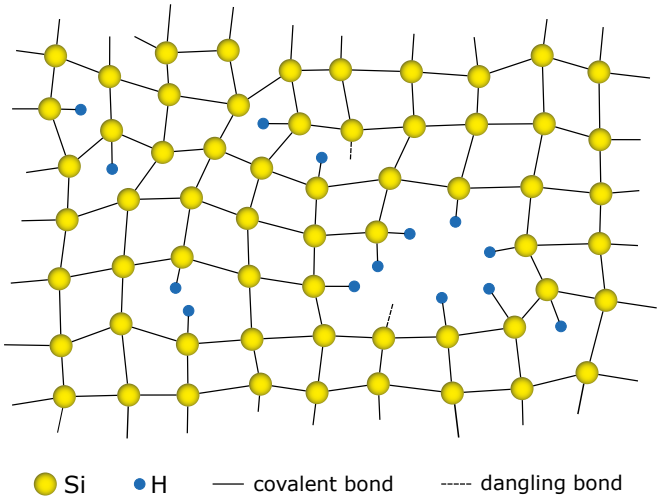


Figure 2.2.: Schematic illustration of a hydrogenated amorphous silicon network. Silicon atoms (yellow) are arranged in a random, amorphous network, while hydrogen atoms (blue) are bonded either within the silicon matrix or at internal void surfaces. Dangling bonds associated with threefold-coordinated silicon atoms are indicated by dashed lines.

including its optical band gap. As the hydrogen concentration increases, the optical band gap and the refractive index increase.[70, pp. 241–242] Further, a higher hydrogen content also leads to a lower film density.[71]

In addition to the total hydrogen content within the a-Si:H film, the microstructure of the Si-H bonding configuration also plays a crucial role in determining the properties of the material. This microstructure can be analyzed by examining the wagging, bending, and stretching vibrations of Si-H_x bonds, which typically exhibit wavenumbers of 640 cm^{-1}, 800–900 cm^{-1}, and 2000–2150 cm^{-1}, respectively.[72] These vibrations are commonly detected using techniques such as Fourier transform infrared (FTIR) or Raman spectroscopy. The most important vibrations are listed in Tables 3.3 and 3.4.

While all modes contribute to the peak at 640 cm^{-1}, only Si-H_2 and Si-H_3 configurations contribute to the wagging mode peak in the range of 800–900 cm^{-1}, with Si-H_3 bending modes are located at slightly higher wave numbers than Si-H_2 bending modes.[72, 73] Several models have been proposed to describe the peaks around 2000–2100 cm^{-1}, with peaks in this region often being assigned to three or more distinct Si-H_x species.[74, 75] However, FTIR and Raman spectra are most commonly fitted using a model involving two separate Gaussian peaks, one around 2000 cm^{-1} and

another around 2100 cm^{-1} as indicated in Figure 2.3. The peak at 2000 cm^{-1} is typically attributed to vibrations of hydrogen bonded to silicon within a dense a-Si network, while the peak at 2100 cm^{-1} is associated with more void-rich and porous material.[72, 76]

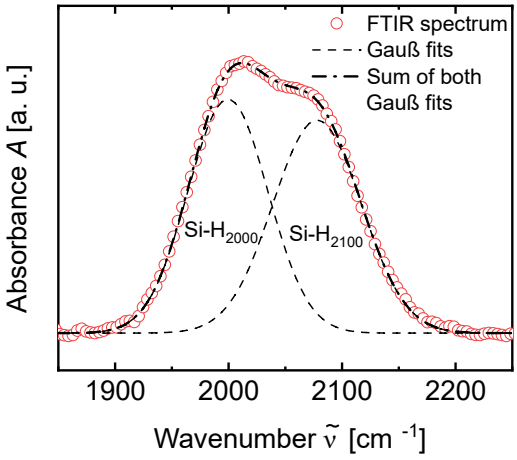


Figure 2.3.: A typical spectrum of the vibrational modes of Si—H bonds in a-Si:H measured by FTIR spectroscopy (red dots). The proportion of H contributing to either the peak at 2000 cm^{-1} ($Si\text{-}H_{2000}$) or 2100 cm^{-1} ($Si\text{-}H_{2100}$) is identified by fitting a Gaussian double peak to the measured signal.Adapted from an illustration originally created for the Master's thesis of the author (B. Fischer, 2022) [77].

In some cases, the peak at 2100 cm^{-1} is primarily assigned to $Si\text{-}H_2$ vibrations.[73, 78] However, this assignment is incomplete, as the 2100 cm^{-1} peak has been observed without the accompanying peak in the 800–900 cm^{-1} region, suggesting that Si-H vibrations at 2100 cm^{-1} originate from Si bonded to only one hydrogen atom.

Since each Gaussian peak in the double-peak structure corresponds to either a more dense or less dense a-Si:H network, the ratio of the two peaks was introduced as a characteristic value to describe the microstructure of a-Si:H. This ratio is referred to as the microstructure parameter R, which is calculated as:[79, 80]

$$R = \frac{I_{2100}}{I_{2100} + I_{2000}}. \tag{2.2}$$

The integrated (absorption) peak intensities I_{2000} and I_{2100} can be determined from Raman or FTIR spectra.[81, 82] In this study, FTIR spectra are used to calculate R. A more detailed procedure for obtaining the peak intensities is provided in Section 3.4.1.

With increasing H content also R increases, since the H is not distributed equally throughout the film but starts to accumulate in voids or clusters, especially for concentrations above 10 at%.[83] Furthermore, it has been observed that hydrogen bonded within a dense network (associated with the 2000 cm^{-1} peak) contributes effectively to the reduction of dangling bonds in a-Si:H material. In contrast, hydrogen bonded in voids (associated with the 2100 cm^{-1} peak) does not contribute to a reduction in defects and may even increase defect density, possibly due to bonding strains resulting from void formation.[84, p. 20, 85]

Diffusion

The microstructure plays a crucial role in determining the diffusion behavior of hydrogen in a-Si:H. The diffusion process can be divided into two main mechanisms, depending on the hydrogen-bonding configuration. The first mechanism involves hydrogen hopping between trapping states, primarily associated with dangling bonds. This type of diffusion can be described by the thermally activated diffusion coefficient D_H [86]:

$$D_H = D_0 \exp\left(-\frac{E_d}{k_b T}\right), \tag{2.3}$$

where D_0 is the diffusion coefficient prefactor, E_d is the diffusion energy, k_b is the Boltzmann constant, and T is the temperature. Studies of hydrogen diffusion in a-Si:H have revealed fluctuations in D_0 [55, 86, 87], suggesting that, in addition to dangling bonds, weak or strained Si-Si bonds act as shallow traps. These bonds can break and form stable Si-H bonds, leading to the creation of new dangling bonds. The energy gained by breaking a weak bond and saturating one of the resulting dangling bonds with hydrogen is lower than that for saturating existing dangling bonds. This is why such hydrogen trapping is referred to as a shallow trap, leading to a different D_0.[86].

The second diffusion process, commonly observed in a-Si:H with a high hydrogen content, is associated with diffusion through interconnected voids. In this mechanism, two hydrogen atoms that are in proximity react to form H_2 and potentially a new Si-Si bond.[86] It was found that molecular hydrogen can diffuse much more easily through the porous amorphous network than hydrogen diffusing by hopping between trapping states. This is in agreement with the fact that effusion experiments have shown that

the H_2 effusion peaks at a lower temperature of 385 °C, compared to the effusion of single atomic hydrogen, which peaks at temperatures above 500 °C.[88, pp. 220–225]

Although no hydrogen effusion experiments were conducted on the films in this study, both hydrogen diffusion and effusion processes are of significant interest since the deposition temperatures used in this exceed 400 °C. This is well above the hydrogen mobility temperature of approximately 100 °C [29, p. 52] and also higher than the effusion temperature of around 300 °C, at which hydrogen begins to be released from the film.

An important aspect to consider when characterizing the material is that deposition at temperatures above 400 °C can lead to significant out-diffusion of hydrogen bonded in voids, which strongly reduces the 2100 cm^{-1} peak in FTIR spectra.[89] In contrast, H bonded in dense material – corresponding to the 2000 cm^{-1} peak – is less effused. As a result, the films might have a low microstructure parameter R, despite the actual presence of voids in the material.

In addition, the fact that H is highly diffusive in a-Si:H will be used to introduce H into the a-Si:H films investigated in this work to improve their quality. Further details of this process are given in Section 3.5.2 and the results are given in Section 4.3.2.1.

2.1.3. Surface passivation via a-Si:H

The passivation process refers to the reduction or elimination of the effects of surface defects, dangling bonds, and surface states that can lead to charge carrier recombination. Basically, two types of passivation are distinguished: i) *chemical passivation* describing the reduction of defect states, and ii) *field effect passivation* leading to the repulsion of minority charge carriers from the defect-rich surface.[92]

Intrinsic a-Si:H layers can act as surface passivation layers for c-Si wafers using both passivation effects.[93] As schematically illustrated in Figure 2.4 a), chemical passivation is achieved by the saturation of c-Si surface defects with hydrogen. Field effect passivation occurs due to band bending at the hetero interface caused by the larger band gap of a-Si:H in contrast to that of c-Si. The band bending acts as an energy barrier that leads to a repulsing effect for charge carriers and can be optimized by appropriate doping. Figure 2.4 b) illustrates the principle of field-effect passivation using the band diagram of a c-Si wafer coated with intrinsic, n-type, and p-type a-Si:H layers, as employed in SHJ solar cells. The figure shows that electrons are repelled on the p-side, while holes are repelled on the n-side, thereby reducing recombination through defect states at the interface (indicated by red bars).

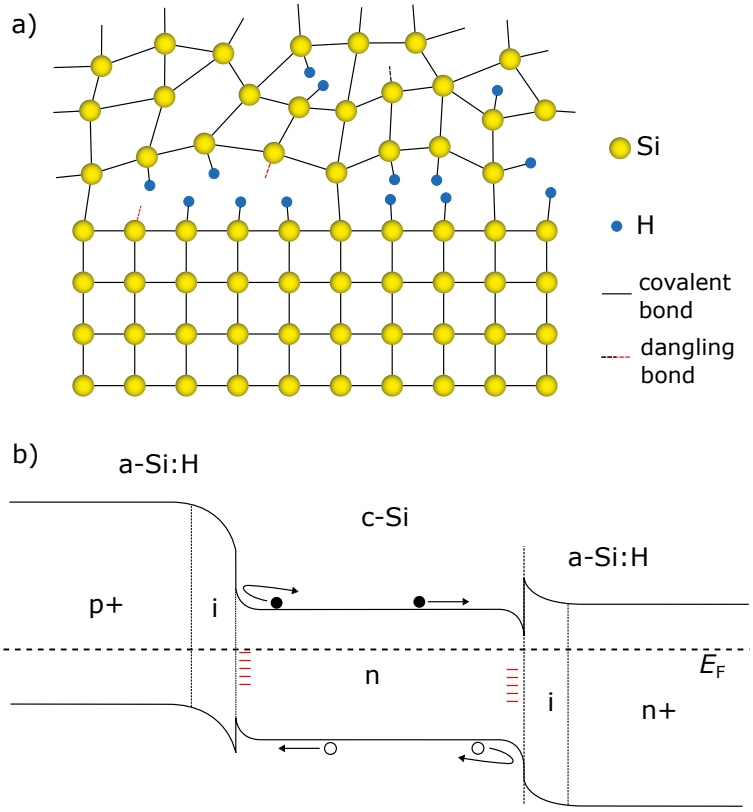


Figure 2.4.: a) Schematic illustration of an a-Si:H/c-Si interface passivated with hydrogen atoms (chemical passivation). Unpassivated dangling bonds at the interface, which significantly reduce the minority carrier lifetime, are indicated by red dashed lines. b) Schematic band diagram of a c-Si wafer passivated with doped and undoped a-Si:H layers, as typically employed in SHJ solar cells. The dashed line indicate the Fermi level. The arrows indicate the field-effect passivation, resulting from the repulsion of electrons at the p-side and holes at the n-side, which effectively suppresses charge-carrier recombination at surface defect states (red bars). Redrawn based on Wang et al. [90] and Shi et al. [91].

A measure of the passivation quality is the effective surface recombination velocity S_{eff}. The lower the surface recombination velocity, the higher the passivation quality. The effective surface recombination velocity inversely correlates with the charge carrier lifetime as [94, pp. 51–52]

$$\frac{1}{\tau} = \frac{1}{\tau_{\text{bulk}}} + \frac{S_{\text{front}}}{W} + \frac{S_{\text{rear}}}{W}\,. \tag{2.4}$$

Here, S_{front} and S_{rear} are the effective surface recombination velocities on the front side and the rear side of the wafer, respectively, and τ_{bulk} is the bulk charge carrier lifetime. Equation 2.4 shows that when using a constant τ_{bulk}, the charge carrier lifetime τ inversely correlates with S_{eff} and therefore is a good measure for the passivation quality of a-Si:H films. This fact will be used in Section 4.3.1.

2.2. Silicon carbide thin films

Silicon carbide (SiC) can exist in various forms similar to silicon, including monocrystalline, polycrystalline, amorphous, and nano- or microcrystalline structures. However, unlike pure silicon, SiC consists of two elements, silicon (Si) and carbon (C), which introduce an additional degree of freedom in its structural variations. This results in a range of crystal formations, known as polytypes. Common examples include cubic (3C-SiC) and hexagonal (4H-SiC or 6H-SiC) structures.[95, pp. 7–8]

Furthermore, altering the Si-to-C ratio can lead to phase mixtures, such as silicon clusters embedded in a hydrogenated amorphous silicon carbide (a-SiC:H) matrix. Each type of SiC possesses distinct electrical and mechanical properties, making the material highly versatile for various industrial applications.[96–98]

Historically, research on SiC, particularly polycrystalline SiC, has focused on its mechanical properties to develop materials with high strength, chemical resistance, thermal stability, and abrasion resistance for applications such as ceramic or steel coatings.[99] More recently, however, attention has expanded to its electro-optical properties. Compared to silicon, SiC offers advantages such as a higher melting temperature, wider band gap, higher optical transmission, exceptional chemical stability, and a high breakdown voltage.[100]

Crystalline and amorphous silicon carbide (SiC) are widely used across various technological fields. In power electronics, SiC-based MOSFETs and diodes enable efficient high-voltage operation, significantly reducing energy losses. Hydrogenated amorphous

SiC (a-SiC:H) finds applications in optoelectronics, including solar cells, thin-film transistors, and antireflection coatings.[1–4] In photovoltaics, SiC is integrated into advanced solar cell architectures such as tunnel oxide passivated contact (TOPCon) and all-silicon tandem solar cells, improving electrical conductivity and surface passivation.[34, 101–103] Additionally, it has been tested in silicon heterojunction (SHJ) structures [2]. Beyond that, SiC is used in sensors, microelectromechanical systems (MEMS), and as a stable protective film in harsh environments.[5, 104, 105] In biomedical applications, SiC serves as a passivation material for implantable devices due to its biocompatibility and resistance to degradation under physiological conditions [6].

Given the numerous structural variations of SiC, this section will focus on the most relevant forms discussed throughout this work, specifically (understoichiometric) a-SiC:H and its crystallized structures, such as polycrystalline SiC (poly-SiC).

2.2.1. Amorphous silicon carbide

The fundamental differences between a-SiC:H and crystalline SiC arise primarily from the absence of a long-range order, a characteristic common to all amorphous materials.[29, p. 3] This lack of structural periodicity eliminates the momentum conservation rule, resulting in a band structure similar to that of a direct band gap material. Further, general effects resulting from the amorphous structure, such as defect formation and DOS are discussed in more detail in Section 2.1.2.

The structure of a-SiC:H consists of a highly disordered tetrahedrally coordinated network of silicon and carbon atoms. While some studies suggest that a-SiC:H contains mainly heteronuclear Si-C bonds, there is also evidence for the presence of homonuclear Si-Si and C-C bonds, which influence its electronic and optical properties [106, 107]. Thermodynamically, C-C bonds have higher bonding energy than Si-Si bonds, making their formation more favorable [108]. However, the relative proportion of these bonds and the overall atomic composition strongly depend on the stoichiometry of the material and its deposition conditions.

Depending on its microstructural properties, the optical band gap of a-SiC:H can be tuned between 1.6 and 3 eV.[1, 108] While the Urbach energy of a-Si:H films typically ranges from 40 to 60 meV, it increases up to 250 meV with the incorporation of carbon into the material due to higher disorder. Moreover, at high carbon concentrations, the absorption edge no longer follows an exponential behavior.

In addition to Si and C, as in a-Si:H, hydrogen is typically present in a-SiC:H, where it plays a crucial role in influencing the electrical properties by passivating dangling

bonds. Due to the higher degree of disorder, a-SiC:H generally exhibits a higher defect density compared to that of a-Si:H. The bonding energy of C-H is typically higher than that of Si-H bonds, which can be attributed to the higher electronegativity of carbon (2.5) compared to silicon (1.74).[108] Within a-SiC:H, the higher electronegativity of carbon strengthens Si-H bonds when carbon is bonded to the silicon atom as a backbond. Vice versa, C-H bonds are weaker, when the carbon has a silicon backbond. The enhanced strength of the Si-H bond contributes to a higher H effusion peak temperature of a-SiC:H compared to a-Si:H.[109, 110]

Fourier transform infrared (FTIR) spectroscopy is commonly used to analyze the hydrogen bonding configuration in a-SiC:H. The Si-H vibrational modes in a-SiC:H occur at wavenumbers similar to those of a-Si:H. Si-H bending vibrations are observed at 640 cm^{-1}, while Si-H stretching modes appear in the same region as in a-Si:H, ranging from 2000 cm^{-1} to 2150 cm^{-1}. However, the peak at 2000 cm^{-1} for H in dense material is typically absent in a-SiC:H, as the wavenumber of Si-H stretching vibrations with a carbon backbond is shifted to 2100 cm^{-1}.[111, 112] The presence of a peak at 2000 cm^{-1} would indicate the formation of large clusters of a-Si:H, suggesting a low carbon content in the a-SiC:H film.

For the Si-H vibrations in voids that occur at 2100 cm^{-1} for a-Si:H, no shift in the wavenumber of those vibrations has been reported in a-SiC:H.[112] Moreover, the classification of Si-H bonds based on their location in dense material or voids is uncommon for a-SiC:H films, probably due to the structural complexity of this three-component (Si, C, and H) system. Consequently, some studies propose that the shift of the Si-H mode to 2100 cm^{-1} is not due to carbon backbond but rather to H in voids or clusters in a-SiC:H.[113] This interpretation suggests that carbon incorporation disorders the silicon network, preventing the uniform distribution of hydrogen in a dense structure. However, this hypothesis contrasts with hydrogen effusion measurements, which indicate higher effusion temperatures for a-SiC:H films compared to a-Si:H films.[110]

Si-H bending vibrations in the range of 800–900 cm^{-1} are typically not analyzed in a-SiC:H films, as they are overlapped by peaks originating from carbon-related vibrations within the material. The most dominant of these is the peak between 720 and 780 cm^{-1}, which corresponds to Si-C stretching vibrations. The exact position of this peak shifts depending on the stoichiometry and microstructure of the a-SiC:H film. Additionally, wagging and rocking vibrational modes arising from C-Si-H_x configurations ($1 \leq x \leq 3$) are observed around 980 cm^{-1}.[111, 114–117] Further C-Si-H_x-related modes appear

in the range of 1250–1500 cm^{-1} [108], although these peaks are typically weaker and often obscured by noise in FTIR measurements. C-H stretching vibration modes can be observed in the range of 2850–2960 cm^{-1}.[108, 114] In contrast, C-C bonds are difficult to detect using FTIR and are challenging to assign unambiguously. However, they can be identified more clearly using Raman spectroscopy, where they appear at approximately 1450 cm^{-1}.[118] The most significant FTIR and Raman modes are listed in Chapter 3.

2.2.2. Crystallized silicon carbide

Hydrogenated amorphous silicon carbide (a-SiC:H) can be transformed into polycrystalline silicon carbide (poly-SiC) through annealing. The transition temperature varies between 800 °C and 1100 °C, depending on the deposition method and the precursor used.[119, 120] For stoichiometric films, the resulting material is polycrystalline silicon carbide (poly-SiC). In contrast, silicon-rich films can crystallize into either a mixture of crystalline silicon (c-Si) and crystalline silicon carbide (c-SiC) or c-Si embedded within an amorphous SiC (a-SiC) matrix.[120] The crystallization temperature of the c-Si grains is strongly influenced by the silicon-to-carbon (Si:C) ratio and decreases with increasing silicon content.[34]

In addition to poly-SiC, c-Si/c-SiC, and c-Si/a-SiC mixtures, an appropriate temperature-to-time ratio during oven annealing may lead to the formation of nanocrystalline silicon carbide (nc-SiC), which corresponds to a c-SiC/a-SiC mixture. However, for technical applications, nc-SiC is typically hydrogenated and is often used for the passivation of monocrystalline Si wafers.[102, 121] The formation of nc-SiC films via annealing results in hydrogen effusion from the film, making this fabrication method unfavorable for the production of nc-SiC films.

As stated at the beginning of Section 2.2, c-SiC can exist in various polytypes.[95, pp. 7–8] While different polytypes exhibit significant variations in material properties, they generally possess a higher band gap and greater conductivity compared to amorphous silicon carbide (a-SiC).[122, 95, pp. 295–302]Consequently, in this work, the annealing of a-SiC:H films will focus on maximizing the crystalline SiC fraction without specifically investigating the polytype structure in detail.

The only measurement technique used in this work that provides information about the polytypes is Raman spectroscopy. Raman spectroscopy of thick, large-grained poly-SiC films exhibits distinct peaks in the spectrum, allowing for differentiation between cubic and hexagonal polytypes. However, for thin poly-SiC films with small

grain sizes, these peaks may appear wider and weaker.[123, 124, pp. 95–98] A detailed discussion of the Raman measurements can be found in Section 5.2.

A reliable indicator of structural changes in SiC is the Si-C stretching peak at 720–780 cm^{-1} in FTIR spectra. A broad Gaussian peak at lower wavenumbers typically indicates an amorphous structure, whereas a sharper Lorentzian peak around 780 cm^{-1} is characteristic of crystalline material.[125] It remains unclear whether the height of the Lorentzian peak directly correlates with the crystalline volume fraction or instead inversely correlates with stress in Si-C bonds.[126] However, since bond stress in amorphous material arises from structural disorder, a reduction in stress can also indicate increased crystallinity. Therefore, following the approach proposed by Weiss et al. [127], in this work the shape and height of the Si-C stretching mode are used as a measure of the crystallinity of the material.

Doping of poly-SiC films enables a wide range of conductivities, with doping efficiency strongly dependent on both the doping type and the deposition process. In PECVD-deposited films, conductivities have been achieved between 10^{-9} and 10^{-3} S cm^{-1} for n-type doping, while p-type doping typically results in conductivities ranging from 10^{-8} to 10^{-5} S cm^{-1}.[128–130] In contrast, HWCVD-deposited films exhibit significantly higher doping efficiencies, with reported conductivities ranging from 10^{-7} to 10^{0} S cm^{-1} for n-type films and 10^{-5} to 10^{-1} S cm^{-1} for p-type films.[131, 132]

During the fabrication of intrinsic poly-SiC films, unintentional n-type doping is often observed as well. Although the exact cause remains unclear, this effect is commonly attributed to the incorporation of nitrogen or oxygen impurities during the deposition process.[131, 133–135]

In this work, nitrogen doping will be investigated. Correlating the intentional increase in nitrogen content and the unintentionally incorporated oxygen content with the electrical conductivity of the films, as discussed in Section 5.2.2, may provide further insight into the nitrogen and oxygen doping processes.

2.3. Deposition of Si and SiC thin films

This section gives an overview of the potential of APCVD as a viable substitute for traditional methods. In addition, the most recent developments in liquid-phase deposition techniques for the growth of silicon and silicon carbide thin films are highlighted.

2.3.1. APCVD as an alternative to traditional methods

Silicon and silicon carbide films can generally be deposited using the same deposition techniques. In all of these processes, a precursor, which can be gaseous, liquid, or solid, is used as the raw material and converted into a thin film. This conversion can be achieved through various methods, with two of the most common approaches for silicon and silicon carbide films being the following:

- **Plasma enhanced chemical vapor deposition (PECVD)**:

  PECVD is one of the most commonly used deposition techniques for thin films in solar cell production.[136] As a precursor, either gases or vaporized liquids are used, such as monosilane for the deposition of a-Si:H. The substrates are placed inside a chamber between two electrodes and heated to temperatures ranging from room temperature to several hundred degrees Celsius. During the deposition process, a plasma is ignited between the electrodes, causing the precursor gas to decompose into reactive radicals. These radicals interact with the substrate surface, leading to the formation of a thin film.

- **Hot wire chemical vapor deposition (HWCVD)**:

  HWCVD is often used for the deposition of highly conductive nc-SiC films. As a precursor for HWCVD, gaseous or vaporized chemical compounds are used as well.[102, 132] The substrates are placed inside a vacuum chamber and heated to moderate temperatures, typically between 200 °C and 600 °C, depending on the desired film properties. During the deposition process, a metal filament (tungsten or rhenium) is heated to high temperatures (around 1,000–2,000 °C). The precursor gas dissociates upon contact with the hot filament, forming reactive radicals that diffuse towards the substrate, where they contribute to thin-film formation.

Further examples are electron beam epitaxy [137], magnetron sputtering [138], pulsed laser deposition [139], photo-enhanced chemical vapor deposition [140], and many others. Most of these methods require expensive infrastructure, such as the creation of ultra-high vacuum conditions, which are necessary for many of the processes.

An alternative to reduce costs by eliminating the need for ultrahigh vacuum pumps and other systems, such as a plasma generator, is thermal-driven **atmospheric pressure chemical vapor deposition (APCVD)**. APCVD is a widely used deposition

technique for thin films, particularly in large-area coatings and industrial applications.[11, 141, 142] Similarly to PECVD, gaseous or vaporized chemical compounds are used as precursors. The substrates are placed in an open reactor or conveyor system and heated to temperatures that typically range from several hundreds to over a thousand degrees, depending on the material being deposited. During the deposition process, precursor gases, which are often diluted with inert gas, flow over the heated substrate at atmospheric pressure, leading to thermal decomposition and subsequent film formation. The absence of vacuum systems makes APCVD a cost-effective and high-throughput method, although it may result in lower film uniformity compared to low-pressure techniques.

When depositing silicon-containing films, APCVD has two main disadvantages: i) A high deposition temperature ($> 600\,°C$ for monosilane [15]) is required to decompose the precursor, leading to thin silicon films with high defect densities due to hydrogen effusion during the deposition process. ii) Silanes are highly toxic and spontaneously ignite upon contact with oxygen.

To prevent precursor exposure to oxygen, the APCVD system needs to be operated in an inert gas atmosphere, for example, using a glove box. The setup of the APCVD system used in this work will be explained in Section 3.2. The challenge of high decomposition temperatures can be addressed by using silicon-containing precursors with lower decomposition temperatures. One approach is to use higher-order silanes (polyhydrosilanes), which contain Si chains that are easier to break than the Si-H bond in monosilane, resulting in a growth rate that is several orders of magnitude higher.[9, 15]

At room temperature, polyhydrosilanes containing more than three Si atoms are typically liquids.[143, p. 21] Recent research on liquid polyhydrosilanes and their use for the deposition of silicon-containing films is discussed in the next section.

2.3.2. Recent developments in liquid silane deposition

Over the past 15 years, efforts have been made to reduce the costs of thin-film deposition by using liquid silane precursors in combination with low-cost deposition techniques. In addition to a full area film production, liquid precursors have significant potential for printed electronics, enabling micropattern formation during the deposition process without the need for post-processing steps.[143, p. 3] In the following, the focus is on the full area thin film deposition using liquid precursors, which forms the

basis for all variations in the deposition process used for the patterned deposition of thin films.

For silicon films, several polyhydrosilane precursors have been tested, with a strong emphasis on the use of cyclopentasilane.[7, 11, 14, 18, 143, 144] Similarly, for silicon carbide (SiC) thin films, a variety of precursors have been explored.[1, 23, 104, 145] For SiC films, either hydrosilanes (only containing Si and H) were mixed with hydrocarbons (only containing C and H) or precursors containing Si, C, and H in one precursor (organosilanes) were used. The most recent developments for both materials are summarized in the following sections.

Liquid processes for silicon thin films

Two main deposition methods are used for the deposition of a-Si:H films using liquid precursors:

- Solidification of silane inks
- Liquid vapor deposition (LVD)

In the solidification process, polyhydrosilanes are treated with UV radiation or ultrasound and dissolved in an organic solvent, typically cyclooctane.[7, 21] This treatment results in the formation of a silicon ink containing long polyhydrosilane chains. For thin-film deposition, the ink is applied to a substrate, and the organic solvent is evaporated. A commonly used method for this is spin coating. A subsequent pyrolysis step at temperatures of 400–450 °C is then required to convert the polyhydrosilane chains into a continuous a-Si:H film, which enhances the electrical properties.[21]

In the liquid vapor deposition (LVD) process described in [143, p. 17], polyhydrosilanes are evaporated and thermally deposited onto a heated substrate. The LVD process can be carried out under an inert gas atmosphere at atmospheric pressure, making it equivalent to the APCVD deposition process introduced in Section 2.3.1. Therefore, the term APCVD will be used in this work to refer to both processes. Although liquid silanes can also be deposited using other methods, such as PECVD, [146, 147] the key advantages of liquid silanes – such as faster thermal decomposition compared to monosilane – are best utilized within the APCVD process.

There are several reasons why cyclopentasilane (CPS) is commonly used for liquid silane processes. Among cyclohydrosilanes (Si_nH_{2n}), cyclopentasilane ($n = 5$) and cyclohexasilane ($n = 6$) offer the best compromise in terms of stability and availability.

For $n < 5$, the molecules tend to be unstable, whereas for $n > 6$, the synthesis becomes more difficult. Since the properties of cyclopentasilane are better understood than those of cyclohexasilane, cyclopentasilane is typically the material of choice for most liquid silane processes [143, pp. 21–22].

Linear polyhydrosilanes (Si_nH_{2n+2}) are liquids at room temperature for $n \geq 3$. However, for $n \geq 4$, polyhydrosilanes are relatively unstable, which is why they are not often used in liquid silane processes [143, pp. 21–22]. Despite that, recently, Ito and Kamath [17] demonstrated the deposition of a-Si:H films using poly-tetrasilane ink for thin-film transistor applications. Shimoda [143, pp. 21–22] noted that trisilane ($n = 3$) is too volatile to be handled at room temperature (boiling point: 52.9 °C). In contrast, Bedini et al. [8] demonstrated the applicability of trisilane-cyclooctane mixtures in an APCVD process. For deposition, trisilane or trisilane ink was dispensed on a Petri dish, which was placed upside down on a hot plate. However, this process was indeed unstable, especially when pure trisilane was used as the precursor.[19] Therefore, improvements to the deposition system have been proposed. A key aspect of this study is the development of a stable APCVD (/ LVD) process using trisilane. Additionally, to the best of my knowledge, the influence of the trisilane/cyclooctane mixing ratio has not yet been investigated. Thus, this work also explores the effect of different concentrations of cyclooctane in the precursor on the properties of a-Si:H films.

Another advantage of using liquid precursors is the ability to introduce white phosphorus or decaborane for n-type and p-type doping, respectively, as alternatives to the hazardous phosphine or diborane gases. Using this method, amorphous silicon films have been achieved with electrical conductivities of up to $10^{-2}\,S\,cm^{-1}$ for n-type films and $10^{-4}\,S\,cm^{-1}$ for p-type films.[143, p. 58].

Films deposited with APCVD typically exhibit a higher quality than those produced by the pyrolysis of solidified silicon inks. This is evidenced, for example, by the higher photosensitivity of up to 10^5 for APCVD (LVD) films without additional treatment, compared to 10^4 for spin-coated films.[148, 149]

Using an advanced APCVD (LVD) system for the deposition of cyclopentasilane, Shen et al. [149] achieved intrinsic a-Si:H films, with the microstructure parameter decreasing from 0.93 to 0.07 as the temperature increased from 300 to 400 °C. Similarly, the band gap decreased from 1.94 to 1.48 eV, and the hydrogen content decreased from nearly 40 to 7.9 at%. The highest photosensitivity was observed for a film deposited at 360 °C, followed by a hydrogen radical treatment, which resulted in a reduction of

the defect density by one order of magnitude. The dark conductivity was measured at approximately $10^{-11}\,\mathrm{S\,cm^{-1}}$, while the photoconductivity was around $10^{-5}\,\mathrm{S\,cm^{-1}}$.

To address the existing knowledge gap, this work will use trisilane to produce films in a manner similar to the process discussed above. Due to the higher decomposition temperature of trisilane, higher deposition temperatures will be tested, which may influence the film properties.

Considering the advantages of APCVD over the solidification process, APCVD was chosen for the deposition of a-Si:H films. Furthermore, controlled chemical vapor deposition in a closed chamber allows the use of highly volatile trisilane without the need for pre-treatment to form long polyhydrosilane chains, as demonstrated by Bedini et al. [19]. This process is promising for producing semiconductor-grade a-Si:H films, achieving a high raw material conversion rate, and minimizing precursor loss.

Liquid processes for silicon carbide thin films

As for silicon thin films, several liquid precursors have been explored in the literature for the deposition of silicon carbide (SiC) thin films. The advantages of liquid processes for SiC are consistent with those for silicon films, such as reducing the cost of the deposition process.

The fabrication of SiC thin films, particularly a-SiC:H films, can be achieved using two main precursor strategies: i) a precursor containing both silicon and carbon, or ii) a mixture of polyhydrosilanes and hydrocarbons. Recently, investigations have focused on the use of cyclopentasilane mixed with hydrocarbons [143, pp. 93–135]. The results of these studies show that the carbon content in the films ranges from 30 at% to 40 at%, as measured by XPS. However, FTIR analysis revealed a Si-C bond density of approximately $3 \times 10^{21}\,\mathrm{cm^{-3}}$, which is an order of magnitude lower than the carbon content found in amorphous SiC (~$4.3 \times 10^{22}\,\mathrm{cm^{-3}}$).[150] This discrepancy is attributed to the clustering of C-C and Si-Si and a high hydrogen content within the films. The problem probably arises from a low number of Si-C bonds in the precursor. For example, a mixture of cyclopentasilane and 1-hexyne, followed by annealing to 50 °C, results in a polydihydrosilane with pendant hexyl groups, containing six carbon atoms and five silane atoms per molecule but only one Si-C bond. Thus, one of the goals of this study is to investigate the potential for increasing the Si-C bond density by using precursors that already contain Si-C bonds.

1,3-Disilabutane ($C_2H_{10}Si_2$) is one example of such precursors and has previously been used to deposit poly-SiC films at high temperatures.[145] Okada et al. [151]

investigated 1,4-disilabutane for Si thin film deposition and found its potential for SiC thin film deposition as well. Although the alternating Si and C atoms in the structure of 1,3-disilabutane might offer advantages, herein the focus is on testing 1,4-disilabutane for the deposition of a-SiC:H films due to its lower cost and better availability. The results of these tests are presented in Chapter 5.

The electrical properties of a-SiC:H films produced by liquid processes differ from those of a-Si:H films.[143, pp. 93–135] I-V measurements reveal a photosensitivity of approximately 10^2, with a photoconductivity of around $10^{-9}\,\mathrm{S\,cm^{-1}}$ and a dark conductivity of about $10^{-11}\,\mathrm{S\,cm^{-1}}$. N-type doping of spin-coated a-SiC:H films slightly improves the dark conductivity to approximately $10^{-9}\,\mathrm{S\,cm^{-1}}$.[143, p. 121] P-type doping was applied to films deposited using an APCVD system as well. However, high doping efficiencies were only achieved for films with low carbon content, suggesting that doping was effective only within the a-Si:H phase.[143, pp. 127–128] Both dopants, phosphorus and boron, were incorporated into the precursor ink using the same method as described for the a-Si:H films in Section 2.3.2. An alternative doping method for a-SiC:H films using the nitrogen-containing precursor 1,1,3,3-tetramethyldisilazane is investigated herein. The results will be discussed in Section 5.1.3, and further details on doping poly-SiC films are provided in Section 5.2.2.

2.3.3. Pyrolysis of Trisilane

The pyrolysis of thin films using liquid silanes can involve a variety of decomposition and deposition reactions.[9, 23, 152–154] In the following, the main reactions associated with trisilane are outlined, as this precursor is studied in more detail regarding its deposition ratio and activation energy in Section 4.2.4.

Several hypotheses for the reaction mechanism underlying the a-Si:H thin film deposition from trisilane have been proposed in the literature.[9, 152–154] The reaction pathways strongly depend on both the deposition temperature and the substrate.[152] In the temperature range between 380 and 600 °C, trisilane exhibits a unique temperature dependence of the a-Si:H film growth rate, resulting in significantly higher deposition rates compared to monosilane.[152, 153] Using a low-pressure CVD process, Gouyé et al. [153] reported growth rates exceeding $10\,\mathrm{nm\,min^{-1}}$ at 550 °C. This is more than an order of magnitude higher than those obtained with monosilane, which exhibited growth rates below $1\,\mathrm{nm\,min^{-1}}$. In their experiments, the precursor flow rates were adjusted so that the atomic silicon flow was identical for both precursors.

The deposition process on a Si substrate can be described as a direct reaction of trisilane with either surface vacancies (open bonds) or hydrogen-passivated Si sites.[152, 153, 155] One possible reaction involves a ligand exchange, in which hydrogen from the surface is exchanged with SiH_3 from the trisilane molecule. This reaction can be described as:[155]

$$Si_3H_8 + H^* \longrightarrow Si_2H_6 + SiH_3^*, \tag{2.5}$$

where the asterisk (*) denotes atoms or molecules bonded to the substrate surface. The fact that this reaction can occur on hydrogen-contaminated surfaces and primarily involves the cleavage of a Si-Si bond in trisilane – which is not possible for monosilane – may explain the higher growth rate at low deposition temperatures (below 600 °C) of trisilane compared to monosilane.[153, 155]

Another proposed model for the reaction chain leading to a-Si:H film growth involves a two-step process: i) initial decomposition of trisilane in the gas phase, resulting in Si_yH_x radical formation, followed by ii) subsequent deposition at the silicon surface.[9, 154] For the initial decomposition, Vanderwielen et al. [154] suggested two main reactions:

$$Si_3H_8 \longrightarrow SiH_2^{\cdot\cdot} + Si_2H_6, \tag{2.6}$$

$$Si_3H_8 \longrightarrow SiH_3SiH^{\cdot\cdot} + SiH_4. \tag{2.7}$$

Here, the dot notation ($\cdot$) denotes open radicals. The activation energies for these two reactions were calculated as 51.9 kcal mol^{-1} for the reaction in Equation 2.6 and 49.2 kcal mol^{-1} for the reaction in Equation 2.7.[154] Both values are close to the Si-Si bond energy E_b in trisilane, which is equal to 54 kcal mol^{-1}.[153] In contrast, radical formation from monosilane requires Si-H bond cleavage, with a bond energy of $E_b = 76$ kcal mol^{-1}, which significantly hinders radical generation and corresponds to the lower growth rates in comparision with trisilane observed in the temperature range between 380 and 600 °C.[9, 153, 154]

Once radicals are formed in the gas phase, they can react with the substrate surface, in a manner analogous to PECVD or HWCVD processes. The adsorption of Si_yH_x radicals on the Si substrate may proceed via multiple pathways. While a detailed discussion of these mechanisms is beyond the scope of this work, they have been extensively investigated in the literature. For instance, Park and Kim recently reported DFT simulations addressing radical adsorption [156]. Additional studies on related mechanisms can be found in [29, 157–161]. When substrates other than Si are used, the initial stages of a-Si:H growth may involve additional reactions and

mechanisms, making the processes even more complex. For instance, Li et al. [162] observed the formation of spherical a-Si:H nucleation islands on glass substrates for a PECVD process. Following their formation, a-Si:H preferentially deposits on these islands, promoting their growth and eventual coalescence. This process can cause significant changes in the microstructure of the a-Si:H layer near the substrate surface.[82]

The exact reaction mechanism underlying a-Si:H deposition from trisilane remains unclear. It is likely that the deposition involves a combination of trisilane gas-phase decomposition followed by radical-surface reactions, as well as direct trisilane-surface reactions.[163]

3. Methods

This chapter outlines the experimental procedures and analytical techniques used throughout this study. The chapter begins with a description of the chemical precursors used in the thin film deposition processes. The following sections detail the configuration and operation of the atmospheric pressure chemical vapor deposition (APCVD) system, including a comprehensive overview of the setup, process conditions, and key characteristics influencing film growth.

Subsequently, the chapter presents the characterization methods used to evaluate the structural, chemical, and electronic properties of the deposited films. These include Fourier transform infrared (FTIR) spectroscopy, Raman spectroscopy, spectroscopic ellipsometry, electron spin resonance (ESR), secondary ion mass spectrometry (SIMS), X-ray photoelectron spectroscopy (XPS), electrical conductivity measurements, and charge carrier lifetime analysis.

Finally, post-treatment steps applied to the films, such as thermal annealing and hot wire chemical vapor deposition (HWCVD), are described. These processes were used to modify and optimize the properties of the film for the intended applications.

3.1. Precursors

The precursors used in this work to produce hydrogenated amorphous silicon (a-Si:H) and silicon carbide (a-SiC:H) films via APCVD are trisilane (TS), 1,4-disilabutane (DB), 1,1,3,3-tetramethyldisilazane (TMD), and cyclooctane (CO). The structural formulas of the materials are shown in Figure 3.1.

Trisilane (TS, Si_3H_8) is used for the deposition of a-Si:H thin films. 1,4-disilabutane (DB, $C_2H_{10}Si_2$) is tested for the deposition of a-SiC:H films. For doping of the a-SiC:H films, DB is mixed with 1,1,3,3-tetramethyldisilazane (TMD, $\left[(CH_3)_2SiH\right]_2NH$). Cyclooctane (CO, C_5H_{16}) is first used as a solvent for TS to increase the precusor volume and therefore improve handling. However, for some deposition parameters, CO was included in the a-Si:H film, which is why it is listed as a precursor here. In

addition, it is used in combination with DB for the deposition of a-SiC:H films. To increase purity and reduce oxygen concentration, CO, purchased from Sigma-Aldrich, was dried over sodium and degassed using evacuate-refill cycles on an N_2-filled Schlenk line. Trisilane was purchased first from the company Voltaix LLC and then from the company Gelest Inc., with the same purity of >99.9 % for both distributors. All other precursors were purchased from Gelest Inc. and directly used for deposition without pretreatment. Further material properties of the precursors are listed in Table 3.1.

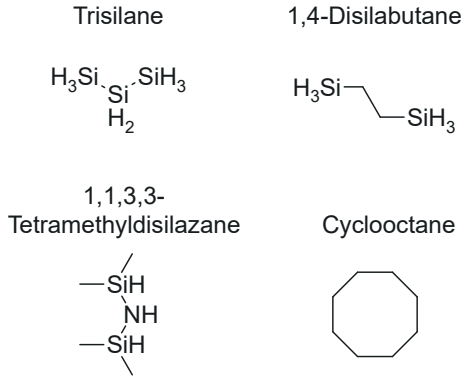


Figure 3.1.: Structural formulas of the precursors used for thin-film deposition via APCVD in this work: trisilane (TS), 1,4-disilabutane (DB), 1,1,3,3-tetramethyldisilazane (TMD), and cyclooctane (CO).

Table 3.1.: Specifications of the liquid precursors used in this study based on the data sheets from the suppliers.

	Trisilane	**1,4-Disila-butane**	**1,1,3,3-Tetra-methyldisilazane**	**Cyclooctane**
Formula	Si_3H_8	$C_2H_{10}Si_2$	$[(CH_3)_2SiH]_2NH$	C_8H_{16}
Molar Mass [g mol^{-1}]	92.32	90.27	133.34	112.21
Density [g cm^{-3}]	0.743	0.697	0.766	0.834
Melting Point [°C]	-117	-	<0	10–13
Boiling Point [°C]	52.9	45–46	99–100	151
Vapor Pressure [hPa]	127 at 0 °C	-	>33.3 at 20 °C	5.5 at 20 °C
Purity [%]	> 99.99	>99	>97	>99

3.2. APCVD system

To deposit a-Si:H and a-SiC:H films from the precursors listed above, a prototype of a low-cost APCVD system was built. While the general system was already designed at the beginning of this work, I have added some substantial improvements to make the system work, such as the inlet cooling system explained later on or a quartz glass plate to prevent contamination with metal atoms of the film and the substrate. The setup, process steps, and characteristics of the system are described in the following.

3.2.1. Setup

In the APCVD process, thin films are deposited onto a heated substrate under atmospheric pressure by means of pyrolysis out of the gas phase. The technical drawing and schematic diagram of the APCVD system are shown in Figure 3.2, a real picture of the system is shown in Figure A.1. For protection against impurities and to prevent a reaction between trisilane and oxygen (O_2), the system is built into a MBraun glove box filled with nitrogen (O_2, $H_2O < 1\,\mathrm{ppm}$). The glove box located in an air-conditioned room makes the process independent of ambient temperature and humidity. Only the ambient pressure has little influence on deposition pressure, as the glove box pressure approximately corresponds to the ambient pressure plus 3 mbar. Since changes in ambient pressure due to different weather conditions are small compared to the absolute pressure, their influence is not considered here.

An Isotemp hot plate from Fisherbrand serves as a heat source. The hot plate heats a $(6 \times 6)\,\mathrm{cm}^2$ stainless steel block and a $(10 \times 10)\,\mathrm{cm}^2$ quartz glass plate with 1 mm thickness on top of the steel block. The glass prevents contamination of sample substrates by diffusion of atoms from the steel block to the substrate. The steel block is used to conduct the heat in an area of $(6 \times 6)\,\mathrm{cm}^2$ on the glass plate because the precursor only reacts at the hot surface areas with temperatures above 400 °C. Thermocouples (type K) are used to monitor the temperature of the steel block and the precursor inlet block. In addition, the temperature of a stainless steel baffle plate is monitored, which prevents direct hitting of the precursor onto the substrate as shown in Figure 3.2 b). The temperature of the steel block is measured through a hole at the edge, which was drilled nearly to the half of the block in which the thermocouple is placed and is used as "deposition temperature" T_d within this work.

To ensure that the precursor is in the liquid phase during pumping/flushing, a Peltier element cools the inlet block that includes the precursor reservoir to temperatures

below 30 °C, well below the boiling point of trisilane (53 °C) and 1,4-disilabutane (46 °C) at 1013 hPa. The Peltier element is controlled by a PID-controller which modulates the pulse width of the Peltier element's power supply. The Peltier element heat sink is thermally connected to a hollow aluminum block through which air flows by means of a fan.

All electrical components of the system, including the dosage pump, magnet valve, Peltier element, and thermocouples, are monitored or controlled via an Arduino Mega 2560 r2 microcontroller programmed in C#. The microcontroller is connected to a computer equipped with a graphical user interface for system interaction.

On top of the hot plate, a height-adjustable head lowered to the hot plate during the process creates a closed deposition chamber with a volume of approximately 0.5 l. No special sealing was included, as no vacuum is needed.

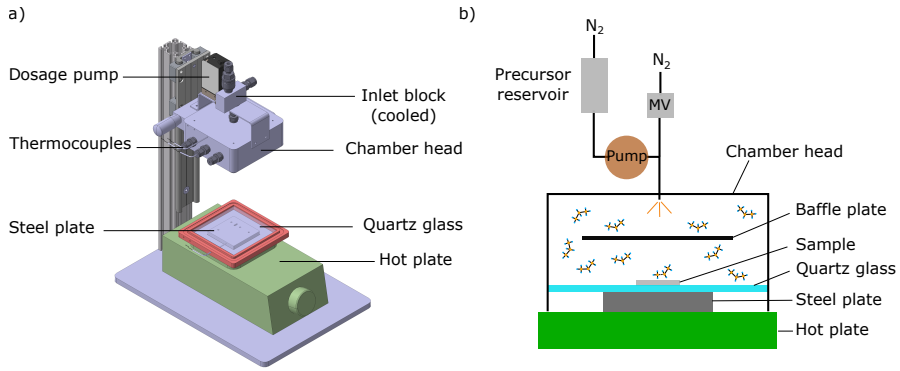


Figure 3.2.: a) Technical drawing and b) schematic of the APCVD system. The main components of the setup are indicated. Adapted from Fischer et al. [164] (2024), licensed under CC BY 3.0.

3.2.2. Process

A detailed flowchart for the application of the APCVD system described in the last section is given in Figure 3.3. Before deposition, the substrates are cleaned in an isopropyl alcohol ultrasonic bath for 10 min and subsequently stored in isopropyl alcohol to prevent contamination of the sample surface. Before being inserted into the glove box for deposition, the substrates were dried using an oil-free nitrogen gun.

As substrates, polished p-type high-resistivity c-Si (100) float-zone wafers (525 µm, 20 Ω cm) with native oxide from Siegert and boro-aluminum silicate glass (1.1 mm) from Corning type Eagel 2000 were used unless stated otherwise. 1 mm quartz glass was used for films treated at high temperatures after deposition. Each substrate was cut into (1.5 × 1.5) cm^2 peaces. One glass substrate (either boro-aluminum-silicate or quartz) and one c-Si substrate were used as substrates for each deposition. Conductivity, ESR, and Raman measurements were performed on the glass substrates. SIMS, FTIR, and XPS measurements were performed on the c-Si wafers.

Before the first deposition of a day, the chamber was flushed 5 min with nitrogen gas to flush out impurities or precursor residues. After that, the substrates are inserted into the chamber, and the chamber is closed by lowering the chamber head. When the steel block temperature reaches equilibrium (±5 °C), the desired precursor volume is inserted into the precursor reservoir of the inlet block.

The injection of the precursor into the deposition chamber, controlled via micro-controller, follows one of two procedures depending on its volume and composition. The steps for the thin film deposition by both procedures are given in Figure 3.4 and explained in the following:

- **i) Injection via dosage pump strokes** (for larger precursor volumes V_P > 100 µl)

  For depositions using larger precursor volumes, the precursor is inserted into the precursor reservoir at the inlet block via an Eppendorf pipette and then precisely dosed using a dosage pump (Micro dosing unit Type 7615 from Bürkert) with at least 5 µl dosage strokes. The precursor is first pumped into a tube located at the top of the chamber head. Then, by opening a magnetic valve for 0.1–1 s, the precursor is flushed into the deposition chamber (cf. Figure 3.2 b)). This method ensures high reproducibility in precursor dosing and film deposition and allows the provision of several precursor injections during the deposition time instead of spraying the entire precursor volume into the chamber at the beginning of the deposition process. This process is used for the sample series Temp2, Time2, Volume2, and Injection in Section 4.2.

- **ii) Injection via flushing** (for small precursor volumes V_P < 100 µl)

  For depositions using pure trisilane or 1,4-disilabutane as precursor, the small precursor volume makes precise dosing via the dosage pump impractical due to its large dead volume of 100 µl. Instead, a precise dosed precursor volume is

manually introduced into the precursor reservoir using an Eppendorf pipette. After pipetting, the precursor is flushed into the chamber by opening the dosage pump and applying nitrogen gas (0.3 bar) for 1 second. During this flushing step, the magnetic valve remains closed. This method introduces higher fluctuations in the actual precursor volume inside the deposition chamber, leading to variations in film thickness. The process is used for all sample series, despite the series Temp2, Time2, Volume2, and Injection in Section 4.2.

In both dosage cases, inside the chamber, the precursor is sprayed onto a baffle plate. There, it evaporates since the baffle plate and the overall chamber exceed 150 °C during deposition due to the heating of the hot plate. In the gas phase, the precursor is distributed within the chamber, decomposes at the hot substrate surface, and deposits as a thin a-Si:H or a-SiC:H film on the substrate. After the designated deposition time required for film growth has been waited, the process is finished by lifting the deposition chamber and removing the samples from the hot plate.

After each deposition process, the opened chamber was flushed for at least 60 seconds by opening the dosage pump and the magnetic valve. To minimize cross-contamination between different deposition runs when using various precursors, several capping depositions were made. This was not done in between each step for mixing ratio series in order to save precursors. However, since the mixing ratios were usually changed in logarithmic steps and because of the flush after every deposition, the effect is negligible when starting with the smallest dilution.

Using this setup, a number of sample series were prepared. The deposition parameters of each sample series are given in tables within the corresponding sections of the result part. The system allows for variation of the deposition temperature T_{d}, deposition time t_{d}, precursor volume V_{P}, number of injections, and test of various precursor mixtures.

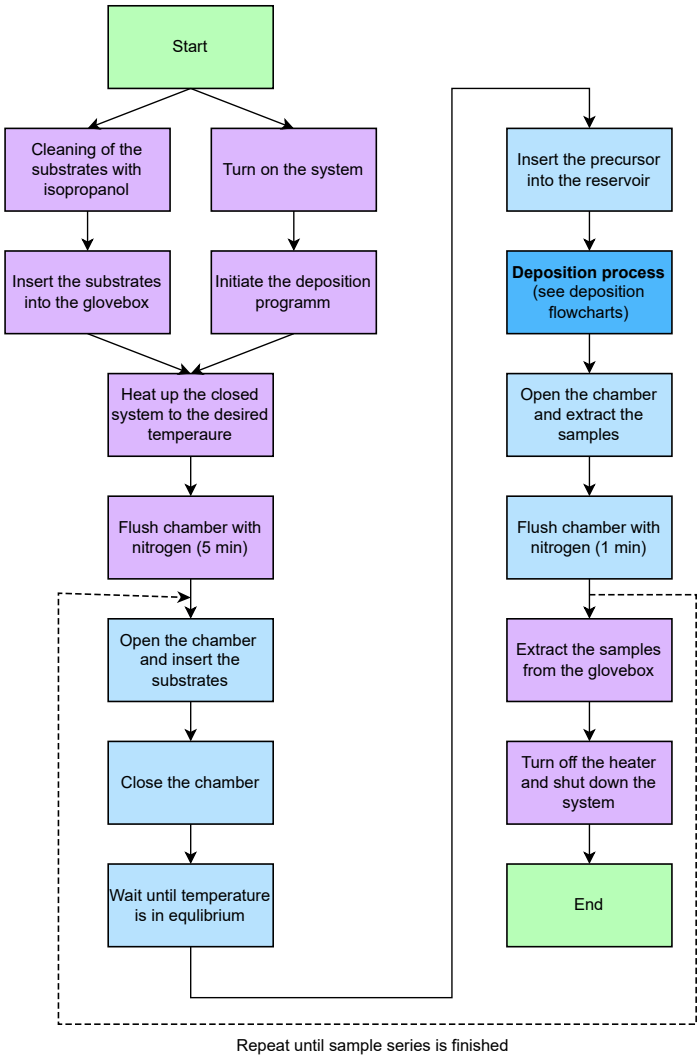


Figure 3.3.: Flowchart of the APCVD process. Steps shown next to each other can be performed simultaneously. Steps that need to be carried out only once for each sample series are marked in violet, while those required for every individual deposition are marked in blue. The dark blue box highlights the film deposition process, which is described in more detail in Figure 3.4.

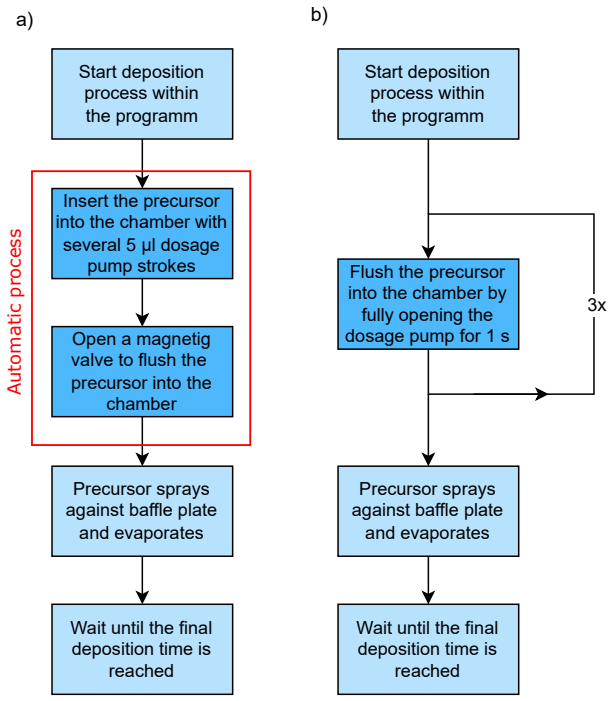


Figure 3.4.: Flowchart of two deposition processes with different precursor injection methods: a) injection via dosage pump strokes, and b) injection via manual flushing. Differences between the processes shown in a) and b) are highlighted in dark blue.

3.2.3. Temperature characteristics

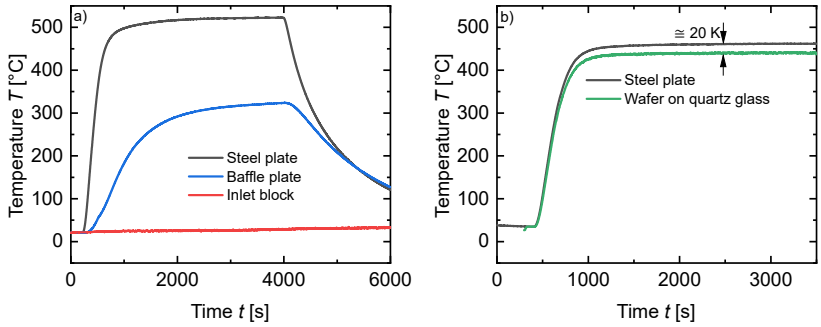


Figure 3.5.: a) Temperature profile of the steel plate, baffle plate, and inlet block during heating up the closed chamber of the APCVD system with subsequent chamber opening. b) Temperature profile of the steel plate and the silicon wafer on the quartz plate after turning on the hot plate with raised chamber head.

Since thermal energy is the primary driving force for precursor decomposition, the precise temperature within the deposition system is of great interest. Figure 3.5 a) presents the temperature profiles of the steel block, the baffle plate, and the inlet block during the heating phase of the closed deposition system.

The curves indicate that after one hour, the steel plate reaches a steady state temperature with a variation of approximately ±5 K. Although the hot plate temperature was set to 475 °C, the final temperature of the steel plate is about 50 K higher. This discrepancy may arise because the small steel plate ($6 \times 6\,\mathrm{cm}^2$) is positioned at the center of the hot plate.

If the temperature control sensor of the hot plate is not located exactly at the center but rather between the center and the edge, and if the heating elements within the hot plate are slightly inhomogeneous, the sensor may register a slightly lower temperature compared to the thermocouple attached to the steel block. This could explain the observed temperature difference.

Since the thermocouple in the steel block registers significantly higher temperatures than the set point of the hot plate, the temperature was verified using infrared (IR) measurements, and the sensors were also exchanged. All measurements were in agreement, with a fluctuation of approximately 10 K.

The baffle plate reaches temperatures above 300 °C, although it is near the top of the chamber. This is way beyond the boiling point of all the precursors and indicates that the temperature inside the chamber head is everywhere high enough to avoid recondensation of the evaporated precursor. In contrast, the cooled inlet block exhibits only a minor increase in temperature over time, reaching a maximum temperature of 30 °C. This temperature control is essential to prevent precursor evaporation from the precursor reservoir.

A quartz plate was placed on top of the steel block to prevent metal contamination of the substrate. However, unlike steel, quartz acts as a thermal insulator, which can result in a lower surface temperature at the quartz-air interface. To assess this effect, a thermocouple with silver paste is attached to a silicon wafer and placed on top of the quartz plate. Figure 3.5 b) compares the temperature profiles of the steel block and the silicon wafer when the hot plate is heated up with the head of the chamber raised. Once thermal equilibrium is reached, the silicon wafer exhibits a temperature approximately 20 K lower than that of the steel block.

The chamber head was raised because the thermocouple, which needed to be connected to its measurement unit, was placed on the quartz plate. Under closed chamber conditions, the temperature gradient between the quartz surface and the steel plate is reduced as a result of overall heating of the chamber. Consequently, the temperature difference between the steel block and the silicon wafer is expected to be even smaller than that in open chamber conditions. Therefore, the actual temperature of the silicon surface (and thus the deposition temperature) is less than 20 K lower than the steel plate temperature, which is used as the deposition temperature throughout this work. The actual temperature on glass substrates is likely slightly lower due to the additional insulating effect of the glass.

During the deposition process, it was ensured that the temperature variation remained within ±5 K. Due to this fluctuation range and for simplicity and better readability, the deposition temperatures provided throughout this work are rounded to the nearest 5 K increment.

3.3. PECVD reference films

To allow a direct comparison between the atmospheric pressure chemical vapor deposition (APCVD) films investigated in this study and current state-of-the-art plasma

enhanced chemical vapor deposition (PECVD) films, intrinsic a-Si:H layers were deposited using the *AK1000* PECVD system from Meyer Burger.

The *AK1000* system operates using a radio frequency (RF) plasma at 13.56 MHz and is equipped with a large area electrode configuration, featuring an electrode area of (500 × 500) mm^2 and an electrode gap of approximately 17 mm. Silane (SiH_4) serves as the primary precursor gas and can be diluted with hydrogen to tailor the properties of the film. This setup enables high-quality, uniform film deposition compatible with industrial SHJ solar cell fabrication processes.

While intrinsic a-Si:H film thicknesses below 10 nm are typically employed in standard SHJ solar cells, in this study, thicker films were deposited using established recipes for the highly passivating, fast-growing i1-layer and the high-quality i2-layer commonly utilized as a layer stack in SHJ device fabrication.[48] The specific deposition parameters for both layers are summarized in Table 3.2.

Table 3.2.: PECVD deposition parameters for intrinsic a-Si:H layers used for SHJ solar cells at the research center in Jülich.

Layer Type	**Temperature T_d [°C]**	**Power P_d [W]**	**Pressure p [mbar]**	**Silane Flow Q_{SiH4} [sccm]**	**Hydrogen Flow Q_{H2} [sccm]**
i1	200	300	2.7	145	650
i2	200	50	2.7	145	900

3.4. Thin film analysis methods

A range of analytical techniques was used to characterize the structural, chemical, optical, and electrical properties of the deposited thin films. FTIR and Raman spectroscopy revealed bonding and microstructure, while ellipsometry provided film thickness and optical constants. ESR, SIMS, and XPS offered insights into the defect densities and decomposition of the films. Electrical conductivity and charge carrier lifetime measurements assessed electronic performance. Together, these techniques offer a comprehensive understanding of the physical and electronic characteristics of the thin films produced in this work.

3.4.1. Fourier transform infrared (FTIR) spectroscopy

Fourier Transform Infrared (FTIR) spectroscopy is a widely used technique for analyzing the transmission spectrum of infrared light through a sample.[72, 114, 165]

This method is particularly useful for studying molecular vibrations because the excitation energies of many covalent bonds correspond to the photon energy of infrared radiation. When infrared light interacts with a material, photons with energies that match the vibrational excitation energies of molecular bonds are absorbed, leading to characteristic absorption features in the transmission spectrum. The absorption spectrum in the infrared region thus provides insights into the chemical bonding and molecular structure of the material.

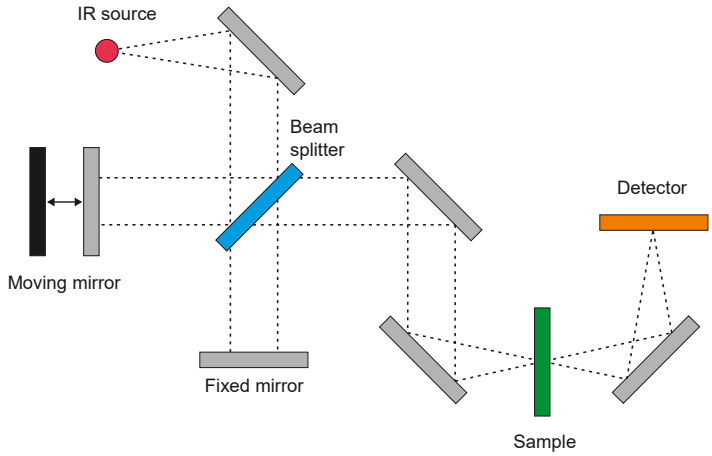


Figure 3.6.: Schematic of the FTIR spectroscopy setup illustrating the main components, including the infrared source, mirrors, moving mirror, sample, detector, as well as the optical path used to generate an interferogram. Adapted from an illustration originally created for the Master's thesis of the author (B. Fischer, 2022) [77].

Figure 3.6 presents a schematic representation of the FTIR measurement setup. In this system, a broad-spectrum infrared light source is directed into an interferometer, which generates an interference pattern dependent on the position of a moving mirror. The light then passes through the sample before reaching a deuterated triglycine sulfate (DTGS) cesium iodide (CsI) detector, which records variations in signal intensity. By continuously varying the mirror position, an interferogram is obtained. This interferogram is subsequently converted into a transmission spectrum via Fourier transformation.

Measurement procedure

To quantify the transmittance T_{IR} of a sample (film + substrate wafer), the intensity of the transmitted signal through the sample I_{s} is compared to a reference measurement I_0, which is carried out using a bare substrate wafer of the same type as the sample wafer. The transmittance is given by:

$$T_{\mathrm{IR}} = \frac{I_{\mathrm{s}}}{I_0}\,. \tag{3.1}$$

In this study, FTIR measurements were performed using a Nicolet 5700 spectrometer from Thermo Electron Corporation. The system outputs the absorbance spectrum as a function of the wavenumber $\tilde{\nu}$ (see Figure 2.3), where absorbance A is related to transmittance T_{IR} by:

$$A = -\log(T_{\mathrm{IR}})\,. \tag{3.2}$$

Furthermore, the relationship between transmittance T_{IR}, absorption coefficient α, and sample thickness d follows:

$$T_{\mathrm{IR}} = \exp(-\alpha d)\,. \tag{3.3}$$

From this, the absorption coefficient α can be determined using the expression:

$$\alpha = \frac{\ln(I_0/I_{\mathrm{s}})}{d} = \frac{A\ln(10)}{d}\,. \tag{3.4}$$

It is important to note that the calculated absorption coefficient includes both absorption and scattering losses. However, in this work, scattering effects are not separately considered, as the primary focus is on variations in the absorption coefficient owing to vibrational excitations. Similarly, internal reflections that might lead to an overestimation of the absorption coefficient are not considered here.[166]

Determination of the bond density

To determine the bond density n within a material, the intensity I of the integrated absorption peak of a vibrational mode of the bond in the FTIR spectrum can be used. In addition, the microstructure parameter R of amorphous silicon films (cf. Section 2.1.2, Equation 2.2) is determined based on the integrated infrared absorption of modes at 2000 $\mathrm{cm^{-1}}$-2100 $\mathrm{cm^{-1}}$.

The integrated absorption intensity I is calculated from the absorption coefficient spectrum using the relation [167]:

$$I = \int \frac{\alpha}{\tilde{\nu}} \, \mathrm{d}\tilde{\nu} \, . \tag{3.5}$$

To evaluate I, the following procedure was employed:

1. **Baseline Correction:** A baseline was established by fitting a suitable function to the left and right of a peak, ensuring accurate quantification of the absorption characteristics. For thin films, a linear baseline correction is sufficient, while for thicker films, interference effects during FTIR measurements lead to a non-linear baseline.[168] For the FTIR spectra shown in this work, a user-defined baseline subtraction was performed using a user-defined approach, employing second-order derivative anchor points and spline interpolation to correct for background contributions and enhance the comparability of the spectra.

2. **Gaussian Fitting:** A Python-based algorithm utilizing the `lstsq` function was employed to fit Gaussian (or Lorentzian) functions to the measured absorption peaks.

3. **Integration:** The integrated absorption intensities I were computed by numerical integration of the fitted Gaussian (or Lorentzian) curves using Equation 3.5.

With the integrated peak absorption, the bond density n can be calculated using the absorption strength A_S using the following relation:

$$n = A_\mathrm{S} I \, . \tag{3.6}$$

In the case of hydrogen, the H concentration c_H, meaning the atomic percentage of H within the a-Si:H film can be determined nutritionally by dividing the H bond density n_H by the atomic density of a-Si:H $n_\mathrm{Si} = 5 \times 10^{22}\,\mathrm{cm^{-3}}$. Therefore, c_H is given as

$$c_\mathrm{H} = \frac{n_\mathrm{H}}{n_\mathrm{Si}} \, . \tag{3.7}$$

A list of the most important vibrational modes, their peak position within the FTIR spectrum, and the corresponding absorption strength used within this work are given in Table 3.3. Note that throughout Chapter 4, the absorption strength of the Si-H bonds ($0.9 \times 10^{-20}\,\mathrm{cm^{-2}}$) was used for all hydrogen content calculations, including in

films containing carbon deposited from trisilane-cyclooctane mixtures. In contrast, for the a-SiC:H films discussed in Chapter 5, the absorption strength of the C-Si-H bonds ($1.4 \times 10^{-20}\,\mathrm{cm}^{-2}$) was applied.

Table 3.3.: Infrared active modes, categorized into C-related, H-related, and O-related modes, along with their absorption strength for the most relevant modes. The bold written absorption strength within a range is used in this work.

Mode Position	**Associated Bonds**	**Vibration Type**	**Absorption Strength** [10^{-20} **cm^{-2}**]	**Reference**
H-Related Modes				
640 cm^{-1}	Si-$H_{1–3}$	wagging/ rolling	0.21	[72, 166, 167]
840–890 cm^{-1}	Si-$H_{2/3}$	bending	-	[72, 73]
2000 cm^{-1}	Si-H	Stretching	0.9	[72, 76, 166, 167, 169]
2070–2110 cm^{-1}	clustered Si-H/Si-H_2	stretching	**0.9**–2.2	[72, 76, 166, 167, 169]
2130–2140 cm^{-1}	Si-H_3	stretching	-	[72, 75, 170]
2080–2135 cm^{-1}	surface Si-$H_{1–3}$	stretching	-	[72, 75, 170, 171]
C-Related Modes				
720–790 cm^{-1}	Si-C	stretching	0.213	[114, 117, 125]
980–1000 cm^{-1}	Si-C-$H_{2/3}$	wagging	-	[111, 114]
2100 cm^{-1}	C-Si-$H_{1/2}$	stretching	1.4	[111, 114]
2850–2960 cm^{-1}	C-$H_{1–3}$	stretching	13.5	[111, 114]
O-Related Modes				
460 cm^{-1}	Si-O_2	rocking	-	[172–174]
800 cm^{-1}	Si-O	bending	-	[173–175]
950–1140 cm^{-1}	Si-$O_{1,2}$	stretching	**0.1**–0.2	[175–177]
2100–2250 cm^{-1}	$O_{1–3}$-Si-$H_{1–3}$	stretching	-	[75, 173, 176]
3450 cm^{-1}	O-H	stretching	-	[178, 179]

3.4.2. Raman spectroscopy

Raman spectra of Si and SiC thin films were acquired using a Renishaw inVia Raman spectrometer equipped with a 532 nm laser in a backscattering configuration. The laser power was attenuated to approximately 0.25–2.5 mW and focused on a measurement spot with a full width at half maximum (FWHM) of 1–2 µm. Preliminary tests confirmed that this laser power neither alters the structure of the films nor compromises the measurement signal quality.

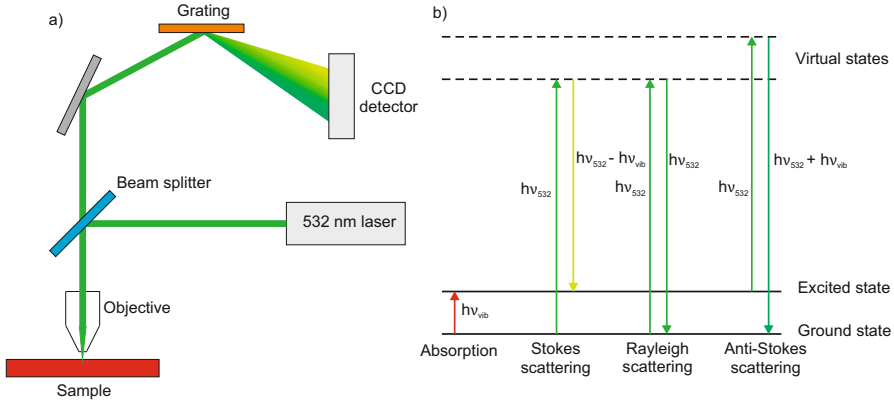


Figure 3.7.: a) Schematic representation of the Raman spectroscopy principle. b) Illustration of vibrational excitation via absorption or scattering. ν_{vib} denotes the photon frequency required to excite a vibrational state by absorption, while ν_{532} represents the frequency of the 532 nm laser used for Raman spectroscopy. Adapted from an illustration originally created for the Master's thesis of the author (B. Fischer, 2022) [77].

In backscattering Raman spectroscopy, a laser beam is focused on the sample surface through an objective lens, as depicted in Figure 3.7 a). A built-in camera captures the reflected laser light to verify the focal positioning of the sample. If necessary, the height of the sample stage is adjusted to ensure optimal focus. The incident laser light undergoes scattering within the sample via Rayleigh, Stokes, or anti-Stokes scattering mechanisms, as illustrated in Figure 3.7 b).

In Rayleigh scattering, a covalent bond is excited to a virtual energy state and relaxes back to the ground state while emitting a photon of the same energy.[180] In Stokes scattering, the bond returns to a vibrationally excited state, resulting in an emitted photon with lower energy than the incident photon, leading to a characteristic wavelength increase known as the Stokes shift.[180] Conversely, in anti-

Stokes scattering, the final energy state is lower than the initial state, causing a wavelength decrease. However, due to the low occupation density of higher-energy states at room temperature, anti-Stokes scattering is negligible in the samples studied and is therefore not considered further.

The objective lens of the spectrometer collects the backscattered light, which then passes through a beam splitter and a diffraction grating. The Raman intensity at different Stokes shifts (henceforth referred to as Raman shifts) is recorded using a CCD detector.

The most important peaks analyzed using Raman spectroscopy are given in Table 3.4.

Table 3.4.: Raman active mode positions with their associated vibrations and literature references. The table includes both amorphous (a-Si:H) and crystalline (c-Si) silicon modes, as well as SiC, C–C cluster, and Si–H stretching vibrations.

Mode Position	**Associated Vibration**	**Reference**
160 cm^{-1}	Si TA (a-Si:H)	[181, 182]
310 cm^{-1}	Si LA (a-Si:H)	[181, 182]
380 cm^{-1}	Si LO (a-Si:H)	[181]
480 cm^{-1}	Si TO (a-Si:H)	[181, 182]
520 cm^{-1}	Si TO (c-Si)	[81, 181]
750–800 cm^{-1}	SiC TO	[103, 119, 183]
840–970 cm^{-1}	SiC LO	[103, 119, 183]
960–1000 cm^{-1}	Si 2TO (a-Si:H/c-Si)	[181, 182]
1330–1580 cm^{-1}	C-C cluster	[118, 119, 184, 185]
2000–2150 cm^{-1}	Si-H stretching (a-Si:H)	[81, 82, 181]

Similarly to FTIR, Raman spectra can be used to analyze the Si-H bond related microstructure of amorphous silicon films by investigating the 2000 to 2100 cm^{-1} peak ratio. However, because of the different measurement principles, the absolute values of the ratio differ for Raman and FTIR and cannot be directly compared. [82]

3.4.3. Spectroscopic ellipsometry

Spectroscopic ellipsometry (SE) is an optical technique used to determine the dielectric properties and thickness of thin film materials by analyzing the change in polarization of light upon reflection. In this method, a polarized light beam is directed at the sample at a specific angle. Comparison of the polarization components of the reflected signal with the incident light provides insights on the complex reflection coefficients and, therefore, the dielectric properties of the material.[70, p. 4]

For thin films, the reflected signal is influenced not only by the thin film but also by the substrate material, which is why an optical model is required to accurately describe the response of the layer stack. This model incorporates oscillators that characterize the microscopic interactions between the material and the electromagnetic excitation. For amorphous layers, the Tauc-Lorentz oscillator model is typically employed, as it effectively combines a Tauc band edge with a Lorentz oscillator. The parameters of this model are fitted to the measured reflection signal, allowing determination of both the dielectric function ϵ and the film thickness d.[70, p. 230]

In this work, a Solar/M2000 from J. A. Woollam was used to conduct SE. Since the fit of the ellipsometry data of the crystallized films was less robust than for the amorphous films, the film thickness of the amorphous films was used for the calculation of the FTIR absorption coefficient (see Section 3.4.1) of the crystalline films. This can lead to an underestimation of the absorption coefficient as a result of shrinking effects of the film during annealing. For example, Heera et al. [186] found a density difference between amorphous and crystalline SiC of 12 %.

3.4.4. Electron spin resonance spectroscopy

For the detection of the paramagnetic defect-related spin density n_{S} and the g-value of the a-Si:H and a-SiC:H films, electron spin resonance (ESR) spectroscopy (a.k.a. electron paramagnetic resonance (EPR)) was used. The g-value in ESR spectroscopy is a fundamental parameter that characterizes the magnetic properties of an electron in a given environment. It is defined by the following equation:

$$g = \frac{h\nu}{\mu_{\mathrm{B}} B}\,, \tag{3.8}$$

where h is Planck's constant, ν is the resonance frequency, μ_B is the Bohr magneton, and B is the applied magnetic field.[187, p. 24] While the free electron g-value is 2.0023,

deviations occur due to spin-orbit coupling, ligand effects, and molecular interactions, providing insight into the electronic structure of paramagnetic species.

The measurements were made in conventional continuous wave (CW) mode using a commercial X-band ($nu = 9.8\,\mathrm{GHz}$) Bruker ELEXSYS E-500 system in an ER 4108 TMHS resonator at room temperature. Two identical thin film pieces on a Corning glass substrate cut in $(5 \times 5)\,\mathrm{mm}^2$ pieces were fixed face to face with scotch tape at the tip of a quartz sample tube of 4 mm diameter and placed in the center of an opaque resonator cavity. To ensure that the substrate or holder does not contribute to the detected signal, a reference measurement was made on substrates without sample films, which showed a negligible baseline compared to the signal detected from the films under test. A calibrated sample of sputtered amorphous silicon with a spin number of 2×10^{15} and a g-value of 2.00565 was used as a reference secondary standard [187, pp. 35–42] for the calibration of the magnetic field and signal intensity for a further evaluation of the g-value and spin density in the measured samples. The spectra were measured at a microwave power of 0.1 mW, a sweep width of 100 G, a magnetic field modulation at a frequency of 100 kHz, and an amplitude of 3 G. It was confirmed that saturation or overmodulation effects do not occur under these conditions.

3.4.5. Secondary ion mass spectroscopy

Secondary ion mass spectroscopy (SIMS) can be used to investigate the elemental structure of thin films as a depth profile. A beam of primary ions bombards the surface of the target material. Upon impact, the kinetic energy of these ions is transferred to the target, initiating a sputtering process. This leads to the ejection of secondary ions from the surface, which are subsequently analyzed using a mass spectrometer to determine the composition of the material.[188, pp. 1–3] For a-Si:H and a-SiC:H films, especially H, Si, O, and C isotopes are investigated. To determine the isotope, the molecular mass of the element and the charge state are usually given next to the element, e.g., for deuterium: $^{2}H^{-}$.

For the doped a-SiC:H films discussed in Sections 5.1.3 and 5.2.2, the depth profile of nitrogen would be interesting. However, due to the low probability of ionization of $^{14}N^{-}$ and its overlay with other ion signals (like $^{14}CH_2^{-}$), the direct detection of nitrogen is difficult. Therefore, instead $^{15}NH^{-}$ or $^{26}CN^{-}$ ions are used to analyze the nitrogen content of the films.

SIMS depth profiles were measured using 1 kV Cs ions for sputtering on an area of $(300 \times 300)\,\mu\mathrm{m}^2$ and 30 kV Bi ions for analysis on an area of $(40 \times 40)\,\mu\mathrm{m}^2$.

Measurements were performed on a ToF-SIMS5.ncs instrument (IONTOF GmbH, Muenster, Germany).

3.4.6. X-ray photoelectron spectroscopy

X-ray photoelectron spectroscopy (XPS) measurements were performed using a Phi 5000 VersaProbe II from ULVAC Phi Inc. The system was equipped with a monochromatic Al-K_α source (1.486 keV). The X-ray settings were adjusted to a power of 50 W at 15 kV with a spot size of 200 µm.

Survey spectra were acquired with a pass energy of 187.5 eV, a step size of 0.8 eV, and a dwell time of 100 ms. High-resolution detail spectra were recorded at a pass energy of 23.5 eV, with a step size of 0.1 eV and the same dwell time.

Using the survey spectra, quantification was performed in atomic percent (at%) with an estimated error of ≥ 10 %, normalized to 100 at%. Shirley background subtraction was applied, and elemental concentrations were determined using empirical relative sensitivity factors. Charge correction was performed by setting the main component of the C 1s signal to 285 eV. The high-resolution spectra were used to determine the atomic bonding partners within the material by fitting several Gaussian peaks within the multiplet of each element (here: Si, C, and O). The information depth of XPS in silicon materials is usually below 10 nm beneath the surface.[189, 190]

3.4.7. Electrical conductivity

The electrical conductivity σ is one of the most important parameters for Si and SiC thin films as a benchmark for its applicability in solar cells, transistors, or other nanoelectronic devices. The electrical conductivity of a thin film (herein mostly called just conductivity) is the inverse of the resistivity, which can be measured using two metal pads with a known width and distance between each other. The conductivity is determined using the relation:

$$\sigma = \frac{I_\sigma l}{U w d}, \tag{3.9}$$

where I_σ represents the measured current, U denotes the voltage applied across the electrodes, l is the gap between the electrodes, w corresponds to the electrode width, and d is the thickness of the film.

As a benchmark for the quality of intrinsic semiconductors, conductivity is measured under two conditions: i) under dark conditions to measure the dark conductivity σ_d,

and ii) under illumination with approximately 1 sun to measure the photoconductivity σ_{ph}. The implications for the film properties that can be derived from the comparison of these conductivities are discussed in more detail in Section 2.1.2.

Conductivity was measured using a custom-built system with a Keithley 6517A as an electrometer applying a voltage of ±100 V and a mercury lamp calibrated to an intensity of one sun as light source. The measurements were made under vacuum conditions (<10^{-4} mbar). Two silver pads with a width of 5 mm and a distance of 0.5 mm were deposited using a silver evaporation system to contact the thin film, as shown in Figure 3.8.

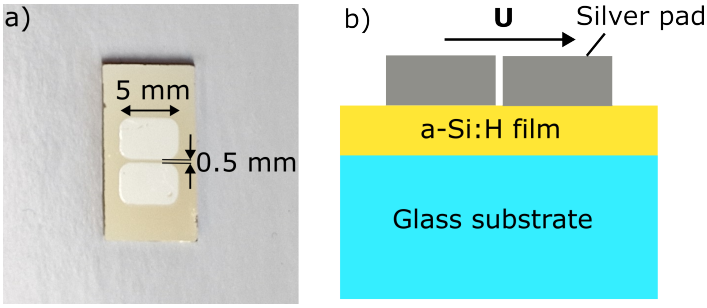


Figure 3.8.: a) Photograph of a sample for conductivity measurements with two silver pads evaporated on top of an a-Si:H film. The pad width and the distance between the pads are indicated. b) Schematic side view of a sample for conductivity measurements.

3.4.8. Charge carrier lifetime measurement

The charge carrier lifetime in double-sided a-Si:H-coated wafers was determined using the WCT-120 measurement system from Sinton Instruments. This setup enables quasi-steady-state photoconductance (QSSPC), generalized photoconductance, and transient photoconductance decay (TPCD) measurements. The system consists primarily of a temperature-controlled baseplate with an integrated RF coil for electrical characterization, a flashlamp for charge carrier generation, a monitoring photodiode, and evaluation software for data processing.

For charge carrier lifetimes exceeding 800 µs, the manufacturer recommends employing the TPCD method. Below 800 µs, the generalized mode is recommended. However, preliminary measurements on samples with charge carrier lifetimes of approximately 800 µs showed that the generalized mode systematically yields lower

lifetime values than the TPCD mode and exhibits greater measurement fluctuations. Therefore, all samples were measured using the TPCD mode to ensure comparable results, particularly within the same sample series.

In the TPCD approach, the sample is initially exposed to a flash pulse with a rise and decay time of approximately 100–200 µs. Following this excitation, the system records the sheet conductance as the sample relaxes over time. The excess carrier density Δn is subsequently derived from the measured sheet conductance using a model developed by Dannhäuser [191] and Krausse [192]. This model iteratively determines the carrier mobility based on the doping concentration and Δn, ensuring a self-consistent evaluation. The charge carrier lifetime τ is then calculated as a function of Δn and its time derivative $\mathrm{d}n/\mathrm{d}t$ according to:

$$\tau = \frac{\Delta n}{\frac{\mathrm{d}\Delta n}{\mathrm{d}t}} \,. \tag{3.10}$$

The charge carrier lifetimes τ given in this study were determined at an excess carrier density of $10^{15}\,\mathrm{cm}^{-3}$.

3.5. Post-treatment processes

Post-deposition treatments enhance material performance and enable the tailored adjustment of film properties to specific application requirements. Therefore, in the following various crystallization methods are described, including furnace annealing, rapid thermal annealing (RTA), and laser annealing. Additionally, hot wire chemical vapor deposition (HWCVD) was employed for hydrogenation and catalytic doping, enabling the precise modification of the composition of the films and electronic properties.

3.5.1. Annealing

For the crystallization of a-Si:H and a-SiC:H, the films are usually annealed at high temperatures (above 700 °C for a-Si:H [33, 193] and above 900 °C for a-SiC:H [34, 183]). Thereby, the annealing parameters like dwell time or heating rate can significantly influence the material properties of the crystallized film. In this work, furnace annealing, rapid thermal annealing, as well as laser annealing, are used. The methods are described below.

Furnace annealing Furnace annealing of the films was conducted in a quartz furnace with a heating rate of 6.67 °C/min and a dwell time of 120 min at the highest temperature. Prior to annealing, the furnace was flushed with N_2 under ambient conditions. Due to the absence of vacuum purging, a significant amount of residual oxygen (O_2) could have remained in the furnace during the annealing process. The highest achievable temperature with this oven is 1100 °C.

Rapid thermal annealing Rapid thermal annealing (RTA) was carried out with an RTP-150 from Unitemp using a heating rate of 1 K s^{-1} and a dwell time of 5 min. After heating, the samples are cooled down with -100 K s^{-1} to 150 °C under N_2 flushing. The highest achievable temperature with the RTA setup is 900 °C.

Laser annealing The local crystallization of a-SiC:H films was tested using a TALON-355-12SHTR (Spectra Physics, USA) UV laser with a wavelength of 355 nm. The Gaussian spot size was set to 60 µm, a power of 92 mW, a pulse frequency of 15 kHz, and a pulse length of 12.5 ns were used. The laser was scanned across a $(9 \times 9)\,\mathrm{mm}^2$ area at a velocity of 9 mm s^{-1}, maintaining a line spacing of 30 µm.

3.5.2. Hot wire chemical vapor deposition

Hot wire chemical vapor deposition (HWCVD) [194], as briefly described in Section 2.3.1, can be used not only for thin-film deposition but also for post-treatment of samples. In this work, HWCVD is used for two treatments: i) hydrogenation of amorphous silicon samples and ii) incorporation of phosphor atoms into amorphous silicon films for doping (catalytic doping).[195, 196]

A schematic of the HWCVD concept is shown in Figure 3.9. A gas containing the atoms to be incorporated into the film flows through a hot filament, where it decomposes. The resulting radicals hit the surface of the heated film and are incorporated. Due to the high diffusivity of hydrogen atoms, they penetrate much deeper into the film compared to much heavier phosphorus atoms, which react with the a-Si:H film primarily near the surface.[30–32, 196, 197]

In the following, the basic parameters for the HWCVD treatments within this work are given. Note that for the hydrogen treatment, a different chamber was used than for the catalytic doping to prevent the intrinsic a-Si:H films from impurities during hydrogenation.

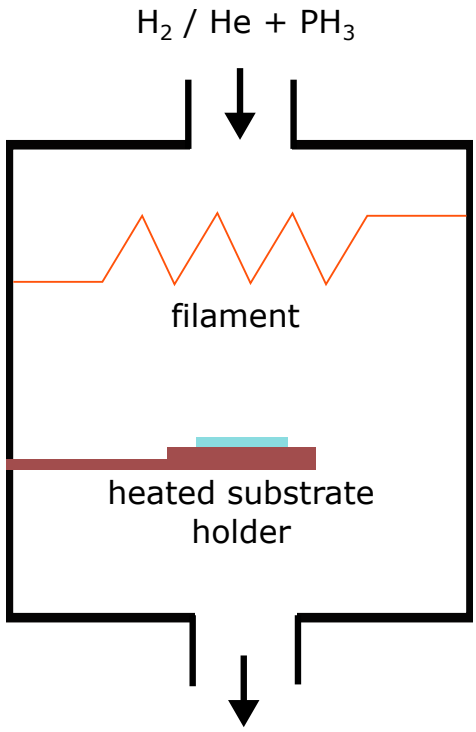


Figure 3.9.: Schematic of a Hot-Wire Chemical Vapor Deposition (HWCVD) system used for hydrogen treatment and catalytic doping. Arrows indicate the direction of gas flow within the chamber.

Hydrogen treatment For the hydrogen treatment, a rhenium filament was used with a temperature of 1300 °C, while the substrate heater was set to 390 °C. The distance between the substrate and the filament was maintained at 71 mm. The H_2 gas flow was set to 50 sccm at a chamber pressure of 0.05 mbar. The duration of treatment was 60 min. Before treatment, the hot wire chamber was preheated for 25 min at a pressure of 0.05 mbar, using H_2 as ambient gas.

Catalytic doping For the catalytic doping, a tantalum filament was used with a temperature of 1900–2200 °C, while the substrate heater was set to 200 °C. The distance between the substrate and the filament was maintained at 90 mm. The gas flow of phosphine (PH_3) was set at 20 sccm at a chamber pressure of 0.05 mbar. The duration of treatment was 60 min. Before treatment, the hot wire chamber was preheated for 20 min at a pressure of 0.5 mbar, using H_2 as ambient gas.

Catalytic doping and hydrogen treatment Combinations of catalytic doping and hydrogenation were conducted in the same chamber as for the catalytic doping only. For the H-treatment in this chamber, the tantalum filament was set at a temperature of 1500–1600 °C, while the substrate heater was set to 380 °C. The distance between the substrate and the filament was maintained at 90 mm. The hydrogen gas flow was set to 100 sccm at a chamber pressure of 0.05 mbar. The duration of treatment was 60 min. Before treatment, the hot wire chamber was preheated for 20 min at a pressure of 0.5 mbar, using H_2 as ambient gas.

4. Amorphous and crystalline silicon films

This chapter presents a comprehensive investigation of hydrogenated amorphous silicon (a-Si:H) thin films deposited using atmospheric pressure chemical vapor deposition (APCVD). The first section explores intrinsic hydrogenated amorphous silicon (a-Si:H) films derived from pure trisilane, examining their structural and electrical properties through a variety of characterization methods, including FTIR spectroscopy, electron spin resonance (ESR), and secondary ion mass spectrometry (SIMS). The subsequent section extends the analysis to films deposited from trisilane diluted with cyclooctane, evaluating the effects of precursor composition on material quality, film growth dynamics, and spatial uniformity. The first two sections are based on a previously published article that was part of my PhD thesis (Fischer et al. [164], 2024). Portions of the text and figures have been adapted from the publication, with additional data, analyses, and discussions incorporated to extend the original content.

The final section highlights several application-relevant aspects of APCVD a-Si:H films, including their potential for surface passivation of crystalline silicon (c-Si) wafers, hydrogenation treatments, catalytic doping processes, and crystallization behavior under different annealing conditions. Each topic is supported by detailed experimental results and corresponding discussions, providing a thorough understanding of the material properties and technological implications of APCVD-deposited silicon films.

4.1. a-Si:H from pure trisilane

In this section, a fundamental evaluation of hydrogenated amorphous silicon films (a-Si:H) deposited using pure trisilane (TS, Si_3H_8) with the optimized atmospheric pressure chemical vapor deposition (APCVD) system is presented. To assess the viability and characteristics of this approach, the resulting films are systematically

compared with those deposited using a conventional plasma-enhanced chemical vapor deposition (PECVD) system.

The comparative analysis focuses on key aspects such as microstructure and electronic properties, providing insights into how the deposition conditions influence the quality of the film. Additionally, electron spin resonance (ESR) and secondary ion mass spectrometry (SIMS) analyses were conducted on APCVD-grown films to investigate defect densities and hydrogen incorporation. The findings are discussed in the context of optimizing the deposition parameters and understanding the material properties of a-Si:H films for potential applications in semiconductor and photovoltaic technologies. A more detailed analysis of the growth mechanism and the reproducibility of the process is presented in Section 4.2.4, using 2 vol% trisilane diluted in cyclooctane as the precursor. The use of a higher volume of diluted trisilane enables a more robust and reproducible deposition process, as discussed in Section 3.2.

4.1.1. FTIR spectra of APCVD and PECVD a-Si:H

A-Si:H is a long-known and well-analyzed material. The first question that arises is whether the a-Si:H deposited by a new system has a structure and properties similar to those of the already known a-Si:H. In the solar cell industry, a-Si:H is most often deposited using PECVD. Therefore, the high-quality and relatively dense intrinsic i2-layer used in SHJ solar cells will serve as a benchmark throughout this work to assess the quality of the APCVD layers produced by the new system. The PECVD system and the specific deposition parameters used to fabricate the i2-layer are detailed in Section 3.3. Table 4.1 presents the results of the measured properties of the i2-layer.

Table 4.1.: Thickness d, H concentration c_{H}, microstructure parameter R, dark and photoconductivity σ_{d} and σ_{ph} of an i2-layer film as used in SHJ solar cells (in a thinner form), produced by PECVD.

Thickness d **[nm]**	**H Conc.** c_{H} **[at%]**	**Microstructure Parameter** R	**Dark Cond.** σ_{d} **[S cm^{-1}]**	**Photocond.** σ_{ph} **[S cm^{-1}]**
34.4	22	0.21	3×10^{-11}	1.6×10^{-6}

The first step in testing the new system for depositing a-Si:H was to confirm that the process indeed produces a-Si:H. FTIR spectra proved particularly suitable for this purpose, because they highlight the distinctive characteristics of a-Si:H and give insight to its microstructure. Figure 4.1 shows the FTIR spectrum of an APCVD film

deposited at $T_d = 400\,°C$, $t_d = 10\,min$ and a trisilane volume V_{TS} of 20 µl on the upper graph and the FTIR spectrum of the PECVD i2-layer at the lower graph. The spectrum of the APCVD film follows a pattern similar to the spectrum of the PECVD film, including peaks at 640 cm^{-1} and in the region from 1900 to 2200 cm^{-1}. These peaks are characteristic of a-Si:H films and are caused by wagging and stretching vibrations of the Si-H bonds.[72, 76, 116, 167] In addition to the Si-H peaks, the spectra of both films show positive or negative peaks around 1000 cm^{-1} followed by a negative peak around 1100 cm^{-1}. In this region peaks from Si-O-Si stretching vibrations can be found.[172, 177, 198] One reason for the increased peak at 1000 cm^{-1} for the APCVD film might be the formation of native oxide layers on the surface of the film and c-Si substrate, as also found for only annealed films in Section 4.3.3. For the PECVD film, the negative peak at 1000 cm^{-1} is probably due to the absence of native oxide layers, since the substrate was HF-etched prior to the deposition, and for the FTIR baseline measurement, a wafer with native oxide is used. The peaks at 1100 cm^{-1} can be attributed to the fluctuation of O bonded within the c-Si substrate and are not related to the properties of the film.

While the spectra in Figure 4.1 confirm that the deposited material was indeed a-Si:H, the microstructure of the APCVD films differs from that of the i2-film. A slight shift to lower $\tilde{\nu}$ and a different form of the double peak structure around 2050 cm^{-1} shown in Figure 4.1 indicate that the Si-H bonds within the APCVD a-Si:H are located in a different microstructural surrounding than the bonds within the PECVD films. In addition, the peak heights at 640 and 2050 cm^{-1} in the APCVD film are approximately half those of the PECVD film, indicating a lower hydrogen content within the APCVD film.

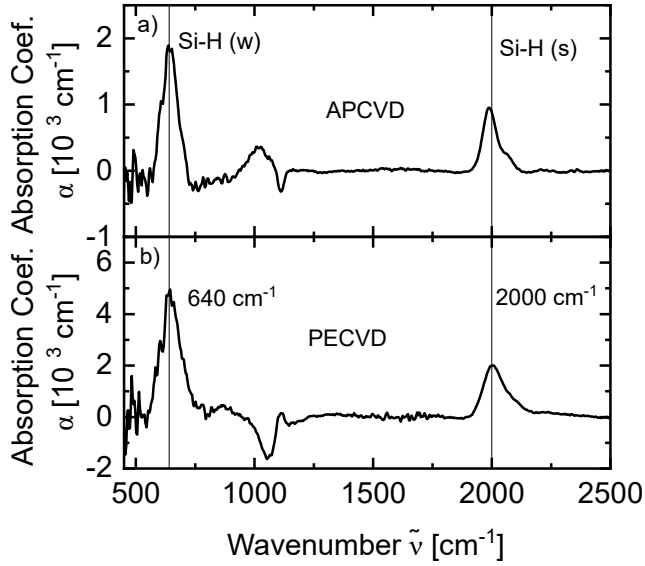


Figure 4.1.: FTIR spectra of a) an APCVD a-Si:H film deposited at 440 °C using 20 µL of trisilane for 10 min and b) a PECVD i2-layer a-Si:H film, with deposition parameters listed in Table 4.1. Si–H wagging and stretching modes are indicated at 640 and 2000 cm^{-1}, respectively.

4.1.2. Microstructure and electrical properties

The microstructure of the a-Si:H films influences the film properties and is highly dependent on the deposition conditions.[25, 86, 148] For this reason, films were deposited with various deposition parameters, namely substrate temperature T_d, deposition time t_d, and precursor volume V_P, using five different sample series shown in Table 4.2.

Table 4.2.: Deposition parameters of various sample series prepared using pure trisilane. The parameter that was varied is shown in bold. The deposition temperature T_d and time t_d are given, as well as the total trisilane volume V_P used as precursor for each deposition.

Series	**Temperature T_d [°C]**	**Time t_d [min]**	**Volume V_P [µl]**
Temp1	**410–580**	10	10
Time1	440, 555	**10, 20, 50**	20
Volume1	440, 555	10	**10, 20, 50**
ESR	440, 495, 555	10, 20	10, 20
SIMS	440, 495, 555	10, 20	10, 20

Dark- and photoconductivity σ_d and σ_ph, thickness d, H concentration, and microstructure parameter R of the pure silane samples of series Temp1, Time1, and Volume1 are summarized in Figure 4.2, while each series is named after its mainly varied parameter. Figure 4.2 a) shows the results for samples of series Temp1. The film thickness of the a-Si:H films increases strongly from 10 to 130 nm with increasing hot plate temperatures between 410 °C and 495 °C, indicating a higher growth rate, in agreement with the literature.[199] For temperatures above 495 °C, the film thickness stops to increase, likely indicating the depletion of the injected precursor. The thickness decreases slightly for temperatures of 555 °C and 580 °C, which can be attributed to two effects. i) The major effect is a larger area that is unintentionally heated up to temperatures allowing a deposition of a-Si:H (e.g., at the walls of the deposition chamber). A larger deposition area at the same precursor volume leads to thinner films on the substrate if the growth process is limited by the precursor volume and not by the deposition time. ii) A slight reduction in film thickness may also result from annealing-related shrinkage of a-Si:H films at elevated temperatures due to hydrogen

effusion, as indicated by a decrease in c_H from 4 at% at $T_d = 440\,°C$ to below 1 at% at $T_d > 525\,°C$.[109, 200]

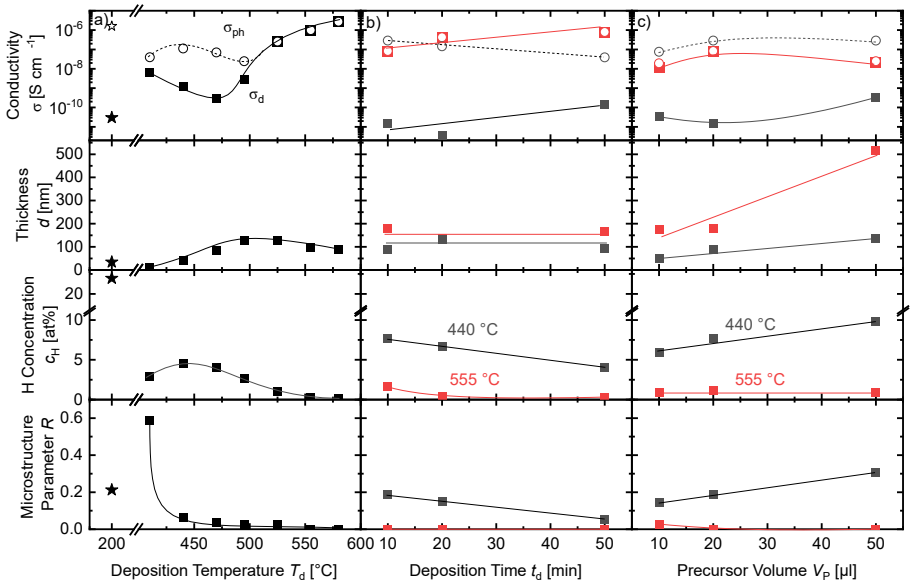


Figure 4.2.: Dark and photoconductivity σ_{ph} and σ_d, thickness d, hydrogen concentration c_H and microstructure parameter R of a-Si:H films deposited with pure trisilane as precursor and a PECVD i2 a-Si:H reference film (marked with an asterisk) as a function of a) deposition temperature T_d, b) deposition time t_d, and c) precursor volume V_P. t_d and V_P were varied at temperatures $T_d = 440\,°C$ (gray) and $555\,°C$ (red). The lines are guides to the eye. Adapted from Fischer et al. [164] (2024), licensed under CC BY 3.0.

The conductivity measurement results in Figure 4.2 a) show a split of σ_{ph} and σ_d for temperatures $T_d \leq 495\,°C$. In this range, the logarithm of σ_{ph} qualitatively follows the curve of c_H. For temperatures above 495 °C, σ_d increases to values nearly equal to those of σ_{ph}. At these higher temperatures, c_H drops significantly to below 1 at%. The conductivity continues to increase with increasing deposition temperature, surpassing $10^{-6}\,S\,cm^{-1}$. This increase may be attributed to a higher density of defects, which could enhance hopping conductivity and might lead to the formation of a conductive defect band.[29, pp. 16–17] The ratio of σ_{ph} to σ_d, known as photosensitivity, is often used to assess the quality of intrinsic a-Si:H for optoelectronic applications.[201–203]

The highest photosensitivity, 2.5×10^2, was observed at 470 °C in the Temp1 series shown in Figure 4.2 a). This photosensitivity is 2 to 3 orders of magnitude lower than that of the PECVD i2-layer, whose photo- and dark conductivities are marked with an asterisk in Figure 4.2 a). The high photosensitivity of the i2-layer deposited at a temperature of 200 °C probably results from the high H concentration of 22 at% within the film, which is available to passivate defects associated with unsaturated Si bonds. Considering the high amount of H within the i2-layer, the microstructure parameter of ~0.2 indicates a rather dense amorphous silicon structure, as desired for i2-layers in SHJ solar cells.[25, 48] The microstructure parameter for the APCVD films is below 0.1 for all films, except for the film deposited at 410 °C. The low R for films deposited at $T_d > 410$ °C can result from two different material properties. i) It can result from dense material with H bonded mainly within the Si-network.[72, 76] ii) It can result from void-rich material where H bonded in voids effused during the deposition process, since the deposition temperature is above the effusion peak temperature at approximately 385 °C of H in voids but below that of H within the Si network at approximately 500 °C.[89] Because of the absence of the H in the voids which would contribute to the 2100 cm^{-1} peak, this could result in a low R despite the presence of voids in the material. The increased R for the film deposited at 410 °C could be a relic of the low film thickness of $d = 9$ nm. For low a-Si:H film thicknesses, the amount of H within the bulk a-Si:H can be of the same order of magnitude as the H bonded at the interface between a-Si:H and c-Si. The interface hydrogen can contribute significantly to the 2100 cm^{-1} peak, leading to a higher R.[82]

Having investigated the influence of T_d on the properties of a-Si:H, the next step was to investigate the influence of the deposition time t_d, in particular its influence on the amount of H effused during deposition. For this, the Time1 series was prepared, where 20 µl of trisilane was injected at 440 °C and 555 °C for durations of 10, 20, and 50 min. The results of this series are shown in Figure 4.2 b). 20 µl of precursor was used to achieve thicker films than those in the Temp1 series for better evaluation. The higher precursor volume also leads to microstructural changes, which are discussed in more detail later when discussing the Volume1 series. The Time1 series shows for $T_d = 440$ °C a decrease in c_H and R with longer deposition times. Specifically, c_H decreases from 8 at% to 4 at%, and R decreases from 0.2 to 0.05. This suggests that hydrogen bonded in a more porous or void-rich structure (associated with the 2100 cm^{-1} peak) effuses out of the film over time. As the deposition time increases,

σ_d increases while σ_{ph} decreases. This trend is consistent with a higher density of defects and a lower hydrogen content, both of which contribute to a lower σ_{ph} and, consequently, reduced photosensitivity.[59, 204] For $T_d = 555\,°C$, c_H is 2 at% for a deposition time of 10 min and decreases to almost 0 for longer deposition times. R is approximately 0, as the 2100 cm^{-1} peak is near or below the detection limit. Both σ_{ph} and σ_d are almost equal, and both increase with longer deposition times. These observations suggest that the effusion of hydrogen and the resulting changes in the film microstructure and defect density significantly influence the conductivity and photosensitivity of the material. The film thicknesses exhibit no clear dependence on the deposition time, which may be attributed to the near-complete consumption of the precursor within the first 10 min. Additionally, significant variations in film thickness are observed, likely caused by the injection mechanism for pure films, as discussed in the experimental Section 3.2.

The effect of the precursor volume injected has been investigated by preparing the sample series Volume1, the measurement results of which are shown in Figure 4.2 c). For two deposition temperatures, $T_d = 440\,°C$ and $T_d = 555\,°C$, precursor volumes of 10, 20 and 50 µl trisilane were used. Increasing the volume of precursor results in increased film thickness. For $T_d = 440\,°C$, R as well as c_H increase with increasing precursor volume, probably due to a higher growth rate with increasing precursor volume leading to more H incorporation and less H effusion during film growth. Conductivity measurements show for all precursor volumes a high photosensitivity up to 10^4. For the deposition at $T_d = 555\,°C$, the growth rate is higher than for the deposition with T = 440 °C leading to a film thickness of 500 nm for the film deposited with 50 µl trisilane. The high temperature probably leads to a high effusion rate, leading to a low c_H and low R for all film thicknesses. Accordingly, the photosensitivity of all films deposited at $T_d = 555\,°C$ is ~1 with conductivities in the range between 10^{-8} to 10^{-7} S cm^{-1}.

In addition to microscopic properties, the macroscopic properties of films are also important for the successful application in devices. Especially blistering, meaning the formation of H-filled bubbles at the interface between c-Si and a-Si:H is a well-known problem often occurring for a-Si:H films, because it leads to an ablation of the film from the substrate. Regarding the films of the series in Figure 4.2 a) for $T_d = 410\,°C$ and $T_d = 440\,°C$, a flat surface without holes is obtained, as shown representatively for $T_d = 440\,°C$ in Figure 4.3 a). No signs of blistering have been observed, possibly due

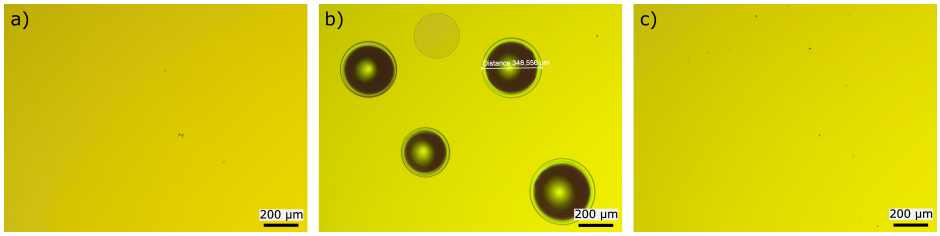


Figure 4.3.: Pictures made with a light microscope at five times magnification of a-Si:H films deposited at a deposition temperature of a) 440 °C, b) 495 °C, and c) 555 °C. The bright circle indicates a burst bubble, and the dark circles indicate bubbles filled with H_2. Reproduced from Fischer et al. [164] (2024), licensed under CC BY 3.0.

to a combination of a small film thickness and a low H-diffusion rate. At $T_d = 495\,°C$, shown in Figure 4.3 b), circular holes were observed. These were found also for the depositions at $T_d = 470$ and 525 °C. I attribute the formation of these holes to blistering due to H_2 accumulated in voids within the film or at the interface to the c-Si substrate.[35] For $T_d = 555\,°C$ and 580 °C, the surface is flat again (shown in Figure 4.3 c)). As a matter of speculation, this might result from a loose film structure with micropores in which the hydrogen can easily effuse without accumulation and subsequent blistering.[35] Also, it is possible that at higher temperatures the hydrogen is ejected from the surface before it can incorporate into the bulk of the material.

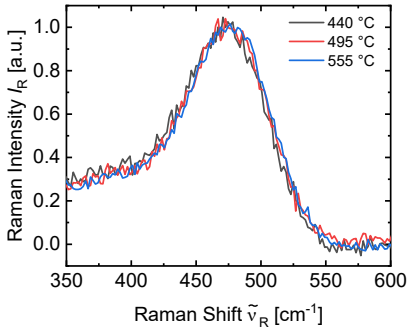


Figure 4.4.: Raman spectra showing the typical peak of Si-Si vibrations in amorphous silicon at 480 cm^{-1} of a-Si:H films deposited at 440, 495, and 555 °C. Adapted from Fischer et al. [164] (2024), licensed under CC BY 3.0.

Another possible explanation for the smooth H effusion without blistering is related to the growth of crystalline structures within the material. These crystalline structures are expected to reveal themselves in Raman spectra. However, the spectra shown in Figure 4.4 show a clear peak at 480 cm^{-1} for all deposition temperatures, indicating that the material is amorphous and not crystalline.[73, 116, 182] For a deposition temperature of 555 °C, the peak is slightly shifted to higher wavenumbers which may be attributed to increased material density or the onset of nanocrystalline growth, which is often observed in this temperature regime for longer annealing times.[137, 193, 205] However, a definitive interpretation is not possible, as the shift is minimal and may also result from signal scattering

4.1.3. ESR analysis of APCVD a-Si:H films

Paramagnetic electronic states in the APCVD a-Si:H films were analyzed for 3 samples via ESR spectroscopy. The deposition parameters of these samples are shown in Table 4.2 in the row "ESR". It is widely accepted that the ESR signal detected in the undoped amorphous silicon originates from Si dangling bonds causing defect states within the band gap.[29, 59] The ESR spectra given in the appendix in Figure A.2 a) show a pronounced featureless, slightly asymmetric single line at a g-value of approx. 2.0055 – typical for dangling bonds in amorphous silicon.[29, 59] Both the intensity of the line and, indirectly, the g-value point at a material with a high density of dangling bond defects.[59] The density of dangling bonds is crucial for the electronic quality of a-Si:H. Astakov et al.[59] showed that photoconductivity is inversely dependent on the spin density in a-Si:H. At the same time, hydrogen passivation can effectively reduce the density of dangling bonds and improve the electronic quality of a-Si:H. Figure 4.5 shows the conductivity, thickness, H-content, ESR spin density, and g-value for the three a-Si:H samples with similar thicknesses (~130 nm) as a function of the hot plate temperature. With increasing temperature, c_H measured by FTIR decreases. This is in line with the increase in the density of dangling bonds detected as an increase in the spin-density n_S measured by ESR.[59, 78] The high amount of dangling bonds can lead to an increase of the σ_d and can be responsible for the reduction of σ_{ph} in agreement with the trends observed in a-Si:H prepared by the traditional methods.[59, 206]

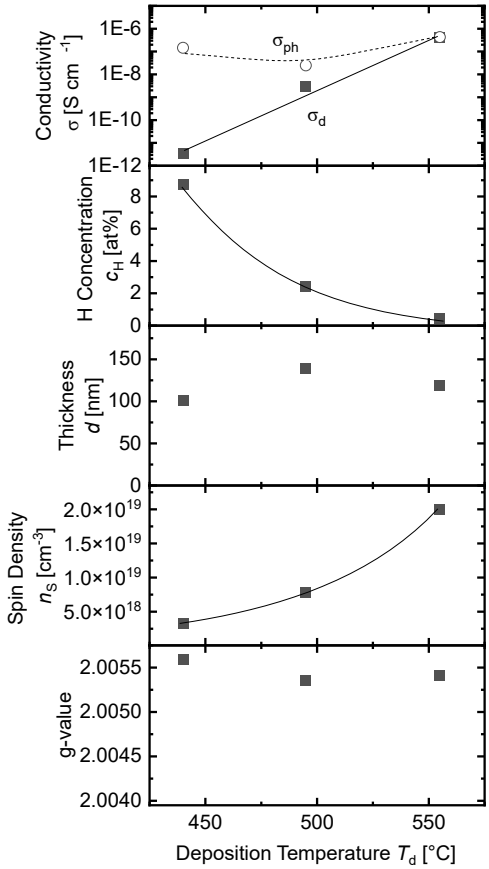


Figure 4.5.: Dark and photoconductivity σ_{ph} and σ_{d}, thickness d, hydrogen concentration c_{H}, spin density n_{S} and g-value of a-Si:H films deposited with pure trisilane as precursor as a function of deposition temperature T_{d}. The lines are guides to the eye. Modified from Fischer et al. [164] (2024), licensed under CC BY 3.0.

4.1.4. Depth-resolved analysis of a-Si:H films using SIMS and KOH etching

In addition to microstructural and electrical properties, the purity and homogeneity of the film composition across the thickness are crucial characteristics of a-Si:H films. Secondary ion mass spectrometry (SIMS) is an ideal technique to accurately analyze the atomic composition and purity of these films. Figure 4.6 presents SIMS depth profiles of a-Si:H films deposited at 440, 495, and 555 °C, along with a reference intrinsic a-Si:H film deposited by PECVD. The samples have similar thicknesses d between 130 and 180 nm. As PECVD reference for SIMS measurement, an a-Si:H film with a thickness of 150 nm was produced following the recipe of the i1-layer used in SHJ solar cells at the FZJ instead of the i2-layer used as reference in Figures 4.1 and 4.2. Although the i1-layer exhibits a lower density compared to the i2-layer, it possesses comparable purity and a higher deposition rate. For this reason, the i1-layer process was selected for the deposition of a 150 nm thick film used as a SIMS reference film. The PECVD deposition parameters of the i1-layer are given in Section 3.3.

The APCVD film deposited at 440 °C shows a purity comparable to the PECVD reference material, with similar C and O contents. However, the H content in the APCVD sample is lower and exhibits an inhomogeneous distribution across the film thickness, decreasing near the surface and the c-Si substrate interface. At higher deposition temperatures, the SIMS depth profiles confirm a reduction in the H content, consistent with the FTIR measurements. Simultaneously, increased deposition temperatures lead to higher C and O contents in the films. While the impurity concentration near the c-Si interface is relatively low, impurity concentrations are steadily increasing closer to the surface. This indicates a higher incorporation of impurities with a lower precursor content within the deposition chamber. The in average increased impurity incorporation at higher temperatures can contribute to an elevated number of defect states observed in Figure 4.5 and changes in σ_{ph} and σ_{d}.[141] A sharp increase in the content of O and C is observed on the film surface for all samples. These impurities are likely not incorporated during film growth but instead attributed to surface contamination from exposure to ambient air. This is also the reason for the sharp increase in O, C, and H content at the interface. The H and C peaks exhibit intensities similar to those of the APCVD and PECVD films. However, the O peak is significantly higher in the APCVD films compared to that in the PECVD film. This difference is attributed to the substrate for the PECVD film

being HF-etched prior to deposition, effectively removing the native oxide layer from the substrate surface.

To further investigate the origin of the inhomogeneous H content and impurity content in the a-Si:H films, a sample was deposited at 440 °C using two trisilane injections of 10 µl each – one at the start of the deposition and the other after 10 min – over a total deposition time of 20 min. In between both layers, the chamber was not opened or purged. The SIMS depth profile, shown in Figure A.3, reveals a distinct two-layer structure corresponding to the two precursor injections. Both layers display inhomogeneous H distributions, with maximum H ion intensity near the accommodating layer or substrate. This suggests that the inhomogeneous H distribution is mainly the result of growth rate variations during deposition. The H content is highest shortly after precursor injection, corresponding to the maximum concentration of H radicals in the chamber as the precursor evaporates and becomes evenly distributed. The second layer (green) exhibits a higher H content than the first (red), likely due to the residual trisilane from the first injection increasing the available precursor during the second deposition phase.

The behavior of the C and O content is inversely correlated with the H content. Higher trisilane concentrations lead to reduced impurity incorporation, while local maxima in the C and O content occur between the two layers. These maxima are attributed to a minimum in the growth rate as a result of trisilane depletion prior to the second precursor injection. The depletion reduces the ratio of trisilane molecules to impurity molecules. Therefore, the available precursor volume highly influences the growth rate and thus the incorporation of H and impurities during deposition. The absence of an H peak at the interface in between both layers highlights the fact that the a-Si:H growth did not stop before the second injection, leading to a smooth transition between both films rather than to a distinct film interface.

The former SIMS results show an inhomogeneous H concentration along the film thickness. To investigate the influence of this inhomogeneity on the microstructure of the a-Si:H films, a-Si:H samples were treated with KOH to form a thickness gradient, allowing a thickness-resolved investigation of the film. The film thickness along the gradient was measured using a Dektak profilometer. To ensure precise alignment, the measurement line was marked by laser ablation. Raman spectroscopy was then performed along the same line as the profilometer measurements, using the laser ablation mark as a guide. A Raman laser with a wavenumber of 532 nm was used with a $\frac{1}{e}$ penetration depth of approximately 100 nm in a-Si:H.[82, 207]. These experiments

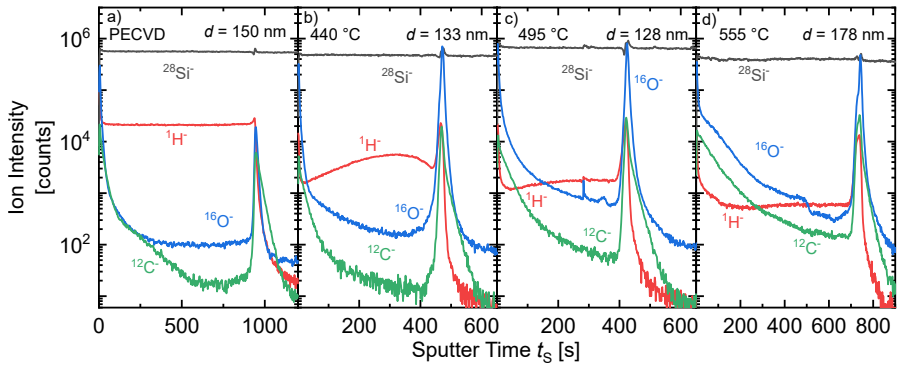


Figure 4.6.: Silicon, hydrogen, carbon, and oxygen SIMS depth profiles of a) an intrinsic PECVD film and APCVD films deposited at b) 440 °C, c) 495 °C and d) 555 °C. The film thickness and the detected isotopes are indicated within the graph. Adapted from Fischer et al. [164] (2024), licensed under CC BY 3.0.

were carried out on a sample deposited on borosilicate glass at 470 °C for 10 min using 10 µl of trisilane, resulting in an initial film thickness of approximately 100 nm. Figure 4.7 a) shows the thickness of a-Si:H along the gradient and the corresponding microstructure parameter R, determined via Raman spectroscopy. Figure 4.7 b) shows Raman spectra measured throughout the film thickness (p4), half the film thickness (p10), at the second last point, where Si-H modes could be observed (p15), and at a place with a fully etched film (p20). For film thicknesses between 100 and 30 nm, the microstructure parameter increases slightly from 0.05 to 0.2 as the thickness decreases. However, for thicknesses below 30 nm, R exhibits a significant increase, reaching a value of 0.7 for the thinnest measurable regions of the film.

The steep increase in R suggests the presence of hydrogen bonded within larger voids near the substrate surface. This trend in R has also been reported in the literature for PECVD films.[82] Si-H vibrations with O backbond are also located at 2100 cm^{-1}. Silicon bonded to the O of the substrate glass or to oxygen-containing impurities on top of the glass could also be the reason for an increased R at the interface. In agreement with this assumption, a peak at 2250 cm^{-1} appears within the raw spectra at p15 and p20 in Figure 4.7 b). This peak indicates Si-H stretching vibrations with 2 or 3 O backbonds.[176]

The more gradual increase in R with decreasing film thickness observed for films between 100 and 30 nm might result from the higher proportion of hydrogen located near the substrate interface relative to the overall Si-H spectrum. This higher proportion arises because of the thinner film thickness, which leads to i) fewer Si-H bonds from the bulk that contribute to the spectrum, and ii) greater light penetration to the interface, thereby enhancing the Raman scattering signal.

Taking into account the SIMS depth profiles shown in Figure 4.6, the gradual increased R may also be attributed to the higher hydrogen content within the film, which could facilitate hydrogen bonding within a more porous structure. However, it is noteworthy that R does not decrease for very thin films, although the hydrogen content decreases near the substrate interface, as shown in Figure 4.6. This discrepancy could be explained by an accumulation of hydrogen atoms at the interface, as revealed by SIMS, which leads to the increased R. However, it remains unclear whether similar accumulation occurs on glass substrates. Finally, it is important to note that the Si-H bonding configuration may be influenced by the KOH etching process itself, potentially due to hydrogen or oxygen incorporation into the film during the treatment.

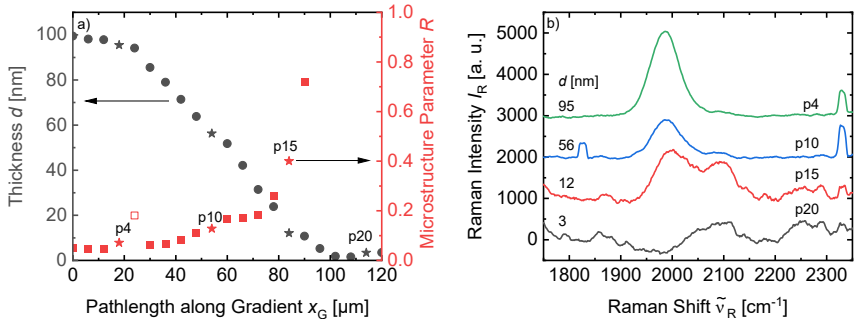


Figure 4.7.: a) R measured by Raman spectroscopy along a thickness gradient at the edge of a crater etched with KOH on an a-Si:H film. The film thickness, determined with a Dektak profilometer along a path from the crater rim toward the center, is shown on the left. The corresponding R values measured at various points along the same path are shown on the right. b) Corresponding Raman raw data measured at the points 4, 10, 15, and 20. The thickness and the point number are given in the graph. The corresponding points in a) are labeled and marked with a star.

4.1.5. Discussion

A-Si:H films deposited with pure trisilane have properties and quality on par with a-Si:H films deposited with similar methods found in the literature. The best photosensitivity of 4×10^4 found for films deposited at 440 or 470 °C is similar to or greater than the values of other films without H treatment investigated by Bedini et al. [21] and Masuda et al. [148] The purity of the low temperature a-Si:H films regarding the incorporation of oxygen and carbon is comparable with the purity of PECVD films, as shown in Figure 4.6. However, the lowest defect density measured by ESR was $3 \times 10^{18}\,\mathrm{cm^{-3}}$, which is rather high compared to standard PECVD films.[59] Masuda et al. [148] found spin densities between 10^{17} and $10^{18}\,\mathrm{cm^{-3}}$ for films deposited with cyclopentasilane at a temperature between 360 and 420 °C.

A c_H of less than 10 at% and a low R were found in all films, which is consistent with the fact that even the lowest deposition temperature used in this work is above the H effusion temperature.[89] Elevated temperatures result in a high rate of hydrogen effusion during the growth process, particularly for hydrogen located in voids leading to a low R. This suggests that the high defect density measured by ESR may be due to insufficient passivation and structural imperfections.[204] In agreement with this, the SIMS measurements shown in Figure 4.1.4 show an inhomogeneous depth profile of H with lower H content near the a-Si:H surface and the a-Si:H/c-Si interface, characteristic for H out-diffusion profiles.[88, pp. 220–225]

A clear correlation between hydrogen concentration and the conductivity of the films was observed, consistent with the findings of Beyer and Wagner [204] and Fritzsche.[78] They suggest that a decrease in c_H can cause an increase in defect densities, leading to a decrease in σ_ph.[59] The film with the best photosensitivity was deposited at 400 °C with $\sigma_\mathrm{d} = 3.4 \times 10^{-12}\,\mathrm{S\,cm^{-1}}$ and $\sigma_\mathrm{ph} = 1.5 \times 10^{-7}\,\mathrm{S\,cm^{-1}}$. These conductivities are in a range similar to that found by other groups.[7, 21, 148]. The APCVD films presented here show potential to achieve slightly lower σ_d than the literature, which shows σ_d from 10^{-11} to $10^{-10}\,\mathrm{S\,cm^{-1}}$. This indicates a high purity with a low amount of unintentional doping. At the same time, the σ_ph of the films investigated herein is slightly lower than found in literature, indicating lower defect passivation. Bedini et al. [21] achieved a photosensitivity of 2.8×10^5 for films made by sonophotolytically synthesized silicon nanoparticle-polymer composite ink from trisilane. In contrast to films investigated here, these films were passivated by a hydrogen radical treatment, which improved the electrical properties. A similar treatment of the a-Si:H samples in this work will be investigated in Section 4.3.2.1. Shen et al. [7] and Masuda et

al. [148] used Cyclopentasilane (CPS, Si_5H_{10}) instead of trisilane to deposit a-Si:H films. Due to the lower decomposition temperature of CPS, low deposition temperatures of 300–400 °C can be used to deposit a-Si:H films with high H concentrations compared to those achieved in this study. In combination with a H radical treatment, this leads to a photosensitivity of almost 10^6. However, films lacking H radical treatment and deposited at similar temperatures (close to 400 °C) as those used in this study show equal or lower photosensitivities compared to the films investigated here.

The a-Si:H films produced by the APCVD setup in this work are characterized by high purity when deposited at temperatures below 495 °C, particularly in terms of low oxygen and carbon incorporation. Although SIMS measurements showed inhomogeneities in the H depth profile with a maximum H content in the middle of the film, KOH etching indicated a homogeneous microstructure over the film thickness, except for a strong increase of R near the interface between the film and the substrate. The observed increase may be attributed to a higher hydrogen content bonded in voids within the nucleation layer located near the surface of the glass substrate. This layer, only a few nanometers thick, originates from the coalescence of spherical nucleation islands that form on the glass surface at the onset of the deposition process.[162] Consequently, this can lead to a higher proportion of void-rich material and, therefore, an increased microstructure parameter within the nucleation layer.[82] Another possible explanation for the increased R is the presence of Si–H vibrations with O backbonds originating from silicon atoms bonded either to oxygen in the glass substrate or to oxygen-containing impurities on the substrate surface, as these vibrations also occur at approximately 2100 cm^{-1}.

The relatively low hydrogen content ($c_H < 10$ at%) in the a-Si:H films presents a challenge for some specific applications. For example, passivating layers of a-Si:H in silicon heterojunction (SHJ) solar cells require higher hydrogen content for effective passivation. To address this issue, one potential solution is post-deposition hydrogenation, as will be discussed in Section 4.3.2.1. A low concentration of H for films deposited at high temperatures $T_d \geq 555$ °C renders them highly suitable for various high temperature processes, including recrystallization, as it significantly reduces the risk of blistering, as will be discussed in Section 4.3.3. The low c_H ($<$ 2 at%) indicates that the deposition time of 10 min is long enough to remove not only nearly all H at internal surfaces (2100 cm^{-1} peak) but also almost all H atoms within the silicon network. In addition, the low c_H and therefore high defect density seem to create a conductive defect band, which increases the σ_d while also speeding up the

recombination of photogenerated carriers, resulting in a photosensitivity around 1.[29, pp. 16–17] The defect density increases by one order of magnitude for a deposition temperature increase from $T_d = 440\,°C$ to $555\,°C$, probably as a result of less H incorporation into the film.[204]

With increasing deposition temperature, the O and C content also increases, with an especially sharp increase near the surface, as shown in Figure 4.6. This can be tentatively attributed to a combination of two effects: i) C and O tails occurring from surface contamination.[163] ii) slower a-Si:H film deposition at the end of the deposition process, due to a depletion of the trisilane concentration during the growth process. The depletion in combination with the high temperature leads to a higher ratio of impurity molecules to trisilane molecules and therefore to a higher incorporation of impurities. Hence, for films deposited at high temperatures, in addition to the lack of H, oxygen impurities can also lead to a greater number of defects within the material.[141, 208] Kinoshita et al. [208] showed a decrease in conductivity with increasing oxygen content. However, they only found a minor reduction in photosensitivity for very high atomic oxygen density up to $10^{21}\,cm^{-3}$, indicating that the reduction of the photosensitivity for high temperatures in Figure 4.2 a) is mainly a result of the low H content available for passivation within the film.

The origin of the C and O atoms within the film can be residues of organic solvents used for other film depositions within the chamber or impurity gases within the glove box, which are not monitored. The very steep increase in C and O counts at the surface of all samples, observed for sputter times $> 100\,s$ in Figure 4.6, can be attributed to impurities on the surface of the samples originating from the transport of the samples at ambient atmosphere.

By varying the deposition time and precursor volume, the film properties can also be varied. A higher precursor volume leads to a higher number of precursor molecules or radicals that can interact with the substrate surface. The increased growth rate due to more radicals can lead to a higher incorporation of H and a more porous or void-rich film, resulting in a higher R.[29] In fact, increasing the deposition time, decreases the average growth rate and can lead to annealing effects. Both a decreased growth rate and thermal annealing reduce c_H and R for films deposited with pure trisilane.

4.2. a-Si:H from trisilane diluted with cyclooctane

In this section, the deposition of hydrogenated amorphous silicon (a-Si:H) films is investigated using trisilane (TS, Si_3H_8) diluted with cyclooctane (CO, C_8H_{16}) as a solvent in the atmospheric pressure chemical vapor deposition (APCVD) process. The use of a liquid-phase precursor dilution approach aims to improve deposition control and enhance film uniformity via improved handling due to a higher precursor volume. In addition, improved TS dilution with CO was used for spin coating processes.[20–22] However, potential influence on the properties of the a-Si:H material due to C incorporation needs to be investigated.

To characterize the resulting films, Fourier transform infrared (FTIR) spectroscopy was employed to analyze the bonding structure, particularly with respect to C within the a-Si:H films. The effect of varying the trisilane-to-cyclooctane (TS-CO) ratio on the film composition and growth characteristics is systematically examined. Furthermore, the spatial uniformity, growth mechanisms, and reproducibility of the films are discussed. Finally, the impact of different precursor injection strategies on film properties is explored before concluding with a broader discussion of the findings.

4.2.1. FTIR spectrum of a-SiC:H films

Table 4.3.: Deposition parameters of various sample series prepared using trisilane-cyclooctane mixtures. The parameter that was varied is shown in bold. The proportion of trisilane in the precursor (TS concentration χ_{TS}) is given in percent by volume. In addition, the deposition temperature and time are given, as well as the total precursor volume, including trisilane and solvent (Volume). The injection number gives the number of flushes used to spray the precursor in equal volumes into the deposition chamber.

Series	**TS Concentration χ_{TS} [vol%]**	**Temperature T_d [°C]**	**Time t_d [min]**	**Volume V_P [µl]**	**Injection #**
Dilution	**1–100**	440, 495, 555	10	10–1000	1
Temp2	2	**410–580**	10	400	1
Time2	2	470	**1–50**	400	1
Volume2	2	470	10	**200–1000**	1
Injection	2	470	10	400	**1–120**

Cyclooctane is often used in APCVD as a solvent for easier handling and growth rate control.[20–22, 209] To study the influence of cyclooctane on the film properties, I deposited films with trisilane concentrations of 1 to 100 vol% diluted in cyclooctane at temperatures of 440, 495, and 555 °C. The deposition parameters for the "Dilution" sample series are summarized in Table 4.3. The film properties were investigated in the same way as for pure trisilane presented in Section 4.1. The FTIR spectra of the "Dilution" series samples were additionally analyzed for carbon-related IR vibrations. Figure 4.8 shows a comparison of the FTIR spectra of a) a film deposited with pure trisilane and b) a film deposited with 2 vol% trisilane diluted in cyclooctane. In Figure 4.8 a) the most dominant peaks arise from Si-H bending and stretching vibrations at 640 and 2100 cm^{-1}.[167] Additionally, from 900 to 1100 cm^{-1} there are Si-O vibrations, either because of impurities or because of the native oxide on the surfaces of the c-Si substrates.[172, 176, 177] In the same region, Si-C-H_2 wagging modes can be found.[111, 114] The sample in Figure 4.8 b) shows Si-C vibrations at 720–780 cm^{-1} and C-H vibrations around 2850–2950 cm^{-1}, which clearly shows that the sample contains carbon.[111, 112] For the films with incorporated carbon, the 2100 cm^{-1} peak is more dominant than the 2000 cm^{-1} peak. This could be caused by a material that is very rich in voids or, more likely, by a higher amount of hydrogen bonded to silicon with a carbon backbond.[111, 112, 167, 210] In addition, the peak at 900–1100 cm^{-1} shifts slightly to a lower wavelength. The shift is likely due to a higher concentration of Si-C-H_x modes compared to Si-O, which are probably dominant within the spectra of the a-Si:H deposited purely shown in Figure 4.8 a). In the following, the Si-C peak at 720–780 cm^{-1} is used to quantify the carbon content within the a-Si:H films.

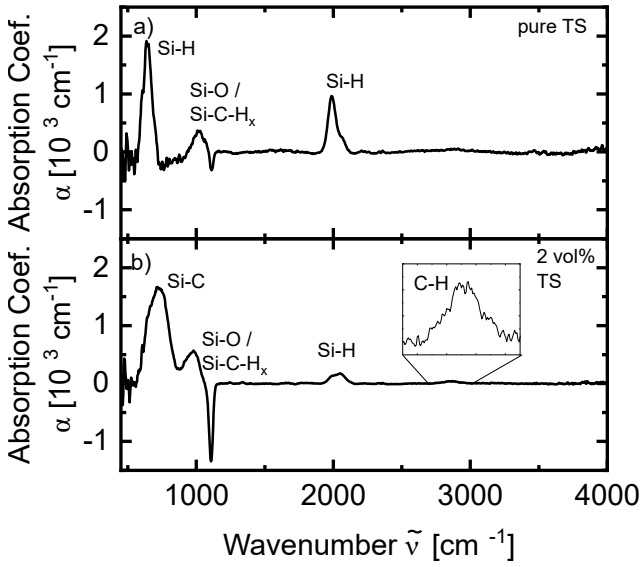


Figure 4.8.: FTIR spectra of a) an a-Si:H film deposited at 440 °C with 20 µl trisilane for 10 min and b) an a-Si:H film deposited at 555 °C with 400 µl of 2 vol% trisilane diluted in cyclooctane for 10 min. The peaks are labeled with the corresponding bonds. In b) the Si-H bending vibration peak at 640 cm^{-1} is overlaid by the strong Si-C peak at around 720–780 cm^{-1}. Adapted from Fischer et al. [164] (2024), licensed under CC BY 3.0.

4.2.2. Impact of the trisilane-to-cyclooctane ratio

Figure 4.9 a) shows the conductivity, thickness, hydrogen content, microstructure parameter R and density of Si-C bonds as a function of trisilane concentration in samples from the Dilution series deposited at 440 °C. Both σ_d and σ_{ph} as well as c_H are mostly unaffected by the cyclooctane dilution. In contrast, the microstructure parameter R increases with decreasing trisilane concentration for trisilane concentrations below 10 vol%. In this series, no significant Si-C modes were detected around 720–780 cm^{-1} with FTIR, as can be seen in the raw date shown in Figure A.4 a). However, SIMS measurements, shown in Figure 4.10, revealed a 3–4 orders of magnitude increase in carbon content compared to films made with pure silane. In addition, the hydrogen content is more uniformly distributed across the film thickness, with a maximum at the interfaces rather than in the middle, as observed in pure a-Si:H films. When changing the CO dilution ratio, the H concentration varies only slightly between 6 and 8 at%. The scatter of the film thickness within the Dilution series is probably due to the manual injection of the precursor (cf. experimental Section 3.2).

Figure 4.9 b) shows the properties of the material versus the dilution ratio for films deposited at 495 °C. The figure shows that c_H and R increase with increasing cyclooctane concentration for films made with less than 10 vol% trisilane content. This trend might be due to the incorporated carbon, which is supported by the increasing Si-C vibrational peak located at 720–780 cm^{-1} (see Figure A.4 b)). The increase in c_H, up to 6 at% might be one reason for the increased photosensitivity observed in samples with trisilane concentrations below 10 vol%. Note that films deposited with higher CO dilutions showed less blistering, maybe due to a stronger H bond to silicon with a carbon backbond.[109, 110] The difference in photosensitivity between 10 vol% and 100 vol% trisilane content is probably due to fluctuations in the deposition conditions. A deposition temperature of 495 °C is close to the critical point where the splitting of photo- and dark conductivity vanishes (as shown in Figure 4.2 a)). Therefore, small differences in temperature or precursor volumes can have a significant impact on photosensitivity.

Figure 4.9 c) shows the properties of the material versus the dilution ratio for films deposited at 555 °C. For trisilane concentrations above 10 vol%, no hydrogen is detected. However, at concentrations below 10 vol%, a significant amount of hydrogen is present in the film, and the microstructure parameter is 1 (see Figure A.4 c)). Despite this, hydrogen does not appear to passivate defects, as the conductivities (σ_{ph} and σ_d) remain similar in all films, regardless of the hydrogen content.

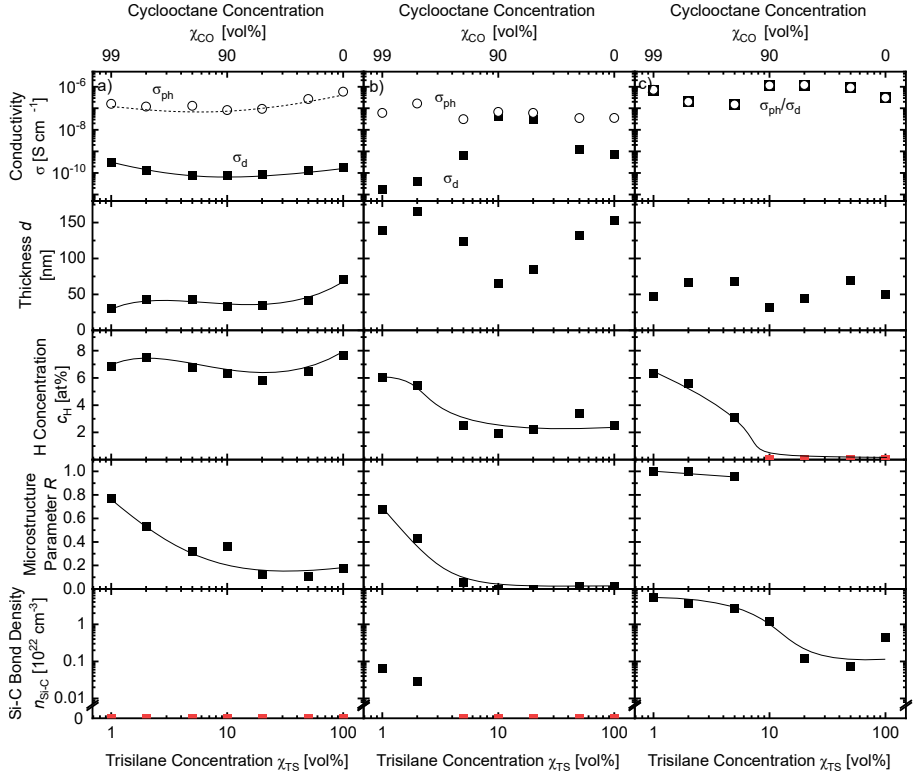


Figure 4.9.: Dark and photoconductivity σ_d and σ_ph, thickness d, hydrogen concentration c_H, microstructure parameter R and Si-C bond density $n_\mathrm{Si\text{-}C}$ of a-Si:H films as a function of the trisilane concentration within the precursor deposited at a deposition temperature T_d of a) 440 °C, b) 495 °C, and c) 555 °C. The red-marked points were set to 0, since the signal-to-noise ratio was too small to determine a peak within the FTIR spectrum. The lines are guides to the eye. Adapted from Fischer et al. [164] (2024), licensed under CC BY 3.0.

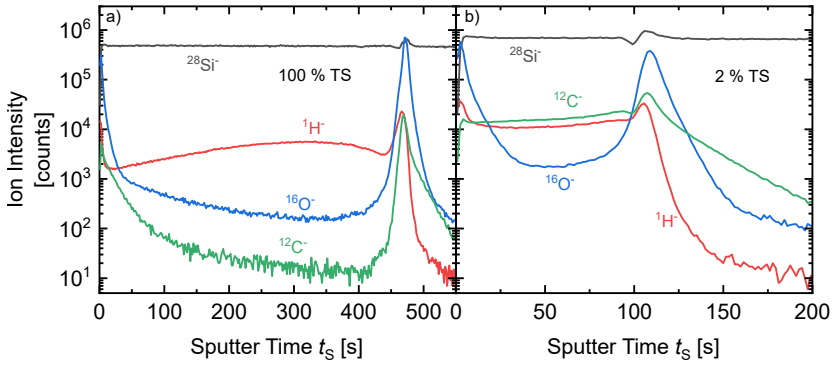


Figure 4.10.: Silicon, hydrogen, carbon, and oxygen SIMS depth profiles of APCVD films deposited at 440 °C with a TS concentration of a) 100 vol% and b) 2 vol% diluted in cyclooctane. Adapted from Fischer et al. [164] (2024), licensed under CC BY 3.0.

A Si-C peak was observed for all dilution ratios. Even in pure trisilane deposition, enough carbon – likely from impurities in the glove box – was incorporated into the film, resulting in a noticeable peak in the FTIR spectrum. Reducing the trisilane concentration leads to increased carbon incorporation, reaching concentration levels comparable to the silicon concentration ($\sim 10^{22}\,\mathrm{cm^{-3}}$).

4.2.3. Films deposited using highly diluted trisilane

A precursor with a trisilane concentration of 2 vol% in cyclooctane was used to investigate the influence of a high cyclooctane dilution on the properties of the a-Si:H film in more detail. Characterization of the a-Si:H material produced with the 2 vol% trisilane solution was also conducted, following the same approach used for the pure trisilane sample. Series were performed varying temperature, deposition time, and precursor volume (Temp2, Time2, Volume2). The deposition parameters of all three series are given in Table 4.3. The Time2 and Volume2 series were made at 470 °C to have an appropriate balance between a high growth rate and high film quality (high c_H and photosensitivity). The measurement results for the series are shown in Figure 4.11.

Figure 4.11 a) shows the results of the Temp2 series. The corresponding FTIR absorption coefficient spectra can be found in Figure A.5. The thickness of the films

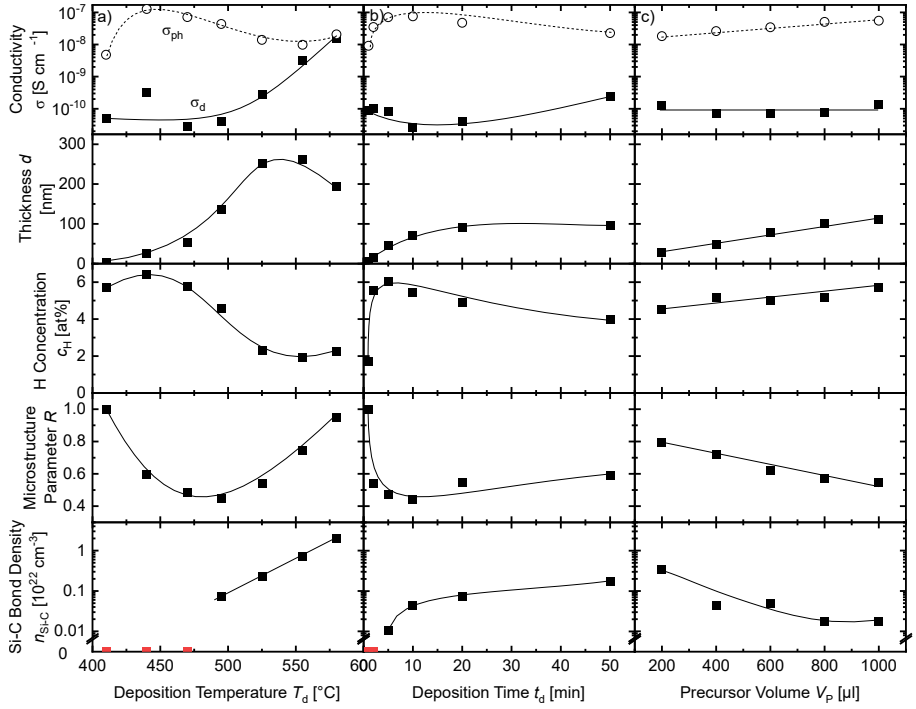


Figure 4.11.: Dark and photoconductivity σ_d and σ_ph, thickness d, hydrogen concentration c_H, microstructure parameter R and Si-C bond density $n_\mathrm{Si\text{-}C}$ of a-Si:H films deposited with 2 vol% trisilane diluted in cyclooctane as precursor as a function of a) deposition temperature T, b) deposition time t_d, and c) precursor volume V_P. Deposition time and precursor volume were varied at a deposition temperature of $T_\mathrm{d} = 470\,°\mathrm{C}$. The red-marked points were set to 0, since the signal-to-noise ratio was too small to determine a peak within the FTIR spectrum. The lines are guides to the eye. Adapted from Fischer et al. [164] (2024), licensed under CC BY 3.0.

increases with increasing deposition temperature for $T < 525\,°C$ and remains almost constant for $T > 525\,°C$. For all films, R is higher than 0.4. The microstructure parameter R decreases with increasing temperature for $T < 495\,°C$, probably due to a lower proportion of H at the interface (which vibrates at a wavenumber of $2100\,cm^{-1}$)[82] relative to the overall Si-H spectrum. In contrast, for $T_d > 495\,°C$, R increases, tentatively due to an increase in carbon content that leads to more Si-H bonds with C backbonds. This more stable bonded H might also lead to a c_H of 2 vol% for layers deposited at $T_d > 495\,°C$, instead of a full H effusion. Except for the film deposited at $T_d = 580\,°C$, all films show a photo response with a maximum at 470 °C, probably due to the higher c_H (σ_d at 440 °C probably an outlier).

In Figure 4.11 b) the results of the Time2 sample series are shown. The photosensitivity increases with the deposition time, with a maximum at t = 10 min. For deposition times greater than 10 min, the photosensitivity decreases. Accordingly, c_H strongly increase from 2 to 6 vol% and R strongly decrease from 1 to 0.4 within the first 5 min. The data of film thicknesses indicates that the growth rate is initially approximately constant and then, for deposition times longer than 5 min, the growth rate decreases to almost 0, due to depletion of the precursor. In addition, a longer deposition time leads to a higher carbon incorporation and lower H incorporation into the film.

Figure 4.11 c) shows the results of the sample series Volume2. An increased precursor volume seems to increase the a-Si:H growth rate. This leads to a (linear) increase in the thickness of the film. Higher film growth is related to an increase of photosensitivity and c_H. The higher growth rate is also accompanied by lower carbon incorporation and lower R, probably because of fewer Si-H bonds with carbon backbonds.

The detection of Si-C and C-H modes in the FTIR spectra suggests that C-C bonds might also be present in the material. However, no significant C-C signals, which typically occur in the range of 1300–1600 cm^{-1}, are observed in the spectra.[211] To further probe the presence of C-C bonds, Raman spectroscopy was performed on the Temp2 series as shown in Figure A.6. The Raman spectra reveal C-C modes in the range of 1400–1450 cm^{-1} in films deposited at temperatures $T_d > 495\,°C$, indicating small amounts of carbon clusters.[184] This indicates that the cyclooctane precursor does not decompose solely into single carbon atoms but also contributes to the formation of carbon chains, or possibly retains whole cyclooctane rings, which also show Raman peaks around 1450 cm^{-1} due to C-H_2 wagging modes.[185]

The presence of C-C bonds may cause a slight underestimate of the carbon content incorporated in the a-Si:H films. Nevertheless, given the limited quantitative precision of Raman spectroscopy and the absence of significant C-C modes in the FTIR spectrum, the Si-C stretching peak in FTIR remains the most reliable measure of the carbon content in these films.

Next, FTIR, Raman spectroscopy, and ESR were used to analyze the material stoichiometry and get insight into the defect density. For one film deposited at $T = 580\,°C$ using the solution with 2 vol% trisilane, an ESR measurement was made to analyze the g-value. This value is a measure of the magnetic properties of an unpaired electron within a material. It is influenced by the interaction of the electron with the direct surrounding material and therefore by the SiC stoichiometry.[212] As shown in Figure A.7, the film with a thickness of 430 nm showed a g-value of 2.004 which is closer to that of amorphous silicon carbide (a-SiC:H) (2.003) rather than a-Si:H (2.0055), in agreement with the high carbon content in the films.[212] The spin density of this sample was with $1.35 \times 10^{19}\,cm^{-3}$ slightly lower than that of the sample deposited with pure trisilane at $T = 555\,°C$, possibly because of the increased c_H and related passivation of defects for films deposited using high cyclooctane concentrations.

4.2.4. Film growth mechanism, spatial uniformity, and reproducibility

The use of cyclooctane as a solvent for trisilane increases the total volume of the precursor solution, allowing for more precise dosing and better reproducibility (cf. Section 3.2). In contrast to the flushing of small volumes of pure precursor (~10 µl), as described in Section 4.1, which is sensitive to precursor losses due to evaporation or uncertainties with Eppendorf pipettes, dosing larger volumes of less volatile TS-CO solution is much less affected by these losses. Therefore, the films deposited by this more robust method are used to investigate the reproducibility, uniformity, and growth mechanism of a-Si:H deposited by APCVD.

Figure A.8 shows the SIMS depth profiles of the APCVD films deposited in three separate runs. The deposition conditions for all three samples were identical, with 600 µl of 2 vol% TS in CO at T = 470 °C for 10 min, resulting in similar film thicknesses of 67, 79, and 80 nm. The SIMS depth profiles exhibit nearly identical curves for the hydrogen, carbon, and oxygen content, demonstrating a high reproducibility of the deposition process.

Beyond reproducibility, the spatial uniformity of the film growth across the deposition area of the APCVD system is crucial. Due to the small deposition area, restricted by the metal plate area, of a maximum of 6 × 6 cm^2, a significant temperature gradient is expected from the center of the deposition area to its edges. To analyze the uniformity of film growth, a film using 400 µl of 2 vol% TS diluted in CO, a deposition time of 10 min, and a T_d of 495 °C is deposited on a 5 × 5 cm^2 Corning glass plate. A picture of the resulting film and the corresponding thickness measurements are shown in Figure 4.12. The film thickness is maximal at the center of the glass plate, reaching ~92 nm, and decreases to a minimum of ~33 nm near the edge of the measured area, spanning 4 × 4 cm^2. This observation aligns with the fact that film growth is primarily temperature-driven, and the reduced film thickness near the edge is attributed to lower temperatures on the metal plate.

The results indicate that within a 4 × 4 cm^2 area, the film thickness varies between 30 and 100 % of the maximum thickness. Within the central 2 × 2 cm^2, the thickness varies roughly between 70 and 100 % of the maximum. Thus, for a consistent sample series, it is critical to place the samples in the same position during all depositions. Considering that sample sizes of 1.5 × 1.5 cm^2 are typically used for this work, the spatial uniformity is sufficient to produce relatively uniform samples. However, it is important to note that uniformity can vary significantly with deposition temperatures different from 495 °C. Especially at higher T_d, uniformity could decrease due to rapid growth rates, potentially leading to a less uniform distribution of precursors within the chamber. Additionally, for most series, one glass substrate and one c-Si substrate were used, leading to non-central positioning of the samples. The samples themselves also influence the spatial heat distribution, which further affects the film thickness. Consequently, within the small prototype system used here, multiple factors influence the uniformity of the film, potentially causing variation in thickness and probably also in other film properties like the H concentration. Even when using small 1.5 × 1.5 cm^2 samples, film characterization measurements should always be performed at the same position on the sample.

After investigating the reproducibility and spatial uniformity of the APCVD a-Si:H films, the focus now shifts to fully characterizing the growth mechanism by examining the factors influencing film growth and developing a model for this process. For pyrolytic-driven CVD, the film growth rate is primarily limited by two factors: temperature and the concentration of precursor gases within the chamber.[163] The

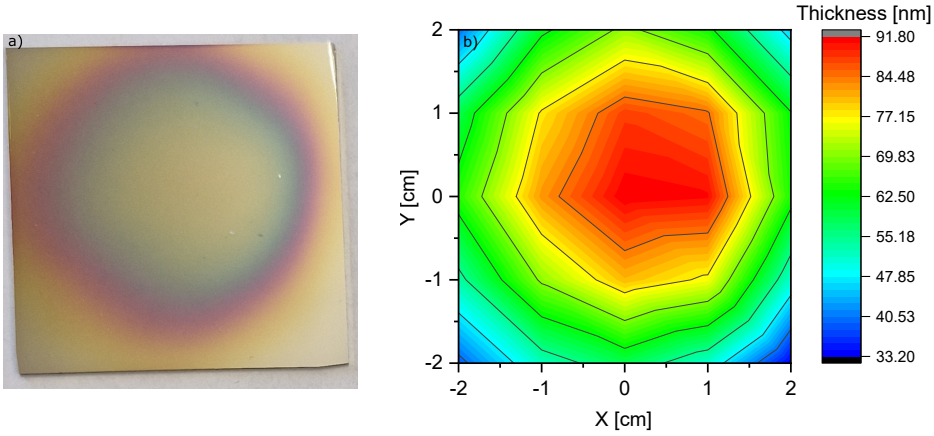


Figure 4.12.: a) Picture and b) heat-map of the thickness measured by ellipsometry of an a-Si:H film on a 5 × 5 cm² corning glass plate deposited with 400 µl of 2 vol% TS diluted in CO, a deposition time of 10 min, and a $T_d = 495$ °C. The heat map shows an area of 4 × 4 cm² in the center of the sample.

precursor gas concentration determines the availability of molecules or radicals for the reaction with the substrate surface or the already grown film.

In a typical CVD process, temperature influences film growth through two key mechanisms: i) It facilitates the desorption of H from the silicon surface, creating open bonds available for reaction with precursor radicals. ii) It regulates the generation of radicals by providing the necessary thermal energy.[29] If the creation of dangling bonds at the surface were the rate-limiting step, varying the precursor volume would have little effect on the deposition rate. However, as shown in Figure 4.11 c), an increase in TS amount correlates linearly with an increase in film thickness. This observation indicates that the availability of precursor radicals (i.e., TS radicals) limits the film growth rate during the deposition process. For trisilane deposited via CVD, an additional growth mechanism has been identified, driven by a direct reaction with the substrate surface without prior radical formation.[152, 153, 155] Since this reaction, analogously to radical formation, is thermally activated, its rate exhibits the same dependence on deposition temperature.

In consideration of the aforementioned findings and in accordance with the linear relationship that has been established between film thickness and TS concentration, it is proposed that the deposition rate will increase linearly with the amount of available

precursor. To quantify this, a temperature-dependent deposition rate, r_d, is defined, representing the percentage of precursor within the chamber that is deposited as a-Si:H film per minute. Furthermore, a percentage loss, r_l, is introduced, accounting for losses due to, for example, imperfect chamber sealing or deposition on the chamber walls. If the time-dependent amount of trisilane molecules within the chamber is defined as $N_\mathrm{TS}(t)$, a differential equation can be derived to describe the amount of precursor within the deposition chamber during the deposition process:

$$\frac{\mathrm{d}N_\mathrm{TS}(t)}{\mathrm{d}t} = -(r_\mathrm{d} + r_\mathrm{l}) \cdot N_\mathrm{TS}(t)\,. \tag{4.1}$$

With the molecular amount N_0 of TS at the beginning of the deposition, a solution for this differential equation is given by:

$$N_\mathrm{TS}(t) = N_0 \cdot e^{-(r_\mathrm{d}+r_\mathrm{l})t}\,. \tag{4.2}$$

The molecular TS amount N_d deposited as a film can then be calculated by

$$\frac{\mathrm{d}N_\mathrm{d}(t)}{\mathrm{d}t} = r_\mathrm{d} \cdot N_\mathrm{TS}(t)\,. \tag{4.3}$$

With the boundary condition that the molecular TS amount $N_\mathrm{d}(0)$ deposited as a film at the beginning of deposition is 0, the following function for $N_\mathrm{d}(t)$ is obtained by integrating Equation 4.3:

$$N_\mathrm{d}(t) = \frac{r_\mathrm{d}}{r_\mathrm{d} + r_\mathrm{l}} N_0 \left(1 - e^{-(r_\mathrm{d}+r_\mathrm{l})t}\right)\,. \tag{4.4}$$

Since the film thickness d grown at a certain area is linear to the molecular TS amount N_d used for deposition with $d = 3N_\mathrm{d}/(n_\mathrm{Si} \cdot A_\mathrm{plate})$, an equation for the time dependent film thickness can be derived by dividing Equation 4.4 by $(n_\mathrm{Si} \cdot A_\mathrm{plate})/3$. n_Si is the atomic density of a-Si:H, A_plate the area where the film is deposited, and the factor 3 accounts for the 3 Si atoms per TS molecule. Therefore, the time dependent film thickness $d(t)$ is given by

$$d(t) = \frac{r_\mathrm{d}}{r_\mathrm{d} + r_\mathrm{l}} d_\mathrm{max} \left(1 - e^{-(r_\mathrm{d}+r_\mathrm{l})t}\right)\,. \tag{4.5}$$

Here, $d_\mathrm{max} = 3N_0/(n_\mathrm{Si} \cdot A_\mathrm{plate})$ corresponds to the maximum achievable film thickness in the ideal case of 100 % utilization ($r_\mathrm{l} = 0$). Using the molar mass of trisilane

$M = 92.32\,\mathrm{g\,mol^{-1}}$, the density $\rho = 0.739\,\mathrm{g\,cm^{-3}}$, the inserted TS volume V_{TS} of 8 µl (2 vol% of 400 µl) and the Avogadro constant N_{A}, the inserted number of TS molecules can be calculated by $N_0 = N_{\mathrm{A}} V_{\mathrm{TS}} \rho M^{-1}$. Assuming a homogeneous film across the deposition area of $6 \times 6\,\mathrm{cm^2}$ results in $d_{\mathrm{max}} = 643\,\mathrm{nm}$. As shown in Figure 4.12, the assumption of a spatially uniform film is not true, and the thickness of the film in the middle of the heated area, where the sample substrates are placed, is higher than the average thickness of the film. In addition, film deposition on the top or walls of the chamber is also not considered, which could reduce the film thickness on the sample. For simplicity and given that these two effects on the film thickness are mutually counteractive, a homogeneous deposition over the metal-block area is assumed.

Using these assumptions, Equation 4.5 is used to fit the time-dependent film thickness d to the measurement results of the Time2 series presented in Figure 4.11 b). This was achieved by adjusting r_{d} and r_{l}. The comparison of the fit of the thickness d with the measured thickness is shown in Figure 4.13. The model aligns well with the measured values, with a leakage rate of approximately $\sim 11.5\,\%\,\mathrm{min^{-1}}$ and the deposition rate is $\sim 2.1\,\%\,\mathrm{min^{-1}}$, meaning that the highest deposition rate at the beginning of the process was $\sim 13.2\,\mathrm{nm\,min^{-1}}$ and a trisilane utilization $u_{\mathrm{TS}} = r_{\mathrm{d}}/(r_{\mathrm{l}} + r_{\mathrm{d}})$ of 15.4 % was achieved.

Building on this, the growth dynamics were further analyzed. Using the temperature dependence of the deposition rate r_{d}, the activation energy (E_{A}) of the growth process can be estimated. Under the highly approximate assumption that, that the loss rate $r_{\mathrm{l}} = 11.5\,\%\ \mathrm{min^{-1}}$ is constant for all deposition temperatures, r_{d} is adjusted to align the film thickness calculated by the growth model with the corresponding measured thicknesses from the Temp2 series. This resulted in deposition rates between 0.1 and $9.5\,\%\,\mathrm{min^{-1}}$, corresponding to a trisilane utilization u_{TS} between 0.9 and 47.5 % for deposition temperatures between 410 and 525 °C. Subsequently, the calculated values of r_{d} are used to construct an Arrhenius plot, as shown in Figure 4.14, to estimate the activation energy E_{A} of the growth process. From the linear fit of the Arrhenius plot, an E_{A} of approximately 1.8 eV was calculated. Note that the determination of the activation energy is only a rough estimate since it is influenced by several estimations and measurement uncertainties.

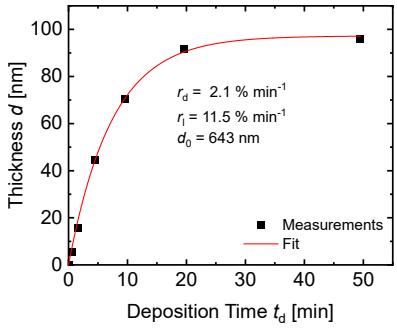


Figure 4.13.: Fit of the thickness d calculated by the growth model (red) to the measured thickness of samples from the Time2 series (black) by using r_d and r_l as fit parameters. r_d and r_l are given within the graph.

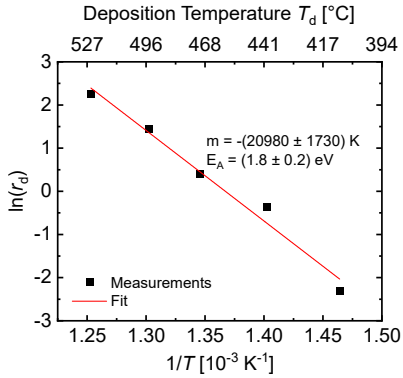


Figure 4.14.: Arrhenius plot obtained by plotting the logarithm of r_d versus the inverse deposition temperature. The slope of the Arrhenius plot m and the corresponding activation energy E_A are given in the graph.

4.2.5. Effect of precursor injection variation

The use of cyclcooctane as a solvent for trisilane not only allowed a more reproducible deposition process but also opened a new parameter space next to the parameters already investigated in Figure 4.11. The increased precursor volume enables the use of precise dosing through the APCVD system dosing pump with minimum dosing steps of 5 µl. In addition, continuous dosing of the precursor during deposition might improve the homogeneity of the a-Si:H films. For the deposition with pure trisilane the precursor volume was less than 50 µl, which was too small to overcome the 100 µl dead volume between the dosage pump exhaust and the N_2-flush inlet, resulting in incomplete precursor transfer to the chamber.

A total volume of 400 µl of 2 vol% trisilane diluted in cyclooctane was used to test the influence of a steady precursor injection during deposition compared to a complete precursor injection at the beginning of the deposition process, as used for the other series of samples in this work. The dosage pump was programmed to deliver in total 600 µl for each deposition in the chamber, compensating for the dead volume and ensuring the complete transfer of the precursor. The volume of 600 µl was divided into 1, 2, 10, 20, or 120 injections, evenly distributed over ten minutes. For example, in the case of 10 injections, 60 µl of the precursor was dosed every 60 seconds. A summary of all the deposition parameters of the "Injection" series is given in Table 4.2. The material properties of the resulting films are presented in Figure 4.15. The photo- and dark conductivities of the samples are similar across all films, while the dark conductivity scatters between slightly above 10^{-10} and slightly below 10^{-11} S cm^{-1}. The film thickness of the films is rather independent of the amount of injections and scatters between 60 and 80 nm. Only the film produced using 120 injections shows a significant decrease in thickness of only 30 nm. The hydrogen content decreases from 7 at% to 3 at% with increasing injections, while R increases from 0.43 to 0.6. However, for films with 1 to 20 injections, it remains unclear whether the observed changes in hydrogen content and R are genuinely correlated with the injection amount or whether the minor variations result from scattering.

The results indicate that the film properties are only minimally influenced by the number of precursor injections, up to 20 injections per deposition. The properties measured so far represent averages over the film thickness and therefore do not reveal potential inhomogeneities along the growth direction. To assess the compositional homogeneity of the films, SIMS depth profiling was employed to determine the atomic composition as a function of depth. Figure 4.16 compares the SIMS depth profiles

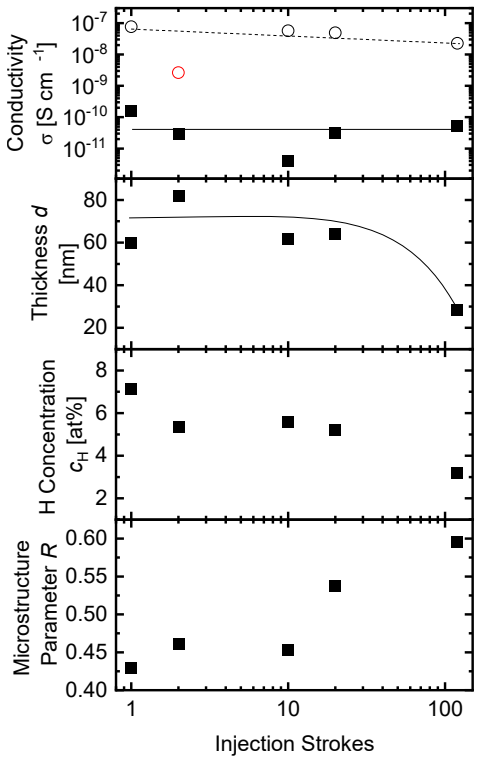


Figure 4.15.: Dark and photoconductivity σ_{d} and σ_{ph}, thickness d, hydrogen concentration c_{H} and microstructure parameter R versus the number of precursor injections of a-Si:H films deposited using with 2 vol% trisilane diluted in cyclooctane at $T_{\mathrm{d}} = 470\,^{\circ}\mathrm{C}$ as precursor. For all samples, a total volume of 400 µl precursor and a total deposition time of 10 min were used. The lines are guides to the eye.

of O, C, H, and Si of films deposited with varying injection numbers. Both H and C exhibit relatively uniform distributions throughout the film thickness, compared to a-Si:H films deposited using pure trisilane (cf. Figure 4.6 b). However, near the surface, the H and C contents are up to 100 % higher than near the interface with the c-Si substrate. This increase is particularly pronounced in the film deposited with a single injection, probably because of the high cyclooctane to trisilane molecule ratio at the end of the deposition process. The C and H content for all films are very similar, aside from a lower H content for the film deposited with 120 injections, which is in agreement with the lower H content found by FTIR shown in Figure 4.15. In contrast, the oxygen content strongly depends on the number of injections, increasing by more than an order of magnitude with a higher number of injections. Furthermore, for films deposited with 2 and 10 injections, distinct oxygen peaks are observed corresponding to each injection. This suggests that the nitrogen flush, which delivers the precursor into the chamber, contains oxygen impurities, possibly due to minor leaks in the nitrogen supply line.

Deposition using multiple injections slightly improved the homogeneity of the C and H content along the thickness of the film. However, both elements exhibited a gradual increase towards the film surface, likely as a result of the accumulation of not decomposed CO in the chamber atmosphere, independent of the number of injections. Additionally, the O content increased with the number of injections. Given this and the observation that the material properties shown in Figure 4.15 are only minimally affected by the number of injections, a single injection was used for all films in this work used for material analyzes to assess the key properties of the film. In addition, for pure trisilane deposition, a single injection was the only feasible approach.

The deposition using multiple injections could slightly improve the homogeneity of the C and H content along the film thickness. However, both increased with ongoing deposition tentatively because of the growing ratio of not decomposed CO in the chamber atmosphere, independent of the injection number. In addition, the O content increased with increasing injection number. Because of that and the fact that the material properties investigated in Figure 4.15 only hardly depend on the amount of injections, it is valid that for all material analysis in this work, only one injection is used to investigate the main film properties. For pure trisilane deposition, this was the only possible option available anyway (see Section 3.2).

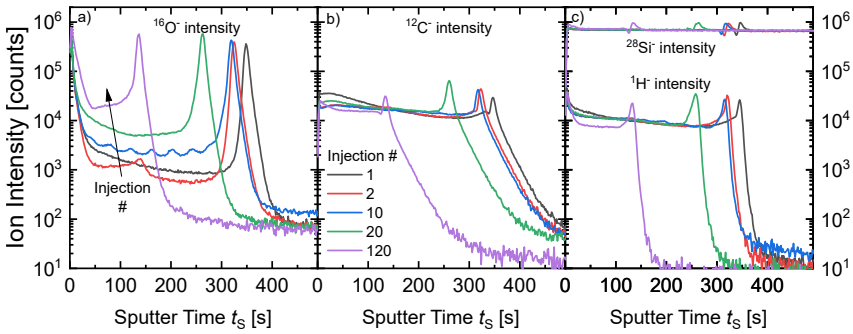


Figure 4.16.: a) Oxygen, b) carbon, and c) hydrogen SIMS depth profiles of intrinsic APCVD films deposited by 1, 2, 10, 20 or 120 precursor injections into the chamber at 470 °C. For all samples, a total volume of 400 µl precursor and a total deposition time of 10 min were used. In c) the silicon SIMS depth profiles are given in addition to the H profiles as a benchmark for the ion intensities. The x and y scales are the same for all graphs.

4.2.6. Discussion

The introduction of cyclooctane as a solvent for trisilane enhances the reproducibility of the deposition process by increasing the precursor volume available and thus better controllable dosage. Films grown with the 2 vol% trisilane solution exhibit greater thickness, particularly at higher temperatures, due to the more efficient utilization of precursors. Specifically, 400 µl of the 2 vol% trisilane solution (equivalent to 8 µl of trisilane) produces a thicker film compared to 10 µl of pure trisilane. For trisilane concentrations above 10 vol% within the precursor, no significant changes in microscopic or macroscopic film properties were observed for all deposition temperatures.

At lower temperatures ($\leq 470\,°C$) but high cyclooctane concentrations (>90 vol%), moderate carbon contamination has minimal impact on conductivity and c_H but increases R. The increase in R for films with a significant carbon content is not a clear indicator of void-rich material as for pure a-Si:H [167] but it can also indicate Si-H bonds with carbon backbonds.[111, 114] Because of the effect of added carbon on R, the R values of films with higher carbon content cannot be directly compared to those of films made with pure trisilane. The change in bonding structure is also indicated by the more homogeneous distribution of H throughout the thickness of the film, as shown in Figure 4.10.

At deposition temperatures above 470 °C and cyclooctane concentrations above 90 vol%, key differences in film properties emerge. Significant carbon incorporation is accompanied by increased hydrogen incorporation and higher R.

Effusion experiments of a-SiC:H show a higher temperature stability of H in a-SiC:H than in a-Si:H [109, 110], in agreement with the fact that a higher carbon content of the films also leads to increased H incorporation at high deposition temperatures and that films deposited with higher CO dilutions showed less blistering. Furthermore, the fact that H bonded in the voids shows even lower effusion temperatures than H bonded in dense a-Si:H without carbon indicates that H found at $2100\,cm^{-1}$ via FTIR can be assigned to H bonded to silicon with a carbon backbond instead of H bonded in a void-rich material. More details can be found in Section 2.2.1.

Due to the higher H content, the incorporation of carbon can improve the photosensitivity of films deposited at temperatures between 495 °C and 555 °C. For films made of pure silane, almost no splitting of the photo- and dark conductivity can be observed for this temperature regime.

The robust and reproducible deposition process using TS-CO mixtures enabled the development of a growth model and fitting of the calculated film thicknesses to the

measured thicknesses. This model revealed a precursor loss rate of approximately 11.5 % min^{-1}, which mainly results from the missing sealing of the deposition chamber. The precursor deposition rate r_d increases with increasing T_d from 0.1 % min^{-1} for T_d = 410 °C to 9.5 % min^{-1} for T_d = 525 °C. Due to the increasing ratio of the deposition rate r_d to the loss rate r_l with increasing temperature, the utilization rate of the precursor increases as well with a maximum of u_{TS} = 47.5 % at T_d = 525 °C. An improved chamber sealing could increase this value and allow a high a-Si:H film deposition with high utilization also at lower deposition temperatures. Note, however, that the calculation of the temperature dependency of r_d is based on the crude assumption of a temperature-independent r_l. Although this assumption is expected to be sufficiently accurate, manual closure of the deposition chamber and thermally induced fluctuations of the gas at elevated temperatures may introduce additional variations in the loss rate.

Using the deposition rates calculated in an Arrhenius plot, an activation energy E_A of approximately 1.8 eV is derived for the a-Si:H deposition via TS. This value is in good agreement with the decomposition temperatures of silanes reported in the literature. For instance, Vanderwielen et al. [154] found an activation energy of 2.1–2.3 eV (48.2–51.9 kcal mol^{-1}) for trisilane decomposition. Similarly, Vincent et al. [163] reported activation energies between 1.3 and 2.2 eV (31–51 kcal mol^{-1}) for a-Si:H film grown from trisilane. The activation energy of the growth process likely reflects the activation energies of the primary decomposition or deposition reactions, as discussed in more detail in Section 2.3.3. These reactions predominantly involve the cleavage of a Si–Si bond within the transition state, which is consistent with the observed activation energy (E_A = 1.8 eV) being close to the Si–Si bond energy in trisilane (E_B = 2.3 eV).

For the calculation of r_d, deposition was assumed to occur only on the metal plate area (36 cm^2) on top of the hot plate. Potential errors in this assumption, such as a-Si:H deposition on chamber walls or inhomogeneous film growth, were compensated within the fit by adjusting r_l. However, assuming a constant r_l across all temperatures may not be entirely valid, as higher T_d leads to increased precursor loss due to chamber wall deposition. This is also why the two highest temperatures of the Temp2 series were excluded from the Arrhenius fit.

If the precursor injection is spread over the deposition time using several injections (up to 20), the properties of the layer are very similar to those where the precursor is injected all at once at the beginning of the deposition, as seen in Figure 4.15. For

a high injection number of 120 injections and therefore a low precursor volume per injection, the film has a lower film thickness due to the higher precursor loss due to flushing out parts of the precursor within the chamber during the pipe flushing with a magnetic valve after every injection. The microstructure parameter increases slightly with increasing injections, maybe caused by a higher O content that leads to more Si-H bonds with an O backbond with a vibration wavenumber of ~2100 cm^{-1}. While the increased O content is not beneficial, an increased injection number can lead to slightly improved homogeneity along the thickness of the film. However, to take full advantage of constant dosing, a way to constantly dose pure trisilane is needed to prevent the incorporation of cyclooctane, which also leads to higher C and H contents with increasing deposition time. In addition, the purity of the N_2 inlet needs to be improved to prevent oxidation. For an industrial application, the spatial film growth uniformity needs to be improved, which can be made by a more qualitative heat source but also is done by itself when the deposition area increases, and therefore the ideal case of an infinite plane area is more closely approached.

A high Si-C peak in FTIR spectra and the g-value of 2.004 observed for a sample deposited at $T_d = 580\,°C$ and with 2 vol% trisilane solved in cyclooctane as precursor demonstrate that for films deposited at high temperature and with high cyclooctane concentrations the material configuration shifts from carbon-polluted a-Si:H to an a-Si:H/a-SiC:H mixture. The silicon-rich a-SiC:H matrix is a promising candidate as a precursor for nanocrystalline silicon embedded in an a-SiC:H matrix, which can be achieved through the process of annealing. This material has a wide applicability in optoelectronic applications.[96, 98, 103, 120, 213]

These results show that the use of cyclooctane as a solvent for silicon precursors can significantly influence the film properties. However, it is also shown that deposition temperatures and cyclooctane concentrations below 495 °C and 90 vol%, as used for most liquid silane processes, are not critical regarding the incorporation of C.[20–22]

4.3. Applications and post-treatments of APCVD a-Si:H films

After detailed analysis of the properties of the a-Si:H films deposited using trisilane and trisilane-cyclooctane mixtures, the next step is to explore their applications and potential post-treatment methods. This section focuses on various processing techniques and modifications that enhance the functionality of these films for different applications.

First, the passivation properties of APCVD a-Si:H films on crystalline silicon (c-Si) wafers are investigated. The passivation results are presented, followed by a detailed discussion. Beyond passivation, the hydrogenation of a-Si:H films is examined, a crucial step in optimizing their electrical and optical properties. Additionally, catalytic doping is used as a method to modify the electronic properties of the films, followed by a discussion that evaluates the impact of this approach on the a-Si:H film conductivity. Finally, the crystallization of a-Si:H films is investigated as a pathway toward enhancing the material performance. Two crystallization techniques are examined: furnace annealing with a slow temperature ramping, which is typically used to crystallize a-Si:H films with high H content without blistering, and rapid thermal annealing, which enables very fast processes and potentially larger crystal grain sizes.

4.3.1. Passivation of c-Si wafer

The passivation of dangling bonds on the c-Si surface is crucial for the performance of various devices.[24, 25, 28, 214, 215] One approach is the deposition of a-Si:H layers on the c-Si surface, which provide H to passivate the dangling bonds. Especially in silicon heterojunction solar cells, silicon surface passivation is a key challenge to achieve high-efficiency devices and is therefore of great interest.[24–28] To achieve good passivation in SHJ solar cells, thin ($< 10\,\mathrm{nm}$) a-Si:H films with a high H concentration ($> 20\,\mathrm{at\%}$) are used to saturate the dangling bonds at the c-Si surface.[24, 78, 204, 216]

The APCVD films investigated in this work exhibit a significantly lower hydrogen content ($< 10\,\mathrm{at\%}$), which may limit their passivation potential. This section explores the limitations of this potential in detail. In addition, the use of APCVD layers instead of the more commonly employed PECVD layers might offer an opportunity to gain

deeper insights into the physical mechanisms underlying the passivation process. This, in turn, helps identify the key film properties responsible for high passivation quality.

One example is the influence of the defect density on the passivation. Although PECVD-deposited a-Si:H films with a high hydrogen content (> 20 at%) generally achieve superior passivation quality, they are also known to exhibit higher defect densities compared to films with moderate hydrogen content (< 10 at%).[84, p. 20, 204] This suggests that passivation quality does not directly correlate with the defect density in a-Si:H. APCVD films, which naturally exhibit higher defect densities due to deposition temperatures exceeding the hydrogen effusion threshold (as discussed in Section 4.1.3), provide a useful platform to investigate this assumption further.

To gain a deeper understanding of the role of hydrogen content in passivation quality, two parameters are introduced:

i) The first parameter is the hydrogen concentration, c_{H}, which can be calculated from FTIR spectra as described in Section 3.4.1.

ii) The second parameter is the hydrogen area concentration, c_{A}, which is defined herein as:

$$c_{\mathrm{A}} = c_{\mathrm{H}} \cdot d\,, \tag{4.6}$$

where d is the thickness of the film. By multiplying the hydrogen concentration c_{H} by the thickness of the film d, this parameter represents the total areal hydrogen content within the a-Si:H layer. It provides a measure of the hydrogen that is theoretically available per unit area to passivate the two-dimensional defective c-Si surface.

As sample substrate, n-type (<100>, 280 µm, 1–5 Ω cm) and p-type (<100>, 525 µm, 20 Ω cm) 4-inch float-zone wafers were used. Since the deposition area of the system is only (6 × 6) cm² the wafers were cut by laser into 4 pieces. For each sample series, pieces from only one wafer are used to minimize the influence of the bulk charge carrier lifetime of the wafer on the results. After the cutting process, the wafers were etched in a diluted hydrofluoric acid solution of 1 % (HF) for 10 min to remove native oxide just before the deposition process. A temperature passivation series (Temp_P1) was deposited, with a-Si:H films formed at various temperatures on both wafer types. Additionally, only on n-type wafers, a deposition time series (Time_P), a precursor volume series (Volume_P) and another temperature series using 2 vol% TS diluted in CO as precursor (Temp_P2) were prepared. The detailed deposition conditions are given in Table 4.4. For each individual wafer, the a-Si:H films on both sides are produced using identical recipes and deposition temperatures. For the deposition,

the wafers were placed on a quartz substrate within the deposition chamber. After deposition of the first layer, the substrate was flipped by 180°, since the film grows only on the side not facing the quartz plate. After rotation, the second film was deposited. To enhance the charge carrier lifetime, the samples from the Time_P series underwent a light soaking procedure, following the protocol commonly applied to SHJ solar cells at the Jülich Research Center.[217]

Table 4.4.: Deposition parameters of the different passivation sample series. The parameter that was varied is shown in bold. The trisilane content of the precursor, the deposition temperature, and time are given, as well as the total precursor volume including trisilane and cyclooctane.

Series	**TS concentration** χ_{TS} **[vol%]**	**Temperature** T_d **[°C]**	**Time** t_d **[min]**	**Volume** V_P **[µl]**
Temp_P1	100	**440–525**	5	15
Time_P	100	470	**2–20**	15
Volume_P	100	470	5	**5–20**
Temp_P2	2	**470–555**	5	600

4.3.1.1. Deposition temperature dependency

Although the H bonding configuration is already analyzed in Section 4.1.2, the temperature series Temp_P1 is used to check the H concentration c_H and the Si-H bonding microstructure of the a-Si:H films used for passivation. Figure 4.17 shows the Fourier transform infrared (FTIR) spectra of the Si-H stretching vibrations located in the range from 2000 cm^{-1} to 2100 cm^{-1} for these films deposited on the n-type wafers. As for the films of the Temp1 series in Section 4.1.2, c_H decreases with increasing temperature. Moreover, the proportion of the 2100 cm^{-1} peak in the total area of the double peak structure decreases with increasing temperature due to a faster effusion of H contributing to this peak in contrast to H contributing to the peak near 2000 cm^{-1}.[109] The decrease in c_H indicates a lower amount of H and therefore more defects, according to Section 4.1.3, where an anti-correlation between the H content and the defect density was observed.[204] Using these films, the temperature dependence of the passivation quality is investigated.

Figure 4.18 a) shows the charge carrier lifetime τ measured by transient photo conductance decay (TPCD) of n-type (gray) and p-type (red) wafers covered with

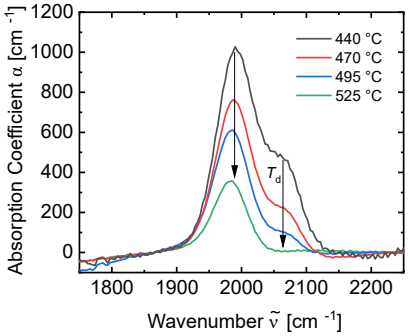


Figure 4.17.: FTIR spectra of a-Si:H films deposited at temperatures of 440, 470, 495, and 525 °C. The spectra show the region of the Si-H vibrational modes. The depositions are performed using 15–20 µl of trisilane at each side of n-type wafers.

a-Si:H layers on both sides, deposited at temperatures between 440 and 525 °C. PL images for the n-type films are additionally shown in Figure A.9. Although the films are deposited with temperatures above the critical H effusion temperature of a-Si:H, all samples show a significant charge carrier lifetime τ (>100 µs). τ is maximum at $T_\mathrm{d} = 470\,°\mathrm{C}$ with $\tau_\mathrm{max} = 1500\,\mu\mathrm{s}$ for n-type and $\tau_\mathrm{max} = 1740\,\mu\mathrm{s}$ for p-type wafer. For higher temperatures, τ decreases, which is expected due to the increased H effusion. Films deposited at 440 °C show a lower τ than films deposited at 470 °C, despite a higher c_H as indicated in Figure 4.17.

One reason for the low τ might be the low thickness of the films deposited at $T_\mathrm{d} = 440\,°\mathrm{C}$, as shown in Figure 4.18 b). In this figure, the mean thickness of both a-Si:H films is shown, where the upper and lower edges of the error bar indicate the film thickness measured on each side of the wafer. The film thickness increases with increasing T_d, indicating a higher growth rate with increasing T_d as already observed in Section 4.1.2. An exception is the deposition at $T_\mathrm{d} = 525\,°\mathrm{C}$ for the n-type wafer. The lower film thickness might be caused by a not fully sealed chamber head leading to higher precursor loss during the deposition or due to a slightly higher inlet temperature leading to a higher evaporation of liquid trisilane before injection and an unwanted deposition at the chamber walls. (see Section 4.2.4 and the corresponding discussion in Section 4.2.6).

Figure 4.18 c) and d) show the H concentration c_H and the H area concentration c_A calculated from the FTIR Si-H stretching modes as shown in Figure 4.17 versus the

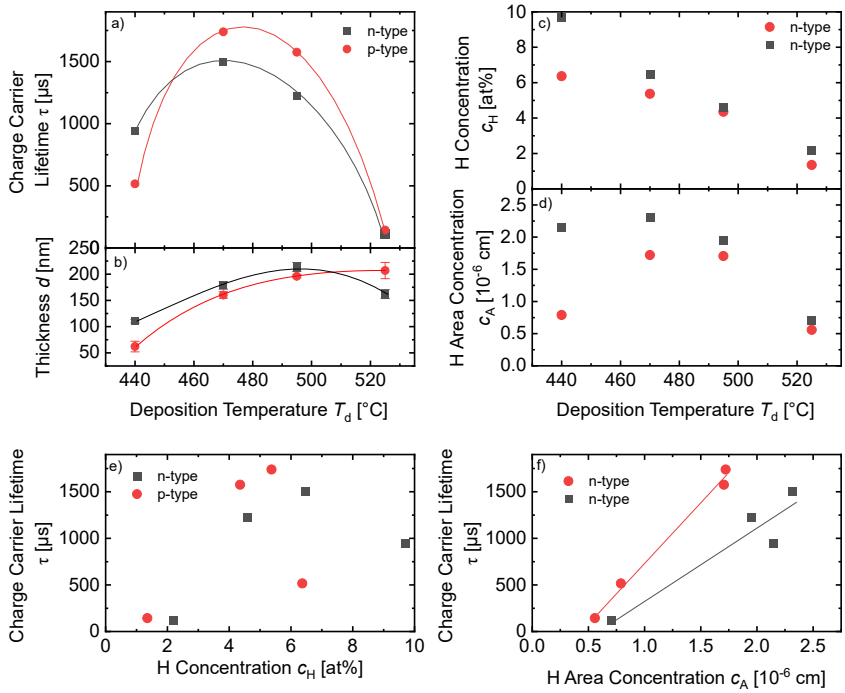


Figure 4.18.: a) Charge carrier lifetime τ of the charge carriers within n-type and p-type c-Si wafers and b) thickness d of a-Si:H passivation layers covering the wafers versus deposition temperature T_d of the a-Si:H layers. The edges of the error bar indicate the thickness of the films on each side of a sample. c) H area concentration c_A and d) H concentration c_H of the same samples versus deposition temperature T_d. Charge carrier lifetime τ versus e) H area concentration c_A and f) H concentration c_H of the same samples. The lines are guides to the eye.

deposition temperature of the a-Si:H films. The hydrogen concentration c_H increases with decreasing deposition temperature. In contrast, the hydrogen area concentration c_A initially increases with increasing deposition temperature, reaching a maximum at T_d = 470 °C, before decreasing again at T_d = 440 °C. The trends of c_A resemble the behavior observed in Figure 4.18 a), which shows the effective charge carrier lifetime τ as a function of T_d.

To investigate potential correlations between hydrogen content and passivation quality, Figure 4.18 e) plots τ as a function of c_H, and Figure 4.18 f) shows τ versus c_A. A clear correlation is observed between τ and the hydrogen area concentration c_A, whereas no obvious correlation is found with the hydrogen concentration c_H alone. This indicates that the total amount of H within the film is crucial for the passivation mechanism, which means that τ is proportional to the product of c_H and the thickness of the film d.

4.3.1.2. Deposition time and precursor volume dependency

To investigate in more detail the influence of film thickness on surface passivation, a deposition temperature of 470 °C was used, as it yielded the highest lifetimes in Figure 4.18. In two separate series, the thickness of the a-Si:H layer on n-type FZ wafers was varied between 46 and 133 nm by adjusting the inserted trisilane volume (Volume_P series) and the deposition time (Time_P series). The precursor volume was varied from 5 to 20 µl in 5 µl steps using a t_d of 5 min, and for the deposition time series, t_d was set to 2, 5, 10, and 20 min using a precursor volume of 15 µl.

The charge carrier lifetimes of the resulting samples and their correlation with the film thickness are shown in Figure 4.19 a). An increase in film thickness from 46 to 133 nm by increasing the precursor volume (gray) leads to an increase in the charge carrier lifetime from 200 µs to 1900 µs. In contrast, an increase in film thickness from 48 to 100 nm by increasing deposition time (red) leads to a decrease in the charge carrier lifetime from 580 µs to 160 µs.

To understand the different behavior of the lifetimes with increasing film thickness, for both series c_H is plotted versus the film thickness in Figure 4.19 b), while the corresponding relationship for c_A is shown in Figure 4.19 c). For the precursor volume variation, both, c_H and c_A, increase with increasing film thickness. The increase in c_H with film thickness can be attributed to the higher growth rate of the film due to the higher precursor volume inserted for the deposition. This leads to a higher c_H due to

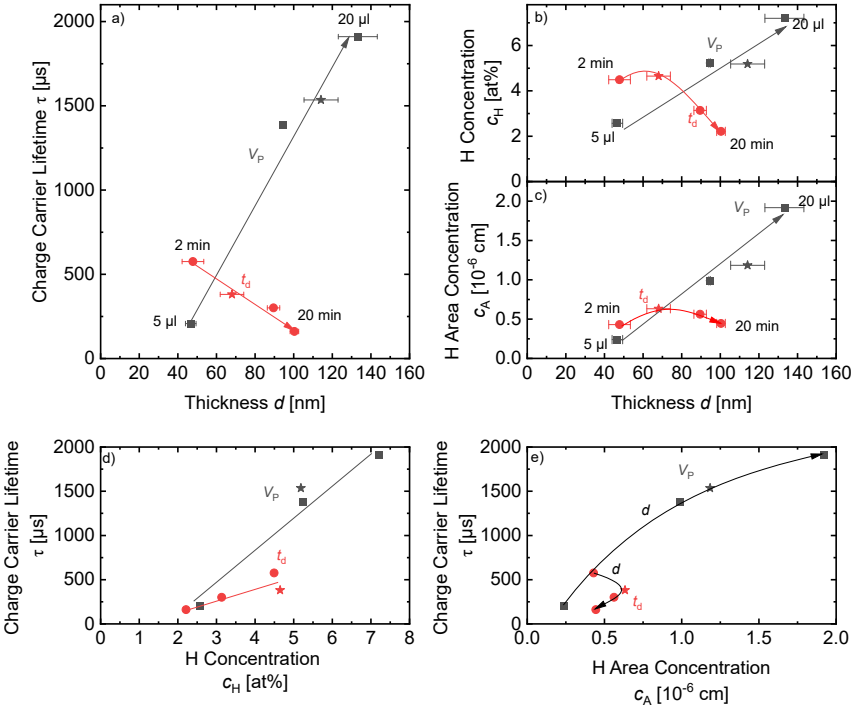


Figure 4.19.: a) Charge carrier lifetime τ of n-type FZ c-Si wafer versus thickness d of the a-Si:H passivation layers covering the wafer. The edges of the error bar indicate the thickness of the films on each side of a sample. b) H area concentration c_A and c) H concentration c_H of the same samples versus thickness d. Charge carrier lifetime τ versus d) H area concentration c_A and e) H concentration c_H of the same samples. The lines are guides to the eye. The layer thicknesses were varied by changing i) the precursor volume V_P (gray) and ii) the deposition time t_d (red). Samples marked with an asterisk were prepared using the same deposition recipe (15 µl, 5 min, 470 °C) in both series.

a higher H incorporation rate, as already shown in Section 4.1.2. The higher c_H and the higher d obviously have a higher c_A as a consequence.

In contrast, for the deposition time series, c_H and c_A decrease with increasing film thickness for films deposited using a deposition time between 5 and 20 min. This could be because a longer deposition time also increases the time available for H effusion, significantly reducing H concentration within the film, as shown in Figure 4.19 c). However, the sample deposited with $t_d = 2$ min shows lower c_H and c_A than the sample deposited with $t_d = 5$ min.

The correlation between c_H and the charge carrier lifetime τ is shown in Figure 4.19 d), while the corresponding relationship for c_A is shown in Figure 4.19 f). For all samples, τ increases with increasing c_H and c_A, except for the film deposited with $t_d = 2$ min. For this film, the lifetime is maximal, although c_A is lower and c_H is similar compared to the sample where the a-Si:H film was deposited for 5 min.

In Figure 4.19, one sample in each series is marked with an asterisk. Those samples were made using the same deposition recipe (15 µl, 5 min, 470 °C) but the Time_P series was made half a year after the Volume_P series. Although made with the same recipe, the lifetime and layer thickness of both films are very different. In addition, c_H for the sample of the deposition time series is slightly lower. Possible reasons for the difference between the samples are discussed in Section 4.3.1.5.

Figure 4.20 presents the Raman spectra of a-Si:H films within the Si-H stretching mode region for both the precursor volume and deposition time series, showing the spectra of each individual film on both sides of a wafer. The Si-H peak heights of the films deposited first are lower than those of the films deposited second, indicating hydrogen effusion from the first layer due to annealing during the deposition process of the second layer.

The trend of the peak heights with varying precursor volume and deposition time is aligned with the trend of c_A in Figure 4.19 b). The Si-H peaks of the first deposited a-Si:H films in the deposition time series (Figure 4.20 c)) appear very similar for all deposition times. This is likely because, although a shorter deposition time reduces the duration for hydrogen effusion during deposition, the preheating phase of approximately 10 min required to achieve a constant deposition temperature for the second layer results in more similar effective annealing times for the films deposited first.

The films of the deposition time series show almost no peak at 2100 cm^{-1}, indicating only a low amount of hydrogen bonded in a less dense Si structure. While the 2000 cm^{-1}

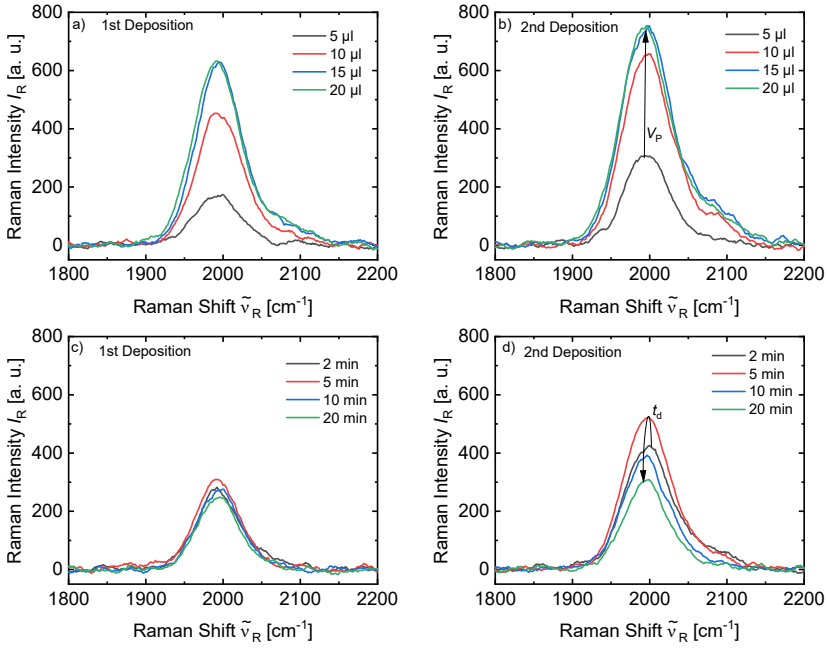


Figure 4.20.: Raman spectra of Si-H modes measured on the front and rear sides of c-Si FZ wafers covered with a-Si:H layers. a) Spectra of the precursor volume series on the side where the a-Si:H film was deposited first. b) Spectra of the precursor volume series on the side where the a-Si:H film was deposited second. c) Spectra of the deposition time series on the side where the a-Si:H film was deposited first. d) Spectra of the deposition time series on the side where the a-Si:H film was deposited second.

peak for the 2-minute deposition is lower than that for the 5-minute deposition, the 2100 cm^{-1} peak appears similar or even slightly higher. This indicates a potentially higher amount of highly diffusive hydrogen bonded in a less dense environment, which might explain the increased lifetime observed for the 2-minute sample.

4.3.1.3. Light soaking

Diffusive H is the driving aspect for intensive light soaking processes for SHJ solar cells.[217–221] Therefore, intensive light soaking was applied to the precursor volume sample series shown in Figure 4.19, following the standard procedure used for solar cells at my institute (FZJ – IMD-3) (process temperature: 210 °C, process time: 180 s, light intensity: 20 suns)[217]. However, as shown in Figure A.10, no significant change in the charge carrier lifetime was observed. This result might indicate that hydrogen, which is diffusive at 210 °C has already effused from the film during deposition or that the hydrogen remaining within the film has already reached its optimal configuration. It is also important to note that the light soaking process was specifically optimized for textured solar cells, rather than polished charge carrier lifetime samples without an Indium Tin Oxide (ITO) layer. This might be one reason for the lack of impact of light soaking on the charge carrier lifetime.

4.3.1.4. Passivation with carbon-containing a-Si:H

The FTIR and Raman spectroscopy results indicate that surface passivation strongly depends on the total hydrogen content within the a-Si:H film. To increase the hydrogen content, particularly in films deposited at higher temperatures, the use of 2 vol% TS diluted in CO was tested as a precursor for the a-Si:H films. As shown in Section 4.2, this approach leads to an increased hydrogen concentration in these films. Therefore, films using 600 µl of 2 vol% TS diluted in CO for 5 min at deposition temperatures (T_d) of 470, 495, 525, and 555 °C were prepared on n-type FZ wafers. A comparison of the resulting passivation and film properties with those of the pure a-Si:H temperature series is presented in Figure A.11.

Despite higher c_A and similar c_H at elevated temperatures compared to lower temperatures, the longest charge carrier lifetime was again measured for the film deposited at 470 °C. This finding is consistent with the low photosensitivity of these films, despite their increased hydrogen concentration, as observed in Section 4.2.3. The lower charge carrier lifetime of the TS-CO sample in contrast to samples passivated with pure a-Si:H films deposited at $T_d = 470$ °C likely results from a wafer with a low

bulk lifetime. A separate test (not shown here) on a p-type FZ wafer at a deposition temperature of 440 °C using a 400 µl TS-CO mixture yielded a charge carrier lifetime of 1.4 ms.

4.3.1.5. Discussion

Successful passivation of float zone c-Si wafers was demonstrated, as indicated by their long charge carrier lifetime of up to 1.9 ms using pyrolytically deposited a-Si:H. This is significantly higher than the charge carrier lifetimes of up to 350 µs reported by Guo et al. [222], who passivated c-Si wafers using CVD of cyclopentasilane. However, they used film thicknesses below 20 nm, whereas the films with the longest lifetimes analyzed here exceed a thickness of 100 nm. Passivation samples with a film thickness of 40–50 nm exhibited charge carrier lifetimes of up to 500 µs, which is much closer to the values reported by Guo et al. [222] and aligns well with the results of Mews et al. [223], who also investigated samples with $d = 50\,\mathrm{nm}$.

Despite high deposition temperatures of 440–555 °C, H concentrations of up to 9 at% were achieved. For passivation layers deposited at $T_\mathrm{d} \geq 470\,^\circ\mathrm{C}$, τ decreases with increasing deposition temperature, probably due to the increased effusion of H from the film. In contrast, the sample deposited at 440 °C, shows a lower τ than the sample deposited at 470 °C, although the H concentration within the sample deposited at 440 °C was higher. This indicated that the H concentration alone is not the limiting factor for the passivation quality. Instead, the areal H concentration c_A, representing the total H content above the surface, showed a linear correlation with the lifetimes of the samples. This indicates that the total amount of H within the film limits passivation rather than the hydrogen concentration c_H in the a-Si:H film.

To understand this fact, the underlying mechanism leading to passivation needs to be discussed. For films made by APCVD, it can be assumed that the H saturation at the c-Si surface corresponds to the frozen equilibrium state present at the end of the deposition process. The rapid cooling (quenching) of the sample at the end of deposition significantly reduces hydrogen mobility, effectively freezing the equilibrium state present just prior to cooling. During the deposition process, the high temperatures lead to a high mobility of H within the film and at the c-Si surface. The number of passivated defects at the c-Si surface depends on the equilibrium between H absorption and desorption at the interface. The H absorption can be increased by increasing the amount of available H within the a-Si:H film. The fact that for the Temp_P1 series, the charge carrier lifetime increases with the areal H concentration c_A indicates that H from the whole sample contributes to the passivation during film deposition. This suggests that c-Si surface passivation is primarily achieved by hydrogen, which can easily diffuse throughout the entire film during the deposition process. Perhaps

passivation is performed by highly diffusive molecular H_2 as proposed by Fischer et al. [216].

Since the 2100 cm^{-1} peak linearly correlates with the total H content, no separate evaluation of the intensity of this peak was performed. However, it should be mentioned that the decrease in the ratio of the 2100 cm^{-1} peak to the 2000 cm^{-1} peak with increasing temperature, as shown in Figure 4.17 usually suggests a reduction in the amount of H bound in voids or inner surfaces, indicating denser films.[72, 116, 167] H in inner voids is known to have a lower diffusion constant than H bound within a dense Si network. The lower amount of this H within the a-Si:H films could be another explanation for the lower passivation quality with increasing deposition temperature.

Another interesting fact that can be observed from the Temp_P1 series is that effective passivation was achieved using a-Si:H films produced at temperatures above the hydrogen effusion threshold, despite concerns about increased defect density at these temperatures. In particular, samples with films deposited at $T_d = 495\,°C$ showed higher lifetimes than films deposited at 440 °C, although a film deposited at 495 °C exhibited a defect density determined by ESR twice as high as for a film deposited at 440 °C. This is a clear indicator that the passivation is mostly independent of the defect density within the films and is dominated more by the a-Si:H/c-Si interface defects. As such, even defective a-Si:H films produced at elevated temperatures can still provide effective surface passivation. This aligns with the findings of Luderer et al. [224], who emphasized that interface effects at the a-Si:H/c-Si junction dominate over bulk a-Si:H properties in determining surface passivation and charge carrier transport in SHJ solar cells.

The Volume_P series in Figure 4.19 shows a correlation of the charge carrier lifetime with the thickness, c_H and c_A. Here, a clear assignment of the increase in τ either to c_H or to c_A is difficult since they correlate linearly. In addition to the increased c_H and c_A, also the thickness of the films might be beneficial for the H passivation at the c-Si surface, since an increased thickness could hinder hydrogen effusion from the first layer deposited during the deposition of the second layer. However, this passivation effect is not the dominant one, since for the Time_P series, τ decreases with increasing film thickness, which is in contrast to the Volume_P series.

The Time_P series shows that τ decreases with increasing deposition time, probably due to a longer time available for H effusion. For the Time_P series, a lifetime correlation with c_H and c_A still holds for deposition times $\geq 2\,min$. However, the

best lifetime was observed for the sample with the lowest total H content, which was deposited using a deposition time of 2 min. It can be concluded that for the evaluation of the passivation quality, c_H and c_A are valuable indicators within a closed series for implications on the lifetime. However, next to those values, other factors such as the equal distribution of H on both sides of the wafer, the silicon density of the a-Si:H film, variations in between the wafers used in each series, and the proportion of H bonded in more porous (2100 cm^{-1}) and of H bonded in more dense (2000 cm^{-1}) material influence the passivation. This leads to a scattering for general cross-series correlations of the H content with the charge carrier lifetime. For instance, the Raman spectra of the sample with a deposition time of 2 min showed a slightly increased 2100 cm^{-1} peak for this sample, maybe indicating a higher amount of highly mobile H, which is available for passivation during the deposition process. Therefore, the higher amount of H available in the voids might explain the longer lifetime of this sample, although the total H content is low.

Samples deposited with the same deposition parameters in the Volume_P and Time_P series (marked with an asterisk in Figure 4.19) showed different charge carrier lifetimes. The lower lifetime for the sample of the Time_P series fits to a lower film thickness. Since the deposition time for this sample is the same as for all samples of the Volume_P series, the lower thickness indicates a lower growth rate, fitting to a slightly lower c_H as well. The Time_P series was made half a year after the Volume_P series. Other depositions and maintenance of the APCVD system at this time may have led to a change in the precursor leak rate r_l, causing a lower film thickness using the same deposition parameters. Additionally, despite the fact that wafers of the same ingot were used, the bulk lifetime of the wafer used for the Time_P series might be low, causing lower achievable effective lifetimes. While these factors make a direct comparison of individual points of both series more difficult, the trend of each series is more valid and comparable since all samples within a film were prepared on the same day on a quarter of the exact same wafer.

Highly diffusive H in a-Si:H is often associated with H, which effuses out of the film already at low temperatures below 400 °C.[25, 86, 216, 225] Light soaking at 210 °C, however, could not change the passivation quality of the with APCVD films passivated samples. This indicates that the H, which is diffusive at temperatures below the deposition temperature, is mainly effused out of the film during deposition. The H leading to passivation seems to be highly diffusive only during the deposition process.

This fits the assumption that the thermally activated H diffusion and therefore a change in surface passivation stops with the deposition process.

By using 2 vol% TS diluted in CO as the precursor for the passivation films, it was demonstrated that carbon-containing a-Si:H films also exhibit good passivation quality, comparable to samples made with pure trisilane. However, despite their higher hydrogen concentration, films deposited with diluted TS at elevated temperatures do not exhibit significant advantages in passivation over those made with pure TS. The high hydrogen concentration at elevated T_d in contrast to films deposited with pure TS is primarily the result of a significant fraction of hydrogen atoms bonded to silicon with carbon as a backbond. This stronger bond enhances thermal stability against H effusion.[109, 110] However, the same effect likely leads to reduced passivation efficiency, as strongly bonded hydrogen atoms have limited diffusivity and are therefore not available for passivating the c-Si interface upon thermal treatment.

In Figures 4.18 and 4.19 the average thickness of the film on both sides of the wafer is plotted and used to calculate c_H. Using the average of both thicknesses for this is justified if the charge carrier lifetime scales linearly with thickness. Although the slope was totally different, a linear change in charge carrier lifetime was observed with thickness for both series in Figure 4.19 a). In this case, variations in the thickness across the wafer, such as a higher thickness on one side, also result in a linear change in the effective surface recombination velocity (S_eff) measured by the Sinton instrument. The reason is that, in the case of high bulk charge carrier lifetimes, the bulk charge carrier lifetime does not limit the overall lifetime τ and can be neglected, resulting in S_eff being reciprocal to the charge carrier lifetime τ (see Section 2.1.3).[94] This reciprocal relationship ensures that the average thickness represents the effect of different film thicknesses on both sides of the wafer corresponding to its effect on τ in a meaningful way. The assumption above is not entirely valid since the films on both sides are produced using different processes. The first layer undergoes an additional annealing step during the deposition of the second layer. However, the assumption remains sufficiently accurate to enable a valid data analysis.

With all these considerations, it must be taken into account that inhomogeneous layer growth, which is system-related here, can also influence the film thickness and H content. The PL picture in Figure A.9, for example, shows the resulting spatial inhomogeneities of the lifetime. By measuring FTIR, ellipsometry and Raman at the

same point for each sample, the influence of such inhomogeneities was minimized as far as possible.

A major problem occurring when depositing a-Si:H passivation layers on both sides of a c-Si wafer with the APCVD system presented herein is that for the second deposition, the already existing film is faced to the bottom of the deposition chamber. During this deposition of the second layer, the first film is just annealed without further film growth. Surprisingly, the annealing does not lead to a full H effusion, although it exceeds the H effusion temperature.[109] This phenomenon may be attributed to two potential causes: i) the emergence of a H_2-saturated gas layer at the interface between the substrate and the quartz plate; ii) an increase in the partial H pressure within the deposition chamber, resulting from the continuous trisilane decomposition that occurs during the deposition process.

Although H within the first layer is not fully effused, Figure 4.20 shows that the H content of the first deposited layer is lower than the H content within the second deposited layer, which is potentially detrimental to the passivation quality of the first layer. While Figure 4.20 d) shows higher amounts of H (beside for the 2 min deposition) with lower deposition times for the second layer, Figure 4.20 c) shows similar H peak intensities for all films of the first deposited layer. This is likely due to an annealing time above 10 min for all films, since this is required to achieve a constant deposition temperature for the second layer. Therefore, a deposition of the a-Si:H films on both sides at the same time would be beneficial and might be addressed in the future.

Overall, the passivation quality widely correlates with c_A and remains largely independent of the thickness of the film across all series. This indicates that the passivation is dominated by highly diffusive H within the film, perhaps of molecular structure. If the H is highly diffusive, the whole film can be used as a reservoir for H migrating through the film and contributing to passivation at the interface. The passivation is rather independent of the defect density within the a-Si:H films. These two observations are likely central to explaining why underdense, void-rich intrinsic a-Si:H films provide excellent surface passivation in SHJ solar cells.[24, 25] For a given temperature and in the investigated parameter range, the lifetime can be optimized by minimizing the deposition time and increasing the precursor volume. Both increase the average growth rate of the film.

4.3.2. Doping and hydrogenation of a-Si:H films

This section investigates strategies to enhance the electrical properties of a-Si:H films, focusing on post-deposition hydrogenation, catalytic doping, and the combined application of both techniques. First, the effects of hydrogenation on film quality and defect saturation are examined. Next, catalytic doping is introduced as a method to increase conductivity. Finally, both processes are combined to assess potential synergistic effects, followed by a discussion of the key findings.

4.3.2.1. Hydrogenation

The previous section demonstrated that a-Si:H films are capable of passivating c-Si wafers. However, these films must be relatively thick (~100 nm) and exhibit lower passivation quality compared to state-of-the-art PECVD passivation layers. This deficiency is primarily due to the low hydrogen concentration available for passivation in the APCVD a-Si:H films.

To address this issue, the hydrogen content was increased by treatment with hydrogen radicals. For this purpose, a hot-wire chamber was utilized, where the samples were placed in a heated holder, and the H_2 gas was passed through filaments that decompose the gas due to the high temperature of the filament into H radicals. For this process, a filament temperature of 1350 °C, a holder temperature of 390 °C, a H_2 flow of 50 sccm at 0.05 mbar, and a process time of 1 h were used. Rhenium filaments were placed 71 mm above the substrate. The HWCVD setup is described in detail in Section 3.5.2.

Figure 4.21 a) shows the FTIR spectra in the region of the vibrational modes of Si-H bonds of films deposited at 440, 495 and 555 °C before (gray) and after (red) H-treatment. The results show that, for all films, the H concentration within the film was increased. Although this clearly indicates the incorporation of H into the film, the H content measured after treatment is probably underestimated since the H-treatment leads to blistering for the films on the c-Si substrate. The blistering effectively removes parts of the a-Si:H film, leading to less absorption of the IR signal in these areas.

As for the as-deposited films, after hydrogenation, the peak at 2000 cm^{-1} is dominant, indicating a dense material. However, for all samples, the peak at 2100 cm^{-1} increases, with the highest increase for the film deposited at 440 °C.

For films on glass substrates, no blistering or delamination of the film was observed, allowing a reliable conductivity measurement. The results of the measurement are shown in Figure 4.21 b). The figure shows that the films deposited at 495 and 555 °C

with former low photosensitivity have a significant increased photosensitivity after H-treatment. The photosensitivity of the film deposited at 440 °C decreases slightly, despite an increase in H content within the film. The decrease is due to an increase in the dark conductivity, maybe due to the incorporation of some impurities during H-treatment, leading to unintentional weak doping. The blue stars in Figure 4.21 indicate the photo- and dark conductivities of the i2-layer reference film from Table 4.1 The photosensitivity of the 440 °C film before treatment, the photosensitivity of the other 495 and 555 °C films, as well as the photosensitivity of the i2-layer film, are very similar. They are in the range between 10^4 and 10^5. However, films deposited at higher temperature and with treatment show with 5×10^{-6} S cm^{-1} a more than 1 order of magnitude higher photoconductivity than the untreated 440 °C film, even exceeding the photoconductivity of the i2 reference film. The dark conductivity was reduced to 6×10^{-11} S cm^{-1}, which is still an order of magnitude higher than for as-deposited films grown at 440 °C. The results show that an H-treatment of hot wire can significantly increase the H content within the a-Si:H films, leading to fewer defects and therefore increased photosensitivity, similar to PECVD films.

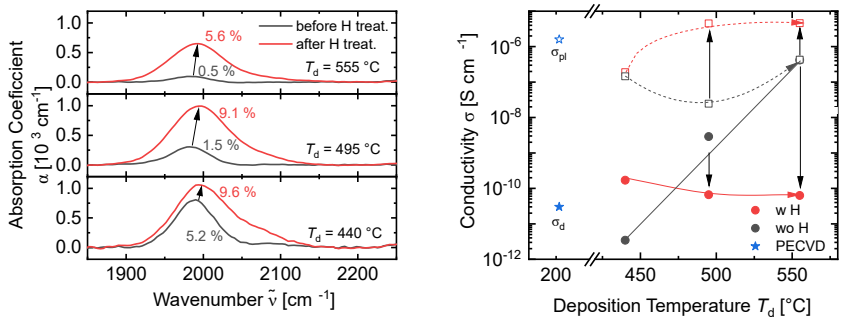


Figure 4.21.: a) FTIR spectra of Si-H vibrational modes within a-Si:H films deposited at various deposition temperatures T_d (indicated within the graph) before (gray) and after (red) H-treatment. b) Corresponding photo- and dark conductivities σ_{ph} and σ_d and conductivity of the a-Si:H reference film from Table 4.1. The lines are guides to the eye.

4.3.2.2. Catalytic doping

The properties of intrinsic a-Si:H films were successfully enhanced by hydrogenation. However, for the application in devices, not only intrinsic but also doped a-Si:H films

are required to improve conductivity and enable the formation of essential electrical structures, such as pn-junctions. There are several approaches for incorporating dopants into a-Si:H films. The most straightforward method involves introducing a dopant-containing precursor during the deposition process. However, due to technical constraints and safety considerations, handling these typically highly toxic precursors within the existing glove box was not feasible.

However, recently a doping process utilizing catalytically activated dopants was established at my institute (FZJ – IMD-3).[31, 32] Similar to the hydrogen treatment described in the previous section, this process is conducted within a hot-wire CVD chamber. For the application on the APCVD a-Si:H films, an existing recipe developed at the institute for catalytic phosphorus doping in SHJ solar cells was employed. The process parameters included a filament temperature of 2200 °C, a phosphine flow of 50 sccm, a substrate temperature of 200 °C, and a chamber pressure of 0.5 mbar. To evaluate catalytic doping, parallel tests were performed on i2-layers fabricated by PECVD (see Table 4.1) with a thickness of approximately 20 nm, serving as a reference, as well as on APCVD layers deposited at 440 °C with thicknesses ranging from 30 to 50 nm.

Liu et al. [31] reported that after the catalytic doping process, a capping layer was used to prevent phosphorus desorption during transport and subsequent measurements. Similarly, Duan et al. [32] described a multilayer stack approach, incorporating successive intrinsic a-Si:H depositions followed by catalytic doping, to increase film thickness and enable conductivity measurements. On the basis of these findings, the deposition of a capping layer, and other treatments following catalytic doping were investigated on APCVD a-Si:H samples.

In a single PECVD process, a-Si:H films were deposited on four Corning glass substrates, and on the other four glass substrates, a-Si:H films were deposited using APCVD. For one sample from each deposition method, the conductivity was measured under the following conditions: i) directly after deposition (as-dep.), ii) after catalytic doping (+ cat), iii) after catalytic doping followed by a 5 nm i2 capping layer deposited via PECVD (+ 5 nm i2), and iv) after catalytic doping, a 5 nm i2 capping layer and a second catalytic doping step (+ cat2). A side view of the various stacks of layers is shown in Figure 4.22.

Figure 4.23 a) show the lateral photo- and dark conductivities, σ_{ph} and σ_{d} of the various layer stacks. The results reveal similar trends for both APCVD and PECVD reference layers. However, the photosensitivity of the PECVD-based films is

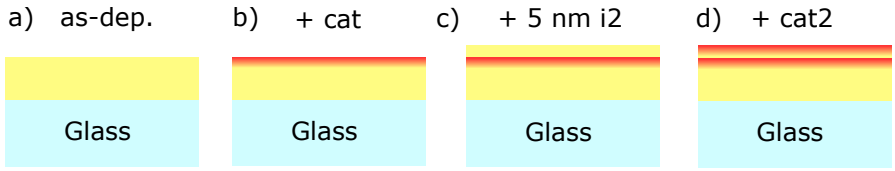


Figure 4.22.: Schematic side view of various catalytic doping layer stacks. a) Directly after deposition (as-dep.), b) after catalytic doping (+ cat), c) after catalytic doping followed by a 5 nm i2 capping layer deposited via PECVD (+ 5 nm i2), and d) after catalytic doping, a 5 nm i2 capping layer, and a second catalytic doping step (+ cat2).

consistently one to two orders of magnitude higher. After the initial catalytic doping step, σ_{ph} and σ_{d} exhibit minimal changes. The subsequent addition of a 5 nm i2 capping layer via PECVD results in an approximate two-order-of-magnitude increase in σ_{ph} for both APCVD and PECVD films. Meanwhile, σ_{d} increases by more than one order of magnitude for the APCVD film and by three orders of magnitude for the PECVD film. The second catalytic doping step has little effect on conductivity, except for a slight decrease in σ_{ph} for both APCVD- and PECVD-based films and a slight reduction in σ_{d} for the PECVD-based film, bringing it to a level similar to that of the APCVD-based film.

These results clearly highlight the necessity of a capping layer to enhance conductivity through catalytic doping. However, the exact mechanisms responsible for this increase in conductivity remain unclear. To investigate this further, an additional sample series was prepared to isolate various processes occurring during capping layer deposition and determine the key factor responsible for conductivity enhancement.

The samples were categorized on the basis of two aspects. The first aspect was whether the films underwent catalytic doping after deposition (w cat) or not (w/o cat). The second aspect classified the films according to the applied post-treatment, including i2-capping layer deposition (5 nm i2), annealing within the PECVD chamber (an.), and APCVD capping layer deposition (APCVD). This resulted in a total of five different processed samples for each type of base film (APCVD and PECVD).

Figure 4.23 b) shows σ_{ph} and σ_{d} of samples processed with an APCVD layer (gray) and a PECVD layer (red) as the base film. In the first process variation, the conductivities of the films were measured directly after deposition without catalytic doping, serving as a reference (w/o cat, as dep.). In the second variation, samples that were not catalytically doped were covered with a 5 nm i2 capping layer (w/o cat,

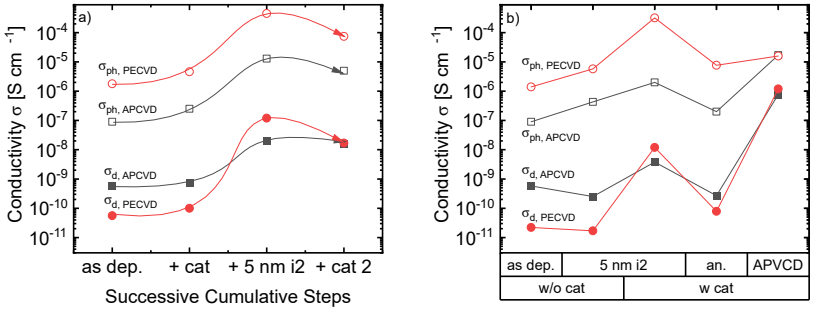


Figure 4.23.: Photo- and dark conductivities σ_{ph} and σ_d of i2-layer PECVD films (red) and APCVD films deposited at $T_d = 440\,°C$ (gray) after various post-deposition processes. In a), the post-treatments accumulate from left to right, meaning that the "+cat2" sample was catalytically doped, then covered with another i2 layer, and catalytically doped again. In b) the conductivities of a-Si:H layers with and without cat doping are shown with various posttreatments that do not add up. As posttreatment an i2 capping layer, annealing within the PECVD chamber, and a capping layer made by APCVD at 440 °C are used.

5 nm i2). This additional capping layer slightly increases the photosensitivity of the samples. However, this increase is minor, suggesting that a catalytic doping step is necessary prior to the capping layer deposition to significantly enhance conductivity. Therefore, the observed conductivity increase is likely not due to unintended oxygen or nitrogen impurities incorporated between the deposition processes. It is important to note that between the first and second (5 nm i2 layer) depositions, the samples were stored under ambient conditions, just like it is needed for the samples with the catalytic doping step.

In the third process variation, samples with catalytic doping and the i2 capping layer (w cat, 5 nm i2) show significant increases in both σ_{ph} and σ_d, as already seen in Figure 4.23 a) for this process recipe. For the fourth variation, the samples were annealed in the PECVD deposition chamber at the same temperature (200 °C) and the duration of the process as used for the i2-layer deposition process following catalytic doping (w cat, an.). The resulting films exhibited conductivities similar to those of the reference films, indicating that annealing alone is insufficient to activate the phosphor doping atoms.

In the fifth process variation, an additional APCVD layer was deposited on the base film after catalytic doping (w cat, APCVD). In this case, the conductivities of the samples with both PECVD and APCVD base films align after the deposition of the APCVD capping layer. The dark conductivity (σ_d) increases significantly, reaching a maximum value of $\sim 10^{-6}\,\mathrm{S\,cm^{-1}}$. For samples with the APCVD base layer, the photoconductivity (σ_{ph}) also reaches its maximum value of approximately $10^{-5}\,\mathrm{S\,cm^{-1}}$. In contrast, for the sample with the PECVD base film, σ_{ph} increases only minor compared to the as-deposited films.

4.3.2.3. Combined catalytic doping and hydrogenation

The previous section demonstrated that effective doping via catalytic incorporation of phosphorus (P) requires the presence of a capping layer. This capping layer likely enhances doping efficiency by promoting the incorporation of P atoms into the a-Si:H network. To eliminate the need for a capping layer, an alternative method is necessary to induce a restructuring of a-Si:H near the surface to facilitate proper integration of P atoms. Hydrogenation has been shown to successfully saturate defects, resulting in the restructuring of the a-Si:H network, as discussed in Section 4.3.2.1. Therefore, it is logical to investigate this process in combination with catalytic doping.

To enable catalytic doping with hydrogen treatment in the HWCVD system for doping, a dedicated H-treatment process was developed to avoid a vacuum break and since the original H-treatment HWCVD chamber was decommissioned during this period. The process parameters are detailed in Section 3.5.2.

To evaluate the combined effects of improved quality of a-Si:H through hydrogenation and enhanced conductivity through catalytic doping, four identical a-Si:H samples were deposited at 555 °C. The samples were subjected to the following treatments:

i) no treatment,

ii) hydrogen treatment (H-treatment),

iii) catalytic doping combined with H-treatment in a single process,

iv) catalytic doping followed by H-treatment in two separate processes.

The process parameters for all treatments are provided in Section 3.5.2, except for combined catalytic doping and H-treatment. In this case, the conditions of the H-treatment were used, with the addition of 20 sccm phosphine (PH_3) to the gas

flow during treatment. This adjustment was necessary because the original catalytic doping conditions (high temperatures around 2200 °C), when combined with hydrogen, produce high-energy hydrogen radicals capable of fully etching the a-Si:H film.

The results of the combined treatments are presented in Figure 4.24. The FTIR spectra in Figure 4.24 a) demonstrate that all treatments involving hydrogenation lead to an increased hydrogen concentration within the films. Figure 4.24 b) shows that the as-deposited film exhibits a conductivity of $4 \times 10^{-7}\,\mathrm{S\,cm^{-1}}$ and a photosensitivity of 1, as expected due to the high defect density typical for films deposited at this temperature. In contrast, the hydrogenated film shows a photosensitivity greater than 10^5 and a photoconductivity exceeding $10^{-5}\,\mathrm{S\,cm^{-1}}$. These results confirm the successful defect saturation achieved by applying the H-treatment within the HWCVD chamber for catalytic doping.

The combined treatment led to a slight improvement in photosensitivity, reaching a value of 10, due to a reduction in σ_d and an increase in σ_ph. The two-step process, comprising standard catalytic doping followed by a subsequent H-treatment, yielded the highest photoconductivity, approaching $10^{-4}\,\mathrm{S\,cm^{-1}}$, along with a dark conductivity of $5 \times 10^{-8}\,\mathrm{S\,cm^{-1}}$. Therefore, this process resulted in both higher photo- and dark conductivities compared to the catalytic doping of APCVD films combined with a PECVD capping layer. The performance approaches that of catalytically doped PECVD films with a PECVD capping layer, as shown in Figure 4.23. These results clearly demonstrate that the use of a capping layer for catalytic doping can be effectively replaced by hydrogenation following the doping step.

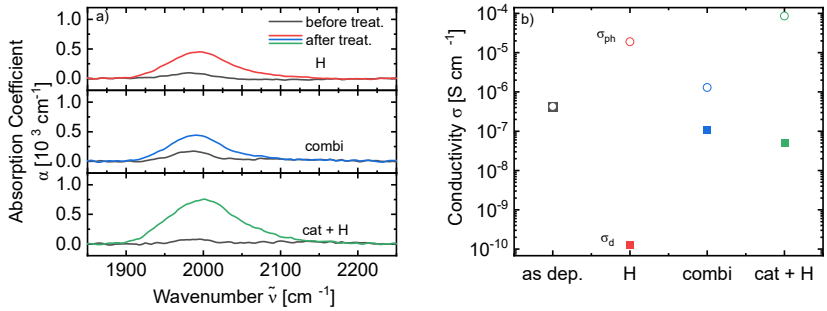


Figure 4.24.: a) FTIR spectra of Si-H vibrational modes within APCVD a-Si:H films deposited at $T_\mathrm{d} = 555\,^\circ\mathrm{C}$ before (gray) and after H-treatment (red), combined catalytic doping and H-treatment (blue) and catalytic doping with subsequent H-treatment (green). b) Photo- and dark conductivities σ_ph and σ_d of the same films after treatment.

4.3.2.4. Discussion

Hydrogenation The hydrogen treatment effectively increased the hydrogen content in the a-Si:H films. The resulting H concentration of all films remained below 10 at%, indicating no substantial improvement beyond the H concentration of the highest as-deposited hydrogenated a-Si:H films from Section 4.1. However, the presence of blistering for films on polished c-Si wafers suggests that the actual hydrogen content in the treated films might be higher than that measured via FTIR, because parts of the film were removed in the process, leading to an underestimation of the absorption. However, blistering is undesirable because it damages the continuity of the film and limits the applicability of hot-wire-treated a-Si:H layers for passivation on polished wafers. To enable practical application, treatment conditions should be refined to minimize blister formation, for example, by adjusting the hydrogen exposure time, pressure, or substrate temperature. The homogeneity of hydrogen incorporation throughout the film thickness was not directly investigated in this work. Although future studies using SIMS measurements could address this question in detail, the observed accumulation of hydrogen at the a-Si:H/c-Si interface leading to film delamination suggests that hydrogen is distributed throughout the entire film.

The absence of blistering on glass could be attributed to differences in adhesion and mechanical stress between the substrate and the a-Si:H film. Unlike crystalline silicon, which has a rigid and well-defined interface with the deposited film, the glass substrate may allow for greater stress relaxation during film growth, preventing film delamination. In addition, a different heating efficiency for the quartz substrate in contrast to the c-Si substrate by the substrate heater might lead to different temperatures of the substrate, which can change the diffusion of H.

Regarding the electrical properties, the H-treatment could significantly enhance the photosensitivity of films deposited at 495 and 525 °C to almost 10^5 with a σ_d of 6×10^{-11} S cm^{-1} and a σ_{ph} of 5×10^{-6} S cm^{-1}. In contrast, the photosensitivity of the film deposited at 440 °C was decreased by hydrogen treatment due to an increase in dark conductivity. This could be due to sample-to-sample variations, as only one sample was measured. However, on the other hand, an increase in dark conductivity fits to a high microstructure parameter for the sample deposited at $T_d = 440$ °C, which indicates a porous material with inner voids and therefore defects.[72, 76, 167] Additionally, H-treatment may promote incorporation of impurities, potentially leading to increased dark conductivity.

When comparing these results with the findings of Section 4.1, another consideration arises. In that section, films deposited at 500 °C did not exhibit blistering, which was previously interpreted as an indication of a less compact film structure. In contrast, the films in this study do exhibit blistering, which would typically suggest a denser structure that traps hydrogen more effectively. This fits to the FTIR results indicating a relatively low microstructure parameter even after hydrogenation. Therefore, it seems more likely that the treated films are indeed denser, which limits excessive hydrogen incorporation but still attains a level where internal stress leads to blister formation. In this case, the reason for the blister-free, as-deposited films from Section 4.1 is the H desorption from the film surface before it is incorporated into the film.

Catalytic doping The results presented in the previous section indicate the successful enhancement of the electrical properties of a-Si:H films made by APCVD through catalytic doping, after capping the doped films with both, either another APCVD or a PECVD layer. However, as for the as-deposited APCVD films, also after catalytic doping, significant differences in conductivity were observed in comparison with the reference PECVD-based films, probably due to a lower H content within the APCVD films and therefore a higher defect density.

The results presented in Figure 4.23 a) are consistent with the findings of Liu et al. [31] and Duan et al. [32], both of whom reported that a capping layer after catalytic doping is essential to achieve increased conductivity. However, in contrast to Duan et al. [32], where a multilayer stack was used to improve film thickness, my study demonstrates that a single stack was sufficient to achieve successful doping, reaching the same dark conductivity of $10^{-7}\,\mathrm{S\,cm^{-1}}$ for PECVD films. This suggests that the increase in thickness is not the primary factor contributing to the enhanced conductivity.

In support of this conclusion, the conductivity increases by two orders of magnitude (i.e., 100 times). If film thickness were the dominant factor, a stack of four catalytically doped layers – effectively four conducting layers in parallel (cf. Figure 4.22) – would only lead to a four-fold increase in conductivity. Additionally, no further improvement in conductivity was observed beyond the second catalytic doping step, reinforcing the idea that another mechanism is responsible for the increase in conductivity.

Liu et al. [31] proposed that the capping layer prevents the desorption of phosphorus atoms after catalytic doping. While this explanation aligns more closely with the findings herein, it raises the following important considerations:

1. All samples were stored in a nitrogen (N_2) box between processing steps, minimizing exposure to ambient conditions that could lead to oxidation. The total exposure time to ambient atmosphere was similar for samples with and without a capping layer, as the intrinsic PECVD process introduces a delay comparable to that of the silver pad evaporation required for conductivity measurements.

2. For samples that only underwent catalytic doping, the most critical process is silver evaporation, which occurs at a low pressure of 10^{-4} mbar. This environment may promote phosphorus desorption. However, since this process does not involve elevated temperatures, its impact is uncertain. In contrast, during capping layer deposition, the samples are exposed to high vacuum conditions and additionally subjected to temperatures of up to 200 °C, which would presumably increase phosphorus desorption rather than prevent it.

Based on these observations, I hypothesize that the capping layer not only serves as a barrier preventing phosphorus desorption but also plays a crucial role in activating the phosphorus atoms at the surface of the catalytically doped films. To determine the exact process responsible for the increase in conductivity, the experimental series shown in Figure 4.23 b) was carried out.

First, the results confirmed that the observed conductivity enhancement is indeed a result of catalytic doping rather than the activation of unintentionally incorporated impurities between the two PECVD deposition steps. Second, they demonstrated that annealing within the PECVD chamber alone does not activate the dopants. However, I found that not only PECVD films but also APCVD films can serve as effective capping layers, indicating that a plasma is not necessary for dopant activation. Rather, the presence of the capping layer itself is critical. Furthermore, annealing at 440 °C prior to APCVD film deposition did not result in complete phosphorus removal, providing additional evidence that phosphorus desorption at room temperature is insufficient to fully explain the need for a capping layer.

The fact that catalytically doped films with an APCVD capping layer exhibit the highest photo- and dark conductivity among APCVD-based films, as well as the highest dark conductivity among PECVD-based films, suggests the most effective dopant activation. However, the simultaneously low photosensitivity indicates a high defect density, likely due to the low hydrogen content within the film due to the high deposition temperatures. Furthermore, a comparison with APCVD films produced using a liquid precursor containing dissolved phosphorus and boron, as reported by

Masuda et al. [11], shows that the highest achieved dark conductivity of $10^{-6}\,\mathrm{S\,cm^{-1}}$ for the films herein is four orders of magnitude lower than that of phosphorus-doped films and two orders of magnitude lower than that of boron-doped films. This highlights significant potential for improving the catalytic doping process.

Combined catalytic doping and hydrogenation The results presented demonstrate that hydrogenation in combination with catalytic doping is a viable approach for improving the electronic quality of a-Si:H films. Hydrogenation facilitates catalytic doping without the need for a capping layer, thereby simplifying the overall process.

Among the hydrogenation and doping combinations tested, the two-step process, consisting of standard catalytic doping followed by hydrogen treatment, proved to be the most effective. This approach yielded the highest photoconductivity, reaching values close to $10^{-4}\,\mathrm{S\,cm^{-1}}$, and an increased dark conductivity of $5 \times 10^{-8}\,\mathrm{S\,cm^{-1}}$ compared to intrinsic hydrogenated a-Si:H films. These values exceed those achieved through catalytic doping of APCVD films with a PECVD capping layer and approach the performance levels observed in PECVD-based catalytic doping processes.

The relatively high dark conductivity compared to the intrinsic a-Si:H films indicates that the phosphorus was not desorbed from the film during the pre-annealing step prior to hydrogen treatment at 380 °C. The successful doping without the use of a capping layer, even after treatment at elevated temperatures, supports the hypothesis that the capping layer not only prevents the desorption of phosphorus atoms following catalytic doping but also promotes their incorporation into the a-Si:H matrix at the film surface.

Hydrogen radicals are known to saturate and break Si-Si bonds on the silicon surface [204], potentially leading to a restructuring of the a-Si:H surface and therefore activation of the phosphorus dopant. Additionally, the elevated substrate temperature of 380 °C during treatment results in a high hydrogen diffusion rate, allowing bond breaking and reformation not only at the surface but also within the bulk of the material. It is conceivable that hydrogen diffusion during the treatment process may also facilitate a deeper incorporation of phosphorus into the film. To further investigate this mechanism, additional analyses such as ToF-SIMS are recommended in future studies.

The combined one-step process, in which phosphine was introduced to the precursor gas during hydrogenation, showed a modest improvement in photosensitivity. The dark conductivity of $10^{-7}\,\mathrm{S\,cm^{-1}}$ is high compared to those of high-quality a-Si:H films,

but similar to the as-deposited film, grown at a deposition temperature of 555 °C. Therefore, it is unclear whether this conductivity results from successful phosphorus doping or from insufficient defect passivation, leading to the formation of a conductive defect band.

Whether phosphorus is actually incorporated into the film during the combined process requires further investigation. In addition, the process conditions for the combined treatment need to be optimized. In particular, it is crucial to avoid etching of the a-Si:H layer caused by high-energy hydrogen radicals while simultaneously ensuring that sufficient energy is available to enable effective phosphorus incorporation.

4.3.3. Crystallization of a-Si:H films

In addition to their direct application in devices, a-Si:H films serve as precursors for polycrystalline silicon (poly-Si) films, which are used, for example, in tunnel oxide passivated contact (TOPCon) solar cell structures. To induce crystallization, the amorphous films are annealed at temperatures above 700 °C, causing a restructuring of the silicon network.[33, 193] During annealing, multiple crystalline silicon nuclei form within the a-Si:H film and grow into crystals with various orientations, resulting in a polycrystalline silicon matrix. The crystal size depends on both the annealing temperature and the heating rate.[103, 193, 226]

A critical issue during the annealing of a-Si:H, particularly for films with a high hydrogen content, is the occurrence of blistering.[36] This phenomenon arises mainly when hydrogen from the a-Si:H film accumulates at the a-Si:H/c-Si interface, leading to a peel off of the amorphous film from the crystalline silicon wafer. This separation results in the formation of H_2 bubbles that can easily burst. Another reason for film delamination can be inner strain, which can results in a delamination of the film in various forms.

Section 4.1.2 demonstrated that the APCVD a-Si:H films exhibit a very low hydrogen content, below 2 at%, for $T_d > 500$ °C. This suggests that these films are well-suited for annealing without the risk of H related blistering. Furthermore, at these elevated temperatures, rapid film growth was observed, which is promising for the development of a fast deposition process for a-Si:H films intended for TOPCon structures. Such structures require polycrystalline silicon layers with a thickness exceeding 100 nm. Therefore, in the following, the application of furnace annealing is investigated as a slow annealing process at high temperatures and rapid thermal annealing (RTA) as

a fast annealing process where the process temperature system-related is limited to 900 °C.

4.3.3.1. Furnace annealing

To evaluate the suitability of APCVD a-Si:H films for the fabrication of polycrystalline silicon, samples were annealed in a quartz furnace with a heating rate of 6.67 °C min^{-1} and a dwell time of 120 min at T_a = 900, 1000, and 1100 °C. Two types of a-Si:H films were prepared: high purity films using pure trisilane as the precursor and carbon-containing films using 2 vol% TS diluted in cyclooctane. All films were deposited at 580 °C to minimize hydrogen content and thereby prevent blistering.

Figure 4.25 presents FTIR and Raman spectra for both as-deposited and annealed samples.

For films deposited from pure trisilane (Figure 4.25 a) and b)), the transverse optical (TO) Si-Si mode in the Raman spectrum shifts from a broad peak at 480 cm^{-1} to a sharp peak near 520 cm^{-1} across all annealing temperatures, confirming the transformation from a-Si:H to poly-Si. At T_a = 900 and 1000 °C, the TO Si-Si peaks appear at 515.5 cm^{-1}, while at 1100 °C, the peak shifts slightly to 517 cm^{-1}. Additionally, side peaks in the 485–510 cm^{-1} range decrease with increasing annealing temperature.

FTIR spectra show the emergence of a peak at 1080 cm^{-1} after annealing, which is higher than the 1000 cm^{-1} peak observed in the as-deposited film. The intensity of the Si-O rocking vibrations around 460 cm^{-1} also increases slightly. Furthermore, a side peak at 1200 cm^{-1} appears, which is attributed to Si-O stretching vibrations, likely due to longitudinal asymmetric stretching. The increased intensity of the Si–O-related peaks after annealing indicates the formation of a silicon oxide surface layer, which is further supported by the SIMS depth profiles shown in Figure A.15. In films annealed at 1000 and 1100 °C, a weak peak at 820 cm^{-1} is observed , which might be related to Si-C vibrations due to impurities. For the as-deposited film and the film annealed at 900 °C, a negative peak at 600 cm^{-1} is present, likely an artifact due to an FTIR reference wafer from a different wafer batch.

Figure 4.25 c) and d) present the Raman and FTIR spectra of the films deposited using the 2 vol% TS-CO mixture as a precursor. These films contain up to 1 × 10^{22} cm^{-3} carbon atoms, corresponding to an concentration of 12 to 20 at%, assuming the density of a-Si:H (5 × 10^{22} cm^{-3}) and a-SiC:H (8 × 10^{22} cm^{-3}) as boundary values.

Unlike the films deposited from pure TS, the carbon-containing films do not exhibit a crystalline Si peak at 520 cm^{-1} for T_a = 900 °C. Instead, the broad peak at 480 cm^{-1}

shifts toward higher Raman shift values. However, as T_a increases, a peak at 520 cm^{-1} gradually emerges. At $T_a = 1100\,°C$, this peak of the TO Si-Si vibration of poly-Si becomes significant and is observed at 513 cm^{-1}.

The FTIR spectrum of the as-deposited film exhibits a broad peak corresponding to the Si-C vibrational modes at 760 cm^{-1}. With increasing T_a, the intensity of the peak increases nearly three times, while its position shifts to 810 cm^{-1}. The peak shape also narrows into a Lorentzian-like form, indicating crystalline SiC. A strong peak at 1000 cm^{-1} is observed in the as-deposited sample, but after annealing, this peak disappears and a new peak emerges at 1080 cm^{-1} with a side peak at 1220 cm^{-1} and another peak at 460 cm^{-1}, which are all characteristic for near stoichiometric SiO_x.[174]

The conductivities of the films deposited from pure TS are shown in Figure A.12 a), while those of the films deposited using 2 vol% TS diluted in CO are presented in Figure A.12 b). Due to the high deposition temperature of 580 °C and consequently the low hydrogen content, both materials exhibit a photosensitivity of approximately 1 in their as-deposited state. For films made from pure TS, crystallization leads to a separation between photo- and dark conductivity in all samples, resulting in a maximum photosensitivity of approximately 3. While the photoconductivity after crystallization at 900 °C remains similar to that of the as-deposited film at $8 \times 10^{-7}\,S\,cm^{-1}$, the dark conductivity decreases, possibly due to a reduction in defects within the crystalline matrix. As T_a increases, both the photo- and dark conductivity increase slightly, with the maximum photoconductivity reaching $8 \times 10^{-6}\,S\,cm^{-1}$.

The carbon-containing films exhibit a similar increase in conductivity. Photo- and dark conductivity increase from 1×10^{-7} to $1 \times 10^{-5}\,S\,cm^{-1}$ at $T_a = 1100\,°C$, while the photosensitivity remains constant at 1 for all films.

4.3.3.2. Rapid thermal annealing

Furnace annealing is a slow process that consumes significant time and energy, making it less suitable for large-scale production. A faster alternative is rapid thermal annealing (RTA), which employs heating rates of several $K\,min^{-1}$ and dwell times of only a few seconds or minutes. Faster annealing can reduce the number of nucleation sites, leading to larger crystal sizes.[103] However, RTA of a-Si:H films often carries a high risk of blistering due to hydrogen release. Given that APCVD films exhibit a low hydrogen content, which is beneficial for preventing blistering, their suitability for RTA was investigated to assess their potential for high-throughput polycrystalline silicon production.

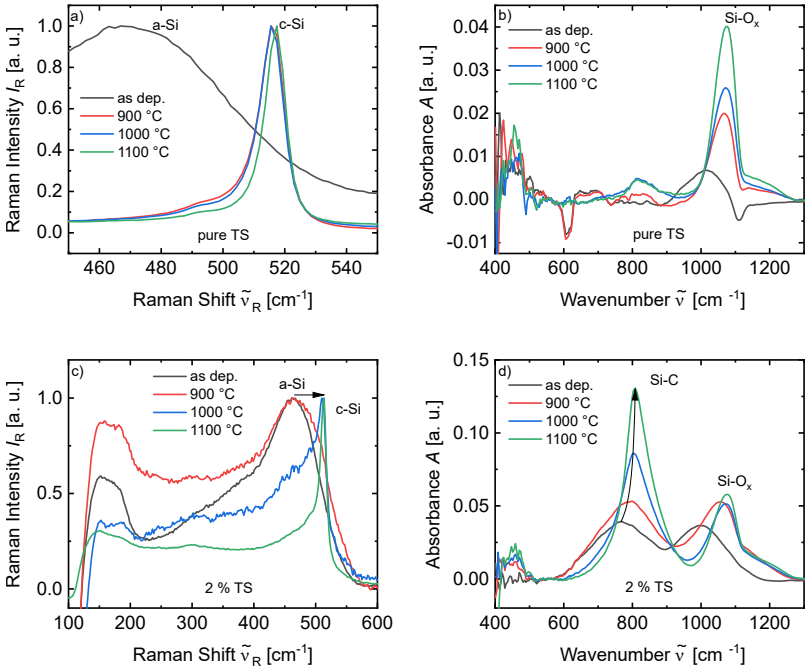


Figure 4.25.: a) Raman and b) FTIR spectra of silicon films deposited using pure trisilane at 580 °C and annealed at T_a = 900, 1000, and 1100 °C. c) Raman and d) FTIR spectra of carbon-containing silicon films deposited using 2 vol% TS in CO as a precursor at 580 °C and annealed under the same conditions. The primary peaks are labeled according to their corresponding vibrational modes.

Since furnace annealing showed that films deposited with 2 vol% TS diluted in CO did not crystallize at $T_a = 900\,°C$, and the RTA system is limited to this maximum temperature, the focus was placed exclusively on films deposited from pure TS. The a-Si:H films were prepared at deposition temperatures of 440 and 580 °C. Films deposited at 440 °C were annealed at 700, 800, and 900 °C, while films deposited at 580 °C were annealed at 825 and 900 °C. None of these samples exhibited blistering after RTA.

Figure 4.26 presents the Raman spectra and conductivity measurements for the RTA-processed samples. The Raman spectra of the films deposited at 580 °C are shown separately in Figure A.13 a).

Figure 4.26 a) shows the normalized Raman spectra for films deposited at 440 °C. The as-deposited material exhibits a broad peak centered at 480 cm^{-1}, characteristic of amorphous silicon. After RTA at 700 °C, the spectrum remains largely unchanged, indicating that crystallization has not yet occurred. However, at higher annealing temperatures, the 480 cm^{-1} peak diminishes, while a sharp c-Si TO phonon peak emerges, confirming the transformation to poly-Si.[193] For both annealing temperatures, 800 and 900 °C, the c-Si TO phonon mode appears at 517 cm^{-1}. The same position is observed in samples deposited with a deposition temperature of 580 °C (Figure A.13 a)).

Figure 4.26 b) compares the electrical conductivities of RTA-treated films deposited at 440 and 580 °C. While furnace-annealed films showed only a slight increase in conductivity (less than one order of magnitude; see Figure A.12), RTA resulted in a significant enhancement in conductivity, reaching values of up to $10^{-1}\,S\,cm^{-1}$. This value far exceeds typical intrinsic crystalline silicon conductivity, which is typically below $10^{-3}\,S\,cm^{-1}$.[227] Even for polycrystalline silicon with large grain sizes and low defect densities, the observed increase in conductivity cannot be attributed solely to improved carrier mobility.

A possible explanation is unintentional doping. Secondary ion mass spectrometry (SIMS) measurements (Figure A.14) reveal a slightly higher phosphorus concentration in RTA-annealed films compared to furnace-annealed samples, suggesting the possibility of unintentional doping. However, the hydrogen concentration is also elevated in these films, and the phosphorus depth profile closely follows that of hydrogen. Thus, the increase in phosphorus signal could result from $^{31}SiH_3^-$ ions rather than $^{31}P^-$ ions.

X-ray photoelectron spectroscopy (XPS) measurements indicate a higher nitrogen concentration of 1.3 at% in the RTA-treated film compared to 0.5 at% in the furnace-annealed counterpart (data not shown), which could contribute to increased

conductivity. This difference may stem from the purer inert gas atmosphere in the RTA process, whereas furnace annealing likely results in an oxide layer that prevents nitrogen incorporation. However, because of the low nitrogen signal in the XPS measurements and the surface sensitivity of the technique, this hypothesis remains uncertain.

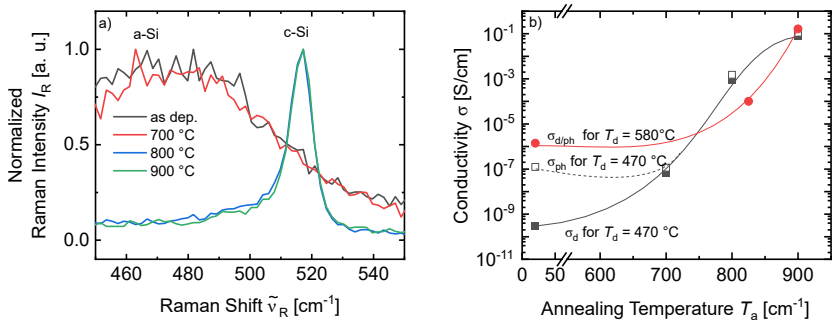


Figure 4.26.: a) Raman spectra of silicon films deposited at 440 °C and annealed via RTA at $T_a = 700$, 800, and 900 °C. b) Photo- and dark conductivity σ_{ph} and σ_d of the same samples and additionally Si films deposited at 580 °C and annealed at $T_a = 825$ and 900 °C.

4.3.3.3. Discussion

Furnace annealing The results in Figure 4.25 confirm that high-purity a-Si:H films crystallize into poly-Si at $T_a = 900\,°C$. The shift of the TO mode from 515.5 cm^{-1} at 900 and 1000 °C to 517 cm^{-1} at 1100 °C suggests an increase in grain size from 6 to 9 nm, as previously observed in similar studies [228]. The decrease in the 485–510 cm^{-1} side peaks with increasing annealing temperature indicates a reduction in grain boundary effects, which is consistent with improved crystallinity.

FTIR spectra show the formation of a near-stoichiometric SiO_2 surface layer at higher annealing temperatures. The significantly larger 1080 cm^{-1} peak after annealing, compared to the peak around 1000 cm^{-1} in the as-deposited film, indicates not only a transition from a homogeneous SiO_x matrix to a mixed Si + SiO_2 matrix but also the formation of a silicon oxide layer on the film surface. This is further confirmed by the SIMS measurements presented in Figure A.15. The presence of these peaks results from residual O_2 within the furnace. Notably, this SiO_2 layer can be removed by hydrofluoric acid etching. The presence of an additional peak at 820 cm^{-1} for films annealed at 1000 and 1100 °C suggests contamination by residual carbon or the appearance of Si-O bending modes, as previously reported by Hinds et al. [174]

In carbon-containing films, the suppression of crystallization at lower T_a, indicated by the absence of a 520 cm^{-1} peak, aligns with previous observations that carbon incorporation raises the crystallization temperature of a-Si:H.[34] The shift of the 480 cm^{-1}, indicating amorphous silicon, to higher Raman shifts point to the initial stages of poly-Si formation. The eventual appearance of the 520 cm^{-1} peak at 1100 °C confirms crystallization. However, the higher relative intensity of the 490 cm^{-1} side peak compared to films deposited from pure TS, together with the TO mode located at 513 cm^{-1}, suggests the presence of smaller silicon crystals.[228]

The appearance of a strong Lorentzian-shaped peak around 800 cm^{-1} indicates the formation of crystalline SiC structures within the carbon-containing films after annealing.[127] While for the as-deposited film, the peak around 1000 cm^{-1} might originate from both Si-O_x and Si-C-H_x vibrational modes [176, 177], after annealing, the peak shifts to 1080 cm^{-1} and can be clearly assigned to Si-O_x vibrations, similar as for Si films made with pure TS.

The conductivity increase from 10^{-7} S cm^{-1} to 10^{-5} S cm^{-1} follow typical behavior observed in intrinsic poly-Si, where crystallization improves carrier transport by increasing the long-range order.[229] The increasing photoconductivity with T_a and

the slight separation between photo- and dark conductivity in pure TS films suggest a reduction in defect density in contrast to TS-CO films.[59]

Rapid thermal annealing The results confirm that RTA effectively crystallizes a-Si:H films into polycrystalline silicon without causing blistering, demonstrating the robustness of APCVD films for high-throughput production. Therefore, this material shows strong potential for the use as a precursor for polycrystalline silicon in TopCon solar cells. The ability of the a-Si:H films to be rapidly deposited and annealed without blistering makes them a superior alternative to a-Si:H films produced by PECVD using silane (SiH_4), which are typically deposited at temperatures below 500 °C, resulting in higher hydrogen content and an increased risk of blistering.

Compared to furnace annealing at 900 °C, RTA results in a Raman TO peak shift toward higher wavenumbers, suggesting larger grain sizes, possibly due to the rapid heating and cooling rates maybe limiting nucleation sites. The peak position of the TO Si-Si mode for RTA-treated films annealed at 900 °C is similar to that of furnace-annealed films treated at 1100 °C, indicating similar grain sizes. Note that Raman spectra from RTA-treated films exhibit greater scattering compared to furnace-annealed films (Figure 4.25), as the Raman measurements were conducted with a tenfold lower laser power.

The significant increase in conductivity in films treated with RTA, reaching up to $10^{-1}\,S\,cm^{-1}$, suggests unintentional doping. According to literature, this conductivity corresponds to a phosphor or boron dopant concentration in microcrystalline silicon of $\sim 10^{15}\,cm^{-3}$.[230, 231] SIMS measurements indeed indicate a higher phosphorus concentration. However, the phosphorous depth profile is correlated with the H depth profile, indicating that the increased phosphor SIMS depth profile results from $^{31}SiH_3^-$ ions rather than $^{31}P^-$ ions. XPS measurements reveal an increase in nitrogen content, which can contribute to the enhanced conductivity as well. However, due to the surface sensitivity of the XPS and the uncertainty of the SIMS results, the exact origin of the high conductivity remains unclear.

Despite these uncertainties, high conductivity at 900 °C is consistently achieved for films deposited at both 440 and 580 °C. This indicates that the higher levels of oxygen and carbon impurities in the fast-growing 580 °C films (see Section 4.1.4) do not significantly hinder crystallization or electrical performance, suggesting that these films remain viable for the production of polycrystalline silicon using RTA.

5. Amorphous and crystalline silicon carbide films

Silicon carbide (SiC) is a material of great technological interest due to its wide band gap, exceptional thermal stability, and robust chemical resistance. These properties make SiC highly suitable for applications in high-temperature electronics, power devices, and photovoltaics. In particular, both amorphous (a-SiC) and polycrystalline SiC (poly-SiC) play crucial roles in advanced silicon-based solar cells, such as TOPCon and tandem structures, by potentially providing excellent optical properties, surface passivation, electrical conductivity, and thermal resilience.

In this chapter, the deposition, properties, and transformation of hydrogenated amorphous silicon carbide (a-SiC:H) into its crystalline form (poly-SiC) are investigated, with a focus on the impact of different processing conditions on microstructure, electrical properties, and doping behavior. Using 1,4-disilabutane (DB) as a precursor, first, the deposition of a-SiC:H films at atmospheric pressure is explored, analyzing their atomic composition, microstructure, and surface characteristics. Furthermore, the incorporation of N is tested using 1,1,3,3-tetramethyldisilazane (TMD) as an N-containing precursor additive to achieve doping of the films and increase their electrical conductivity.

The crystallization process is then examined, with an emphasis on the formation of undoped and doped poly-SiC films through furnace and laser annealing. The impact of annealing temperature and nitrogen incorporation on film conductivity is discussed in detail, highlighting improvements in electrical performance.

Finally, to increase the carbon content within the SiC films, the study was extended to SiC films deposited from a combination of disilabutane and cyclooctane, investigating their as-deposited properties and subsequent structural transformations upon annealing. The comparative analysis of these different approaches provides valuable insight into scalable and cost-effective pathways for SiC film fabrication, with potential applications in photovoltaics and nanoelectronics. The chapter is based on a previously published

article that was part of my PhD thesis (Fischer et al. [232], 2025). Portions of the text and figures have been adapted from the publication, with additional data, analyses, and discussions incorporated to extend the original content.

5.1. a-SiC:H deposition using disilabutane

In this section, the deposition of a-SiC:H films is explored using 1,4-disilabutane (DB) as a liquid precursor in an atmospheric pressure chemical vapor deposition (APCVD) process. DB offers advantages for the deposition at temperatures below 600 °C over conventional gaseous precursors, such as lower decomposition temperatures and improved handling, making it a promising candidate for scalable SiC film fabrication.

The analysis begins with the microstructure and electrical properties of the deposited a-SiC:H films, followed by a detailed investigation of the near-surface atomic structure using X-ray photoelectron spectroscopy (XPS). The effect of nitrogen doping on film conductivity is then discussed, providing insight into optimizing electrical performance for potential device applications. Finally, a comprehensive discussion of the results is presented, comparing the findings with existing deposition methods and highlighting the advantages of DB-based APCVD for cost-effective and high-quality a-SiC:H film growth.

5.1.1. Microstructure and electrical properties

To evaluate the suitability of 1-4-DB for producing a-SiC:H layers, thin films were deposited at temperatures ranging from 500 °C to 600 °C, and their composition was analyzed using FTIR and Raman spectroscopy. FTIR spectra around the characteristic IR peaks of a-SiC:H are shown in Figure 5.1.[111, 114, 115] In Figure 5.1 a) mainly three modes contribute to the spectra: the Si-H wagging mode at 640 cm^{-1}, the SiC stretching mode in the range between 720 and 780 cm^{-1} and the Si-C-H_x wagging modes around 980 cm^{-1}.[111, 114–117] The Si-H mode at 640 cm^{-1} is strongly overlapped by the dominant SiC mode. The Si-C-H_x wagging modes may overlap with Si-O_x or Si-O-Si modes located at a similar wavelengths.[176, 177] The broad SiC peak with a peak maximum located clearly below 780 cm^{-1} indicates that the as-deposited material is amorphous.[111, 114] Figure 5.1 b) shows the Si-H stretching modes around 2100 cm^{-1} and Figure 5.1 c) the C-H stretching modes at 2850 cm^{-1}.[114, 116, 167]

The C-H stretching peak at 2850 cm^{-1} increases proportionally with the peak at 980 cm^{-1}, as shown in Figure A.16. This suggests that the 980 cm^{-1} peak is more likely due to Si-C-H_x wagging modes rather than Si-O_x and Si-O-Si modes. The ratio of the Si-C-H_x wagging mode peak to the Si-C peak decreases as the deposition temperature increases. This indicates a lower amount of C-H_x bonds within the film.

This trend is also shown in Figure 5.1 d), which shows the densities of Si-C, Si-H, and C-H bonds in the films. Note that in contrast to the spectra shown in Figure 5.1 a)–c), which show the absorbance of the films, the calculation of the bond density takes into account the thickness of the film. These densities were calculated from their respective stretching vibrations, as described in reference [114]. While the Si-C bond density increases with temperature, the Si-H and C-H bond densities decrease, with a steeper decrease for the C-H bond density.

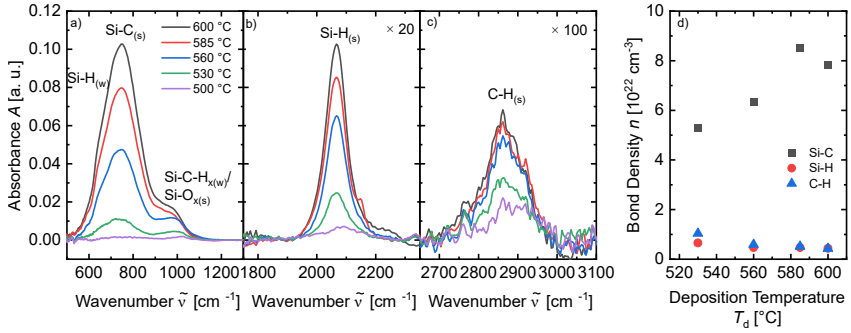


Figure 5.1.: FTIR spectra of a-SiC:H films deposited at temperatures between 500 and 600 °C. a) Si-H wagging, Si-C stretching, and Si-C-H_x wagging modes; b) Si-H stretching modes; c) C-H stretching modes. d) Density of Si-C, Si-H, and C-H bonds as a function of the deposition temperature. Adapted from Fischer et al. [232] (2025), licensed under CC BY 4.0.

The increase of the Si-C bond density with temperature indicates that the atomic carbon density n_C of the films increases as well. The observation is supported by the SIMS depth profiles in Figure 5.2. By comparing with a reference sample with a known implanted n_C of 6 × 10^{19} cm^{-3} in the peak maximum, the average n_C within the a-SiC:H films was determined to 0.97 × 10^{22} cm^{-3} for $T_d = 530$ °C, 1.29 × 10^{22} cm^{-3} for $T_d = 560$ °C, 1.34 × 10^{22} cm^{-3} for $T_d = 585$ °C and 1.33 × 10^{22} cm^{-3} for $T_d = 600$ °C. The ionization cross-section in SIMS strongly depends on the material and its structure. Due to the difference of more than two orders of magnitude in n_C between the

implantation standard and the samples, SIMS can only give a rough estimation of the absolute n_C. However, the n_C of ~ 1.3 × 10^{22} cm^{-3} for T_d = 585 and 600 °C roughly fits to a FTIR-determined Si-C bond density of ~ 8 × 10^{22} cm^{-3} which corresponds to a n_C of 2 × 10^{22} cm^{-3} if a 4-fold bonding to Si of all C atoms is assumed. On a logarithmic scale, the SIMS depth profiles indicate homogeneous film growth with minor changes in C, H, and O and Si concentrations throughout the film thickness. Near the interface to the c-Si wafer as well as at the film surface, Figure 5.2 shows peaks in O intensity. The peak at the interface likely occurs due to native oxide on the c-Si substrate that was not removed prior to deposition. Oxygen at the film surface probably results from a native oxide layer often emerging when a-SiC:H films are exposed to ambient air.[105, 233] However, on a linear scale, the n_C near the surface is higher than near the c-Si interface, possibly due to a gradual shift in the C radical to Si radical ratio within the deposition chamber atmosphere. The shift observed during deposition may result from preferential incorporation of Si over C, leading to increased Si consumption. This leads to n_C differences along the film thickness of ± 25 % compared to the average, disregarding surface or interface effects. The minimum and maximum values of n_C are given in Table 5.1. In agreement with this, the Si depth profiles for films deposited at 585 and 600 °C exhibit a complementary behavior to the C depth profiles, showing a lower Si intensity near the surface compared to the region near the interface. For the film deposited at 600 °C, the Si content decreases by more than 10 %. Assuming an initial atomic Si density of 4 × 10^{22} cm^{-3}, this corresponds to a reduction of over 4 × 10^{21} cm^{-3}. This value is in reasonable agreement with the observed increase in carbon content of approximately 5.4 × 10^{21} cm^{-3}. For films deposited at 530 and 560 °C, a distinct decrease in Si ion intensity near the film surface is not observed. This is likely due to the lower film thickness at these deposition temperatures, which increases the influence of edge effects on the depth profiles.

The SIMS spectra in Figure 5.2 show that the O content slightly decreases with increasing deposition temperature. When compared with hydrogenated amorphous silicon (a-Si:H) deposited in the same system, as analyzed in Section 4.1, all films exhibit relatively high O concentration, maybe caused by the lower purity of DB (97 %) in contrast to TS (99 %) and therefore higher amount of unwanted O-containing substances, or due to higher oxidation probability of C containing Si films.[105, 233] In the FTIR spectra in Figure 5.1 oxygen could not be distinctly detected, due to the overlap of Si-O_x modes with the Si-C-H_x modes around 980 cm^{-1}.

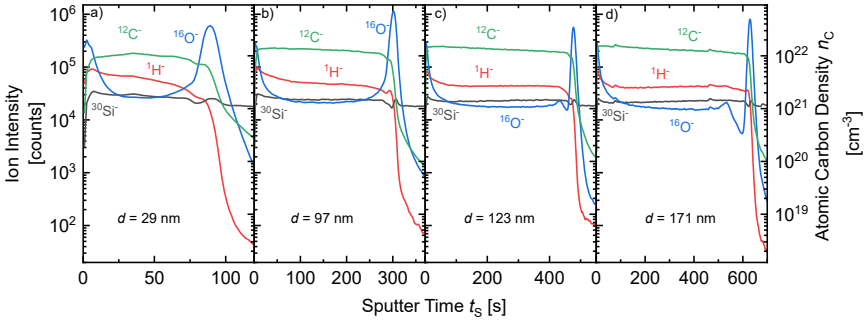


Figure 5.2.: SIMS depth profiles of a-SiC:H thin films deposited at a) 530 °C, b) 560 °C, c) 585 °C, and d) 600 °C. On the left y-axis, the ion intensities of SIMS counts for H, Si, and O are given; the right y-axis corresponds to the atomic carbon density n_C. Film thicknesses are shown at the bottom of the graphs. Adapted from Fischer et al. [232] (2025), licensed under CC BY 4.0.

Table 5.1.: Minimum, average, and maximum atomic carbon density n_C according to the SIMS depth profiles of a-SiC:H films shown in Figure 5.2. Adapted from Fischer et al. [232] (2025), licensed under CC BY 4.0.

T_d [°C]	Minimum n_C [10^{22} cm^{-3}]	Average n_C [10^{22} cm^{-3}]	Maximum n_C [10^{22} cm^{-3}]
530	0.69	0.97	1.12
560	1.09	1.29	1.41
585	1.16	1.34	1.52
600	1.09	1.33	1.63

The SIMS depth profiles and FTIR spectra indicate that the films deposited by DB are silicon-rich a-SiC:H layers. This can be verified by the analysis of the Raman spectra shown in Figure 5.3. Here, the Raman spectra of the a-SiC:H films deposited at various temperatures are compared with the spectra of a Corning glass substrate and an APCVD a-Si:H film deposited at 580 °C. All a-SiC:H films show a TA Si mode around 160 cm^{-1}, typical for amorphous silicon.[182] The shape of the TO Si mode at 480 cm^{-1} of the a-SiC:H films clearly differs from the shape of this mode for the a-Si:H film. The peak is less sharp and, especially for films deposited at low deposition temperatures, resembles the Si-O peak of the glass substrate without film, which is located in the same region.[234] The spectrum of the film deposited at 500 °C, which has a thickness of only 3 nm almost exactly resembles the overall spectrum of the glass substrate. Only a slightly sharper 480 cm^{-1} peak and the TA Si mode at 160 cm^{-1} indicate the existence of a-Si.

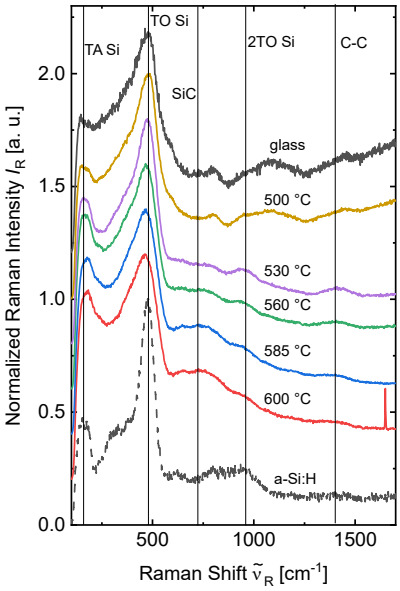


Figure 5.3.: Raman spectra of a-SiC:H films deposited at temperatures between 500 and 600 °C. Additionally, a Raman spectrum of a corning glass substrate without film and a spectrum of an a-Si:H film deposited at 580 °C are shown for comparison with the a-SiC:H films.

With increasing T_d up to 560 °C, the shape of the Raman spectra is less dominated by the modes of the glass substrate due to the greater film thickness. A more pronounced TA and TO Si mode emerge as well as the second-order transversal optical (2TO) Si mode, confirming the high Si content within the a-SiC:H films. In addition, a peak at 1450 cm^{-1} emerges, indicating the existence of C-C bonds within the material.[118] With further increasing T_d, a peak at ~750 cm^{-1} occurs, which might be assigned to SiC vibrational bonds.[103, 183] However, in the region between 700 and 1000 cm^{-1}, second-order longitudinal optical (2LO) and second order TO modes of Si occur as well, which might overlap with the Si-C modes, which makes a clear classification difficult.[235]

The 480 cm^{-1} broadens with higher T_d, and next to the TA Si peak at ~160 cm^{-1}, a side peak at ~200 cm^{-1} rises. Both can be a result of emerging SiC modes in this range [118], fitting to the higher C content within the film, already observed with FTIR spectroscopy and SIMS.

5.1.2. Surface analysis

X-ray photoelectron spectroscopy (XPS) was used to analyze the atomic composition and bonding structure of the a-SiC:H films. Since X-rays are absorbed within the first 10 nm of the a-SiC:H films [189, 190], this method primarily provides information about the surface composition rather than the bulk material. Despite HF etching prior to measurement, the near-surface material is significantly affected by oxidation, probably due to the high oxidation affinity of a-SiC.[105] Consequently, for the films investigated here, XPS is not a reliable technique to determine the oxygen content. However, the composition of the near-surface material, when combined with data from FTIR, SIMS, and Raman measurements, can provide valuable insight into the bulk material.

Figure 5.4 presents the XPS atomic composition near the surface of a-SiC:H films deposited at various temperatures. The percentage values consider only Si, C, and O bonds, ensuring that their combined atomic contributions sum up to 100 %. Hydrogen atoms are neglected, and no significant nitrogen peak was detected. The total proportions of Si (yellow), O (blue), and C (orange) were determined by integrating the corresponding peak intensities within the survey spectra, recorded with a step size of 0.8 eV, and scaling them using empirical relative sensitivity factors. To analyze bonding configurations, high-resolution detail spectra with a step size of 0.1 eV were used, in which multiple Gaussian peaks were fitted to each Si- or C-related multiplet. The peak

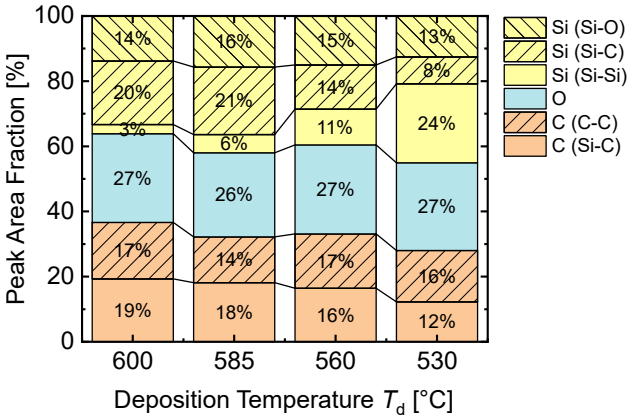


Figure 5.4.: Atomic composition at the surface of a-SiC:H films deposited at temperatures between 500 and 600 °C measured by XPS. For the percentage values, it was assumed that the material consists only of Si, C, and O.

area fractions shown in Figure 5.4 represent the product of the relative contribution of a specific bonding configuration within a multiplet and the total elemental proportion obtained from the survey spectrum. Because the Si and C multiplets were fitted independently, discrepancies may arise between the amount of C bonded to Si derived within the C multiplet and Si bonded to C derived within the Si multiplet.

All films exhibit an oxygen content of 26 to 27 at%, likely due to surface oxidation. Consistent with the results of FTIR spectroscopy, Raman spectroscopy, and SIMS, the silicon content within the films decreases with the deposition temperature, while the carbon content increases. For the film deposited at $T_d = 600$ °C, the XPS measurements indicate an equal atomic concentration of carbon and silicon at the surface. This suggests a higher C-to-Si ratio at the surface compared to the bulk composition, as determined by FTIR and SIMS. While the absolute atomic concentrations at the surface differ significantly from those in the bulk, the temperature-dependent trends observed in XPS are likely qualitatively comparable to those of the bulk material.

The Raman spectra in Figure 5.3 reveal a more dominant peak at 480 cm^{-1}, indicating an increased proportion of a-Si:H within the film. This correlates with a high fraction of Si atoms bound to other Si, reaching up to 24 at% according to XPS. As the deposition temperature increases, the proportion of Si atoms bound to C, as well as C atoms bound to Si, also increases. In contrast, the fraction of C atoms bonded to other

C remains relatively constant at 14–17 at% across all films, showing no significant temperature dependence.

5.1.3. Conductivity and nitrogen doping

For applications in solar cells and other technical devices, the electrical conductivity of a material is a critical property that must be tailored to meet the specific requirements of the device. Figure 5.5 a) show σ_{ph} and σ_{d} for the a-SiC:H temp series discussed in Section 5.1.1. The dark conductivity increases by three orders of magnitude with increasing deposition temperature, reaching a maximum value of approximately $2 \times 10^{-7}\,\mathrm{S\,cm^{-1}}$. While for $T_{\mathrm{d}} = 500$ and $T_{\mathrm{d}} = 530\,^{\circ}\mathrm{C}$, the photosensitivity is ~10, for higher T_{d}, the photosensitivity is 1. For the application in solar cells, higher conductivities and photosensitivities would be beneficial for better charge carrier transport and low recombination rate due to defects.

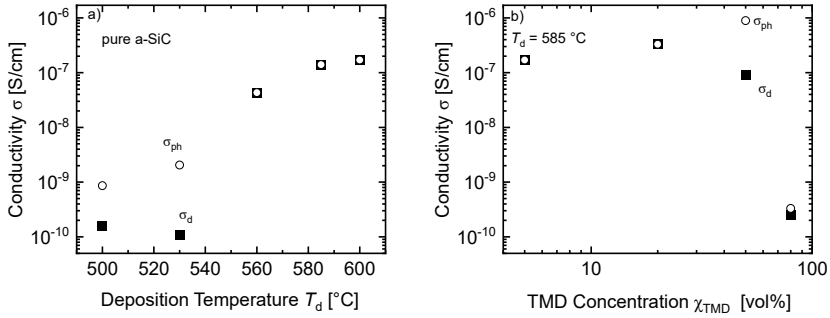


Figure 5.5.: Photo- and dark conductivity σ_{ph} and σ_{d} of a-SiC:H films a) deposited with pure DB at temperatures between 500 and 600 °C and b) deposited at 585 °C using various TMD concentrations χ_{TMD} solved in DB to incorporate N as dopant.

To increase conductivity, SiC is often doped with nitrogen.[102, 121, 125] Unlike phosphorus, nitrogen is present in several less toxic precursors, which potentially allows in situ doping during film growth within the glove box used in this work. However, the incorporation of N only with thermal energy and without plasma or hot filament usually requires high substrate temperatures to decompose gases such as N_2 or NH_3. Therefore, I searched for a liquid precursor molecule that has already N embedded within a hydrogen-silicon carbide matrix, which can be mixed with

DB. During deposition, the molecule might be easier incorporated into the film as a result of radical formation via bond braking of Si-C, Si-H, or C-H bonds of the molecule instead of breaking the more robust N-H and N-N bonds. For this purpose, 1,1,3,3-tetramethyldisilazane (TMD, $[(CH_3)_2SiH]_2NH$) was used, which meets these requirements. Various TMD–DB mixtures were prepared, and a-SiC:H films were deposited at 585 °C. This temperature was used since it leads to the highest Si-C bond density, as found in Section 5.1.1.

Figure 5.5 b) shows the conductivity of a-SiC:H films deposited using 5–80 vol% TMD in DB as precursor. Up to 20 vol% TMD, the conductivity is slightly above 10^{-7} S cm^{-1} and the photosensitivity is 1, similar to the film made from pure DB. The film deposited with 50 vol% TMD shows a photosensitivity of 10 with a slightly higher σ_{ph} of almost 10^{-6} S cm^{-1}. For a TMD content of 80 vol%, the conductivity decreases drastically, maybe due to a high incorporation of the TMD molecule.

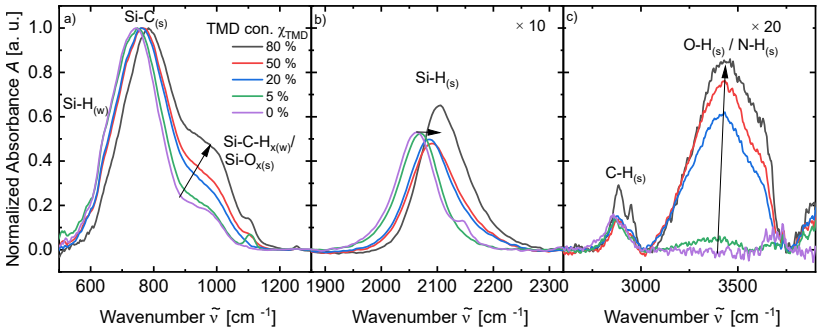


Figure 5.6.: FTIR spectra of nitrogen-containing a-SiC:H films deposited with a TMD concentration χ_{TMD} within the precursor of 0–80 vol%. a) Si-H wagging, Si-C stretching, and Si-C-H_x wagging or Si-O modes; b) Si-H stretching modes; c) C-H stretching modes and N-H/O-H modes.

To evaluate whether N is incorporated within the a-SiC:H film and its influence on the microstructure, FTIR spectra were measured. Figure 5.6 presents the spectra of films deposited with varying TMD contents, normalized to the Si-C stretching peak. With increasing TMD content within the precursor, the 980 cm^{-1} peak increases, possibly caused by increasing Si-O_x, Si-C-H_x, or Si-N modes.[114, 176, 177, 236, 237] At the same time, the peak around 2100 cm^{-1} shifts to higher wavenumbers. The C-H vibration peaks at 2850 cm^{-1} shown in Figure 5.6 c) are similar for all films, except

for the film deposited with 80 vol% TMD, where the C-H peak is notably enhanced. In addition, the films deposited with TMD show an additional peak at 3450 cm^{-1}, which increases with increasing TMD content within the precursor. In this region, N-H modes and O-H modes occur.[179, 236]

While the FTIR spectra clearly show a change in the microstructure of the films deposited with TMD-DB mixtures, it remains unclear which atoms exactly lead to the changes within the FTIR spectra, since O, N, and C incorporation can lead to peaks at similar positions. Therefore, SIMS measurements shown in Figure 5.7 of a pure DB a-SiC:H film and an 80 vol% TMD in DB film were made to investigate the atomic composition of the films. The depth profiles show a reduction of the Si content and an increase in the O, H, and N content for the film deposited with TMD. The N content is indirectly shown by the content of $^{15}NH^-$ ions, since N generally has an extremely low ionization probability in SIMS and an isobaric interference with $^{14}CH_2^-$ ions. The depth profiles show that N incorporation in a-SiC:H films via a liquid precursor is possible using TMD. However, at the same time, at least for very high proportions of TMD as used here (80 vol%), a significant amount of O is unintentionally incorporated as well. A more detailed investigation of the N incorporation is given in Section 5.2.2, where the doping of crystallized films is investigated made with significantly lower concentrations of TMD (~10 vol%) within the precursor.

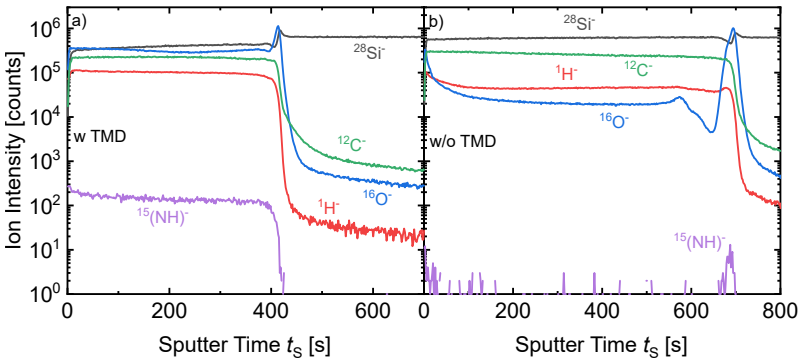


Figure 5.7.: Silicon, hydrogen, carbon, oxygen and imidogen (NH) SIMS depth profiles of a-SiC:H films deposited using a) pure DB and b) a mixture of 80 vol% TMD and 20 vol% DB as a precursor at 585 °C.

5.1.4. Discussion

The study showed that liquid precursors, specifically 1,4-DB and 1,1,3,3-TMD, can be used effectively for a-SiC:H film deposition at atmospheric pressure, offering a cost-effective and scalable alternative to traditional vacuum-based CVD methods. By using TMD, a significant incorporation of N into the films was achieved at deposition temperatures below 600 °C, which is lower than typical doping temperatures above 1000 °C when using N_2 or NH_3.[238, 239] However, the incorporated N within the film could not increase electrical conductivity, probably due to a lack of dopant activation or a high density of defects that are electrically active and therefore hinder the charge transport via the conducting band by trapping the charge carrier. The FTIR spectra shown in Figure 5.1 show a dominant SiC stretching mode peak and a significant Si-C-H_x wagging modes peak typical for amorphous SiC and also found for a-SiC:H films made by PECVD.[105, 114] The Si-C bond density up to $8 \times 10^{22}\,cm^{-3}$ and a H number density between 0.8 and $1.7 \times 10^{22}\,cm^{-3}$ found in Figure 5.1 aligns perfectly with the density of a-SiC:H films reported by Kaneko et al. [114], who reported Si-C densities up to $6 \times 10^{22}\,cm^{-3}$. This demonstrates the applicability of this process for the deposition of a-SiC:H films, which might be directly used as passivation layer in solar cells.[240] Further enhancement of the hydrogen content could potentially be achieved by increasing the growth rate.[164] However, the hydrogen content is inherently limited by the significant hydrogen effusion rates that occur at the elevated deposition temperatures required for the decomposition of DB. Figure 5.1 d) shows that, especially for low deposition temperatures, there are more C-H than Si-H bonds within the a-SiC:H films. The higher ratio of C-H to Si-H vibrations for low deposition temperatures might be due to lower thermal energy, leading to less C-C bond breaking during the deposition process. This agrees with a more pronounced C-C peak for lower deposition temperatures observed by Raman spectroscopy in Figure 5.3. While the peak caused by C-C vibrations clearly indicates C within the films, other Si-C-related features are less pronounced, probably due to the low Raman scattering efficiency of Si-C vibrations in contrast to, e.g., Si-Si vibrations.[118] In contrast, the presence of amorphous Si clusters is clearly indicated by the presence of both the TA Si-Si mode at $160\,cm^{-1}$ and the TO Si-Si mode at $480\,cm^{-1}$.

The SIMS depth profiles in Figure 5.2 show an increase in the incorporation of C into the film with increasing growth duration. The calculated decrease in the atomic Si density of $4 \times 10^{21}\,cm^{-3}$ for the film deposited at 600 °C aligns well with the observed atomic carbon density increase of $5.4 \times 10^{21}\,cm^{-3}$. Minor deviations may

result from matrix-dependent ionization probabilities of the secondary ions, which affect the quantitative accuracy of SIMS measurements.

These gradients in C and Si content might result from fewer Si atoms remaining in the precursor gas, leading to a higher amount of C radicals compared to Si radicals. This indicates that the Si to C ratio within the film can be adjusted by adding additional precursors containing only C-H complexes to increase the n_C within the film or only Si-H complexes to increase the atomic Si density. The maximum average n_C of $1.34 \times 10^{22}\,cm^{-3}$ (cf. Table 5.1) and a n_C of $\sim 2 \times 10^{22}\,cm^{-3}$ according to FTIR indicates a carbon deficiency in the SiC relative to its stoichiometric composition. Assuming an atomic density range of 5 to $8.6 \times 10^{22}\,cm^{-3}$ for pure a-Si:H and SiC:H [150], respectively, the highest n_C of $1.34 \times 10^{22}\,cm^{-3}$ corresponds to an proportion of 16 to 27 at%. However, since the reference sample had a n_C three orders of magnitude lower and since the density of the a-SiC:H films is unknown, estimating the absolute C to Si ratio is challenging.

A system allowing higher deposition temperatures might allow for higher n_C within the film. However, the current system is already at its limit when operating at 600 °C. The use of other, carbon-rich precursors can also lead to higher C incorporation, but these precursors must match the decomposition temperature of DB. Further research is needed to find suitable precursors and their optimal mixing ratios with DB.

XPS measurements largely resemble the assumptions regarding atomic composition and bonding structure derived from SIMS, FTIR, and Raman spectroscopy. The Si-C bond density increases with temperature, and at lower temperatures there is a higher proportion of C-C and Si-Si clusters within the film. However, since XPS is a surface-sensitive measurement, the absolute atomic composition measured by XPS does not represent the composition of the bulk material due to a high fraction of oxidized surface atoms leading to oxygen concentrations of 26–27 at% and probably a higher fraction of C-atoms near the surface, as already observed via SIMS measurements (see Figure 5.2).

However, SIMS measurements, shown in Figure 5.2, reveal that a significant amount of oxygen is also present in the bulk material in the films compared to the a-Si:H films discussed in Section 4.1 (see Figure 4.6. The higher oxygen content within the a-SiC:H films can be attributed to three reasons: i) The decomposition temperature of trisilane is lower than for disilabutane, which is why the ratio of the precursor radicals to oxygen impurity radicals is higher. This leads to fewer impurities within the film. ii) In contrast to disilabutane, trisilane highly reacts with oxygen, forming solid silicon

oxide. This leads to self-purification of the process by reducing the O_2 content not only within the deposition chamber but within the whole glove box. iii) The purity of the trisilane precursor (>99.9 %) is higher than for the disilabutane (99 %). The lower purity might lead to a higher amount of O-containing solvents, which are incorporated into the material during film growth. However, the exact composition of the remaining 1 % of the precursor is not specified in the certificate of analysis document.

To reduce the O concentration due to solvents, precursors with higher purity can be used. Another possibility to reduce the O content is to increase T_d as indicated in Figure 5.2. The lower O content with increased T_d might result from higher amounts of precursor radicals to impurity radicals.

The dark conductivity of the undoped a-SiC:H films ranges from 10^{-10} S cm^{-1} to 10^{-7} S cm^{-1}. Only for the films deposited at $T_d = 500$ and 530 °C the photoconductivity is with 10^{-9} S cm^{-1} significant higher than the corresponding dark conductivity. These values agree with a photoconductivity of ~10^{-9} and a dark conductivity of ~10^{-11} found for a-SiC:H films made by Masuda et al. [23]. Note, however, that these films were made by a self-synthesized precursor deposited at temperatures between 320 and 420 °C.

The conductivity could only hardly be improved by adding TMD as a nitrogen-containing precursor for doping. However, SIMS and FTIR measurements indicated an incorporation of N. Therefore, in the next section, annealing is tested to activate the N as dopants within a crystalline SiC matrix. The use of TMD as precursor can increase the O content as well, as indicated by the increased $^{16}O^-$ intensity in the SIMS depth profiles shown in Figure 5.7. In agreement with this, the FTIR spectra show a large peak around 3450 cm^{-1}, which probably originate from O-H bonds.[178, 179, 241] However, also N-H stretching modes can be found in the same region.[236] The reason for the higher O content might be a more porous structure allowing the diffusion of O and H_2O into the film or a precursor with a low purity of 97 %, maybe causing a higher amount of O and O-H radicals within the deposition chamber due to O-containing solvents. Since the conductivity significantly decreases for the film deposited with 80 vol% TMD, indicating substantial microstructural changes, TMD concentrations way below 80 vol% will be used for the annealing tests in the next section to minimize the influence of O on the film properties.

5.2. Crystallization of a-SiC:H films

In addition to amorphous SiC films, crystalline SiC films are also used in a wide range of applications.[34, 101, 102, 242–244] The crystalline films have the potential for improved electrical and optical properties in contrast to amorphous films. Therefore, in this section the crystallization of the a-SiC:H films discussed in the Section 5.1.1 will be investigated and the properties of the resulting films are discussed.

The crystallization of a-SiC:H films was examined through different annealing techniques. First, the formation of undoped poly-SiC films by furnace annealing is explored, and the structural changes induced by varying the annealing temperature are analyzed. The effects of doping on poly-SiC are then investigated, with a focus on how nitrogen incorporation influences conductivity and crystallinity. Additionally, laser annealing is evaluated as an alternative method for achieving localized crystallization, which could enable more precise material modifications for device integration.

Finally, the implications of these crystallization processes are discussed, comparing their effectiveness and applicability for industrial applications. By optimizing the annealing conditions and doping strategies, the goal is to improve the material properties of poly-SiC films.

5.2.1. Undoped poly-SiC films

Crystallizing amorphous SiC films through furnace annealing is a common step in the fabrication of solar cell devices such as TOPCon solar cells and all-silicon tandem solar cells.[34, 245] To determine the optimal crystallization process, the annealing temperature T_a was varied between 900 and 1100 °C. Further details are given in Section 3.5.1. A-SiC:H films deposited at $T_d = 585$ °C were used for crystallization to maximize the Si-C bond fraction, as shown in Section 5.1.1. All the annealed films were blistering-free. Figure 5.8 shows that already at $T_a = 900$ °C, the SiC peak increases and shifts to higher wavenumbers, indicating a higher fraction of crystalline SiC within the film. Further, increasing the temperature to 1000 °C leads to a more Lorentzian than Gaussian-shaped peak form, significantly increases the peak height, and shifts the peak maximum to wavenumbers above 800 cm^{-1}. At 1100 °C, the absorption coefficient maximum further increases slightly to a value three times higher than that of the as-deposited film.

Crystallinity can be measured by the ratio of the Lorentzian to Gaussian peak contributions to the SiC stretching mode, shown in Figure 5.8 b) (see Section 2.2.2).[127]

Crystallinity increases with higher annealing temperatures, reaching a maximum of 60 % at $T_a = 1100\,°C$. For all annealing temperatures, H was completely effused from the films, as indicated by the disappearance of the 2100 cm^{-1} mode in the FTIR spectra (not shown). Besides changes in the Si-C peak, a new peak emerges around 1080 cm^{-1}, while the peak around 980 cm^{-1} vanishes. The comparison of the SIMS depth profiles of i) an as-deposited a-SiC:H film and ii) an at 1100 °C annealed SiC film in Figure 5.9 shows that during annealing, a layer with high oxygen content emerges at the surface of the film. This suggests that oxygen is incorporated during annealing from the surrounding atmosphere, which, although purged with nitrogen (N_2), is not fully evacuated before the process begins. As shown in Figure A.17, most of this oxygen can be removed with an HF dip without etching any SiC. The absence of a significant Si-O_x peak within the FTIR spectrum after the HF dip indicates that the oxygen content within the bulk of the film is less than 5 at%. For the calculation of the O content the peak at 1080 cm^{-1} was used, using an absorption coefficient of $0.1 \times 10^{20}\,cm^{-2}$ (see Section 3.4.1).

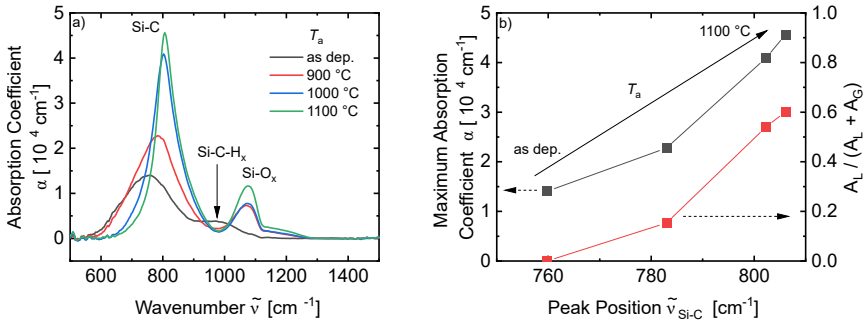


Figure 5.8.: a) FTIR spectra of SiC films as-deposited and after annealing at 900, 1000, and 1100 °C. b) Absorption coefficient maximum (left) and Lorentzian to Gaussian peak proportion ratio (right) of the Si-C stretching peak versus the SiC peak position ν_{Si-C}. The increasing peak position ν_{Si-C} with increasing annealing temperature is indicated with an arrow. Adapted from Fischer et al. [232] (2025), licensed under CC BY 4.0.

Since the FTIR and SIMS measurements of the amorphous material in Section 5.1.1 indicated a non-stoichiometric, silicon-rich material, the Raman spectra, shown in Figure 5.10, are used to investigate the formation of crystalline Si clusters within the

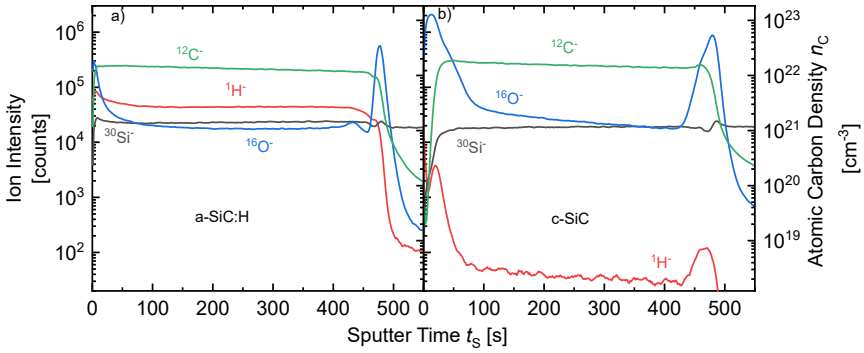


Figure 5.9.: Silicon, hydrogen, carbon, and oxygen SIMS depth profile of a) an at $T_d = 585\,°C$ deposited a-SiC:H film and b) a SiC film deposited under the same conditions but after post-annealing at 1100 °C. The SIMS counts for H, Si, and O are given on the left axis. On the right axis, the atomic carbon density n_C is given, calculated by comparing with a reference sample with a known amount of incorporated C in Si. Adapted from Fischer et al. [232] (2025), licensed under CC BY 4.0.

films during annealing. The features of the as-deposited film were already discussed in Section 5.1.1. The spectrum of the film annealed at 900 °C is similar.

At a T_a of 1000 °C, a small peak at 520 cm^{-1} emerges, which gets stronger for $T_a = 1100\,°C$. This clearly shows the formation of c-Si clusters within the SiC film. The fact that this peak occurs only for $T_a \geq 1000\,°C$, indicates a substantial concentration of C since the crystallization temperature of Si increases with increasing C content.[120, 183]

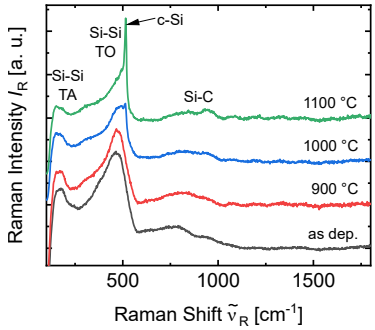


Figure 5.10.: Raman spectra of SiC films as-deposited and after annealing at 900, 1000, and 1100 °C. The corresponding vibrational modes of the major peaks are indicated. Adapted from Fischer et al. [232] (2025), licensed under CC BY 4.0.

5.2.2. Doped poly-SiC

Knowing from Figure 5.8 that annealing at $T_a = 1100\,°C$ leads to the highest crystallinity in SiC samples, this temperature was used to crystallize N-containing SiC films as already analyzed in their as-deposited state in Section 5.1.3. Figure 5.11 a) shows the conductivity of the films after annealing at 1100 °C as a function of the TMD content within the precursor. By varying the TMD content, the conductivity can be adjusted over three orders of magnitude. Below 1 vol% TMD content, no doping effect is observed in the SiC film. Between 1 and 5 vol% TMD content, the conductivity increases dramatically, indicating sufficient incorporation of N to dope the material. For higher TMD contents, the conductivity saturates at values up to 0.03 S cm^{-1}.

Increasing N concentration within the SiC films alters the chemical and electrical properties of the material, potentially shifting the Si-C vibrational modes.[184, 237] Therefore, the vibrational modes were investigated via FTIR. Figure 5.11 b) shows the normalized FTIR spectra of selected films from Figure 5.11 a) made with TMD contents between 1 and 20 vol%, along with a spectrum of an as-deposited sample. With increasing TMD content in the precursor, the SiC peak broadens. The broadening between 850 and 950 cm^{-1} of the Si-C peak within the FTIR spectra is likely caused by emerging Si-N peaks located in this wavelength regime, fitting to an increased N incorporation with higher TMD content.[125] The broadening to lower wavelengths might be caused by changes in the electrostatic environment of the Si-C bonds due to

N inclusion or a higher amorphous SiC fraction resulting from N incorporation.[125] Raman measurements on the films also reveal a higher amorphous fraction, as evidenced by the reduction of the 520 cm^{-1} peak with increasing TMD content. This trend is illustrated in Figure A.18, where with increasing TMD content, the increase in the amorphous peak relative to the crystalline peak, used for spectral normalization, is observed.

In addition to an increased amount of N, the changes in the shape of the peaks in the Raman and FTIR spectra might also be caused by an increased O content, as was already indicated in Figure 5.7 within the previous Section 5.1.3. However, note that for the crystallized samples here, a lower concentration of TMD was used than for the film analyzed in Figure 5.7.

Figure 5.11 c) shows the dependence of the conductivity on T_a for undoped samples and samples doped with a precursor containing 20 vol% TMD. The samples were deposited at a temperature of 585 °C, which is why the T_a of the as-deposited samples is set to 585 °C on the x-axis. As-deposited, the doped and undoped samples exhibit a similar conductivity of $\sim 2 \times 10^{-7}$ S cm^{-1}, indicating that the introduced N is not active as a dopant. Annealing at $T_a = 900$ °C increases the conductivity of both undoped and doped SiC to almost 10^{-4} S cm^{-1}. This increase might be due to an increase in the number of dangling bonds due to H effusion or other restructuring of the SiC configuration, as indicated by a change in the Si-C FTIR peak position shown in Figure 5.11 d). Further, increasing the T_a does not change the conductivity of the undoped sample, even though a structural change from amorphous to crystalline SiC occurs, as shown in Figure 5.8 and the content of silicon nanocrystals (nc-Si) increases as shown in Figure 5.10. However, in contrast to undoped samples, the transition from the amorphous to the crystalline phase in doped samples is accompanied by a significant increase in conductivity up to 3×10^{-2} S cm^{-1}. This increase is most likely due to the activation of the N dopants within the crystalline SiC structure.

In Figure 5.12, SIMS spectra of crystallized SiC films either deposited with (10 vol% TMD) or without doping are compared to investigate changes in nitrogen and oxygen content after doping. As a measure of the nitrogen content within the film, the SIMS counts of $^{16}CN^-$ ions are given. Both spectra show a significant but similar amount of oxygen. In contrast, the doped film shows 2 orders of magnitude increased SIMS counts of $^{16}CN^-$ ions, indicating that the incorporation of nitrogen is the main reason for the increased conductivity of the films. The fact that also for the undoped film, a significant amount of $^{16}CN^-$ ions are detected might be due to low amounts of N that

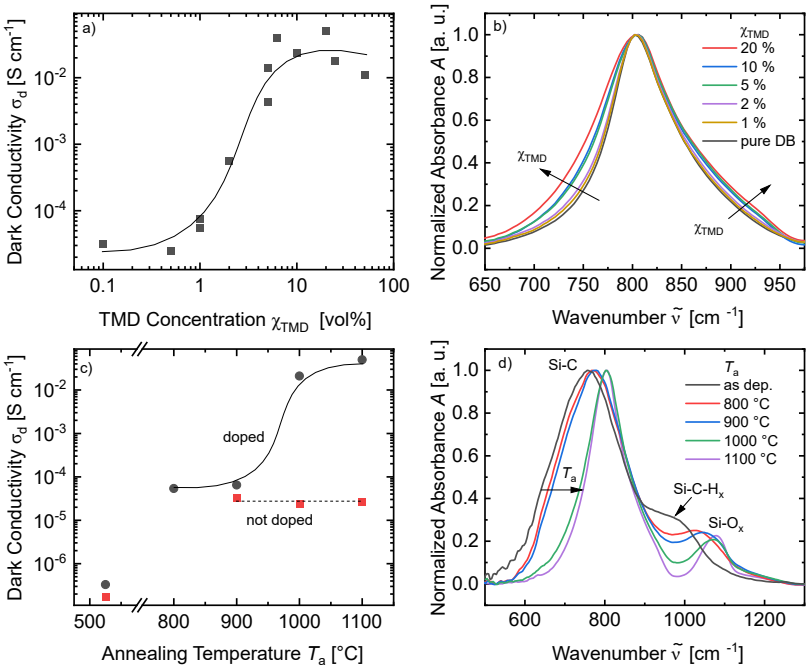


Figure 5.11.: a) Dark conductivity σ_d of at $T_a = 1100\,°C$ crystallized SiC films versus the concentration of TMD diluted in DB used as precursor. b) FTIR spectra of Si-C modes within selected films of a). c) Dark conductivity σ_d of undoped (red) and doped (gray) crystallized SiC films versus annealing temperature T_a. For the doped films, a precursor with 20 vol% TMD was used. d) FTIR spectra of Si-C modes within the doped films, whose σ_d is shown in c). Adapted from Fischer et al. [232] (2025), licensed under CC BY 4.0.

are within the film or due to overlapping peaks from other ions, e.g., C_2H_2. However, the strong increase over two orders of magnitude in ion intensity for doped samples is probably caused by N, since the other atomic ions, in particular C and H, show far less significant changes in ion intensity. In agreement with this, XPS measurements showed no nitrogen atoms for undoped crystallized SiC films and up to 2 at% nitrogen for the film doped with 10 vol% TMD (see Figure A.19). Other atomic contributions (Si, C, and O) show only minor changes, underlining the results from SIMS.

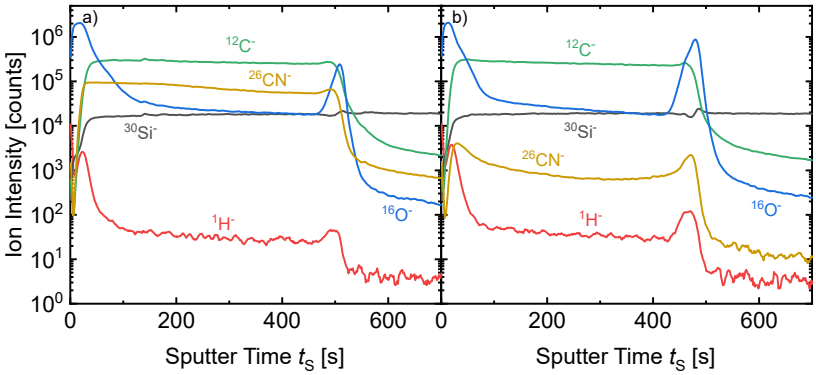


Figure 5.12.: Silicon, hydrogen, carbon, oxygen and cyanide (CN) SIMS depth profiles of a) a with 10 vol% TMD doped poly-SiC film and b) an undoped poly-SiC film. Adapted from Fischer et al. [232] (2025), licensed under CC BY 4.0.

5.2.3. Laser annealing

In the previous two sections, it was demonstrated that the a-SiC:H films produced by the APCVD system can be successfully crystallized via oven annealing. Although oven annealing results in full-area crystallization, localized crystallization of SiC films may be beneficial for several semiconductor devices. For example, transistors or microelectromechanical systems (MEMS) feature localized structures, potentially necessitating localized poly-SiC structures.[5]

To achieve localized crystallization, an a-SiC:H sample prepared at $T_d = 585\,°C$ was illuminated with a UV laser (wavelength: 355 nm, Gaussian spot size: 60 µm, power: 92 mW, pulse frequency: 15 kHz, pulse length: 12.5 ns). The laser was scanned over an area of $(9 \times 9)\,mm^2$ at a speed of $9\,mm\,s^{-1}$ with a line distance of 30 µm.

A microscope image of the resulting structure is shown in Figure 5.13. The laser scanning produced a continuous crystalline structure over the entire treated area, with slight optically visible variations between the laser focus and the overlap of two laser lines. Additionally, small black dots observed at the laser focus may indicate hydrogen effusion during the annealing process.

Figure 5.14 presents the FTIR spectra of the film before and after laser treatment. Two major aspects can be observed: (i) The peak at 720 cm^{-1}, associated with Si-C bonds in an amorphous environment, increases in intensity and shifts to higher wavenumbers, indicating the formation of crystalline SiC. (ii) The peaks around 2050 cm^{-1} and 2850 cm^{-1}, corresponding to Si-H and C-H stretching modes, respectively, decrease to one-fourth of their original height after laser treatment but do not fully vanish. This suggests that residual a-Si:H remains within the film either across the full treated area or possibly only at the laser spot edges due to lower annealing temperatures. Raman measurements along a pathway perpendicular to the laser scanning direction shown in Figure A.20 reveal consistent peak heights for the 2050 cm^{-1} Si-H stretching mode, indicating that the remaining hydrogen is distributed uniformly throughout the treated area.

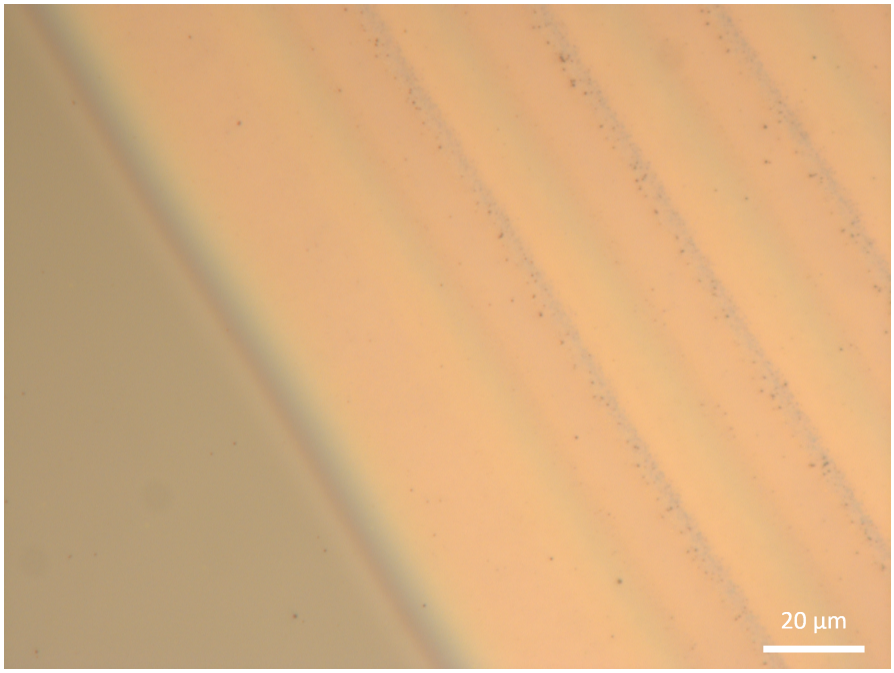


Figure 5.13.: Microscope image of a laser-crystallized SiC film at the edge of the crystallized area using a magnification of 50×.

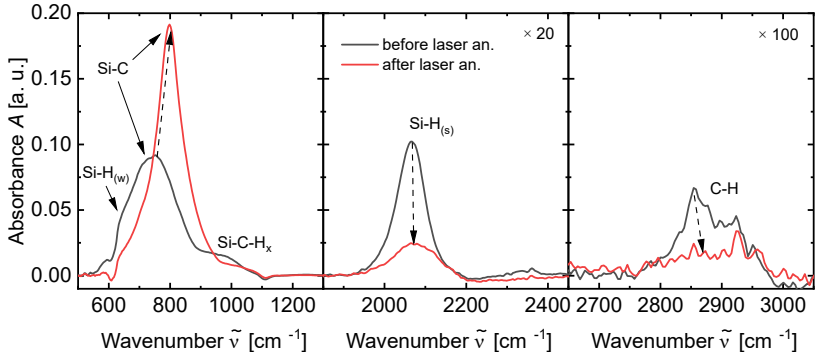


Figure 5.14.: FTIR spectra of a SiC film before and after laser crystallization. a) Si-H wagging, Si-C stretching, and Si-C-H_x wagging modes; b) Si-H stretching modes; c) C-H stretching modes.

5.2.4. Discussion

Furnace annealing of a-SiC:H films at 1000 and 1100 °C results in the formation of crystalline silicon carbide (c-SiC) as well as nanocrystalline Si clusters within the material, as shown in Figures 5.8 and 5.10. While carbon clusters were also detected by Raman spectroscopy (see Figure 5.3), it remains unclear whether they crystallized during annealing.

The successful crystallization of the a-SiC:H films aligns with the existing literature and confirms the feasibility of the annealing process in enhancing the properties of the material.[34, 96, 125, 213, 242] However, the Raman signal of the Si-C modes (750–800 cm^{-1}) in Figure 5.10 is too weak and too broad to draw conclusions about the polytype of the SiC crystals. This is probably due to the small crystal size and low film thickness.[123, 124, pp. 95–98]

In FTIR spectra, the crystallized films show Si-C peaks at 800 cm^{-1}, which is slightly higher than the typical position of the SiC peak at 780 cm^{-1}. This shift might be caused by an over-stoichiometric Si concentration within the film, as also observed by Weiss et al. [127]. By comparing the Lorentzian fraction with the Gaussian fraction of the peak, a maximum crystallinity of 60 % was found. A crystallinity below 100 % for non-stoichiometric Si-C is in agreement with the findings in Weiss et al. [127] and may also be influenced by the relatively high O concentration within the films, as found via SIMS measurements (see Figures 5.2 and 5.9).

The formation of a c-Si peak at high temperatures (1000–1100 °C) within the Raman spectra indicates a significant C content within the films, since for a-Si:H films, crystallization can already be observed at 700–800 °C as shown in Section 4.3.3. Song et al. [183] found similar Raman spectra for non-stoichiometric SiC as shown in Figure 5.10. Song et al. [183] give a correlation between the c-Si formation temperature and the C concentration within the films. Comparing the c-Si formation temperature of the APCVD films analyzed here with the results of Song et al., a C concentration between 24 and 39 at% can be concluded, which is in good agreement with the concentrations found using FTIR spectroscopy.

The increase in conductivity from 2×10^{-4} S cm^{-1} to 0.03 S cm^{-1}, shown in Figure 5.11 for the films deposited using a mixture of >5 vol% TMD in DB demonstrates the effectiveness of a liquid precursor for the incorporation of active dopants. The conductivity is within the typical range for crystalline, solar-grade SiC doped with N.[122, 246, 247] Anwar et al. [248] reviewed several series of SiC samples with conductivities ranging from 10^{-9} S cm^{-1} to 10^{2} S cm^{-1}. The conductivities observed in the work presented here

align well with this range and, spanning five orders of magnitude, cover a broader conductivity range than most other standalone sample series. Compared with the work of Miyajima et al. [128, 131] the maximum achieved conductivity of $0.03\,\mathrm{S\,cm^{-1}}$ is higher than for nitrogen doped PECVD ($10^{-3}\,\mathrm{S\,cm^{-1}}$) films but lower than for nitrogen-doped HWCVD films ($10^{1}\,\mathrm{S\,cm^{-1}}$).

The observed increase in conductivity is likely attributable to the formation of doped SiC or Si crystals. The most significant improvement in conductivity occurred between annealing temperatures of 900 °C and 1000 °C, a range that coincides with substantial c-SiC formation as shown in Figure 5.8 and only minimal crystalline Si formation, which increases more for $T_\mathrm{a} = 1100\,°\mathrm{C}$, as shown in Figure 5.10. This suggests that the doped c-SiC phase is the primary contributor to the observed conductivity improvements, supported by a significant broadening of the SiC mode within the FTIR spectrum, which indicates nitrogen incorporation into the SiC matrix. Therefore, an optimization of the c-SiC content by using stoichiometric Si:C mixtures might be beneficial to further improve the conductivity for other semiconductor applications such as transistors.[242, 243] Routes to achieve more stoichiometric SiC are discussed in 5.1.4.

Optimizing the N doping process could also yield higher conductivities, and exploring other dopants like aluminum may further enhance the properties of the film.[249] Additionally, a post-treatment for the incorporation of H could further increase the conductivity, making the film feasible for application as a passivation layer in TOPCon solar cells.[34, 36]

Not only near-stoichiometric SiC films, but also a-SiC:H films with lower n_C than the films used for crystallization in this work are utilized in nanoelectronic or optoelectronic devices. Reducing n_C lowers the crystallization temperature of nc-Si below that of SiC, potentially resulting in conductive nc-Si embedded within an a-SiC:H matrix, thereby enabling tunability of the optical band gap.[96, 98, 103, 120, 213] This reduction in n_C can be readily achieved by decreasing the deposition temperature or by mixing 1,4-DB with a silicon-rich precursor like trisilane, making the process suitable for the deposition of films designed for the formation of nc-Si within an a-SiC:H matrix.

In Section 5.1, via SIMS measurements, high O contents were found within a-SiC:H in comparison with a-Si:H made with pure TS. In FTIR, the corresponding Si-O peak is overlapped with the Si-C-H_x peak at the same position, making a clear assignment difficult. However, the $980\,\mathrm{cm^{-1}}$ peak was mainly attributed to Si-C-H_x vibrations due to its correlation with the C-H peak, as found in Section 5.1.

After crystallization, the peak at 980 cm^{-1} vanished and a new peak at 1080 cm^{-1} emerged. If the 980 cm^{-1} was due to Si-O_x and Si-O-Si vibrations, its reduction could be explained by a shift to higher wavelengths due to the reordering of the Si-O_x and Si-O-Si bonds.[175] These bonds would then contribute to the 1080 cm^{-1} peak shown in Figure 5.8 a). Assuming that the 980 cm^{-1} peak is attributed to Si-C-H_x vibrations, an alternative explanation for the disappearance of the 980 cm^{-1} peak could be due to the restructuring of carbon within the crystals formed during the annealing and the effusion of H from the film. The appearance of the 1080 cm^{-1} peak might not be directly related to the 980 cm^{-1} peak. Figure A.15 shows a sharp O peak at the surface of the film. Therefore, the O peak at 1080 cm^{-1} mainly occurs due to an oxide layer at the surface. This assumption is supported by the fact that an HF-etching of the sample led to a drastic decrease of the 1080 cm^{-1} peak while the Si-C peak height was maintained (cf. Figure A.17).

The unintentional incorporation of oxygen into the film can have significant effects on both the electrical and structural properties of the material. The acceptable amount of oxygen within the film depends on the application. Avila et al. [250] found significant structural changes of the material for oxygen contents > 15 at%. However, mechanical properties can be changed significantly for lower O content already.[251] For the application in electric devices, at grain boundaries and surfaces, oxygen can lead to the formation of SiO_2, an insulating phase that can interrupt conductive paths and thus reduce the overall conductivity of the SiC films. In contrast, in small amounts, oxygen can also act as an (unintentional) dopant, influencing the charge carrier concentration.[248] While oxygen incorporation can potentially enhance certain properties of SiC films, careful control of its content is critical to maintaining the desired electrical and structural characteristics for electronic and photovoltaic applications. The SIMS analysis in Figure 5.12 used to detect and quantify both nitrogen and oxygen in the films shows that after doping with TMD, the oxygen concentration in the film remains comparable to that of the undoped film. However, the amount of nitrogen increased significantly, indicating that the increased conductivity is indeed due to nitrogen doping instead of unintentional oxygen doping. This is in agreement with the findings of Lebedev et al. [135] and contradicts the assumption that doping is due to oxygen incorporation. However, a mechanism involving both N and O atoms is still conceivable.

The evaluation of the O content within the a-SiC:H films of Section 5.1 through FTIR was challenging due to overlap of the Si-O_x modes with the Si-C-H_x modes.

However, the FTIR spectrum after the HF dip in Figure A.17 allows a clear assignment of the peaks within the region from 1000 to 1200 cm^{-2} to Si-O_x modes, since most of the H effused out of the material due to annealing. The spectrum shows almost no Si-O peak, indicating an oxygen content of less than 5 at% in the bulk crystalline SiC material.

Finally, Figures 5.13 and 5.14 show that the a-SiC:H film can be locally crystallized using a Gaussian-shaped UV laser. The observation of Si–H modes after crystallization via FTIR and Raman spectroscopy indicates that an a-SiC:H layer persists after crystallization. Given that a UV laser was used, which is strongly absorbed in Si and therefore probably in the here used under stoichiometric a-SiC:H as well [252–254], it is likely that the residual amorphous layer is located near the interface with the c-Si wafer, where only a low intensity fraction of the UV light penetrates and is absorbed within the film. This might be beneficial for passivation applications.

To achieve a fully crystallized SiC film, a laser with a higher wavelength would allow more uniform annealing of the film due to a higher penetration depth. The microscopic image shows minor layer destruction, which probably occurs due to an accumulation of H at the laser line edge after the 1st laser-line scan and then abrupt H effusion during the scan of the next line, since for this line the focus is on the edge of the 1st line. This destruction could be prevented by an optimization of the laser power and the distance between each line.

The APCVD method for the SiC film deposition reduces operational costs and simplifies the scaling process, making it feasible for large-scale manufacturing. The structural integrity and electrical properties of these films make them promising candidates for applications requiring high thermal stability and efficient charge transport, such as TOPCon solar cells and all-silicon tandem solar cells.

5.3. Silicon carbide films from disilabutane diluted with cyclooctane

Depending on the application, SiC films with various Si-to-C ratios are required for electrical devices. In this chapter, it has already been established that depositing a-SiC:H films using DB results in films with an overstoichiometric Si content. Films with even higher Si concentrations can be readily achieved by optimizing the TS-to-DB ratio within the precursor, as TS decomposes at temperatures lower than those of DB (cf. 5.1). A confirmation of this hypothesis can be found in Figure A.21, where the number density of SiC bonds is shown for 3 films made of TS, DB, and a 50:50 mixture of both. The bond number density clearly decreases with decreasing DB concentration.

In contrast, increasing the carbon content presents a challenge, as the decomposition temperature of conventional precursors containing only C and H is potentially higher than that of DB or due to desorption mechanisms of carbon chains during deposition.[151] However, Section 4.2 showed, that mixtures of TS and CO can be used to produce SiC films with low C content. Therefore, in this section, the use of DB and CO mixtures as precursors is explored to potentially enhance the carbon content in a-SiC:H films and achieve a stoichiometric Si:C ratio.

5.3.1. a-SiC:H films from disilabutane and cyclooctane

When the Si-to-C ratio approaches a stoichiometric level, the number of Si-C bonds increases. To investigate these changes, FTIR spectroscopy was employed to analyze the Si-C bond density as a function of the precursor mixture. The resulting FTIR spectra are presented in Figure 5.15.

As shown in Figure 5.15 a), the Si-C bond peak exhibits only minor variations for DB concentrations ranging from 100 vol% to 10 vol%. However, further dilution with CO leads to a pronounced increase in the peak at 1000 cm^{-1}, while the Si-C peak diminishes. At the same time, the film thickness increases significantly (see Figure 5.15 d)). As discussed in Section 5.1, the enhancement of the peak around 1000 cm^{-1} suggests an increased presence of Si-C-H_3 or Si-O bonds. Furthermore, the position of the Si-H stretching modes, shown in Figure 5.15 b), shifts to higher wavelengths for films deposited with DB concentrations below 10 vol%. In addition, a distinct triple peak structure emerges at approximately 2100, 2150, and 2250 cm^{-1},

strongly indicating the presence of Si-H bonds with oxygen backbond.[176] Consistent with this observation, Figure 5.15 c) reveals the appearance of a broad peak around 3450 cm^{-1}, corresponding to O-H vibrational modes within the film.[178, 179, 241] Furthermore, a slight increase in C-H bond absorption is observed with decreasing DB concentration. It should be noted that the absolute values of the absorption coefficient for films deposited with 5 vol% and 2 vol% DB may deviate as the thicknesses may deviate due to the higher mean square error in the fitting of the ellipsometry data for these samples.

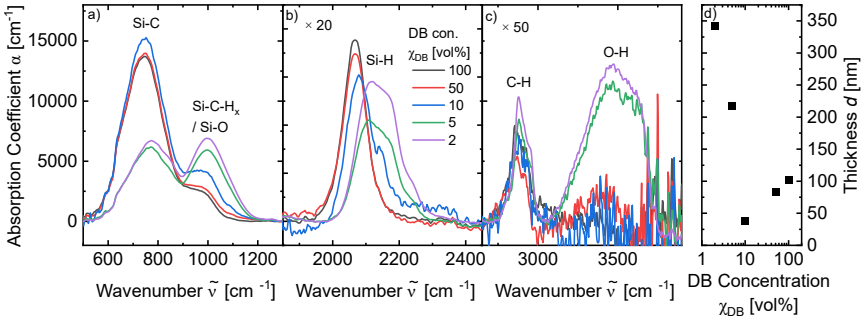


Figure 5.15.: FTIR spectra of a-SiC:H films deposited using a DB concentration χ_{DB} of 1 to 100 vol% diluted in cyclooctane as precursor. a) Si-H wagging, Si-C stretching, and Si-C-H_x wagging or Si-O modes; b) Si-H stretching modes; c) C-H stretching modes and N-H/O-H modes. d) Thickness d of the films, measured via ellipsometry.

5.3.2. Poly-SiC films from disilabutane and cyclooctane

To further characterize the properties of the films deposited with DB diluted in CO, the samples were annealed at 1100 °C in a furnace. The FTIR spectra obtained after annealing are presented in Figure 5.16 a). All samples exhibit a sharper peak around 780 cm^{-1}, indicating the transition from amorphous SiC to a more crystalline SiC structure.[127]

Consistent with observations for amorphous films, the Si-C peak intensity for annealed films remains nearly unchanged for films deposited with DB concentrations ranging from 100 vol% to 10 vol% but decreases for films deposited at higher dilution levels. As observed for films deposited with pure DB (see Section 5.2), annealing causes the peak at 1000 cm^{-1} to disappear while a new peak emerges at 1080 cm^{-1}.

This peak is associated with the formation of a silicon-oxide layer at the film surface. The peak is particularly pronounced for the film deposited with 10 vol% DB, as the reduced film thickness enhances the influence of surface silicon oxide on the absorption coefficient spectrum.

To remove the SiO_x layer, the annealed films were subjected to HF etching, and the FTIR spectra were remeasured. The results, shown in Figure 5.16 b), reveal that for films deposited with 50 vol% and 100 vol% DB, the 1080 cm^{-1} peak is almost entirely eliminated, suggesting that it originates primarily from a silicon oxide layer formed at the surface during annealing. However, for films deposited with lower concentrations of DB, the 1080 cm^{-1} peak, along with a side peak around 1200 cm^{-1}, partially persist even after etching. This indicates a significant incorporation of oxygen into the film during deposition, consistent with the presence of Si-O and O-H peaks in the FTIR spectra of the amorphous films shown in Figure 5.15. In agreement with this, the conductivity of the crystallized film decreases significantly with increasing dilution for films deposited with a DB concentration below 10 vol% as shown in Figure A.22.

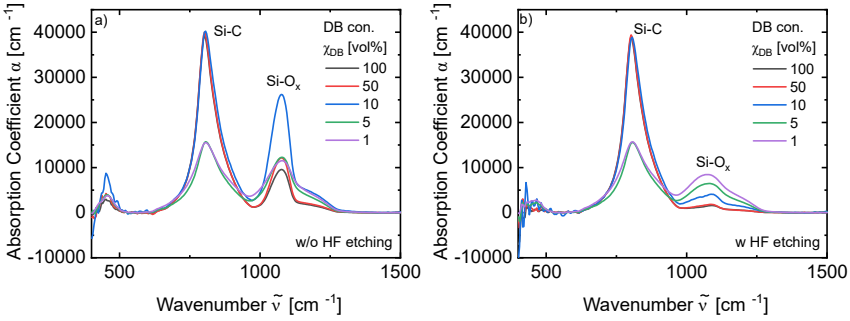


Figure 5.16.: FTIR spectra of Si-C stretching and Si-O_x stretching modes after annealing of the a-SiC:H films from Figure 5.15 deposited using a DB concentration χ_{DB} of 1 to 100 vol% diluted in cyclooctane as precursor. The spectra a) directly after annealing and b) after subsequent HF etching are shown.

5.3.3. Discussion

The deposition of a-SiC:H films using DB diluted with CO did not increase the Si-C bond density within the material. For DB concentrations between 10 vol% and 100 vol% in the precursor, the carbon content (as indicated by the Si-C peak in FTIR) remains constant, but it decreases significantly for DB concentrations below 10 vol%. Instead, oxygen is incorporated into the film, as evidenced by O-H vibrations in the FTIR spectra of the amorphous film (Figure 5.15) and Si-O_x modes in the FTIR spectra of the crystallized films (Figure 5.16 b). The increased oxygen content may result from either a higher level of oxygen impurities in CO, which is consistent with the findings in Section 4.2, where an increased O content was observed in films with higher CO concentrations in the precursor, or from a porous film structure that facilitates oxidation upon exposure to ambient air.

The highest absorption coefficient found for the Si-C peak was $4 \times 10^4\,\mathrm{cm^{-1}}$ after crystallization for DB concentrations between 10 vol% and 100 vol%. This is half of the maximum peak value reported for SiC films produced via HWCVD by Köhler et al. [255]. This finding is consistent with the results of Section 5.1, where the carbon concentration in films deposited using disilabutane was determined by SIMS to be approximately 16–27 at%, compared to the 50 at% expected for stoichiometric films. Köhler et al. [255] correlated the maximum Si-C peak height with the grain size of the SiC crystal. If the influence of carbon concentration is disregarded, the peak height of $4 \times 10^4\,\mathrm{cm^{-1}}$ observed in this work corresponds to a grain size of approximately 8 nm.

When comparing the FTIR spectra in Figure 5.15 with those of the a-SiC:H films incorporating nitrogen in Section 5.1.3 (Figure 5.6), both materials exhibit a very similar peak around $3450\,\mathrm{cm^{-1}}$. While in Section 5.1.3 it remained unclear whether this peak originates from N-H or O-H modes, the films deposited using the DB-CO mixture are not expected to contain nitrogen, suggesting that the peak originates primarily from O-H modes. However, substantial differences are observed in other regions of the FTIR spectra. While the peak at $3450\,\mathrm{cm^{-1}}$ is significantly more pronounced in the DB-TMD films, only a minor shift of the $2100\,\mathrm{cm^{-1}}$ peak and a slight increase in the $1000\,\mathrm{cm^{-1}}$ peak are observed compared to the FTIR spectra of the DB-CO films. Both peak changes indicate the presence of Si bonded to O. Therefore, the increase in the peak at $3450\,\mathrm{cm^{-1}}$ appears to be decoupled from other typical oxygen-related peaks, which potentially indicates that, in the DB-TMD films, this peak is indeed related to N-H modes or that a different O-H bond incorporation mechanism occurs compared to the DB-CO films.

The significant increase in oxygen content for films deposited with a DB concentration below 10 vol% can have substantially influence on the film properties [248, 250, 251], which aligns with the pronounced drop in conductivity observed for these films, as shown in Figure A.22. This decrease in conductivity further supports the conclusion that, for the TMD-doped films discussed in Section 5.2.2, the increase in conductivity is not due to unintentional oxygen doping but rather a result of the successful incorporation of nitrogen dopants.

To enhance carbon incorporation, the use of precursors with lower decomposition temperatures might be advantageous. This is supported by the observation that the introduction of TS, which decomposes at a lower temperature than DB, into the precursor mixture resulted in a significant increase in the silicon content within the film. However, identifying a suitable carbon precursor remains challenging because of the high bond strength of C-C bonds, which hinders efficient decomposition. The introduction of a catalyst may be necessary to facilitate the formation of reactive carbon radicals capable of interacting with the film surface.

When films produced using TS-CO mixtures, DB-CO mixtures, and pure DB are compared, those deposited with pure DB exhibit the highest density of Si-C bonds while also achieving the highest film purity, particularly with respect to oxygen impurities. Therefore, pure DB is the optimal precursor for depositing a-SiC:H films that meet these two criteria.

6. Conclusions and Outlook

This work investigated the deposition of a-Si:H and a-SiC:H films using liquid precursors in an atmospheric pressure chemical vapor deposition (APCVD) process. A new APCVD prototype was built to pave the way for the industrial application of this process and to demonstrate the potential for using the layers in solar cells and other semiconductor devices.

The successful use of pure trisilane for controlled deposition of a-Si:H films fills a gap in the field of liquid silane pyrolysis, which has focused primarily on cyclopentasilane or nanoparticle polysilicon inks so far.[21, 143, 149] Furthermore, a wide range of trisilane-cyclooctane (TS-CO) mixtures was explored to define the limits of the trisilane dilution to achieve minimal impact of the carbon-containing solvent on the a-Si:H film properties. For the first time, 1,4-disilabutane (DB) was employed for the intentional deposition of a-SiC:H films, thus extending the parameter space for liquid-precursor-based a-SiC:H deposition.

For both a-Si:H and a-SiC:H, new application pathways in semiconducting structures were explored, particularly their crystallization into poly-Si and poly-SiC films. This work thereby combines a detailed understanding of film properties with well-founded suggestions for how these properties can be optimized or adapted for specific applications, while also identifying limitations. The key findings related to silicon and silicon carbide films are summarized as follows.

6.1. Silicon Films

Using a custom-built APCVD prototype and the readily available liquid precursor trisilane, a-Si:H films were deposited with qualities comparable to those achieved using cyclopentasilane.[7, 148] By adjusting the deposition parameters, hydrogen content between 0 and 10 at% and microstructure parameters between 0 and 0.6 were obtained. Among these parameters, the deposition temperature was identified as the most critical: higher temperatures led to higher hydrogen effusion rates during

deposition, resulting in a reduced hydrogen content. In addition, higher temperatures also promoted the incorporation of carbon and oxygen impurities. Films deposited at lower temperatures (440–470 °C), on the other hand, exhibited higher hydrogen concentrations and purities comparable to PECVD-deposited films used in solar cell applications, as shown in Section 4.1.

Varying the deposition time and precursor volume allows for tuning of the film properties as well. A higher volume of precursor increases the probability of precursor molecules or radicals interacting with the substrate surface. This increases the growth rate and leading to higher hydrogen incorporation and a more porous film, which raises R. In contrast, longer deposition times lower the average growth rate and may induce annealing, both of which reduce the hydrogen concentration and R in films made with pure trisilane.

The lowest defect density observed in this work was $3 \times 10^{18}\,\mathrm{cm^{-3}}$, which is significantly higher than that of PECVD films. This elevated defect density is likely due to the lower degree of defect saturation stemming from the relatively low hydrogen content. The photosensitivity of the films was directly correlated with the hydrogen content, with the highest photosensitivity values reaching 4×10^{4} in as-deposited films, with a dark conductivity of $3.4 \times 10^{-12}\,\mathrm{S\,cm^{-1}}$ and a photoconductivity of $1.5 \times 10^{-7}\,\mathrm{S\,cm^{-1}}$. Post-deposition hydrogenation via hot-wire CVD further increased the photosensitivity to values exceeding 10^{5}. This treatment was particularly effective for films deposited at higher temperatures and with initial low hydrogen content, while films with higher initial hydrogen levels showed little to no improvement.

Due to a precursor volume of only a few microliters, films deposited with pure trisilane showed considerable thickness variation. The dilution with cyclooctane significantly improved the reproducibility and precursor utilization by enabling a more precise dosing by the dosage pump. Therefore, a film series deposited with a highly diluted TS-CO mixtures (2 vol% TS) was used for a detailed analysis of the a-Si:H film growth mechanism. A growth model was established, revealing that the thickness of the film over time is governed by a temperature-dependent deposition rate, a precursor loss rate, and the total precursor volume in the chamber. The activation energy of the a-Si:H growth process was estimated at 1.8 eV. The precursor loss rate, primarily due to the lack of a proper chamber seal, was determined to be approximately $11.5\,\%\,\mathrm{min^{-1}}$. The model indicated that the deposition process is limited by the availability of decomposable precursor rather than by the generation of reactive silicon surface sites, which are the main limiting factors in a CVD process.[29, pp. 20–35]

The dilution of trisilane with cyclooctane influences the properties of the a-Si:H film through carbon incorporation, which depends on the deposition parameters. The following three regimes can be distinguished:

- $\chi_{\mathrm{TS}} \geq 10\,\mathrm{vol\%}$**:**

  No significant changes in macroscopic or microscopic film properties compared to those deposited with pure trisilane.

- $\chi_{\mathrm{TS}} \leq 10\,\mathrm{vol\%}$ **and** $T_{\mathbf{d}} \leq 470\,$**°C:**

  Moderate carbon contamination had minimal effects on conductivity and hydrogen content but increased R due to the formation of Si-H bonds with carbon backbonds.

- $\chi_{\mathrm{TS}} \leq 10\,\mathrm{vol\%}$ **and** $T_{\mathbf{d}} > 470\,$**°C:**

  Significant carbon incorporation occurred, increasing both c_{H} and R. The films transitioned to a mixed phase of a-Si:H and a-SiC:H.

The silicon-rich a-SiC:H films formed under regime 3 are promising precursors for producing nanocrystalline silicon embedded in an a-SiC:H matrix via post-deposition annealing. The increase in hydrogen content for films made with highly diluted TS-CO mixtures slightly improved the photosensitivity of films deposited at 495–555 °C. However, as long as the material is a mixture of Si and SiC clusters, the overall film properties are only hardly improved by increased hydrogen incorporation, since most additional incorporated H when depositing with TS-CO mixtures is bonded to Si with a carbon backbond while silicon clusters within the films still exhibit a high defect density.

Films exhibited inhomogeneities in hydrogen, carbon, and oxygen content across their thickness due to the initial precursor injection method. The distribution of precursor injections over time mitigated this issue, but led to increased oxygen incorporation, possibly from impurities in the N_2 carrier gas. To fully leverage continuous dosing, future work should aim to develop a method for the constant supply of pure trisilane to avoid contamination.

Significant carbon incorporation occurs only at deposition temperatures above 470 °C and for trisilane contents below 10 vol%. Consequently, most studies in the literature

employ conditions within these limits and therefore indeed report the formation of pure a-Si:H films with low carbon concentrations.[20–22]

Passivation

Although the as-deposited a-Si:H films exhibited high defect densities, they were still effective in passivating polished c-Si wafers, achieving charge carrier lifetimes up to 1.9 ms at a deposition temperature of 470 °C, which exceeds previously reported values.[19, 222, 223] This shows that defects within the a-Si:H films themselves have a minor influence on the passivation of c-Si wafers.

The results indicate that the charge carrier lifetime of the wafers cannot be correlated with a single material characteristic but depends on several factors such as film thickness, hydrogen content, or differences of the a-Si:H film on each side of the wafer. The total hydrogen content within the film is more critical for passivation than its concentration, suggesting that passivation is mediated by highly mobile hydrogen species, possibly molecular hydrogen (H_2), as proposed in previous studies.[216, 256] If the H is highly diffusive, the whole film can be used as a reservoir for H that migrates through the film and contributes to passivation at the interface.

Shorter deposition times and higher precursor concentrations generally led to higher lifetimes, since higher average growth rates led to more H incorporated into the film. Light-soaking treatments had no effect on the passivation quality, indicating that hydrogen, which is mobile at light-soaking temperatures (200–300 °C), had already been effused during deposition and the H configuration is frozen to the condition that is established in the end of the film deposition.

Due to the relatively low hydrogen content (<10 at%), only thick films (>100 nm) achieved effective passivation. Consequently, improvements in hydrogen content are necessary for application in SHJ solar cells. To increase the H content within the films, carbon-containing films from cyclooctane-diluted trisilane were tested for passivation. However, the films showed no improvement in passivation despite higher hydrogen contents, likely due to its bonding within strong Si-H bonds with C backbond. Simultaneous deposition on both sides of the wafers may also increase the H content within the films because of a reduction of the hydrogen loss within the first film during the deposition of the second film. Furthermore, post-deposition hydrogen radical treatment of hydrogenated a-Si:H films, as investigated as well in this study, can enhance the hydrogen content and should be explored as potential passivation layers for SHJ solar cells in future studies.

Doping and hydrogenation

The electronic quality of a-Si:H films was improved through hydrogenation and catalytic doping, both individually and in combination. While hydrogenation increased hydrogen incorporation, its effectiveness was limited by film blistering on polished c-Si substrates. The blistering leads to an underestimation of the hydrogen content via FTIR, which was found to be a maximum of 10 at%. Thus, the treatment conditions must be refined to prevent delamination. It was not investigated whether H was incorporated homogeneously through the film thickness. While this can be addressed in the future via SIMS measurements, the accumulation of H at the a-Si:H/c-Si interface leading to the film delamination indicates a distribution of H throughout the whole film thickness. The highest photosensitivities of $\sim 10^5$ were achieved for films deposited at a temperature of 555 °C with a dark conductivity of $6 \times 10^{-11}\,\mathrm{S\,cm^{-1}}$ and a photoconductivity of $5 \times 10^{-6}\,\mathrm{S\,cm^{-1}}$.

Catalytic doping substantially increased the conductivity of APCVD a-Si:H films, especially when followed by deposition of a capping layer. Herein, it was found that the capping layer not only prevents phosphorus desorption as suggested by Liu et al. [31], but likely promotes dopant activation by modifying the surface during deposition. Both PECVD and APCVD capping layers were effective, demonstrating that plasma is not essential for activation.

Despite these improvements, doped APCVD films still showed lower conductivities than their PECVD counterparts, likely due to reduced hydrogen content and higher defect densities. However, combining catalytic doping with hydrogen treatment proved particularly promising. A two-step process, doping followed by hydrogenation, achieved high photoconductivities close to $10^{-4}\,\mathrm{S\,cm^{-1}}$ and rather high dark conductivities of $5 \times 10^{-8}\,\mathrm{S\,cm^{-1}}$ compared to intrinsic hydrogenated a-Si:H films, outperforming the doping-plus-capping layer approach and simplifying the process by eliminating the need for an additional deposition step. These findings suggest that hydrogen radicals may aid both dopant activation by bulk/surface restructuring and defect saturation.

The combined use of hydrogenation and catalytic doping offers a promising route to significantly enhance the performance of a-Si:H films. Future work should focus on process optimization to reduce defect densities, mitigate blistering, and improve dopant incorporation, ideally achieving parity with state-of-the-art PECVD films. Further, a more detailed investigation of the hydrogenated and doped samples using techniques such as SIMS or ESR could provide deeper insights into the distribution

of hydrogen and phosphorus within the films and changes in their defect densities, potentially allowing further optimization of these processes.

Crystallization

The relatively low hydrogen content (<10 at%) of the as-deposited APCVD a-Si:H films makes them excellent candidates for crystallization into polycrystalline silicon, as this mitigates blistering, which is a major issue during poly-Si formation on c-Si substrates. Indeed, films deposited at 440–555 °C were successfully crystallized through both the furnace and rapid thermal annealing (RTA) without blister formation. Because most PECVD-deposited films show blistering during the RTA process, the use of APCVD films for crystallization is beneficial, enabling a high-throughput crystallization process.

RTA-treated films exhibited grain sizes larger than those annealed in a furnace, likely because of rapid heating and cooling, which limit nucleation. These films also showed significantly increased conductivities up to $10^{-1}\,\mathrm{S\,cm^{-1}}$, which exceeds the intrinsic conductivity of crystalline silicon. Although the precise mechanism remains unclear, SIMS and XPS measurements indicated the incorporation of nitrogen or phosphor atoms, leading to unintentional doping during the crystallization process.

The potential to crystallize APCVD a-Si:H films blistering free using fast and high-throughput annealing processes and their high purity support their suitability for poly-Si formation in TOPCon solar cells. Further investigations should focus on the crystallization of doped a-Si:H films, potentially by combining catalytic doping with subsequent annealing.

6.2. SiC Films

This study demonstrates that atmospheric pressure chemical vapor deposition (APCVD) using 1,4-disilabutane (DB) as a single source precursor enables the deposition of hydrogenated amorphous silicon carbide (a-SiC:H) films at intermediate temperatures. The process yields strong Si-C and C-H bonding features within the film as verified by FTIR and Raman spectroscopy, with Si and C clustering also observed via XPS and Raman. The formation of Si-C bonds is less effective at lower temperatures (< 555 °C), likely due to insufficient cleavage of the C-C bond.

At a deposition temperature of 585 °C, a-SiC:H films with atomic carbon densities of $2 \times 10^{22}\,\mathrm{cm^{-3}}$ according to FTIR and $1.34 \times 10^{22}\,\mathrm{cm^{-3}}$ based on SIMS analysis were obtained. The carbon incorporation is similar to a-SiC:H films made by

PECVD [105, 114] and exceeds that of most other low temperature pyrolyzed a-SiC:H films, particularly those deposited from binary precursors.[1, 23]

In terms of electrical performance, the dark conductivity of the films increases from $10^{-10}\,\mathrm{S\,cm^{-1}}$ to $10^{-7}\,\mathrm{S\,cm^{-1}}$ with higher deposition temperatures. Nitrogen incorporation was attempted using 1,1,3,3-tetramethyldisilazane (TMD) in combination with DB as a precursor, introducing N atoms into the films without significantly affecting the electrical properties. This may result from ineffective incorporation of N into the a-SiC:H network or the presence of a high density of electrically active defects.

Oxygen contamination was more pronounced in the a-SiC:H films than in the a-Si:H films, as revealed by SIMS, but not greater than 5 at% as indicated by FTIR. The increased O content is attributed to either higher deposition temperatures or the use of precursors with lower purity for the a-SiC:H film deposition. To achieve SiC films with high purity and an exceptionally low oxygen content ($\ll 0.1$ at%), it may be necessary to purify the precursor and lower the oxygen concentration within the glove box to below 1 ppm.

Post-deposition annealing induced structural transitions from amorphous a-SiC:H to nanocrystalline SiC (nc-SiC) and nanocrystalline Si (nc-Si), as confirmed by the emergence of Lorentzian-shaped peaks originating from Si-C stretching modes in FTIR spectra and a typical transversal optical mode for crystalline silicon in Raman spectra. While carbon clusters were detected via Raman spectroscopy as well, it remains unclear whether they underwent crystallization. Because of the small crystal grain size, the Si-C-related peaks in the Raman spectra were weak and broadened, hindering accurate identification of the SiC polytype. A minimum temperature of 1000 °C was identified as necessary for the formation of SiC crystals. Higher temperatures increase the proportion of crystalline material. The phase transition from an undoped amorphous material to crystalline material leads to an increase in conductivity from $2 \times 10^{-7}\,\mathrm{S\,cm^{-1}}$ to almost $10^{-4}\,\mathrm{S\,cm^{-1}}$.

In addition to furnace annealing, localized crystallization was demonstrated using a Gaussian-shaped pulsed UV laser. This approach allows for spatially controlled transformations, but further optimization is needed to ensure uniform crystallization throughout the film and to prevent surface damage due to hydrogen effusion.

For nitrogen-containing a-SiC:H films, annealing at 900–1000 °C led to conductivity improvements that exceeded three orders of magnitude, resulting in a maximum conductivity of $0.03\,\mathrm{S\,cm^{-1}}$. This enhancement suggests successful N doping of the crystallized poly-SiC matrix. The achieved conductivity surpasses the maximum

reported for nitrogen-doped PECVD films ($10^{-3}\,S\,cm^{-1}$) found by Miyajima et al. [128], but remains below that of nitrogen-doped HWCVD films ($10^{1}\,S\,cm^{-1}$) found in another study of Miyajima et al. [131].

Since oxygen levels remained similar between doped and undoped samples, the increase in conductivity can be attributed to nitrogen rather than unintentional oxygen doping. These results show the possibility to produce doped crystalline films with an adjustable conductivity over several orders of magnitude using a low-temperature APCVD process employing low-cost liquid precursors only.

By adding trisilane to the DB precursor, the carbon content in the a-SiC:H films could be reduced in a controlled manner, potentially enabling the formation of conductive nc-Si phases within the SiC matrix. This tunability supports band gap engineering and opens avenues for tailoring the material for specific device applications. On the other hand, using mixtures of DB and cyclooctane as precursors for the a-SiC:H deposition did not enhance Si-C bond formation compared to the use of pure DB. Instead, oxygen incorporation was observed, indicated by O-H vibrations in the FTIR spectra of amorphous films and Si-O modes in the spectra after crystallization. This suggests that cyclooctane may introduce unwanted oxygen contamination rather than contributing additional carbon. Future work could explore alternative carbon-containing precursors with decomposition temperatures better matched to DB, to enable more effective carbon incorporation and control. Approaching near-stoichiometric Si:C ratios and optimizing both the dopant species and post-deposition treatments-such as hydrogenation-could further enhance the electrical properties of these materials, supporting their use in electronic and photovoltaic applications.

6.3. APCVD Process Optimization and Future Perspectives

To further improve the APCVD process, the implementation of an advanced precursor injection mechanism would be beneficial. Such a system should enable robust and reproducible dosing of small volumes of undiluted precursor, either continuously or in discrete injection strokes. One potential solution is the integration of a suitable precursor evaporation system. In addition, optimizing the deposition chamber sealing could help reduce precursor losses and enhance film purity. Improved sealing would also facilitate the introduction of various ambient gases, such as hydrogen, which may contribute to improved film quality.

In the current APCVD setup, the films deposited on an area of $2 \times 2\,\mathrm{cm}^2$ exhibited a thickness reduction of approximately 30 % at the edges compared to the center. This highlights a key scalability challenge: achieving a uniform temperature distribution across the substrate and ensuring consistent precursor delivery. However, concepts from existing large-area pyrolysis systems could be readily adapted to the APCVD configuration presented here.[145]

While this work has already explored two n-type doping strategies: catalytic a-Si:H doping and in situ a-SiC:H doping via TMD, future efforts should further investigate both n-type and p-type in-situ doping of a-Si:H, a-SiC:H, and their polycrystalline counterparts to broaden the application potential of these materials.

Moreover, the process offers promise for development into a direct, localized thin-film deposition technique, such as laser-based local annealing or inkjet printing. This could enable advanced applications in microelectromechanical systems (MEMS), interdigitated back contact (IBC) solar cells, and other devices utilizing patterned thin-film structures. A laser-based local deposition system, based on the results presented in this work, is currently being developed.

In conclusion, APCVD stands out as a scalable and cost-effective approach for fabricating a-Si:H, a-SiC:H, poly-Si, poly-SiC, and nc-Si/nc-SiC films for advanced electronic and photovoltaic applications. With further refinement in precursor chemistry and thermal processing, these materials show strong potential for integration into technologies such as TOPCon or heterojunction solar cells, all-silicon tandem architectures, thin-film transistors, MEMS, and biomedical devices.

Bibliography

[1] Takashi Masuda, Zhongrong Shen, Hideyuki Takagishi, Keisuke Ohdaira, and Tatsuya Shimoda. "Amorphous silicon carbide films prepared using vaporized silicon ink". In: *Japanese Journal of Applied Physics* 53.3 (2014), p. 031304. DOI: 10.7567/JJAP.53.031304.

[2] T. Itoh, Y. Hasegawa, T. Fujiwara, A. Masuda, and S. Nonomura. "Wide gap and low resistive hetero-structured SiC/sub X/ films for wide gap window of heterojunction solar cells". In: *Proceedings of 3rd World Conference on Photovoltaic Energy Conversion, 2003.* Vol. 2. May 2003, 1706–1709 Vol.2.

[3] N.I. Klyui, V.G. Litovchenko, A.G. Rozhin, V.N. Dikusha, M. Kittler, and W. Seifert. "Silicon solar cells with antireflection diamond-like carbon and silicon carbide films". In: *Solar Energy Materials and Solar Cells* 72.1 (2002), pp. 597–603. DOI: 10.1016/S0927-0248(01)00209-4.

[4] M. Estrada, A. Cerdeira, L. Resendiz, R. García, B. Iñiguez, L. F. Marsal, and J. Pallares. "Amorphous silicon carbide TFTs". In: *Solid-State Electronics* 50.3 (2006), pp. 460–467. DOI: 10.1016/j.sse.2006.03.001.

[5] Pasqualina M Sarro. "Silicon carbide as a new MEMS technology". In: *Sensors and Actuators A: Physical* 82.1 (2000), pp. 210–218. DOI: 10.1016/S0924-4247(99)00335-0.

[6] Scott Greenhorn, Edwige Bano, Valérie Stambouli, and Konstantinos Zekentes. "Amorphous SiC Thin Films Deposited by Plasma-Enhanced Chemical Vapor Deposition for Passivation in Biomedical Devices". In: *Materials* 17.5 (2024), p. 1135. DOI: 10.3390/ma17051135.

[7] Zhongrong Shen, Takashi Masuda, Hideyuki Takagishi, Keisuke Ohdaira, and Tatsuya Shimoda. "Fabrication of high-quality amorphous silicon film from cyclopentasilane by vapor deposition between two parallel substrates". In: *Chemical Communications* 51.21 (2015), pp. 4417–4420. DOI: 10.1039/C4CC09026H.

[8] Andrew P. Cádiz Bedini, Long D. Trieu, Stefan Muthmann, Uwe Rau, and Reinhard Carius. "Approaching Solar-Grade a-Si:H for Photovoltaic Applications via Atmospheric Pressure CVD Using a Trisilane-Derived Liquid Precursor". In: *Solar RRL* 1.7 (2017), p. 1700030. DOI: 10.1002/solr.201700030.

[9] E. M. Tebben and M. A. Ring. "Pyrolysis of disilane and trisilane". In: *Inorganic Chemistry* 8.8 (1969), pp. 1787–1789. DOI: 10.1021/ic50078a050.

[10] Tatsuya Shimoda, Yasuo Matsuki, Masahiro Furusawa, Takashi Aoki, Ichio Yudasaka, Hideki Tanaka, Haruo Iwasawa, et al. "Solution-processed silicon films and transistors". In: *Nature* 440.7085 (2006), pp. 783–786. DOI: 10.1038/nature04613.

[11] Takashi Masuda, Hideyuki Takagishi, Zhongrong Shen, Keisuke Ohdaira, and Tatsuya Shimoda. "Phosphorus- and boron-doped hydrogenated amorphous silicon films prepared using vaporized liquid cyclopentasilane". In: *Thin Solid Films* 589 (2015), pp. 221–226. DOI: 10.1016/j.tsf.2015.05.040.

[12] Sijin Han, Xuliang Dai, Phillip Loy, John Lovaasen, Joshua Huether, Justin M. Hoey, Andrew Wagner, et al. "Printed silicon as diode and FET materials – Preliminary results". In: *Journal of Non-Crystalline Solids* 354.19 (2008), pp. 2623–2626. DOI: 10.1016/j.jnoncrysol.2007.10.090.

[13] Ho Yee Hui, María de la Mata, Jordi Arbiol, and Michael A. Filler. "Low-Temperature Growth of Axial Si/Ge Nanowire Heterostructures Enabled by Trisilane". In: *Chemistry of Materials* 29.8 (2017), pp. 3397–3402. DOI: 10.1021/acs.chemmater.6b03952.

[14] Takashi Masuda, Narihito Tatsuda, Kazuhisa Yano, and Tatsuya Shimoda. "Silicon deposition in nanopores using a liquid precursor". In: *Scientific Reports* 6.1 (2016), p. 37689. DOI: 10.1038/srep37689.

[15] K. H. Chung, N. Yao, J. Benziger, J. C. Sturm, K. K. Singh, D. Carlson, and S. Kuppurao. "Ultrahigh growth rate of epitaxial silicon by chemical vapor deposition at low temperature with neopentasilane". In: *Applied Physics Letters* 92.11 (2008), p. 113506. DOI: 10.1063/1.2897325.

[16] A. M. Abyzov and E. P. Smirnov. "Kinetics of SiC chemical vapor deposition from methylsilane". In: *Inorganic Materials* 36.9 (2000), pp. 884–890. DOI: 10.1007/BF02758698.

[17] Mao Ito and Arvind Kamath. "Polysilicon TFTs fabricated using poly-tetrasilane ink". In: *MRS Communications* 12.1 (2022), pp. 124–129. DOI: 10.1557/s43579-022-00152-1.

[18] Phan Viet Dung, Pham Tien Lam, Nguyen Dinh Duc, Ayumu Sugiyama, Tatsuya Shimoda, and Dam Hieu Chi. "First-principles study of the thermally induced polymerization of cyclopentasilane". In: *Computational Materials Science* 49.1 (2010), S21–S24. DOI: 10.1016/j.commatsci.2010.02.042.

[19] Andrew Paolo Cádiz Bedini, Uwe Rau, and Bernhard Hidding. *Sonochemical synthesis of silicon hydride polymers and silicon nanoparticles from liquid silanes*. Schriften des Forschungszentrums Jülich. Reihe Energie & Umwelt/ Energy & environment 423. Jülich: Forschungszentrum Jülich GmbH, Zentralbibliothek, Verlag, 2017. 132 pp.

[20] Torsten Bronger, Paul H. Wöbkenberg, Jan Wördenweber, Stefan Muthmann, Ulrich W. Paetzold, Vladimir Smirnov, Stephan Traut, et al. "Solution-Based Silicon in Thin-Film Solar Cells". In: *Advanced Energy Materials* 4.11 (2014), p. 1301871. DOI: 10.1002/aenm.201301871.

[21] Andrew P. Cádiz Bedini, Stefan Muthmann, Jan Flohre, Björn Thiele, Sabine Willbold, and Reinhard Carius. "Sonophotolytically Synthesized Silicon Nanoparticle-Polymer Composite Ink from a Commercially Available Lower Silane". In: *Macromolecular Chemistry and Physics* 217.15 (2016), pp. 1655–1660. DOI: 10.1002/macp.201600005.

[22] Tobias Sontheimer, Daniel Amkreutz, Katharina Schulz, Paul H. Wöbkenberg, Christian Guenther, Vadym Bakumov, Joachim Erz, et al. "Solution-Processed Crystalline Silicon Thin-Film Solar Cells". In: *Advanced Materials Interfaces* 1.3 (2014), p. 1300046. DOI: 10.1002/admi.201300046.

[23] Takashi Masuda, Akira Iwasaka, Hideyuki Takagishi, and Tatsuya Shimoda. "Polymeric precursor for solution-processed amorphous silicon carbide". In: *Journal of Materials Chemistry C* 3.47 (2015), pp. 12212–12219. DOI: 10.1039/C5TC03169A.

[24] Wenzhu Liu, Liping Zhang, Renfang Chen, Fanying Meng, Wanwu Guo, Jian Bao, and Zhengxin Liu. "Underdense a-Si:H film capped by a dense film as the passivation layer of a silicon heterojunction solar cell". In: *Journal of Applied Physics* 120.17 (2016), p. 175301. DOI: 10.1063/1.4966941.

[25] Hitoshi Sai, Hung-Jung Hsu, Po-Wei Chen, Pei-Ling Chen, and Takuya Matsui. "Intrinsic Amorphous Silicon Bilayers for Effective Surface Passivation in Silicon Heterojunction Solar Cells: A Comparative Study of Interfacial Layers". In: *physica status solidi (a)* 218.9 (2021), p. 2000743. DOI: 10.1002/pssa.202000743.

[26] Raghu V. K. Chavali, Stefaan De Wolf, and Muhammad A. Alam. "Device physics underlying silicon heterojunction and passivating-contact solar cells: A topical review". In: *Progress in Photovoltaics: Research and Applications* 26.4 (2018), pp. 241–260. DOI: 10.1002/pip.2959.

[27] Makoto Tanaka, Mikio Taguchi, Takao Matsuyama, Toru Sawada, Shinya Tsuda, Shoichi Nakano, Hiroshi Hanafusa, and Yukinori Kuwano. "Development of New a-Si/c-Si Heterojunction Solar Cells: ACJ-HIT (Artificially Constructed Junction-Heterojunction with Intrinsic Thin-Layer)". In: *Japanese Journal of Applied Physics* 31.11 (1992), p. 3518. DOI: 10.1143/JJAP.31.3518.

[28] Stefaan De Wolf, Antoine Descoeudres, Zachary C. Holman, and Christophe Ballif. "High-efficiency Silicon Heterojunction Solar Cells: A Review". In: *Green* 2.1 (2012), pp. 7–24. DOI: 10.1515/green-2011-0018.

[29] R. A. Street. *Hydrogenated amorphous silicon*. Cambridge solid state science series. Cambridge ; New York: Cambridge University Press, 1991. 417 pp.

[30] Junichi Seto, Keisuke Ohdaira, and Hideki Matsumura. "Catalytic doping of phosphorus and boron atoms on hydrogenated amorphous silicon films". In: *Japanese Journal of Applied Physics* 55.4 (2016), 04ES05. DOI: 10.7567/JJAP.55.04ES05.

[31] Yong Liu, Manuel Pomaska, Weiyuan Duan, Depeng Qiu, Shenghao Li, Andreas Lambertz, Alaaeldin Gad, et al. "Phosphorus Catalytic Doping on Intrinsic Silicon Thin Films for the Application in Silicon Heterojunction Solar Cells". In: *ACS Applied Materials & Interfaces* 12.50 (2020), pp. 56615–56621. DOI: 10.1021/acsami.0c17416.

[32] Weiyuan Duan, Gilbert Mains, Habtamu Tsegaye Gebrewold, Karsten Bittkau, Andreas Lambertz, Binbin Xu, Volker Lauterbach, et al. "Enhancing the Selectivity and Transparency of the Electron Contact in Silicon Heterojunction Solar Cells by Phosphorus Catalytic Doping". In: *Advanced Functional Materials* 34.3 (2024), p. 2310552. DOI: 10.1002/adfm.202310552.

[33] J. B. Rem, M. C. V. de Leuw, J. Holleman, and J. F. Verweij. "Furnace and rapid thermal crystallization of amorphous GexSi1-x and Si for thin film transistors". In: *Thin Solid Films*. European Materials Research Society 1996 Spring Meeting, Symposium B: Thin Film Materials for Large Area Electronics 296.1 (1997), pp. 152–156. DOI: 10.1016/S0040-6090(96)09355-8.

[34] Zhiyu Xu, Ke Tao, Shuai Jiang, Rui Jia, Wei Li, Ying Zhou, Zhi Jin, and Xinyu Liu. "Application of polycrystalline silicon carbide thin films as the passivating contacts for silicon solar cells". In: *Solar Energy Materials and Solar Cells* 206 (2020), p. 110329. DOI: 10.1016/j.solmat.2019.110329.

[35] Hassan Ali Bosan, Wolfhard Beyer, Uwe Breuer, Friedhelm Finger, Nelli Hambach, Maurice Nuys, Frank Pennartz, et al. "Investigation of Thermal Stability Effects of Thick Hydrogenated Amorphous Silicon Precursor Layers for Liquid-Phase Crystallized Silicon". In: *physica status solidi (a)* 218.9 (2021), p. 2000435. DOI: 10.1002/pssa.202000435.

[36] Jingming Zheng, Zhenhai Yang, Linna Lu, Mengmeng Feng, Yuyan Zhi, Yiran Lin, Mingdun Liao, et al. "Blistering-free polycrystalline silicon carbide films for double-sided passivating contact solar cells". In: *Solar Energy Materials and Solar Cells* 238 (2022), p. 111586. DOI: 10.1016/j.solmat.2022.111586.

[37] J. R. Partington. *A History of Chemistry*. London: Macmillan Education UK, 1964. DOI: 10.1007/978-1-349-00554-3.

[38] Ryoichi Ishihara, Jin Zhang, Miki Trifunovic, Michiel van der Zwan, Hideyuki Takagishi, Ryo Kawajiri, Tatsuya Shimoda, and C.I.M. Beenakker. "Single-Grain Si TFTs Fabricated by Liquid-Si and Long-Pulse Excimer-Laser". In: *ECS Transactions* 50.8 (2013), pp. 49–53. DOI: 10.1149/05008.0049ecst.

[39] Baolin Wu, Chunguang Chen, Dmitri L. Danilov, Rüdiger-A. Eichel, and Peter H. L. Notten. "All-Solid-State Thin Film Li-Ion Batteries: New Challenges, New Materials, and New Designs". In: *Batteries* 9.3 (2023), p. 186. DOI: 10.3390/batteries9030186.

[40] Hitoshi Sai, Po-Wei Chen, Hung-Jung Hsu, Takuya Matsui, Shota Nunomura, and Koji Matsubara. "Impact of intrinsic amorphous silicon bilayers in silicon heterojunction solar cells". In: *Journal of Applied Physics* 124.10 (2018), p. 103102. DOI: 10.1063/1.5045155.

[41] Paul A. Basore. “Defining terms for crystalline silicon solar cells”. In: *Progress in Photovoltaics: Research and Applications* 2.2 (1994), pp. 177–179. DOI: 10.1002/pip.4670020213.

[42] Simon M. Sze, Yiming Li, and Kwok K. Ng. *Physics of Semiconductor Devices*. 4th ed. Hoboken, New Jersey: John Wiley & Sons, 2021. 944 pp.

[43] W. Bludau, A. Onton, and W. Heinke. “Temperature dependence of the band gap of silicon”. In: *Journal of Applied Physics* 45.4 (1974), pp. 1846–1848. DOI: 10.1063/1.1663501.

[44] Robert Hull. *Properties of Crystalline Silicon*. IET, 1999. 1054 pp.

[45] Y. M. Yang, A. Yu, B. Hsu, W. C. Hsu, A. Yang, and C. W. Lan. “Development of high-performance multicrystalline silicon for photovoltaic industry”. In: *Progress in Photovoltaics: Research and Applications* 23.3 (2015), pp. 340–351. DOI: 10.1002/pip.2437.

[46] Xiaoning Ru, Minghao Qu, Jianqiang Wang, Tianyu Ruan, Miao Yang, Fuguo Peng, Wei Long, et al. “25.11% efficiency silicon heterojunction solar cell with low deposition rate intrinsic amorphous silicon buffer layers”. In: *Solar Energy Materials and Solar Cells* 215 (2020), p. 110643. DOI: 10.1016/j.solmat.2020.110643.

[47] Hao Lin, Miao Yang, Xiaoning Ru, Genshun Wang, Shi Yin, Fuguo Peng, Chengjian Hong, et al. “Silicon heterojunction solar cells with up to 26.81% efficiency achieved by electrically optimized nanocrystalline-silicon hole contact layers”. In: *Nature Energy* (2023), pp. 1–11. DOI: 10.1038/s41560-023-01255-2.

[48] Weiyuan Duan, Andreas Lambertz, Karsten Bittkau, Depeng Qiu, Kaifu Qiu, Uwe Rau, and Kaining Ding. “A route towards high-efficiency silicon heterojunction solar cells”. In: *Progress in Photovoltaics: Research and Applications* 30.4 (2022), pp. 384–392. DOI: 10.1002/pip.3493.

[49] Armin G Aberle. “Surface passivation of crystalline silicon solar cells: a review”. In: *Progress in Photovoltaics: Research and Applications* 8.5 (2000), pp. 473–487. DOI: 10.1002/1099-159X(200009/10)8:5<473::AID-PIP337>3.0.CO;2-D.

[50] Jonathon Dore, Rhett Evans, Ute Schubert, Bonne D. Eggleston, Daniel Ong, Kyung Kim, Jialiang Huang, et al. “Thin-film polycrystalline silicon solar cells formed by diode laser crystallisation”. In: *Progress in Photovoltaics: Research and Applications* 21.6 (2013), pp. 1377–1383. DOI: 10.1002/pip.2282.

[51] Bishal Kafle, Baljeet Singh Goraya, Sebastian Mack, Frank Feldmann, Sebastian Nold, and Jochen Rentsch. “TOPCon – Technology options for cost efficient industrial manufacturing”. In: *Solar Energy Materials and Solar Cells* 227 (2021), p. 111100. DOI: 10.1016/j.solmat.2021.111100.

[52] Ahmadreza Ghahremani and Aly E. Fathy. “High efficiency thin-film amorphous silicon solar cells”. In: *Energy Science & Engineering* 4.5 (2016), pp. 334–343. DOI: 10.1002/ese3.131.

[53] A. Lambertz, V. Smirnov, T. Merdzhanova, K. Ding, S. Haas, G. Jost, R.E.I. Schropp, et al. “Microcrystalline silicon–oxygen alloys for application in silicon solar cells and modules”. In: *Solar Energy Materials and Solar Cells* 119 (2013), pp. 134–143. DOI: 10.1016/j.solmat.2013.05.053.

[54] Thomas Grundler, Andreas Lambertz, and Friedhelm Finger. “N-type hydrogenated amorphous silicon oxide containing a microcrystalline silicon phase as an intermediate reflector in silicon thin film solar cells”. In: *physica status solidi c* 7.3 (2010), pp. 1085–1088. DOI: 10.1002/pssc.200982872.

[55] Chris G. Van De Walle and R. A. Street. “Silicon-Hydrogen Bonding and Hydrogen Diffusion in Amorphous Silicon”. In: *MRS Online Proceedings Library (OPL)* 377 (1995), p. 389. DOI: 10.1557/PROC-377-389.

[56] Hiroshi Umishio, Hitoshi Sai, Takashi Koida, and Takuya Matsui. “Nanocrystalline-silicon hole contact layers enabling efficiency improvement of silicon heterojunction solar cells: Impact of nanostructure evolution on solar cell performance”. In: *Progress in Photovoltaics: Research and Applications* 29.3 (2021), pp. 344–356. DOI: 10.1002/pip.3368.

[57] K Fukutani, M Kanbe, W Futako, B Kaplan, T Kamiya, C M Fortmann, and I Shimizu. “Band gap tuning of a-Si:H from 1.55 eV to 2.10 eV by intentionally promoting structural relaxation”. In: *Journal of non-crystalline solids* 227 (1998), pp. 63–67.

[58] R. Carius, F. Finger, U. Backhausen, M. Luysberg, P. Hapke, L. Houben, M. Otte, and H. Overhof. “Electronic Properties of Microcrystalline Silicon”. In: *MRS Online Proceedings Library (OPL)* 467 (1997), p. 283. DOI: 10.1557/PROC-467-283.

[59] Oleksandr Astakhov, Reinhard Carius, Friedhelm Finger, Yuri Petrusenko, Valery Borysenko, and Dmytro Barankov. “Relationship between defect density and charge carrier transport in amorphous and microcrystalline silicon”. In: *Physical Review B* 79.10 (2009), p. 104205. DOI: 10.1103/PhysRevB.79.104205.

[60] Bohdan Andriyevsky, Leszek Bychto, Aleksy Patryn, Ulrich Schade, Ljiljana Puskar, Alexander Veber, Nikolay Abrosimov, and Andrii I. Kashuba. “Investigations of free electrons in doped silicon crystals derived from Fourier transformed infrared measurements and ab initio calculations”. In: *Opto-Electronics Review* (2025), pp. 153756–153756. DOI: 10.24425/opelre.2025.153756.

[61] W. E. Spear and P. G. Le Comber. “Substitutional doping of amorphous silicon”. In: *Solid State Communications* 17.9 (1975), pp. 1193–1196. DOI: 10.1016/0038-1098(75)90284-7.

[62] R. A. Street, D. K. Biegelsen, and J. C. Knights. “Defect states in doped and compensated *a*-Si:H”. In: *Physical Review B* 24.2 (1981), pp. 969–984. DOI: 10.1103/PhysRevB.24.969.

[63] A. A. Langford, A. H. Mahan, M. L. Fleet, and J. Bender. “Effect of fluorine on the structural and electronic properties of a-Si:H:F”. In: *Physical Review B* 41.12 (1990), pp. 8359–8371. DOI: 10.1103/PhysRevB.41.8359.

[64] W. Beyer. “Structutral and electrical properties of silicon-based amorphous alloys”. In: *Journal of Non-Crystalline Solids* 97 (1987), pp. 1027–1034. DOI: 10.1016/0022-3093(87)90247-X.

[65] Z E. Smith and S. Wagner. “Band tails, entropy, and equilibrium defects in hydrogenated amorphous silicon”. In: *Physical Review Letters* 59.6 (1987), pp. 688–691. DOI: 10.1103/PhysRevLett.59.688.

[66] R. A. Street and K. Winer. “Defect equilibria in undoped a-Si:H”. In: *Physical Review B* 40.9 (1989), pp. 6236–6249. DOI: 10.1103/PhysRevB.40.6236.

[67] K. Winer. “Chemical-equilibrium description of the gap-state distribution in a-Si:H”. In: *Physical Review Letters* 63.14 (1989), pp. 1487–1490. DOI: 10.1103/PhysRevLett.63.1487.

[68] M. Stutzmann. “The defect density in amorphous silicon”. In: *Philosophical Magazine B* 60.4 (1989), pp. 531–546. DOI: 10.1080/13642818908205926.

[69] M. J. Powell and S. C. Deane. “Defect-pool model and the hydrogen density of states in hydrogenated amorphous silicon”. In: *Physical Review B* 53.15 (1996), pp. 10121–10132. DOI: 10.1103/PhysRevB.53.10121.

[70] Hiroyuki Fujiwara and Robert W. Collins, eds. *Spectroscopic Ellipsometry for Photovoltaics: Volume 1: Fundamental Principles and Solar Cell Characterization*. Vol. 212. Springer Series in Optical Sciences. Cham: Springer International Publishing, 2018. 594 pp. DOI: 10.1007/978-3-319-75377-5.

[71] Z Remeš, M Vaněček, P Torres, U Kroll, A.H Mahan, and R.S Crandall. “Optical determination of the mass density of amorphous and microcrystalline silicon layers with different hydrogen contents”. In: *Journal of Non-Crystalline Solids* 227-230 (1998), pp. 876–879. DOI: 10.1016/S0022-3093(98)00207-5.

[72] M. Cardona. “Vibrational Spectra of Hydrogen in Silicon and Germanium”. In: *physica status solidi (b)* 118.2 (1983), pp. 463–481. DOI: 10.1002/pssb.2221180202.

[73] G. Lucovsky, R. J. Nemanich, and J. C. Knights. “Structural interpretation of the vibrational spectra of a-Si:H alloys”. In: *Physical Review B* 19.4 (1979), pp. 2064–2073. DOI: 10.1103/PhysRevB.19.2064.

[74] A. H. M. Smets, T. Matsui, and M. Kondo. “Infrared analysis of the bulk silicon-hydrogen bonds as an optimization tool for high-rate deposition of microcrystalline silicon solar cells”. In: *Applied Physics Letters* 92.3 (2008), p. 033506. DOI: 10.1063/1.2837536.

[75] H. Fujiwara, Y. Toyoshima, M. Kondo, and A. Matsuda. “Interface-layer formation mechanism in a-Si:H thin-film growth studied by real-time spectroscopic ellipsometry and infrared spectroscopy”. In: *Physical Review B* 60.19 (1999), pp. 13598–13604. DOI: 10.1103/PhysRevB.60.13598.

[76] H. Wagner and W. Beyer. “Reinterpretation of the silicon-hydrogen stretch frequencies in amorphous silicon”. In: *Solid State Communications* 48.7 (1983), pp. 585–587. DOI: 10.1016/0038-1098(83)90520-3.

[77] Benedikt Fischer. “Investigations of the Practical Efficiency Limit of Silicon Heterojunction Solar Cells with the Focus on the Intrinsic Hydrogenated Amorphous Silicon Layers”. Master’s thesis. Aachen: RWTH Aachen University, 2022.

[78] H. Fritzsche. “Characterization of glow-discharge deposited a-Si:H”. In: *Solar Energy Materials* 3.4 (1980), pp. 447–501. DOI: 10.1016/0165-1633(80)90001-5.

[79] D. Jousse, E. Bustarret, and F. Boulitrop. “Disorder and defects in sputtered a-SiH from subgap absorption measurements”. In: *Solid State Communications* 55.5 (1985), pp. 435–438. DOI: 10.1016/0038-1098(85)90844-0.

[80] A. H. Mahan, P. Raboisson, and R. Tsu. “Influence of microstructure on the photoconductivity of glow discharge deposited amorphous SiC:H and amorphous SiGe:H alloys”. In: *Applied Physics Letters* 50.6 (1987), pp. 335–337. DOI: 10.1063/1.98192.

[81] V. A. Volodin and D. I. Koshelev. “Quantitative analysis of hydrogen in amorphous silicon using Raman scattering spectroscopy: Infrared and Raman spectroscopy study of a-Si:H films”. In: *Journal of Raman Spectroscopy* 44.12 (2013), pp. 1760–1764. DOI: 10.1002/jrs.4408.

[82] Benedikt Fischer, Andreas Lambertz, Maurice Nuys, Wolfhard Beyer, Weiyuan Duan, Karsten Bittkau, Kaining Ding, and Uwe Rau. “Insights into the Si—H Bonding Configuration at the Amorphous/Crystalline Silicon Interface of Silicon Heterojunction Solar Cells by Raman and FTIR Spectroscopy”. In: *Advanced Materials* 35.47 (2023), p. 2306351. DOI: 10.1002/adma.202306351.

[83] A. H. M. Smets and M. C. M. van de Sanden. “Relation of the Si-H stretching frequency to the nanostructural Si-H bulk environment”. In: *Physical Review B* 76.7 (2007), p. 073202. DOI: 10.1103/PhysRevB.76.073202.

[84] Arvind Shah. *Thin-Film Silicon Solar Cells*. EPFL Press, 2010. 472 pp.

[85] K.H. Kim, E.V. Johnson, A. Abramov, and P. Roca i Cabarrocas. “Light induced electrical and macroscopic changes in hydrogenated polymorphous silicon solar cells”. In: *EPJ Photovoltaics* 3 (2012), p. 30301. DOI: 10.1051/epjpv/2012005.

[86] W Beyer. “Diffusion and evolution of hydrogen in hydrogenated amorphous and microcrystalline silicon”. In: *Solar Energy Materials and Solar Cells* 78.1 (2003), pp. 235–267. DOI: 10.1016/S0927-0248(02)00438-5.

[87] W. Beyer and H. Wagner. “Determination of the hydrogen diffusion coefficient in hydrogenated amorphous silicon from hydrogen effusion experiments”. In: *Journal of Applied Physics* 53.12 (1982), pp. 8745–8750. DOI: 10.1063/1.330474.

[88] Wolfhard Beyer. “Chapter 5 - Hydrogen Phenomena in Hydrogenated Amorphous Silicon”. In: *Semiconductors and Semimetals*. Ed. by Norbert H. Nickel. Vol. 61. Semiconductors and Semimetals. Elsevier, 1999, pp. 165–239. DOI: 10.1016/S0080-8784(08)62707-6.

[89] W. Beyer and H. Wagner. “Hydrogen evolution from plasma-deposited amorphous silicon films”. In: *Le Journal de Physique Colloques* 42.C4 (1981), pp. 783–786. DOI: 10.1051/jphyscol:19814171.

[90] Jianqiang Wang, Xiaoning Ru, Tianyu Ruan, Yunfei Hu, Yongzhe Zhang, and Hui Yan. “Performance of heterojunction solar cells with different intrinsic a-Si:H thin layers deposited by RF- and VHF-PECVD”. In: *Journal of Materials Science: Materials in Electronics* 32.20 (2021), pp. 25327–25331. DOI: 10.1007/s10854-021-06991-3.

[91] Cuihua Shi, Jiajian Shi, Zisheng Guan, and Jia Ge. “Surface Cleaning and Passivation Technologies for the Fabrication of High-Efficiency Silicon Heterojunction Solar Cells”. In: *Materials* 16.8 (2023), p. 3144. DOI: 10.3390/ma16083144.

[92] Fiacre E. Rougieux, Chandany Sen, Malcolm Abbott, and Bram Hoex. “Light-activated surface passivation for more efficient silicon heterojunction solar cells: Origin, physics and stability”. In: *Solar Energy Materials and Solar Cells* 269 (2024), p. 112789. DOI: 10.1016/j.solmat.2024.112789.

[93] A. Descoeudres, L. Barraud, Stefaan De Wolf, B. Strahm, D. Lachenal, C. Guérin, Z. C. Holman, et al. “Improved amorphous/crystalline silicon interface passivation by hydrogen plasma treatment”. In: *Applied Physics Letters* 99.12 (2011), p. 123506. DOI: 10.1063/1.3641899.

[94] Stefan Rein. *Lifetime spectroscopy: a method of defect characterization in silicon for photovoltaic applications*. Springer series in materials science. Berlin Heidelberg New York: Springer, 2005. 489 pp.

[95] Jiyang Fan and Paul K. Chu. *Silicon Carbide Nanostructures: Fabrication, Structure, and Properties*. Engineering Materials and Processes. Cham: Springer International Publishing, 2014. DOI: 10.1007/978-3-319-08726-9.

[96] U. Coscia, G. Ambrosone, S. Lettieri, P. Maddalena, and S. Ferrero. "Microcrystalline silicon–carbon films deposited by silane–methane mixture highly diluted in hydrogen". In: *Thin Solid Films* 511-512 (2006), pp. 399–403. DOI: 10.1016/j.tsf.2005.12.084.

[97] Chih-Hsien Cheng, Chung-Lun Wu, Yung-Hsiang Lin, Wen-Long Yan, Min-Hsiung Shih, Jung-Hung Chang, Chih-I Wu, et al. "Strong optical nonlinearity of the nonstoichiometric silicon carbide". In: *Journal of Materials Chemistry C* 3.39 (2015), pp. 10164–10176. DOI: 10.1039/C5TC01791B.

[98] Dan Shan, Daoyuan Sun, Mingjun Tang, Ruihong Yang, Guangzhen Kang, Tao Tao, and Yunqing Cao. "Structures, Electronic Properties and Carrier Transport Mechanisms of Si Nano-Crystalline Embedded in the Amorphous SiC Films with Various Si/C Ratios". In: *Nanomaterials* 11.10 (2021), p. 2678. DOI: 10.3390/nano11102678.

[99] T. D. Gulden. "Mechanical Properties of Polycrystalline β-SiC". In: *Journal of the American Ceramic Society* 52.11 (1969), pp. 585–590. DOI: 10.1111/j.1151-2916.1969.tb15845.x.

[100] Noraini Marsi, Burhanuddin Yeop Majlis, Faisal Mohd-Yasin, Hafzaliza Erny Zainal Abidin, and Azrul Azlan Hamzah. "A Review: Properties of Silicon Carbide Materials in MEMS Application." In: *International Journal of Nanoelectronics & Materials* 13 (2020), pp. 113–128.

[101] Bernd Steinhauser, Frank Feldmann, Jana-Isabelle Polzin, Leonard Tutsch, Varun Arya, Benjamin Grübel, Andreas Fischer, et al. "Large Area TOPCon Technology Achieving 23.4% Efficiency". In: *2018 IEEE 7th World Conference on Photovoltaic Energy Conversion (WCPEC) (A Joint Conference of 45th IEEE PVSC, 28th PVSEC & 34th EU PVSEC)*. June 2018, pp. 1507–1510. DOI: 10.1109/PVSC.2018.8547683.

[102] Malte Köhler, Manuel Pomaska, Paul Procel, Rudi Santbergen, Alexandr Zamchiy, Bart Macco, Andreas Lambertz, et al. "A silicon carbide-based highly transparent passivating contact for crystalline silicon solar cells approaching efficiencies of 24%". In: *Nature Energy* 6.5 (2021), pp. 529–537. DOI: 10.1038/s41560-021-00806-9.

[103] Zhenyu Wan, Shujuan Huang, Martin A. Green, and Gavin Conibeer. "Rapid thermal annealing and crystallization mechanisms study of silicon nanocrystal in silicon carbide matrix". In: *Nanoscale Research Letters* 6.1 (2011), p. 129. DOI: 10.1186/1556-276X-6-129.

[104] Di Gao. "Characterization of residual strain in SiC films deposited using 1,3-disilabutane for MEMS application". In: *Journal of Micro/Nanolithography, MEMS, and MOEMS* 2.4 (2003), p. 259. DOI: 10.1117/1.1610478.

[105] J. Huran, P. Boháček, V. Sasinková, A. Kleinová, M. Mikolášek, and A.P. Kobzev. "Amorphous silicon carbide thin films doped with P or B for the photoelectrochemical water splitting devices". In: *Current Applied Physics* 34 (2022), pp. 101–106. DOI: 10.1016/j.cap.2021.11.014.

[106] Manabu Ishimaru, In-Tae Bae, Yoshihiko Hirotsu, Syo Matsumura, and Kurt E. Sickafus. "Structural Relaxation of Amorphous Silicon Carbide". In: *Physical Review Letters* 89.5 (2002), p. 055502. DOI: 10.1103/PhysRevLett.89.055502.

[107] J. Tersoff. "Chemical order in amorphous silicon carbide". In: *Physical Review B* 49.23 (1994), pp. 16349–16352. DOI: 10.1103/PhysRevB.49.16349.

[108] J. Bullot and M. P. Schmidt. "Physics of Amorphous Silicon–Carbon Alloys". In: *physica status solidi (b)* 143.2 (1987), pp. 345–418. DOI: 10.1002/pssb.2221430202.

[109] Wolfhard Beyer and Florian Einsele. "Hydrogen Effusion Experiments". In: *Advanced Characterization Techniques for Thin Film Solar Cells*. John Wiley & Sons, Ltd, 2016, pp. 569–595. DOI: 10.1002/9783527699025.ch20.

[110] S. S. Camargo, M. N. P. Carreño, and I. Pereyra. "Hydrogen effusion from highly-ordered near-stoichiometric a-SiC:H". In: *Journal of Non-Crystalline Solids*. Proceedings of the 20th International Conference on Amorphous and Microcrystalline Semiconductors 338-340 (2004), pp. 70–75. DOI: 10.1016/j.jnoncrysol.2004.02.024.

[111] Dong S Kim and Young H Lee. "Room-temperature deposition of a-SiC:H thin films by ion-assisted plasma-enhanced CVD". In: *Thin Solid Films* 283.1 (1996), pp. 109–118. DOI: 10.1016/0040-6090(96)08820-7.

[112] R. A. C. M. M. van Swaaij, A. J. M. Berntsen, W. G. J. H. M. van Sark, H. Herremans, J. Bezemer, and W. F. van der Weg. "Local structure and bonding states in a-$Si_{1-x}C_x$:H". In: *Journal of Applied Physics* 76.1 (1994), pp. 251–256. DOI: 10.1063/1.357136.

[113] Mark A. Petrich, Karen K. Gleason, and Jeffrey A. Reimer. "Structure and properties of amorphous hydrogenated silicon carbide". In: *Physical Review B* 36.18 (1987), pp. 9722–9731. DOI: 10.1103/PhysRevB.36.9722.

[114] Tsutomu Kaneko, Dai Nemoto, Atsushi Horiguchi, and Nobuaki Miyakawa. "FTIR analysis of a-SiC:H films grown by plasma enhanced CVD". In: *Journal of Crystal Growth* 275.1 (2005), e1097–e1101. DOI: 10.1016/j.jcrysgro.2004.11.128.

[115] S. W. King, M. French, J. Bielefeld, and W. A. Lanford. "Fourier transform infrared spectroscopy investigation of chemical bonding in low-k a-SiC:H thin films". In: *Journal of Non-Crystalline Solids* 357.15 (2011), pp. 2970–2983. DOI: 10.1016/j.jnoncrysol.2011.04.001.

[116] M. H. Brodsky, Manuel Cardona, and J. J. Cuomo. "Infrared and Raman spectra of the silicon-hydrogen bonds in amorphous silicon prepared by glow discharge and sputtering". In: *Physical Review B* 16.8 (1977), pp. 3556–3571. DOI: 10.1103/PhysRevB.16.3556.

[117] M Vetter. "IR-study of a-SiCx:H and a-SiCxNy:H films for c-Si surface passivation". In: *Thin Solid Films* 451-452 (2004), pp. 340–344. DOI: 10.1016/j.tsf.2003.10.125.

[118] Partha P. Dey and Alika Khare. "Tailoring of stoichiometry and band-tail emission in PLD a-SiC thin films by varying He deposition pressure". In: *SN Applied Sciences* 2.6 (2020), p. 1059. DOI: 10.1007/s42452-020-2865-2.

[119] Matthias Kuenle, Stefan Janz, Oliver Eibl, Christoph Berthold, Volker Presser, and Klaus-Georg Nickel. "Thermal annealing of SiC thin films with varying stoichiometry". In: *Materials Science and Engineering: B* 159-160 (2009), pp. 355–360. DOI: 10.1016/j.mseb.2008.10.056.

[120] Dengyuan Song, Eun-Chel Cho, Gavin Conibeer, Yidan Huang, Chris Flynn, and Martin A. Green. "Structural characterization of annealed $Si_{1-x}C_x$/SiC multilayers targeting formation of Si nanocrystals in a SiC matrix". In: *Journal of Applied Physics* 103.8 (2008), p. 083544. DOI: 10.1063/1.2909913.

[121] Alexander Eberst, Alexandr Zamchiy, Kaifu Qiu, Peter Winkel, Habtamu T. Gebrewold, Andreas Lambertz, Weiyuan Duan, et al. “Optical Optimization Potential of Transparent-Passivated Contacts in Silicon Solar Cells”. In: *Solar RRL* 6.6 (2022), p. 2101050. DOI: 10.1002/solr.202101050.

[122] Alexander Eberst, Andreas Lambertz, Weiyuan Duan, Vladimir Smirnov, Uwe Rau, and Kaining Ding. “Material Properties of Nanocrystalline Silicon Carbide for Transparent Passivating Contact Solar Cells”. In: *Solar RRL* 7.7 (2023), p. 2300013. DOI: 10.1002/solr.202300013.

[123] Hiroshi Harima. “Raman scattering characterization on SiC”. In: *Microelectronic Engineering* 83.1 (2006), pp. 126–129. DOI: 10.1016/j.mee.2005.10.037.

[124] Stefan Janz. “Amorphous Silicon Carbide for Photovoltaic Applications”. PhD thesis. Universität Konstanz, 2006. 227 pp.

[125] Charlotte Weiss, Manuel Schnabel, Slawomir Prucnal, Johannes Hofmann, Andreas Reichert, Tobias Fehrenbach, Wolfgang Skorupa, and Stefan Janz. “Formation of silicon nanocrystals in silicon carbide using flash lamp annealing”. In: *Journal of Applied Physics* 120.10 (2016), p. 105103. DOI: 10.1063/1.4962262.

[126] Florian Köhler. *Zur Mikrostruktur siliziumbasierter Dünnschichten für die Photovoltaik*. Forschungszentrum Jülich, 2012. 115 pp.

[127] Charlotte Weiss, Manuel Schnabel, Andreas Reichert, Philipp Löper, and Stefan Janz. “Structural and optical properties of silicon nanocrystals embedded in silicon carbide: Comparison of single layers and multilayer structures”. In: *Applied Surface Science* 351 (2015), pp. 550–557. DOI: 10.1016/j.apsusc.2015.05.153.

[128] Shinsuke Miyajima, Makoto Sawamura, Akira Yamada, and Makoto Konagai. “Properties of n-type hydrogenated nanocrystalline cubic silicon carbide films deposited by VHF-PECVD at a low substrate temperature”. In: *Journal of Non-Crystalline Solids*. Amorphous and Nanocrystalline Semiconductors 354.19 (2008), pp. 2350–2354. DOI: 10.1016/j.jnoncrysol.2007.09.085.

[129] Shinsuke Miyajima, Makoto Sawamura, Akira Yamada, and Makoto Konagai. “Effects of Hydrogen Dilution Ratio on Properties of Hydrogenated Nanocrystalline Cubic Silicon Carbide Films Deposited by Very High-Frequency Plasma-

Enhanced Chemical Vapor Deposition". In: *Japanese Journal of Applied Physics* 46.7 (2007), p. L693. DOI: 10.1143/JJAP.46.L693.

[130] Daisuke Hamashita, Shinsuke Miyajima, and Makoto Konagai. "Preparation of Al-doped hydrogenated nanocrystalline cubic silicon carbide by VHF-PECVD for heterojunction emitter of n-type crystalline silicon solar cells". In: *Solar Energy Materials and Solar Cells* 107 (2012), pp. 46–50. DOI: 10.1016/j.solmat.2012.07.029.

[131] Shinsuke Miyajima, Akira Yamada, and Makoto Konagai. "Characterization of Undoped, N- and P-Type Hydrogenated Nanocrystalline Silicon Carbide Films Deposited by Hot-Wire Chemical Vapor Deposition at Low Temperatures". In: *Japanese Journal of Applied Physics* 46.4 (2007), p. 1415. DOI: 10.1143/JJAP.46.1415.

[132] Tao Chen, Florian Köhler, Anna Heidt, Reinhard Carius, and Friedhelm Finger. "Hot-wire chemical vapor deposition prepared aluminum doped p-type microcrystalline silicon carbide window layers for thin film silicon solar cells". In: *Japanese Journal of Applied Physics* 53.5 (2014), 05FM04. DOI: 10.7567/JJAP.53.05FM04.

[133] F. Finger, O. Astakhov, T. Bronger, R. Carius, T. Chen, A. Dasgupta, A. Gordijn, et al. "Microcrystalline silicon carbide alloys prepared with HWCVD as highly transparent and conductive window layers for thin film solar cells". In: *Thin Solid Films* 517.12 (2009), pp. 3507–3512. DOI: 10.1016/j.tsf.2009.01.115.

[134] C. Sellmer, T. Bronger, W. Beyer, and R. Carius. "Thermopower and Hall-effect investigations of microcrystalline silicon films". In: *physica status solidi c* 7.3 (2010), pp. 670–673. DOI: 10.1002/pssc.200982776.

[135] A. A. Lebedev. "Deep level centers in silicon carbide: A review". In: *Semiconductors* 33.2 (1999), pp. 107–130. DOI: 10.1134/1.1187657.

[136] Onno Gabriel, Simon Kirner, Max Klingsporn, Felice Friedrich, Bernd Stannowski, and Rutger Schlatmann. "On the Plasma Chemistry During Plasma Enhanced Chemical Vapor Deposition of Microcrystalline Silicon Oxides: Plasma Chemistry During Microcrystalline Silicon Oxide PECVD". In: *Plasma Processes and Polymers* 12.1 (2015), pp. 82–91. DOI: 10.1002/ppap.201400114.

[137] M. Karaman, M. Aydın, S.H. Sedani, K. Ertürk, and R. Turan. "Low temperature crystallization of amorphous silicon by gold nanoparticle". In: *Microelectronic Engineering* 108 (2013), pp. 112–115. DOI: 10.1016/j.mee.2013.02.075.

[138] Jae Keun Seo, Yeun-Ho Joung, Young Park, and Won Seok Choi. "Substrate temperature effect on the SiC passivation layer synthesized by an RF magnetron sputtering method". In: *Thin Solid Films* 519.20 (2011), pp. 6654–6657. DOI: 10.1016/j.tsf.2011.04.052.

[139] G. Socol, A.C. Galca, D. Craciun, M. Hanna, C.R. Taylor, E. Lambers, and V. Craciun. "Pulsed laser deposition of nanocrystalline SiC films". In: *Applied Surface Science* 306 (2014), pp. 66–69. DOI: 10.1016/j.apsusc.2014.01.201.

[140] S. Yagi, T. Okabayashi, K. Abe, A. Yamada, and M. Konagai. "Novel carbon source (1,3-disilabutane) for the deposition of microcrystalline silicon carbon". In: *Proceedings of 3rd World Conference on Photovoltaic Energy Conversion, 2003.* Vol. 2. May 2003, 1687–1690 Vol.2.

[141] J. Woerdenweber, T. Merdzhanova, R. Schmitz, A. Mück, U. Zastrow, L. Niessen, A. Gordijn, et al. "Influence of base pressure and atmospheric contaminants on a-Si:H solar cell properties". In: *Journal of Applied Physics* 104.9 (2008), p. 094507. DOI: 10.1063/1.3009384.

[142] Xian Lin, Denis Endisch, Xiaomeng Chen, and Alain Kaloyeros. "Silicon Nitride Films Deposited by Atmospheric Pressure Chemical Vapor Deposition". In: *MRS Proceedings* 495 (1997), p. 107. DOI: 10.1557/PROC-495-107.

[143] Tatsuya Shimoda. *Nanoliquid Processes for Electronic Devices: Developments of Inorganic Functional Liquid Materials and Their Processing.* Singapore: Springer, 2019. DOI: 10.1007/978-981-13-2953-1.

[144] Pham Tien Lam, Ayumu Sugiyama, Takashi Masuda, Tatsuya Shimoda, Nobuo Otsuka, and Dam Hieu Chi. "Ab-initio study of intermolecular interaction and structure of liquid cyclopentasilane". In: *Chemical Physics* 400 (2012), pp. 59–64. DOI: 10.1016/j.chemphys.2012.02.010.

[145] Roya Maboudian, Christopher S. Roper, Carlo Carraro, and Roger T. Howe. "Silicon Carbide Thin Films using 1,3-Disilabutane Single Precursor for MEMS Applications - A Review". In: *ECS Transactions* 3.10 (2006), pp. 267–280. DOI: 10.1149/1.2357267.

[146] Konstantin Pokhodnya, Joseph Sandstrom, Chris Olson, Xuliang Dai, Philip R. Boudjouk, and Douglas L. Schulz. "Comparative study of low-temperature PECVD Of amorphous silicon using mono-, di-, trisilane and cyclohexasilane". In: *2009 34th IEEE Photovoltaic Specialists Conference (PVSC)*. Philadelphia, PA, USA: IEEE, June 2009, pp. 001758–001760. DOI: 10.1109/PVSC.2009.5411459.

[147] Wenhui Du, Xiesen Yang, Henry Povolny, Xianbo Liao, and Xunming Deng. "Impact of hydrogen dilution on microstructure and optoelectronic properties of silicon films deposited using trisilane". In: *Journal of Physics D: Applied Physics* 38.6 (2005), pp. 838–842. DOI: 10.1088/0022-3727/38/6/008.

[148] Takashi Masuda, Yasuo Matsuki, and Tatsuya Shimoda. "Pyrolytic transformation from polydihydrosilane to hydrogenated amorphous silicon film". In: *Thin Solid Films* 520.21 (2012), pp. 6603–6607. DOI: 10.1016/j.tsf.2012.07.028.

[149] Zhongrong Shen, Takashi Masuda, Hideyuki Takagishi, Keisuke Ohdaira, and Tatsuya Shimoda. "Fabrication of High-Quality Amorphous Silicon Film from Cyclopentasilane Vapor Deposition between Two Parallel Substrates". In: (2012), p. 6.

[150] L.L. Snead and S.J. Zinkle. "Structural relaxation in amorphous silicon carbide". In: *Nuclear Instruments and Methods in Physics Research Section B: Beam Interactions with Materials and Atoms* 191.1 (2002), pp. 497–503. DOI: 10.1016/S0168-583X(02)00599-2.

[151] L. A Okada, A. C Dillon, A. W Ott, and S. M George. "Adsorption and decomposition of 1,4-disilabutane ($SiH_3CH_2CH_2SiH_3$) on Si(100) 2×1 and porous silicon surfaces". In: *Surface Science* 418.2 (1998), pp. 353–366. DOI: 10.1016/S0039-6028(98)00653-0.

[152] W.L.M. Weerts, M.H.J.M. de Croon, and G.B. Marin. "The adsorption of silane, disilane and trisilane on polycrystalline silicon: a transient kinetic study". In: *Surface Science* 367.3 (1996), pp. 321–339. DOI: 10.1016/S0039-6028(96)00876-X.

[153] A. Gouyé, O. Kermarrec, A. Halimaoui, Y. Campidelli, D. Rouchon, M. Burdin, P. Holliger, and D. Bensahel. "Low-temperature RPCVD of Si, SiGe alloy, and $Si_{1-y}C_y$ films on Si substrates using trisilane (Silcore®)". In: *Journal of Crystal Growth* 311.13 (2009), pp. 3522–3527. DOI: 10.1016/j.jcrysgro.2009.04.011.

[154] A. J. Vanderwielen, M. A. Ring, and H. E. O'Neal. "Kinetics of the thermal decomposition of methyldisilane and trisilane". In: *Journal of the American Chemical Society* 97.5 (1975), pp. 993–998. DOI: 10.1021/ja00838a008.

[155] Matty Caymax, Frederik Leys, Jérôme Mitard, Koen Martens, Lijun Yang, Geoffrey Pourtois, Wilfried Vandervorst, et al. "The Influence of the Epitaxial Growth Process Parameters on Layer Characteristics and Device Performance in Si-Passivated Ge pMOSFETs". In: *Journal of The Electrochemical Society* 156.12 (2009), H979. DOI: 10.1149/1.3240880.

[156] Hwanyeol Park and Ho Jun Kim. "Adsorption of silane radicals governing plasma silicon deposition with dilution gases". In: *Physics of Fluids* 37.4 (2025), p. 043607. DOI: 10.1063/5.0260990.

[157] Shyam Ramalingam, Dimitrios Maroudas, and Eray S. Aydil. "Atomistic simulation study of the interactions of SiH_3 radicals with silicon surfaces". In: *Journal of Applied Physics* 86.5 (1999), pp. 2872–2888. DOI: 10.1063/1.371136.

[158] Stephen P Walch, Shyam Ramalingam, Saravanapriyan Sriraman, Eray S Aydil, and Dimitrios Maroudas. "Mechanisms and energetics of SiH_3 adsorption on the pristine Si(0 0 1)-(2×1) surface". In: *Chemical Physics Letters* (2001).

[159] Mayur S. Valipa, Eray S. Aydil, and Dimitrios Maroudas. "Atomistic calculation of the SiH_3 surface reactivity during plasma deposition of amorphous silicon thin films". In: *Surface Science* 572.2 (2004), pp. L339–L347. DOI: 10.1016/j.susc.2004.08.029.

[160] W.M.M Kessels, R.J Severens, M.C.M van de Sanden, and D.C Schram. "Temperature and growth-rate effects on the hydrogen incorporation in a-Si:H". In: *Journal of Non-Crystalline Solids* 227-230 (1998), pp. 133–137. DOI: 10.1016/S0022-3093(98)00028-3.

[161] Akihisa Matsuda. "Growth mechanism of microcrystalline silicon obtained from reactive plasmas". In: *Thin Solid Films* 337.1 (1999), pp. 1–6. DOI: 10.1016/S0040-6090(98)01165-1.

[162] D. Li, G. L. Liu, Y. Yang, J. H. Wu, and Z. R. Huang. "Nucleation and Growth Mechanism of Si Amorphous Film Deposited by PIAD". In: *Journal of Nanomaterials* 2013 (2013), pp. 1–7. DOI: 10.1155/2013/383867.

[163] B. Vincent, R. Loo, W. Vandervorst, G. Brammertz, and M. Caymax. "Low temperature Si homo-epitaxy by reduced pressure chemical vapor deposition using dichlorosilane, silane and trisilane". In: *Journal of Crystal Growth* 312.19 (2010), pp. 2671–2676. DOI: 10.1016/j.jcrysgro.2010.06.013.

[164] Benedikt Fischer, Maurice Nuys, Oleksandr Astakhov, Stefan Haas, Michael Schaaf, Astrid Besmehn, Peter Jakes, et al. "Advanced atmospheric pressure CVD of a-Si:H using pure and cyclooctane-diluted trisilane as precursors". In: *Sustainable Energy & Fuels* (2024). DOI: 10.1039/D4SE01308E.

[165] Paola Pisciella and Mario Pelino. "FTIR spectroscopy investigation of the crystallisation process in an iron rich glass". In: *Journal of the European Ceramic Society* 25.11 (2005), pp. 1855–1861. DOI: 10.1016/j.jeurceramsoc.2004.06.012.

[166] A. A. Langford, M. L. Fleet, B. P. Nelson, W. A. Lanford, and N. Maley. "Infrared absorption strength and hydrogen content of hydrogenated amorphous silicon". In: *Physical Review B* 45.23 (1992), pp. 13367–13377. DOI: 10.1103/PhysRevB.45.13367.

[167] W. Beyer and M.S. Abo Ghazala. "Absorption Strengths of Si-H Vibrational Modes in Hydrogenated Silicon". In: *MRS Proceedings* 507 (1998), p. 601. DOI: 10.1557/PROC-507-601.

[168] Jacob Filik, Mark D. Frogley, Jacek K. Pijanka, Katia Wehbe, and Gianfelice Cinque. "Electric field standing wave artefacts in FTIR micro-spectroscopy of biological materials". In: *The Analyst* 137.4 (2012), p. 853. DOI: 10.1039/c2an15995c.

[169] P. Danesh, B. Pantchev, and B. Schmidt. "Infrared absorption strengths of ion-implanted hydrogenated amorphous silicon". In: *Thin Solid Films* 516.10 (2008), pp. 3383–3386. DOI: 10.1016/j.tsf.2007.10.068.

[170] M. Z. Burrows, U. K. Das, R. L. Opila, S. De Wolf, and R. W. Birkmire. "Role of hydrogen bonding environment in a-Si:H films for c-Si surface passivation". In: *Journal of Vacuum Science & Technology A: Vacuum, Surfaces, and Films* 26.4 (2008), pp. 683–687. DOI: 10.1116/1.2897929.

[171] S.N. Granata, T. Bearda, F. Dross, I. Gordon, J. Poortmans, and R. Mertens. "Effect of an in-Situ H2 Plasma Pretreatment on the Minority Carrier lifetime

of a-Si:H(i) Passivated Crystalline Silicon". In: *Energy Procedia* 27 (2012), pp. 412–418. DOI: 10.1016/j.egypro.2012.07.086.

[172] G. Lucovsky, J. Yang, S. S. Chao, J. E. Tyler, and W. Czubatyj. "Oxygen-bonding environments in glow-discharge-deposited amorphous silicon-hydrogen alloy films". In: *Physical Review B* 28.6 (1983), pp. 3225–3233. DOI: 10.1103/PhysRevB.28.3225.

[173] D. V. Tsu, G. Lucovsky, and B. N. Davidson. "Effects of the nearest neighbors and the alloy matrix on Si–H stretching vibrations in the amorphous SiO_r:H (0 < r < 2) alloy system". In: *Physical Review B* 40.3 (1989), pp. 1795–1805. DOI: 10.1103/PhysRevB.40.1795.

[174] B. J. Hinds, F. Wang, D. M. Wolfe, C. L. Hinkle, and G. Lucovsky. "Investigation of postoxidation thermal treatments of Si/SiO_2 interface in relationship to the kinetics of amorphous Si suboxide decomposition". In: *Journal of Vacuum Science & Technology B* 16.4 (1998), pp. 2171–2176. DOI: 10.1116/1.590302.

[175] L X Yi, J Heitmann, R Scholz, and M Zacharias. "Phase separation of thin SiO layers in amorphous SiO/SiO_2 superlattices during annealing". In: *Journal of Physics: Condensed Matter* 15.39 (2003), S2887–S2895. DOI: 10.1088/0953-8984/15/39/012.

[176] G. Lucovsky. "A structural interpretation of the infrared absorption spectra of a-Si:H:O alloys". In: *Solar Energy Materials* 8.1 (1982), pp. 165–175. DOI: 10.1016/0165-1633(82)90060-0.

[177] A.O. Zamchiy, E.A. Baranov, I.E. Merkulova, S.Ya. Khmel, and E.A. Maximovskiy. "Determination of the oxygen content in amorphous SiO_x thin films". In: *Journal of Non-Crystalline Solids* 518 (2019), pp. 43–50. DOI: 10.1016/j.jnoncrysol.2019.05.015.

[178] I M Joni, L Nulhakim, M Vanitha, and C Panatarani. "Characteristics of crystalline silica (SiO_2) particles prepared by simple solution method using sodium silicate (Na_2 SiO_3) precursor". In: *Journal of Physics: Conference Series* 1080 (2018), p. 012006. DOI: 10.1088/1742-6596/1080/1/012006.

[179] E Moncada, R Quijada, and J Retuert. "Nanoparticles prepared by the sol–gel method and their use in the formation of nanocomposites with polypropylene". In: *Nanotechnology* 18.33 (2007), p. 335606. DOI: 10.1088/0957-4484/18/33/335606.

[180] Bernhard Schrader. “Chemische Anwendungen der Raman-Spektroskopie”. In: *Angewandte Chemie* 85.21 (1973), pp. 925–950. DOI: 10.1002/ange.19730852102.

[181] Dionisio Bermejo and Manuel Cardona. “Raman scattering in pure and hydrogenated amorphous germanium and silicon”. In: *Journal of Non-Crystalline Solids* 32.1 (1979), pp. 405–419. DOI: 10.1016/0022-3093(79)90085-1.

[182] Kawtar Belrhiti Alaoui, Saida Laalioui, Zakaria Naimi, Badr Ikken, and Abdelkader Outzourhit. “Photovoltaic and impedance spectroscopy characterization of single-junction a-Si:H p–i–n solar cells deposited by simple shadow masking techniques using PECVD”. In: *AIP Advances* 10.9 (2020), p. 095315. DOI: 10.1063/5.0022889.

[183] Dengyuan Song, Eun-Chel Cho, Young-Hyun Cho, Gavin Conibeer, Yidan Huang, Shujuan Huang, and Martin A. Green. “Evolution of Si (and SiC) nanocrystal precipitation in SiC matrix”. In: *Thin Solid Films* 516.12 (2008), pp. 3824–3830. DOI: 10.1016/j.tsf.2007.06.150.

[184] N. I. Fainer, A. G. Plekhanov, A. N. Golubenko, Yu M. Rumyantsev, V. I. Rakhlin, E. A. Maximovski, and V. R. Shayapov. “PECVD Synthesis of Silicon Carbonitride Layers Using Methyltris(diethylamino)silane as the New Single-Source Precursor”. In: *ECS Journal of Solid State Science and Technology* 4.1 (2014), N3153. DOI: 10.1149/2.0201501jss.

[185] H.E. Bellis and E.J. Slowinski. “The vibrational spectra and structure of cyclooctane”. In: *Spectrochimica Acta* 15 (1959), pp. 1103–1117. DOI: 10.1016/S0371-1951(59)80413-6.

[186] V. Heera, F. Prokert, N. Schell, H. Seifarth, W. Fukarek, M. Voelskow, and W. Skorupa. “Density and structural changes in SiC after amorphization and annealing”. In: *Applied Physics Letters* 70.26 (1997), pp. 3531–3533. DOI: 10.1063/1.119223.

[187] Claus Malten. *Pulsed electron spin resonance of amorphous and microcrystalline semiconductors*. Berichte des Forschungszentrums Jülich 3273. Jülich: Forschungszentrum Jülich GmbH, 1996. 94 pp.

[188] J. C. Vickerman and David Briggs. *ToF-SIMS: Materials Analysis by Mass Spectrometry*. Chichester: IM Publications, 2013. 742 pp.

[189] E Böhmer and H Lüth. "Photoelectron spectroscopy studies of microcrystalline/amorphous silicon interfaces". In: *Journal of Non-Crystalline Solids* 266-269 (2000), pp. 1038–1043. DOI: 10.1016/S0022-3093(99)00901-1.

[190] Bruno Alessi, Manuel Macias-Montero, Chiranjeevi Maddi, Paul Maguire, Vladimir Svrcek, and Davide Mariotti. "Bridging energy bands to the crystalline and amorphous states of Si QDs". In: *Faraday Discussions* 222 (2020), pp. 390–404. DOI: 10.1039/C9FD00103D.

[191] F. Dannhäuser. "Die abhängigkeit der trägerbeweglichkeit in silizium von der konzentration der freien ladungsträger—I". In: *Solid-State Electronics* 15.12 (1972), pp. 1371–1375. DOI: 10.1016/0038-1101(72)90131-1.

[192] J. Krausse. "Die abhängigkeit der trägerbeweglichkeit in silizium von der konzentration der freien ladungsträger—II". In: *Solid-State Electronics* 15.12 (1972), pp. 1377–1381. DOI: 10.1016/0038-1101(72)90132-3.

[193] Won-Eui Hong and Jae-Sang Ro. "Kinetics of solid phase crystallization of amorphous silicon analyzed by Raman spectroscopy". In: *Journal of Applied Physics* 114.7 (2013), p. 073511. DOI: 10.1063/1.4818949.

[194] Hideki Matsumura and Keisuke Ohdaira. "Cat-CVD (Catalytic-CVD); Its Fundamentals and Application". In: *ECS Transactions* 25.8 (2009), p. 53. DOI: 10.1149/1.3207575.

[195] Hideki Matsumura, Taro Hayakawa, Tatsunori Ohta, Yuki Nakashima, Motoharu Miyamoto, Trinh Cham Thi, Koichi Koyama, and Keisuke Ohdaira. "Cat-doping: Novel method for phosphorus and boron shallow doping in crystalline silicon at 80 °C". In: *Journal of Applied Physics* 116.11 (2014), p. 114502. DOI: 10.1063/1.4895635.

[196] Yoo Sakuma, Keisuke Ohdaira, Takashi Masuda, Hideyuki Takagishi, Zhongrong Shen, and Tatsuya Shimoda. "Effect of annealing and hydrogen radical treatment on the structure of solution-processed hydrogenated amorphous silicon films". In: *Japanese Journal of Applied Physics* 53.4 (2014), 04ER07. DOI: 10.7567/JJAP.53.04ER07.

[197] Takashi Masuda, Naoya Sotani, Hiroki Hamada, Yasuo Matsuki, and Tatsuya Shimoda. "Fabrication of solution-processed hydrogenated amorphous silicon single-junction solar cells". In: *Applied Physics Letters* 100.25 (2012), p. 253908. DOI: 10.1063/1.4730614.

[198] Leila Alipour, Mai Hamamoto, Satoru Nakashima, Rika Harui, Masanari Furiki, and Osamu Oku. "Infrared Microspectroscopy of Bionanomaterials (Diatoms) with Careful Evaluation of Void Effects". In: *Applied Spectroscopy* 70.3 (2016), pp. 427–442. DOI: 10.1177/0003702815626665.

[199] Yoshinori Ashida, Yasuyoshi Mishima, Masataka Hirose, Yukio Osaka, and Kenichi Kojima. "Hydrogenated Amorphous Silicon Produced by Pyrolysis of Disilane in a Hot Wall Reactor". In: *Japanese Journal of Applied Physics* 23 (1984), pp. L129–L131. DOI: 10.1143/JJAP.23.L129.

[200] W. Beyer. "Infrared absorption and hydrogen effusion of hydrogenated amorphous silicon-oxide films". In: *Journal of Non-Crystalline Solids* 266-269 (2000), pp. 845–849. DOI: 10.1016/S0022-3093(99)00853-4.

[201] S. Yasuda, T. Chikyow, S. Inoue, N. Matsuki, K. Miyazaki, S. Nishio, M. Kakihana, and H. Koinuma. "Pulsed laser deposition of photosensitive a-Si thin films". In: *Applied Physics A* 69.1 (1999), S925–S927. DOI: 10.1007/s003390051560.

[202] Kyung Ha Lee, Jae Ho Yoo, Byeong Yeon Moon, Jae Hoon Jung, Jin Jang, S.M. Pietruszko, Min Koo Han, and Hyuk Ryeol Park. "Low temperature fabrication of APCVD a-Si thin film transistors with ion doped layer". In: *Journal of Non-Crystalline Solids* 198-200 (1996), pp. 1141–1145. DOI: 10.1016/0022-3093(96)00065-8.

[203] Srinivasan Guruvenket, Justin M. Hoey, Kenneth J. Anderson, Matthew T. Frohlich, Robert A. Sailer, and Philip Boudjouk. "Aerosol assisted atmospheric pressure chemical vapor deposition of silicon thin films using liquid cyclic hydrosilanes". In: *Thin Solid Films* 589 (2015), pp. 465–471. DOI: 10.1016/j.tsf.2015.05.069.

[204] W Beyer and H Wagner. "The role of hydrogen in a-Si:H — results of evolution and annealing studies". In: *Journal of Non-Crystalline Solids*. Proceedings of the Tenth International Conference on Amorphous and Liquid Semiconductors 59-60 (1983), pp. 161–168. DOI: 10.1016/0022-3093(83)90547-1.

[205] C. Smit, R. A. C. M. M. van Swaaij, H. Donker, A. M. H. N. Petit, W. M. M. Kessels, and M. C. M. van de Sanden. "Determining the material structure of microcrystalline silicon from Raman spectra". In: *Journal of Applied Physics* 94.5 (2003), pp. 3582–3588. DOI: 10.1063/1.1596364.

[206] J. M. Shannon and A. D. Annis. "Current-induced defect conductivity in hydrogenated silicon-rich amorphous silicon nitride". In: *Philosophical Magazine Letters* 72.5 (1995), pp. 323–329. DOI: 10.1080/09500839508242470.

[207] Wolfhard Beyer, Gudrun Andrä, Joachim Bergmann, Uwe Breuer, Friedhelm Finger, Annett Gawlik, Stefan Haas, et al. "Temperature and hydrogen diffusion length in hydrogenated amorphous silicon films on glass while scanning with a continuous wave laser at 532 nm wavelength". In: *Journal of Applied Physics* 124.15 (2018), p. 153103. DOI: 10.1063/1.5038090.

[208] Toshihiro Kinoshita, Masao Isomura, Yoshihiro Hishikawa Yoshihiro Hishikawa, and Shinya Tsuda Shinya Tsuda. "Influence of Oxygen and Nitrogen in the Intrinsic Layer of a-Si:H Solar Cells". In: *Japanese Journal of Applied Physics* 35.7 (1996), p. 3819. DOI: 10.1143/JJAP.35.3819.

[209] Hideki Tanaka, Haruo Iwasawa, Daohai Wang, Naoyuki Toyoda, Takashi Aoki, Ichio Yudasaka, Yasuo Matsuki, et al. "Spin-on n-Type Silicon Films Using Phosphorous-doped Polysilanes". In: *Japanese Journal of Applied Physics* 46.10 (2007), p. L886. DOI: 10.1143/JJAP.46.L886.

[210] A. H. M. Smets, W. M. M. Kessels, and M. C. M. van de Sanden. "Vacancies and voids in hydrogenated amorphous silicon". In: *Applied Physics Letters* 82.10 (2003), pp. 1547–1549. DOI: 10.1063/1.1559657.

[211] A. C. Ferrari, S. E. Rodil, and J. Robertson. "Interpretation of infrared and Raman spectra of amorphous carbon nitrides". In: *Physical Review B* 67.15 (2003), p. 155306. DOI: 10.1103/PhysRevB.67.155306.

[212] A. Morimoto, T. Miura, M. Kumeda, and T. Shimizu. "Defects in hydrogenated amorphous silicon-carbon alloy films prepared by glow discharge decomposition and sputtering". In: *Journal of Applied Physics* 53.11 (1982), pp. 7299–7305. DOI: 10.1063/1.329879.

[213] Debjit Kar and Debajyoti Das. "Conducting wide band gap nc-Si/a-SiC:H films for window layers in nc-Si solar cells". In: *Journal of Materials Chemistry A* 1.46 (2013), pp. 14744–14753. DOI: 10.1039/C3TA12878D.

[214] Kyungsoo Jang, Youngkuk Kim, Pham Duy Phong, Younjung Lee, Joonghyun Park, and Junsin Yi. "Improvement of Electrical Performance in P-Channel LTPS Thin-Film Transistor with a-Si:H Surface Passivation". In: *Materials* 12.1 (2019), p. 161. DOI: 10.3390/ma12010161.

[215] Chung-Mo Yang, Dong-Seok Kim, Seong-Gil Lee, Jae-Hoon Lee, Yong Soo Lee, and Jung-Hee Lee. "Improvement in Electrical and Optical Performances of GaN-Based LED With SiO_2/Al_2O_3 Double Dielectric Stack Layer". In: *IEEE Electron Device Letters* 33.4 (2012), pp. 564–566. DOI: 10.1109/LED.2012.2185675.

[216] Benedikt Fischer, Wolfhard Beyer, Andreas Lambertz, Maurice Nuys, Weiyuan Duan, Kaining Ding, and Uwe Rau. "The Microstructure of Underdense Hydrogenated Amorphous Silicon and its Application to Silicon Heterojunction Solar Cells". In: *Solar RRL* 7.10 (2023), p. 2300103. DOI: 10.1002/solr.202300103.

[217] Benedikt Fischer, Hitoshi Sai, Zhihao Xu, Maurice Nuys, Andreas Lambertz, Volker Lauterbach, Kaining Ding, et al. "Light soaking of silicon heterojunction solar cells by applying high-intensity line-shaped laser scans". In: *Cell Reports Physical Science* 6.5 (2025), p. 102558. DOI: 10.1016/j.xcrp.2025.102558.

[218] Jordi Veirman, Arnaud Joel Kinfack Leoga, Léo Basset, Wilfried Favre, Olivier Bonino, Antonin Le Priol, Névine Rochat, and Denis Rouchon. "Understanding the improvement of silicon heterojunction solar cells under light soaking". In: *AIP Conference Proceedings* 2487.1 (2022), p. 020017. DOI: 10.1063/5.0089284.

[219] Shaojuan Bao, Liyou Yang, Jin Huang, Yanhui Bai, Ji Yang, Jilei Wang, Linfeng Lu, et al. "The rapidly reversible processes of activation and deactivation in amorphous silicon heterojunction solar cell under extensive light soaking". In: *Journal of Materials Science: Materials in Electronics* 32.4 (2021), pp. 4045–4052. DOI: 10.1007/s10854-020-05146-0.

[220] Matthew Wright, Anastasia H. Soeriyadi, Moonyong Kim, Brendan Wright, Bruno Vicari Stefani, Dmitry Andronikov, Ilia Nyapshaev, et al. "On the kinetics of high intensity illuminated annealing of n-type SHJ solar cells: 0.4%abs efficiency gain in one second". In: *Solar Energy Materials and Solar Cells* 248 (2022), p. 112039. DOI: 10.1016/j.solmat.2022.112039.

[221] Eiji Kobayashi, Stefaan De Wolf, Jacques Levrat, Gabriel Christmann, Antoine Descoeudres, Sylvain Nicolay, Matthieu Despeisse, et al. "Light-induced performance increase of silicon heterojunction solar cells". In: *Applied Physics Letters* 109.15 (2016), p. 153503. DOI: 10.1063/1.4964835.

[222] Cheng Guo, Keisuke Ohdaira, Hideyuki Takagishi, Takashi Masuda, Zhongrong Shen, and Tatsuya Shimoda. "Formation of amorphous silicon passivation films with high stability against postannealing, air exposure, and light soaking using liquid silicon". In: *Japanese Journal of Applied Physics* 55.4 (2016), 04ES12. DOI: 10.7567/JJAP.55.04ES12.

[223] Mathias Mews, Christoph Mader, Stephan Traut, Tobias Sontheimer, Odo Wunnicke, Lars Korte, and Bernd Rech. "Solution-processed amorphous silicon surface passivation layers". In: *Applied Physics Letters* 105.12 (2014), p. 122113. DOI: 10.1063/1.4896687.

[224] Christoph Luderer, Dilara Kurt, Anamaria Moldovan, Martin Hermle, and Martin Bivour. "Intrinsic layer modification in silicon heterojunctions: Balancing transport and surface passivation". In: *Solar Energy Materials and Solar Cells* 238 (2022), p. 111412. DOI: 10.1016/j.solmat.2021.111412.

[225] Jeong-Ho An, Joon-Ho Oh, Kyung Taek Jeong, Ohmin Kwon, Soong Ju Oh, Kyoung-Ho Kim, Sun-Wook Kim, et al. "Silicon–Hydrogen Bonding Configuration Modified by Layer Stacking Sequence in Silicon Heterojunction Solar Cells". In: *ACS Applied Energy Materials* 5.12 (2022), pp. 15029–15037. DOI: 10.1021/acsaem.2c02668.

[226] A. Szekeres, M. Gartner, F. Vasiliu, M. Marinov, and G. Beshkov. "Crystallization of a-Si:H films by rapid thermal annealing". In: *Journal of Non-Crystalline Solids* 227-230 (1998), pp. 954–957. DOI: 10.1016/S0022-3093(98)00263-4.

[227] A. B. Sproul and M. A. Green. "Improved value for the silicon intrinsic carrier concentration from 275 to 375 K". In: *Journal of Applied Physics* 70.2 (1991), pp. 846–854. DOI: 10.1063/1.349645.

[228] Yukun Gao and Penggang Yin. "Origin of asymmetric broadening of Raman peak profiles in Si nanocrystals". In: *Scientific Reports* 7.1 (2017), p. 43602. DOI: 10.1038/srep43602.

[229] M. Peisl and A.W. Wieder. "Conductivity in polycrystalline silicon—physics and rigorous numerical treatment". In: *IEEE Transactions on Electron Devices* 30.12 (1983), pp. 1792–1797. DOI: 10.1109/T-ED.1983.21447.

[230] W. R. Thurber, R. L. Mattis, Y. M. Liu, and J. J. Filliben. "Resistivity-Dopant Density Relationship for Phosphorus-Doped Silicon". In: *Journal of The Electrochemical Society* 127.8 (1980), p. 1807. DOI: 10.1149/1.2130006.

[231] W. R. Thurber, R. L. Mattis, Y. M. Liu, and J. J. Filliben. "Resistivity-Dopant Density Relationship for Boron-Doped Silicon". In: *Journal of The Electrochemical Society* 127.10 (1980), pp. 2291–2294. DOI: 10.1149/1.2129394.

[232] Benedikt Fischer, Maurice Nuys, Stefan Haas, Oliver Thimm, Gunnar Schöpe, Pascal Foucart, Astrid Besmehn, and Uwe Rau. "Synthesis and Characterization of Nitrogen-Doped Crystallized SiC Films from Liquid Precursors". In: *ACS Applied Electronic Materials* (2025). DOI: 10.1021/acsaelm.4c01992.

[233] Philipp Moll, Georg Pfusterschmied, Sabine Schwarz, Michael Stöger-Pollach, and Ulrich Schmid. "Impact of alternating precursor supply and gas flow on the LPCVD growth behavior of polycrystalline 3C-SiC thin films on Si". In: *Sensors and Actuators A: Physical* 372 (2024), p. 115376. DOI: 10.1016/j.sna.2024.115376.

[234] R. S. Krishnan. "Raman spectra of the second order in crystals". In: *Proceedings of the Indian Academy of Sciences - Section A* 22.5 (1945), p. 329. DOI: 10.1007/BF03173959.

[235] P. G. Spizzirri, J.-H. Fang, S. Rubanov, E. Gauja, and S. Prawer. *Nano-Raman spectroscopy of silicon surfaces*. 2010. DOI: 10.48550/arXiv.1002.2692. arXiv: 1002.2692 [cond-mat.mtrl-sci].

[236] N I Fainer, A N Golubenko, Yu M Rumyantsev, V G Kesler, B M Ayupov, V I Rakhlin, and M G Voronkov. "Tris(diethylamino)silane—A New Precursor Compound for Obtaining Layers of Silicon Carbonitride". In: *Glass Physics and Chemistry* 38.1 (2012), pp. 15–26. DOI: 10.1134/S1087659612010051.

[237] Jozef Huran, Albín Valovič, Michal Kučera, Angela Kleinová, Eva Kovačcová, Pavol Boháček, and Mária Sekáčová. "Hydrogenated amorphous silicon carbon nitride films prepared by PECVD technology: properties". In: *Journal of Electrical Engineering* 63.5 (2012), pp. 333–335. DOI: 10.2478/v10187-012-0049-z.

[238] Fang Liu, Carlo Carraro, Albert P Pisano, and Roya Maboudian. "Growth and characterization of nitrogen-doped polycrystalline 3C-SiC thin films for harsh environment MEMS applications". In: *Journal of Micromechanics and Microengineering* 20.3 (2010), p. 035011. DOI: 10.1088/0960-1317/20/3/035011.

[239] G Krötz, H Möller, M Eickhoff, S Zappe, R Ziermann, E Obermeier, and J Stoemenos. "Heteroepitaxial growth of 3C-SiC on SOI for sensor applications". In: *Materials Science and Engineering: B* 61-62 (1999), pp. 516–521. DOI: 10.1016/S0921-5107(98)00464-4.

[240] Mathieu Boccard and Zachary C. Holman. "Amorphous silicon carbide passivating layers for crystalline-silicon-based heterojunction solar cells". In: *Journal of Applied Physics* 118.6 (2015), p. 065704. DOI: 10.1063/1.4928203.

[241] Yongcai Qiu, Shihe Yang, Hong Deng, Limin Jin, and Weishan Li. "A novel nanostructured spinel $ZnCo_2O_4$ electrode material: morphology conserved transformation from a hexagonal shaped nanodisk precursor and application in lithium ion batteries". In: *Journal of Materials Chemistry* 20.21 (2010), pp. 4439–4444. DOI: 10.1039/C0JM00101E.

[242] L. Calcagno, P. Musumeci, F. Roccaforte, C. Bongiorno, and G. Foti. "Crystallisation mechanism of amorphous silicon carbide". In: *Applied Surface Science*. Proceeding of the European Materials Research Soceity 2001-Symposium F "Amorphous and crystalline Silicon Carbide: material and applications" 184.1 (2001), pp. 123–127. DOI: 10.1016/S0169-4332(01)00487-1.

[243] Muthu B.J Wijesundara, Conrad R Stoldt, Carlo Carraro, Roger T Howe, and Roya Maboudian. "Nitrogen doping of polycrystalline 3C–SiC films grown by single-source chemical vapor deposition". In: *Thin Solid Films* 419.1 (2002), pp. 69–75. DOI: 10.1016/S0040-6090(02)00782-4.

[244] Gwiy-Sang Chung and Jeong-Hak Ahn. "Characterization of polycrystalline 3C–SiC thin film diodes for extreme environment applications". In: *Microelectronic Engineering* 85.8 (2008), pp. 1772–1775. DOI: 10.1016/j.mee.2008.05.007.

[245] Kaifu Qiu, Manuel Pomaska, Shenghao Li, Andreas Lambertz, Weiyuan Duan, Alaaeldin Gad, Matthias Geitner, et al. "Development of Conductive SiC_x:H as a New Hydrogenation Technique for Tunnel Oxide Passivating Contacts". In: *ACS Applied Materials & Interfaces* 12.26 (2020), pp. 29986–29992. DOI: 10.1021/acsami.0c06637.

[246] Lihong Xiao, Oleksandr Astakhov, Reinhard Carius, Tao Chen, Haiyan Wang, Martin Stutzmann, and Friedhelm Finger. "Paramagnetic states in µc-SiC:H thin films prepared by Hot-Wire CVD at low temperatures". In: *physica status solidi c* 7.3 (2010), pp. 778–781. DOI: 10.1002/pssc.200982871.

[247] F. Demichelis, C. F. Pirri, and E. Tresso. “Microcrystallization formation in silicon carbide thin films”. In: *Philosophical Magazine B* 66.1 (1992), pp. 135–146. DOI: 10.1080/13642819208221301.

[248] Muhammad Shoaib Anwar, Syed Zaighum Abbas Bukhari, Jang-Hoon Ha, Jongman Lee, In-Hyuck Song, and Young-Wook Kim. “Controlling the electrical resistivity of porous silicon carbide ceramics and their applications: A review”. In: *International Journal of Applied Ceramic Technology* 19.4 (2022), pp. 1814–1840. DOI: 10.1111/ijac.14034.

[249] Lihong Xiao, Oleksandr Astakhov, Tao Chen, Martin Stutzmann, and Friedhelm Finger. “Aluminum doped silicon carbide thin films prepared by hot-wire CVD: Investigation of defects with electron spin resonance”. In: *Thin Solid Films* 519.14 (2011), pp. 4519–4522. DOI: 10.1016/j.tsf.2011.01.320.

[250] A. Avila, I. Montero, L. Galán, J. M. Ripalda, and R. Levy. “Behavior of oxygen doped SiC thin films: An x-ray photoelectron spectroscopy study”. In: *Journal of Applied Physics* 89.1 (2001), pp. 212–216. DOI: 10.1063/1.1332796.

[251] Dong Feng, Quanxing Ren, Hongqiang Ru, Wei Wang, Yan Jiang, Shiyuan Ren, and Cuiping Zhang. “Effect of oxygen content on the sintering behaviour and mechanical properties of SiC ceramics”. In: *Ceramics International* 45.18 (2019), pp. 23984–23992. DOI: 10.1016/j.ceramint.2019.08.100.

[252] Martin A. Green and Mark J. Keevers. “Optical properties of intrinsic silicon at 300 K”. In: *Progress in Photovoltaics: Research and Applications* 3.3 (1995), pp. 189–192. DOI: 10.1002/pip.4670030303.

[253] J. Serra, J. Andreu, G. Sardin, C. Roch, J. M. Asensi, J. Bertomeu, and J. Esteve. “Hydrogen related effects in a-Si:H studied by photothermal deflection spectroscopy”. In: *Physica B: Condensed Matter* 170.1 (1991), pp. 269–272. DOI: 10.1016/0921-4526(91)90136-3.

[254] L. Magafas, N. Georgoulas, D. Girginoudi, and A. Thanailakis. “Structural and optical properties of a-SiC:H thin films”. In: *Journal of Non-Crystalline Solids* 139 (1992), pp. 146–150. DOI: 10.1016/S0022-3093(05)80816-6.

[255] Malte Köhler, Manuel Pomaska, Alexandr Zamchiy, Andreas Lambertz, Weiyuan Duan, Florian Lentz, Shenghao Li, et al. “Optimization of Transparent Passivating Contact for Crystalline Silicon Solar Cells”. In: *IEEE Journal of Photovoltaics* 10.1 (2020), pp. 46–53. DOI: 10.1109/JPHOTOV.2019.2947131.

[256] M. Dürr and U. Höfer. "Dissociative adsorption of molecular hydrogen on silicon surfaces". In: *Surface Science Reports* 61.12 (2006), pp. 465–526. DOI: 10.1016/j.surfrep.2006.08.002.

Acknowledgements

Well, thanks are due to so many people, and I'm sure I will forget someone who has been essential in supporting me throughout the writing of this thesis. Still, you're only as good as your effort – so I will try to provide a broad overview of all the wonderful people who have helped me over the past three years and even before.

First and foremost, I would like to express my deepest gratitude to my supervisor, Professor Uwe Rau, for his invaluable guidance, support, and encouragement throughout the past three years. His expertise, patience, and insightful feedback were essential to the completion of this work. I also want to thank my direct supervisor, Professor Maurice Nuys, who was always available for questions, quick discussions, and for finding solutions that helped drive this work forward. My sincere thanks also go to my group leader, Professor Stefan Haas, who gave me the opportunity and the freedom to attend insightful conferences and to carry out my research stay at the National Institute of Advanced Industrial Science and Technology (AIST) in Japan – an experience I consider the most formative of my doctoral studies. In Japan, I was warmly welcomed by my supervisor Professor Takuya Matsui and his colleague Dr. Hitoshi Sai. Their support helped me advance my research and introduced me to the rich nature and culture of Japan. I am very thankful to both of them.

Furthermore, I would like to extend my sincere thanks to my second assessor, [Here Name], for the time, interest in my work, and the valuable contribution in supporting me toward the attainment of my doctoral degree.

Scientific work, especially in experimental research, depends not only on supervision but also on the invaluable support of colleagues. A special thank-you goes to Gunnar Schöpe, who assisted me with countless experiments and the construction of my APCVD setup. I would also like to thank Brigitte Zwaygardt, Frank Pennartz, Pascal Foucart, Alain Doumit, Volker Lauterbach, Andra Lye, Dr. Astrid Besmehn, Dr. Zhihao Xu, and Peter Jakes for their support with sample preparation and measurements. My gratitude also goes to Dr. Sascha Astakhov for his assistance with ESR measurements, his thoughtful analyses, and for our engaging discussions

on a-Si:H thin films and their properties. Thanks to Dr. Benjamin Klingebiel for his support with chemical questions and Glovebox maintenance, and to Michael Schaaf for helping design, build, and continually improve the APCVD chamber. I would also like to thank Alexander Eberst and Binbin Xu for their helpful discussions and support with hydrogenation and catalytic doping of my samples using HWCVD.

I wish to acknowledge Dr. Wolfhard Beyer, who passed away during the first year of my PhD. Even in the short time I knew him, he gave me deep insights into both the world of amorphous materials and the life of a scientist. I remain grateful for that time.

Beyond the scientific environment, I want to thank all my friends – from home, school, apprenticeship, and university – for their encouragement, motivation, and for providing memorable adventures that helped me recharge and step away from the daily routine.

Above all, my deepest gratitude goes to my family, who have done the most to put me on the path I'm on today. They supported me in every possible way and helped me through every challenge that arose during this journey. A special thank-you goes to the most legendary three uncles in the world – Axel, Michael, and Markus – along with my aunts Inge and Renate, and my cousin Marius. I am especially grateful to my grandmother Oma Nelli, who has always supported me and continues to keep her door open in any situation. I also want to express my appreciation and remembrance for my other grandparents – Meta, Ludwig, and Willi – who sadly passed away but whose influence still means a lot to me. Finally, I want to end this section with my greatest supporters: my sister Tamara, my father Thomas, and my mother Carmen. Thank you so much for always being there, for putting up with me throughout my life, and for continuing to support me unconditionally.

I hope that one day, I can give back all the support and everything I've learned – whether directly to you or by helping someone else when they need it most.

List of Publications

List of publications related to this thesis

[1] Benedikt Fischer, Maurice Nuys, Oleksandr Astakhov, Stefan Haas, Michael Schaaf, Astrid Besmehn, Peter Jakes, et al. "Advanced atmospheric pressure CVD of a-Si:H using pure and cyclooctane-diluted trisilane as precursors". In: *Sustainable Energy & Fuels* (2024). DOI: 10.1039/D4SE01308E.

[2] Benedikt Fischer, Maurice Nuys, Stefan Haas, Oliver Thimm, Gunnar Schöpe, Pascal Foucart, Astrid Besmehn, and Uwe Rau. "Synthesis and Characterization of Nitrogen-Doped Crystallized SiC Films from Liquid Precursors". In: *ACS Applied Electronic Materials* (2025). DOI: 10.1021/acsaelm.4c01992.

Patent applications

[1] Benedikt Fischer, Maurice Nuys, and Michael Schaaf. "Dünnschichten aus Silizium hergestellt durch CVD mittels Flüssigsilanen mit einstellbarem Kohlenstoffgehalt". Patent WO 2025/016981 A1 (DE). Forschungszentrum Jülich GmbH. 2025.

[2] Benedikt Fischer and Maurice Nuys. "Siliziumkarbid-Dünnschichten, hergestellt durch CVD mittels flüssigen Präkursor enthaltend Silizium und Kohlenstoff". Patent (DE). Forschungszentrum Jülich GmbH. 2025.

[3] Benedikt Fischer, Maurice Nuys, and Walter Carolin. "Verfahren und Vorrichtung zur Materialanlagerung". Patent (DE). Forschungszentrum Jülich GmbH. 2025.

List of other publications in the period of this study

[1] Benedikt Fischer, Wolfhard Beyer, Andreas Lambertz, Maurice Nuys, Weiyuan Duan, Kaining Ding, and Uwe Rau. "The Microstructure of Underdense Hydro-

genated Amorphous Silicon and its Application to Silicon Heterojunction Solar Cells". In: *Solar RRL* 7.10 (2023), p. 2300103. DOI: 10.1002/solr.202300103.

[2] Benedikt Fischer, Andreas Lambertz, Maurice Nuys, Wolfhard Beyer, Weiyuan Duan, Karsten Bittkau, Kaining Ding, and Uwe Rau. "Insights into the Si—H Bonding Configuration at the Amorphous/Crystalline Silicon Interface of Silicon Heterojunction Solar Cells by Raman and FTIR Spectroscopy". In: *Advanced Materials* 35.47 (2023), p. 2306351. DOI: 10.1002/adma.202306351.

[3] Benedikt Fischer, Hitoshi Sai, Zhihao Xu, Maurice Nuys, Andreas Lambertz, Volker Lauterbach, Kaining Ding, et al. "Light soaking of silicon heterojunction solar cells by applying high-intensity line-shaped laser scans". In: *Cell Reports Physical Science* 6.5 (2025), p. 102558. DOI: 10.1016/j.xcrp.2025.102558.

[4] Patrick Weber, Andreas Petzold, Oliver F. Bischof, Benedikt Fischer, Marcel Berg, Andrew Freedman, Timothy B. Onasch, and Ulrich Bundke. "Relative errors in derived multi-wavelength intensive aerosol optical properties using cavity attenuated phase shift single-scattering albedo monitors, a nephelometer, and tricolour absorption photometer measurements". In: *Atmospheric Measurement Techniques* 15.11 (2022), pp. 3279–3296. DOI: 10.5194/amt-15-3279-2022.

[5] Patrick Weber, Oliver F. Bischof, Benedikt Fischer, Marcel Berg, Jannik Schmitt, Gerhard Steiner, Lothar Keck, et al. "A new working fluid for condensation particle counters for use in sensitive working environments". In: *Aerosol Research* 1.1 (2023), pp. 1–12. DOI: 10.5194/ar-1-1-2023.

[6] Patrick Weber, Oliver F. Bischof, Benedikt Fischer, Marcel Berg, Susanne Hering, Steven Spielman, Gregory Lewis, et al. "Characterisation of a self-sustained, water-based condensation particle counter for aircraft cruising pressure level operation". In: *Atmospheric Measurement Techniques* 16.14 (2023), pp. 3505–3514. DOI: 10.5194/amt-16-3505-2023.

Conferences

[1] B. Fischer, W. Beyer, A. Lambertz, M. Nuys, W. Duan, and K. Ding. "Investigation of the Microstructure of Underdense Hydrogenated Amorphous Silicon Layers by Raman Spectroscopy and Hydrogen Effusion". In: *SiliconPV 2023, 13th International Conference on Crystalline Silicon Photovoltaics*. Apr. 2023.

[2] B. Fischer, M. Nuys, A. Lambertz, W. Duan, K. Ding, and U. Rau. "Investigation of the Microstructure of Underdense Hydrogenated Amorphous Silicon Layers for Silicon Heterojunction Solar Cells by Raman Spectroscopy and Hydrogen Effusion". In: *2023 IEEE 50th Photovoltaic Specialists Conference (PVSC)*. June 2023. DOI: 10.1109/PVSC48320.2023.10359953.

[3] B. Fischer, M. Nuys, A. Lambertz, and U. Rau. "Low-cost Grown a-Si:H Using Trisilane and its Application to Post Deposition Processes". In: *2024 AVS 70th International Symposium and Exhibition*. Nov. 2024.

Curriculum Vitae

June 17th, 2026	Doctoral Examination for Dr. rer. nat.
2025–2026	Project Manager / Research Associate Institute of Energy Materials and Devices – Photovoltaics (IMD-3) Forschungszentrum Jülich GmbH, Germany
2022–2025	Research Assistant and Doctoral Candidate Institute of Energy Materials and Devices – Photovoltaics (IMD-3) Forschungszentrum Jülich GmbH, Germany
2024	JSPS Research Stipendium National Institute of Advanced Industrial Science and Technology (AIST) Tsukuba, Japan
2020–2022	Studies of Physics (Specialization: Nanoelectronics) RWTH Aachen University, Germany
May 2020	Master of Science
2016–2020	Studies of Physical Engineering FH Aachen, University of Applied Sciences, Germany
February 2020	Bachelor of Engineering
2015–2019	Apprenticeship as Physics Laboratory Technician Forschungszentrum Jülich GmbH, Germany
2007–2015	General Higher Education Entrance Qualification (Abitur) Franziskus Gymnasium Vossenack, *Hürtgenwald, Germany*
1997	Born in *Simmerath, Germany*

A. Supplementary Figures

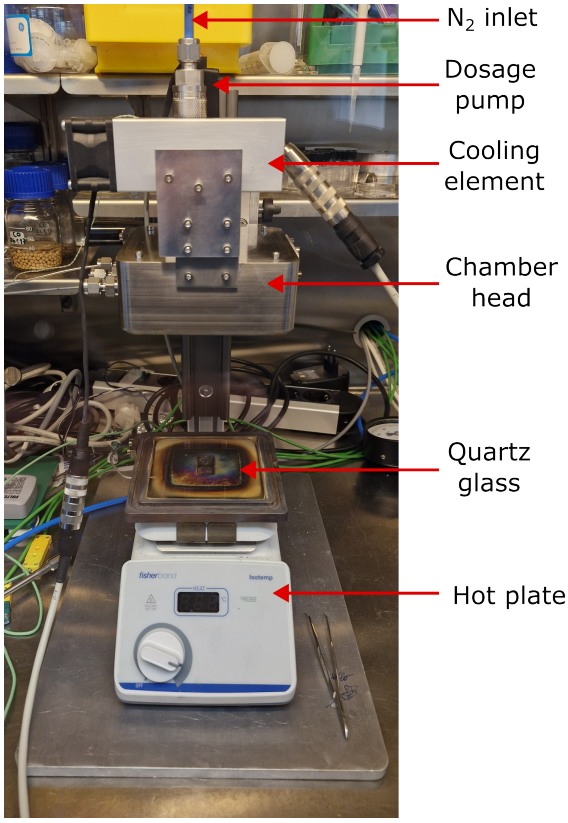


Figure A.1.: Photograph of the APCVD deposition system assembled inside a glove box. The hot plate is visible at the bottom, and the chamber head is raised to its upper position, with cooling elements on top for the inlet block (not visible here), which is located just behind these elements. The quartz glass is already coated with several a-Si:H and a-SiC:H layers from former depositions.

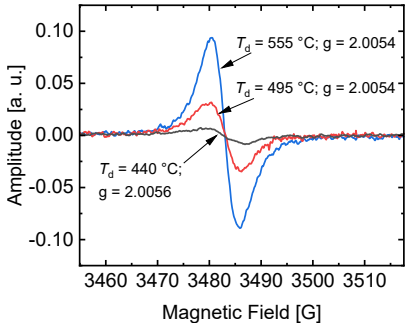


Figure A.2.: ESR spectra of the a-Si:H films of the "ESR" series deposited with pure trisilane. The deposition temperature T_d and the g-value determined by the spectra are given in the graph. Adapted from Fischer et al.[164] (2023), licensed under CC BY 3.0.

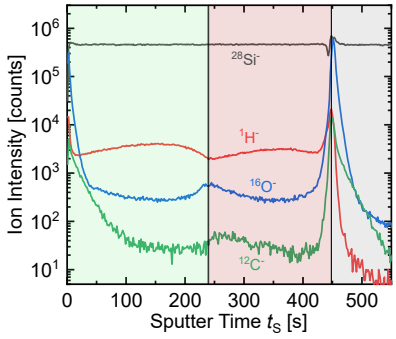


Figure A.3.: Silicon, hydrogen, carbon, and oxygen SIMS depth profiles of an APCVD a-Si:H film deposited by two precursor injections of 10 µl each, one at the beginning of deposition and the second after 10 min. The total treatment time was 20 min at 440 °C.

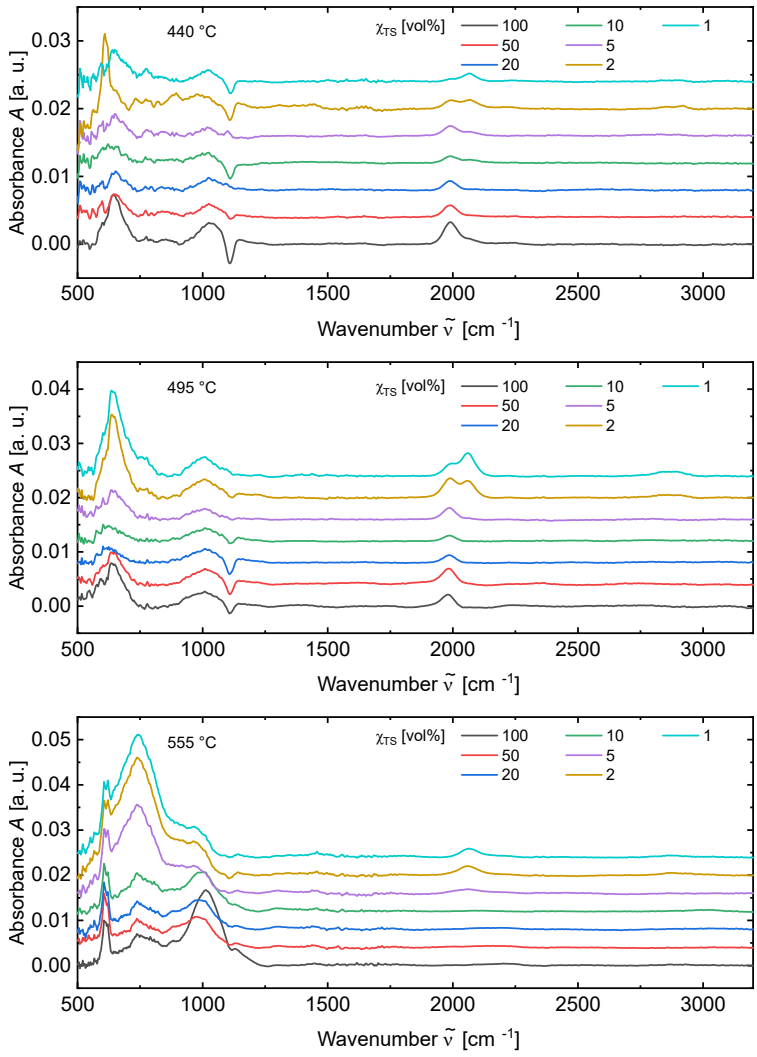


Figure A.4.: FTIR spectra of a-Si:H films deposited using trisilane concentrations of 1–100 vol% diluted in cyclooctane at three different temperatures: a) 440 °C, b) 500 °C and c) 555 °C. The spectra are bases for the data given in Figure 4.9. Sharp peaks at 610 cm^{-1} are related to wafer artifacts, and the increased peak at 1000 cm^{-1} for the film deposited with 100 vol% TS shown in c) probably is due to increased O content within the chamber since it was the first deposition on that day.

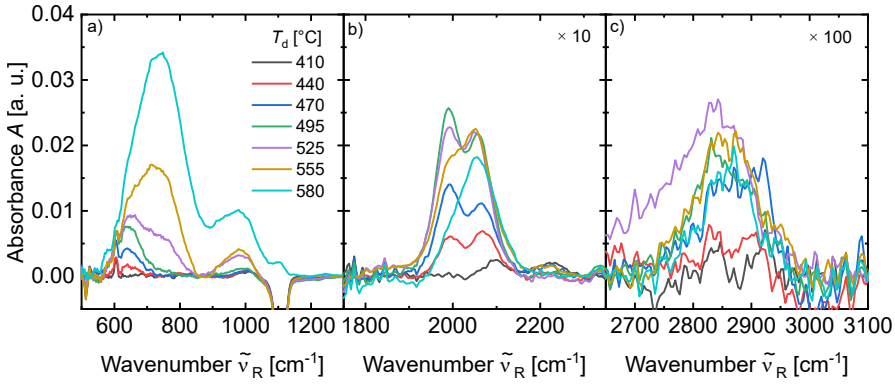


Figure A.5.: FTIR spectra of a-Si:H films deposited with 2 vol% trisilane diluted in cyclooctane at deposition temperatures T_d between 410 and 580 °C. a) Si-H wagging, Si-C stretching, and Si-C-H_x wagging modes; b) Si-H stretching modes; c) C-H stretching modes.

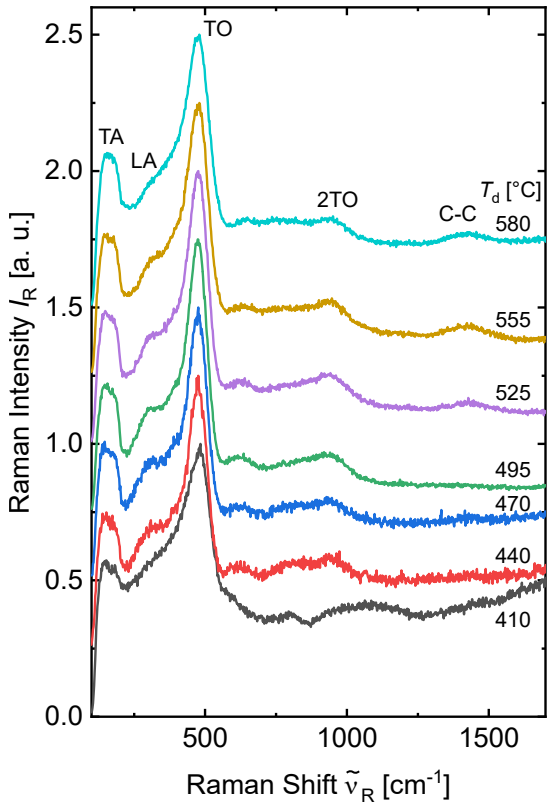


Figure A.6.: Raman spectra of a-Si:H films deposited using 2 vol% trisilane diluted in cyclooctane at deposition temperatures T_d between 410 and 580 °C. The deposition temperatures as well as the origin of the most significant peaks are indicated within the graph. The following modes are indicated: transversal acoustic (TA) Si-Si, longitudinal acoustic (LA) Si-Si, transversal optical (TO) Si-Si, Si-H stretching, and C-C cluster modes.

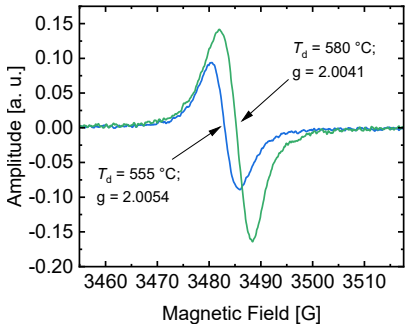


Figure A.7.: ESR spectra of an a-Si:H film deposited with 2 vol% trisilane diluted in cyclooctane in comparison with a film deposited with pure silane. The deposition temperature T_d and the g-value determined by the spectra are given in the graph. Adapted from Fischer et al.[164] (2023), licensed under CC BY 3.0.

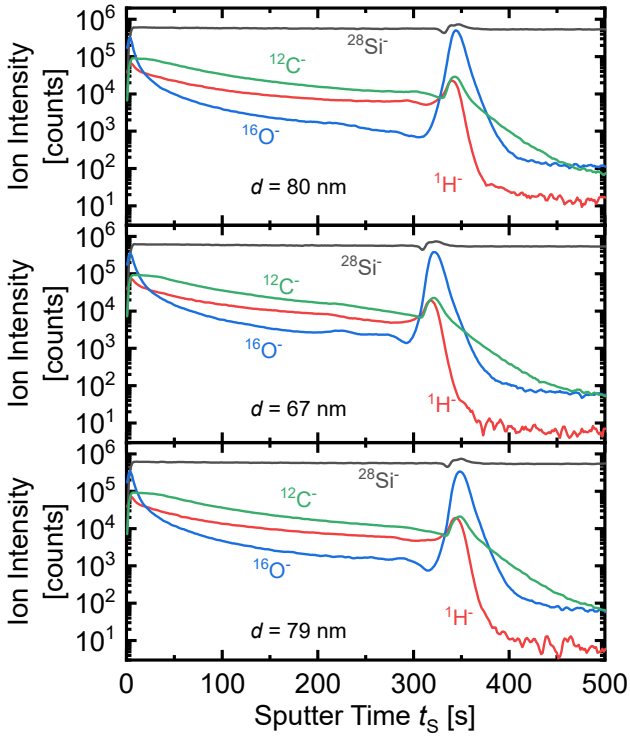


Figure A.8.: Silicon, hydrogen, carbon, and oxygen SIMS depth profiles of APCVD films deposited using three different deposition processes under identical conditions, with 600 µl of 2 vol% TS at T_d = 470 °C for 10 min. Film thicknesses for the samples are indicated within the graph.

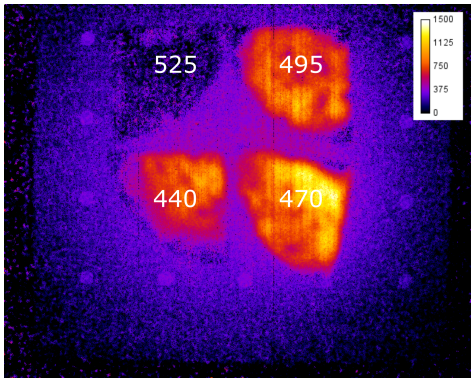


Figure A.9.: PL image of a quartered n-type float-zone c-Si wafer (original diameter: 4 inches), symmetrically coated on both sides with a-Si:H passivation layers deposited at 440, 470, 495, and 525 °C. The deposition temperature for each sample is indicated within the image.

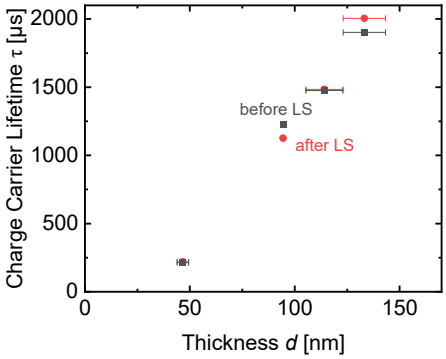


Figure A.10.: a) Charge carrier lifetime τ of n-type CZ c-Si wafer versus thickness d of the a-Si:H passivation layers covering the wafer before and after intensive light soaking. The edges of the error bar indicate the thickness of the films on each side of a sample.

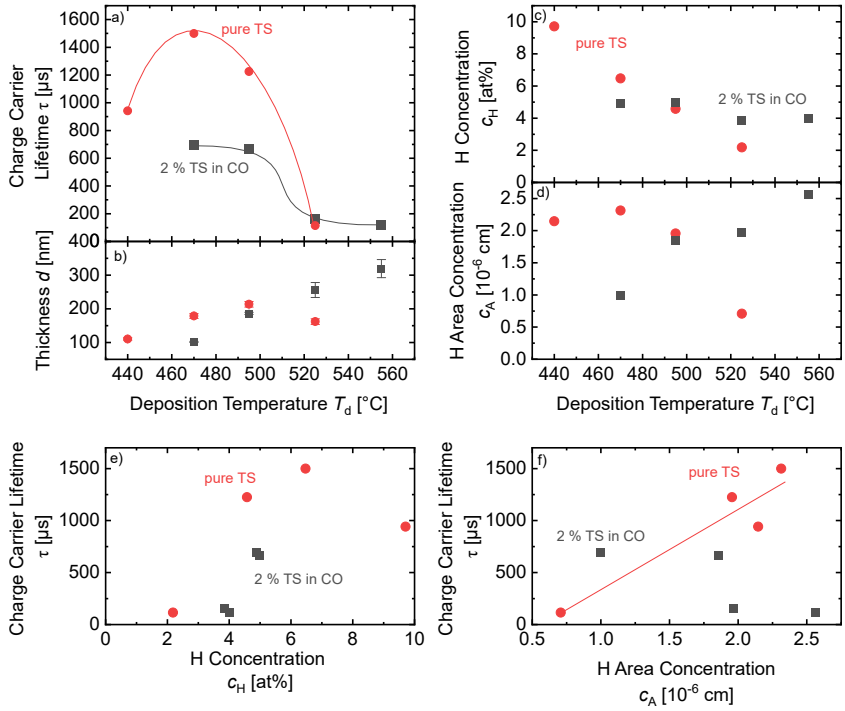


Figure A.11.: a) Charge carrier lifetime τ of p-type c-Si wafers covered with a-Si:H films and b) thickness d of those a-Si:H passivation layers versus their deposition temperature T_d. The edges of the error bar indicate the thickness of the films on each side of a sample. c) H area concentration c_A and d) H concentration c_H of the same samples versus deposition temperature. Charge carrier lifetime t versus e) H area concentration c_A and f) H concentration c_H of the same samples. The lines are guides to the eye. Gray squares mark data points of a-Si:H films made with 2 vol% TS diluted in CO and red circles mark data points of a-Si:H films made with pure TS.

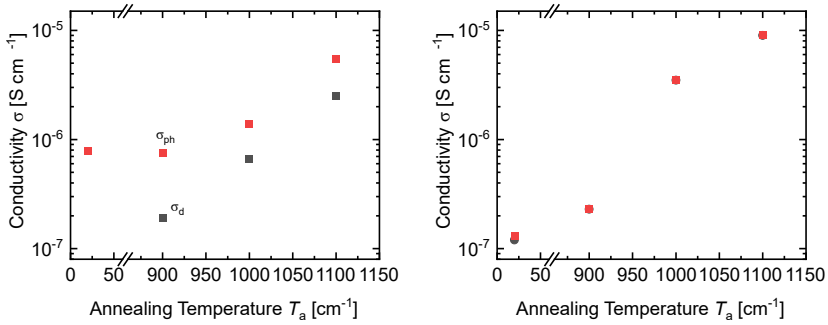


Figure A.12.: Photo- and dark conductivity σ_{ph} and σ_{d} of silicon films deposited using a) pure TS and b) 2 vol% TS in CO as a precursor at 580 °C and annealed at $T_{\mathrm{a}} = 900$, 1000, and 1100 °C.

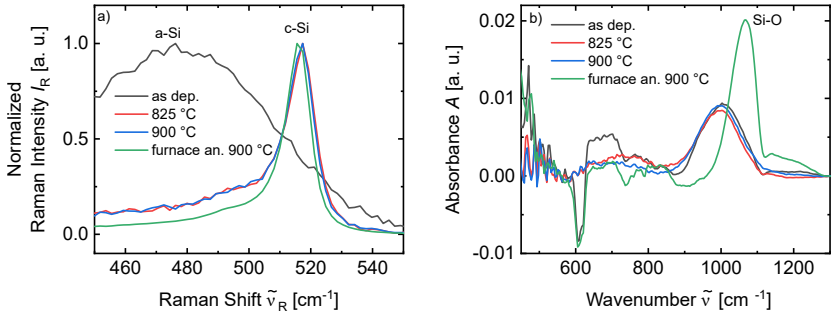


Figure A.13.: a) Raman and b) FTIR spectra of silicon films deposited using pure TS at 580 °C and annealed at $T_{\mathrm{a}} = 825$, and 900 °C via RTA, and at 900 °C via furnace.

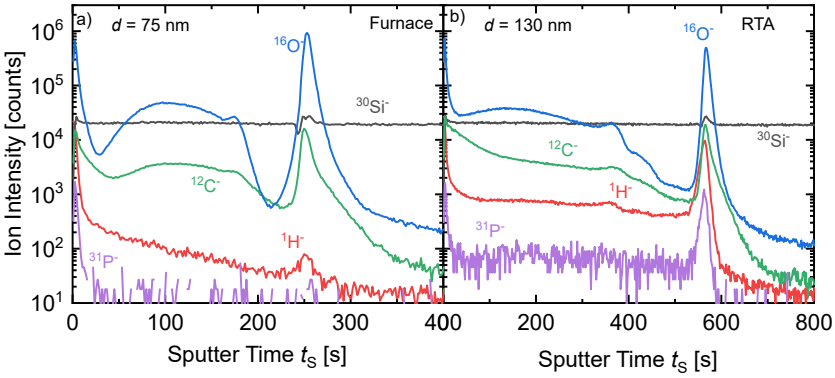


Figure A.14.: Silicon, hydrogen, carbon, oxygen, and phosphor SIMS depth profiles of via a) furnace annealing and b) rapid thermal annealing crystallized a-Si:H films deposited at 580 °C. Film thicknesses are given on the upper left of the graphs.

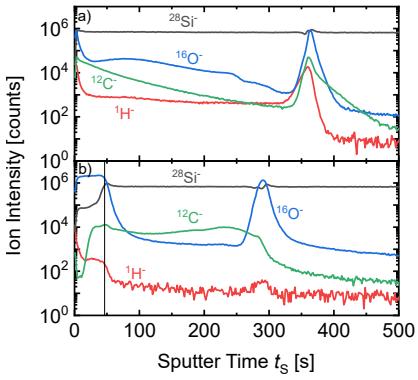


Figure A.15.: Silicon, hydrogen, carbon, and oxygen SIMS depth profiles of a) an a-Si:H film deposited at 555 °C using pure TS and b) a film deposited at the same conditions but after furnace annealing at 1100 °C. In b), the black horizontal line indicates the interface between the silicon oxide layer formed during annealing and the underlying recrystallized silicon film.

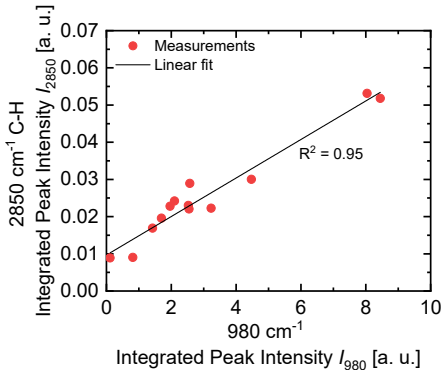


Figure A.16.: Integrated peak intensity of the C-H mode at 2850 cm^{-1} measured via FTIR on a-SiC:H films versus the peak intensity of the Si-O/Si-C-H_x peak at 980 cm^{-1}. The integrated peak intensity here is calculated via Equation 3.5, but using the absorbance A instead of the absorption coefficient α.

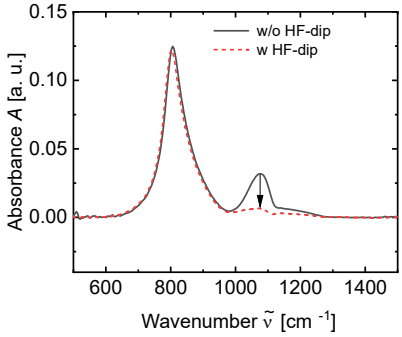


Figure A.17.: FTIR spectra of SiC films crystallized at $T_a = 1100\,°C$ before (gray) and after (red) HF-etching of the surface oxide. The arrow indicates the reduction of the Si-O_x peak due to the etching of an O-rich film near the surface. Adapted from Fischer et al.[232] (2025), licensed under CC BY 4.0.

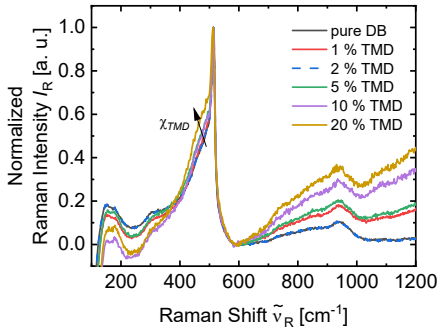


Figure A.18.: Raman spectra of SiC films crystallized at $T_a = 1100$ °C, deposited with $T_d = 585$ °C using various concentrations χ_{TMD} of TMD. The spectra were normalized using the c-Si peak as 1 and the minimum after the peak as 0. The arrow indicates the increase of the amorphous to the c-Si fraction.

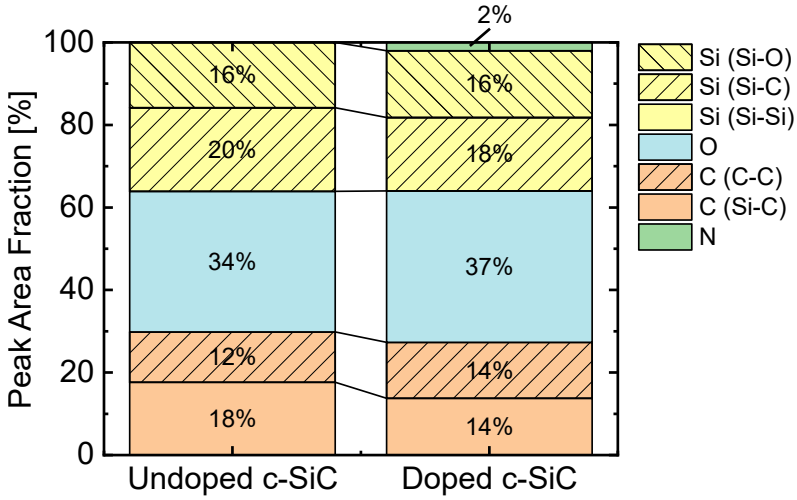


Figure A.19.: Atomic composition at the surface of undoped and doped c-SiC films deposited at a temperature T_d of 585 °C measured by XPS. For the percentage values, it was assumed that the material consists only of Si, C, N, and O.

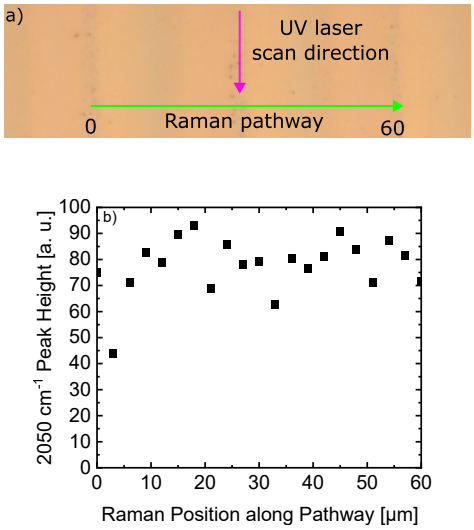


Figure A.20.: a) Microscopic image of a crystallized SiC film after UV laser treatment. The purple arrow indicates the direction of the UV laser used for annealing, while the green arrow marks the path along which Raman measurements were performed at intervals of 3 µm. b) Corresponding plot of the maximum peak heights of the Si-H stretching mode observed at a Raman shift of ~2050 cm^{-1}.

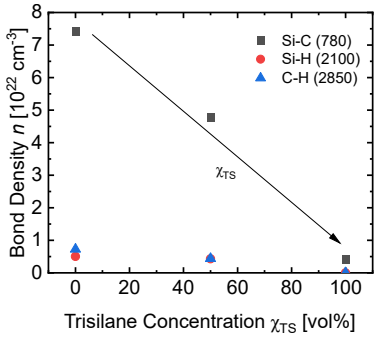


Figure A.21.: Bond densities n of Si-C, Si-H and C-H bonds as measured by FTIR in c-SiC films deposited using TS-DB mixtures.

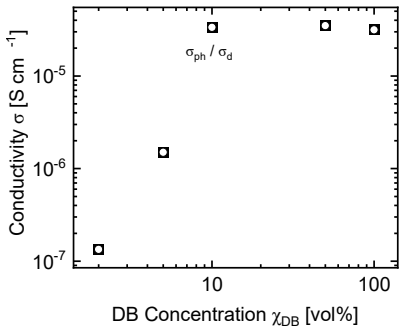


Figure A.22.: Photo- and dark conductivity σ_{ph} and σ_{d} after annealing of the a-SiC:H films from Figure 5.15 deposited using 1 to 100 vol% disilabutane diluted in cyclooctane as precursor.

Band / Volume 722
Combining Lattice Boltzmann Simulation and Synchrotron Imaging to Study Bubble Dynamics in Electrodes of Vanadium Redox Flow Batteries
K. Duan (2026), xxiii, 116 pp
ISBN: 978-3-95806-954-1 (Print)
ISBN: 978-3-95806-955-8 (E-Book)

Band / Volume 723
Geophysical characterization of landscapes along a climate and vegetation gradient in the Chilean coastal cordillera
I. Dal Bo (2026), 138 pp
ISBN: 978-3-95806-956-5 (Print)
ISBN: 978-3-95806-957-2 (E-Book)

Band / Volume 724
Model informed assessment of observation impact for emission rate optimization using four-dimensional variational data assimilation
A. Hermanns (2026), xvi, 109 Seiten
ISBN: 978-3-95806-958-9 (Print)
ISBN: 978-3-95806-959-6 (E-Book)

Band / Volume 725
Synthese und Bewertung hochaktiver Katalysatoren zur Herstellung höherer Alkohole aus Methanol als Kraftstoff
J. Häusler (2026), xiii, 265 Seiten
ISBN: 978-3-95806-962-6 (Print)
ISBN: 978-3-95806-963-3 (E-Book)

Band / Volume 726
Development and Characterization of Ni_3Fe Layered Double Hydroxide-Based Oxygen-Evolution Electrodes for Anion Exchange Membrane Water Electrolysis
I.Galkina (2026), vii, 173, xxxiii Seiten
ISBN: 978-3-95806-966-4 (Print)
ISBN: 978-3-95806-967-1 (E-Book)

Band / Volume 727
Surface Regeneration of Plasma-Facing Components by Wire-Based Laser Metal Deposition
J. Tweer (2026), XX, 186 pp
ISBN: 978-3-95806-970-1 (Print)
ISBN: 978-3-95806-971-8 (E-Book)

Band / Volume 728
Reducing the noble metal and titanium content of anode PTLs in PEM water electrolysis – performance and degradation
S. Zerressen (2026), XIII, 235 pp
ISBN: 978-3-95806-972-5 (Print)
ISBN: 978-3-95806-973-2 (E-Book)

Schriften des Forschungszentrums Jülich
Reihe Energie & Umwelt / Energy & Environment

Band / Volume 729
Gasfernleitungsnetze und deren Umstellung auf Wasserstoff
T. A. Triesch (2026), 364 pp
ISBN: 978-3-95806-978-7 (Print)
ISBN: 978-3-95806-979-4 (E-Book)

Band / Volume 730
Land-Atmosphere Coupling in a Changing Climate: Understanding Variability, Extremes, and Human Influence through Regional Climate Modeling
Y. Zhang (2026), 135 pp
ISBN: 978-3-95806-980-0 (Print)
ISBN: 978-3-95806-981-7 (E-Book)

Band / Volume 731
Abbildung gekoppelter Infrastrukturen in Energiesystemmodellen
P. Freitag (2026), XIX, 322 pp
ISBN: 978-3-95806-984-8 (Print)
ISBN: 978-3-95806-985-5 (E-Book)

Band / Volume 732
Cost-reduced and Sustainable Interconnects and their Coatings for Solid Oxide Cells
M. Hilger (2026), viii, 185 pp
ISBN: 978-3-95806-988-6 (Print)
ISBN: 978-3-95806-989-3 (E-Book)

Band / Volume 733
Liquid-Phase Synthesis of Silicon and Silicon Carbide Thin-Films via Atmospheric Pressure Chemical Vapor Deposition
B. Fischer (2026), xxii, 211, A15
ISBN: 978-3-95806-990-9 (Print)
ISBN: 978-3-95806-991-6 (E-Book)

Weitere ***Schriften des Verlags im Forschungszentrum Jülich*** unter
http://wwwzb1.fz-juelich.de/verlagextern1/index.asp

Energie & Umwelt / Energy & Environment
Band / Volume 733
ISBN 978-3-95806-991-6

Mitglied der Helmholtz-Gemeinschaft

JÜLICH
Forschungszentrum